이학박사학위논문

Experimental verification of photonic band-tail states and their use for shaping laser properties

광자 띠꼬리 상태의 실험적 입증과 이에 기반한 레이저 특성의 제어

2018년 2월

서울대학교 대학원

물리천문학부

이 명 재

Experimental verification of photonic band-tail states and their use for shaping laser properties

by
Myungjae Lee

Supervised by
Professor Heonsu Jeon

A Dissertation Submitted to the Faculty of
Seoul National University
in Partial Fulfillment of the Requirements
for the Degree of
Doctor of Philosophy

February 2018

Department of Physics and Astronomy
Graduate School
Seoul National University

Experimental verification of photonic band-tail states and their use for shaping laser properties

광자 띠꼬리 상태의 실험적 입증과
이에 기반한 레이저 특성의 제어

지도교수 전 헌 수

이 논문을 이학박사 학위논문으로 제출함.
2018년 2월

서울대학교 대학원
물리천문학부
이 명 재

이명재의 박사학위 논문을 인준함.
2018년 2월

위 원 장 박 건 식 (인)

부 위 원 장 전 헌 수 (인)

위 원 김 대 식 (인)

위 원 차 국 린 (인)

위 원 박 규 환 (인)

Abstract

Experimental verification of photonic band-tail states and their use for shaping laser properties

Myungjae Lee
Department of Physics and Astronomy
The Graduate School
Seoul National University

Shaping light to generate desired optical properties is one of the important topics in optics and photonics that has been studied for a long time. A complete control over the light intensity, polarization, frequency, phase, and even the spatio-temporal distribution of electromagnetic fields is the long-sought primary objective of light shaping, which can be the base technology for applied science and industry that handles the shape of light, leading to advanced optical functionalities and next generation photonic devices.

The study of light shaping is considered to be the process of controlling the shape of light by manipulating the spatial and temporal optical properties of material, with understanding of electromagnetic properties of the medium in which light propagates. Historically, material properties of media have been a major methodology, which is represented by the dispersion relation on wavelength, birefringence on polarization, and nonlinearity. However, research on structural properties such as reflection, diffraction, and scattering at the interface, originated from the spatial arrangement of materials, is being actively

carried out as well, consisting a large branch of modern photonics including photonic crystals, metamaterials, and topological photonics. The essence of studying light shaping is then to generate the structured light, using these material and structural methodologies, in order to improve an existing optical system and to develop new photonic devices.

Thus, within a finite material pool, the issues of shaping light eventually result in a problem of the spatio-temporal arrangement of materials. The structure based on the periodic arrangement is used in many fields due to the intuitive design, but this approach is difficult to apply to optical systems which require complexity, because of the limited structural parameters. On the other hand, an optically disordered system which randomly arranges materials without specific restrictions provides vast degrees of structural freedom that increase according to the system size, but consumes a large amount of resources in order to predict optical properties and to form desired light shapes. That is, the structural degree of freedom and the predictability are complementary.

In this thesis, a photonic crystal alloy is proposed as an ideal compromise that can easily predict and design optical properties while ensuring sufficient structural degrees of freedom to shape light with complexity corresponding to the real world. Here, the degree of freedom increases with the diversity of photonic atoms, however, the scattering strength at each lattice site can be controlled individually and independently to design the entire system in a pixelated scheme since the underlying crystalline structure is maintained.

The spectral characteristics are then investigated to reveal that the eigenmode of the proposed system is the photonic band-tail state existing in the photonic band-gap. For this state, it is experimentally confirmed that the energy range in which the states are distributed is determined by the crystalline structure and the scattering strength, and that the spatial near-field distribution

varies in a wide range, including the weak and strong localization, depending on the energy of the mode and the scattering strength of the structure. These observations prove the localization of the photonic band-tail state, which was theoretically predicted in 1987. In addition, the modal properties of the photonic band-tail states are distributed in a wide spectro-spatial range across the complete band-gap and from only a few lattices to the entire structure, which is a great advantage for light shaping.

The band-tail laser, a conceptually novel laser device that uses the band-tail state as a resonant mode, is proposed, and the light shaping within a membrane is demonstrated by realizing the band-tail laser in a slab waveguide embedding InAsP/InP multiple-quantum-well structure. Using only the structural parameters of the photonic crystal alloy, monotonic control of modal density from multi-mode to single-mode, and precise manipulation of both the modal energy and modal extents of a single-mode operating band-tail laser are demonstrated. Furthermore, the near-field profile of a mode can be modulated in various shapes from the fundamental shape to high-order shapes including orbital angular momentum and spiral pattern.

The design of light shaping, based on structural degrees of freedom in the band tail laser, is far more intuitive and effective than any disordered system, and the range of controllable modal properties and demonstrated shaping capabilities are superior to any known laser platform. The performance of band tail lasers is also comparable to the modern cavity lasers. Therefore, the photonic band-tail state and the band-tail laser, proposed in this thesis as a light shaping platform, could incorporate the currently known small library of lasing platform and even expand its boundary by realizing elaborate light shaping with various near-field shapes, which contributes to the development of various fields that deal with the shape of light.

Keyword: Shaping light, Structured light, Near-field shaping,
Light localization, Photonic band-tail states, Band-tail lasers,
Photonic crystal alloys, Random lasers

Student number: 2011-23275

Contents

List of Figures

Chapter 1 – Introduction

Chapter 2 – Photonic crystal alloys

Chapter 3 – Photonic band-tail states

Chapter 4 – Shaping band-tail states

Chapter 5 – Conclusion and outlook

Chapter 1 – Introduction

1.1. Shaping light

1.1.1. Current status of light shaping

Shaping light has attracted great interest in the history of optical science in order to increase available spatial and temporal degrees of freedom of light. Our modern technologies on light shaping is concerned with these degrees of freedom because it directly exerts on the number and accuracy of channels that transfer information, manipulate matters, and inspect systems. For example, most of the process of quantum communication such as encoding quantum information into photon polarization, maintaining quantum coherence on a macroscopic scale, and reading quantum bits from photons, is heavily dependent on state-of-the-art techniques of light shaping [1]. There are many other important needs in the field where the light-matter interaction is a fundamental principle for operation. Some obvious examples are particle manipulation [2], optical sensing [3], optical imaging [4], optical data storage [5], optical communication [6], cavity quantum electrodynamics [7], and quantum information science [8].

The shape of light is defined by distribution of electromagnetic vector fields [9]. The process of shaping light is then to redistribute intensity, polarization, and phase of an optical field to obtain the desired light shape, aiming a complete control over the spatial and temporal profiles, polarization, coherence, divergence angle, far-field profile, and any other properties of interest. Arguably, the laser and laser shaping are the most popular branches of this field because of their controllability on energy and coherence required in both fundamental and industrial aspects although the coherence of a light source is not a limiting factor in light shaping. In many applications, passive

optical components are sufficient to achieve the desired optical properties of interest. Nonetheless, an integration with active modulators that utilize the electro-optic, magneto-optic, or acousto-optic effects leads to cutting-edge technologies of this era, including spatio-temporal focusing [10], ultra-fast modulation [11], real-time wavefront correction [12], and vortex beam generation [13].

1.1.2. Shaping light within a membrane

Shaping the propagating beam has long been studied and widely used. In the similar context, confining and shaping light within a membrane have also brought a broad interest and impact to the various photonics fields because it enables to control over unique and important properties of confined light required for the research and application of the most advanced fields of photonics. In this approach, the shape of light fields is controlled by modulating the permittivity of materials constituting the membrane and cladding. Photonic crystals [14], metamaterials [15], and topological photonics [16] are branches of this field, which arrange dielectrics and metals in a periodic pattern on the wavelength scale of light. Reasonably, attempts have been made to utilize random structures for managing complex light shapes beyond the periodic nature.

The light-matter interaction in this approach is mainly mediated by the near-field (or, an evanescent field) dispersed over a membrane. It allows the information of light shapes to be encoded, manipulated, transmitted and inspected using unique principles such as transverse spin [17] and spin-momentum locking [18], and unidirectional excitation [19], originated from the spin-orbit interactions of confined light [20]. These intrinsic features of confined light are observable at any interface that supports evanescent fields, and resemble to those of surface states of topological insulators inherent in the quantum spin hall effect [21], although the surface photon state is not

a fermion. In fact, this subject has been studied in depth and is expected to extend to the core technology for the next generation optical devices that shape the light.

Shaping light within a membrane also has obvious advantages in terms of engineering. First, the mechanical stability of the device can be secured by the mechanical properties of the membrane, which can be further developed to realize flexible and foldable membranes as needed. Second, well-developed modern top-down process technologies can be applied due to the two-dimensional nature of the membrane. Third, with these advantages, various optical functions can be implemented within the membrane to replace bulk optical components conventionally used for light shaping, which require too much space. These concepts of chip-scale components have already been realized for passive components that perform a variety of basic operations [22]: lens, polarizer, coupler, splitter, drop filter, and phase shifter. For an active modulation, the electro-optic properties of organic or semiconductor membranes are mainly studied, driven by the all-optical method using a pump laser although there are alternative approaches such as implanting an electrical drivability to the membrane with proper doping and electrode design. Based on these methods, active on-chip components including intensity modulator, polarization modulator, and phase modulator are developed so far [23]. By integrating these unit operators into a photonic integrated circuit, high-level devices for shaping light can been realized within the membrane on chip-scale.

1.1.3. Shaping light using periodic materials

The process of light shaping within the membrane is mostly based on top-down fabrications, realizing a variety of functionalized membranes. It mainly controls the permittivity and refractive index of materials constituting the membrane and cladding to arrange the materials in a periodic manner on the wavelength scale of light. With this approach, it is possible to gain extensive controls over optical properties such as phase and group velocities, dispersion relations, and photonic band-gap, which are hard to be achieved by manipulating pure material properties. Many exotic artificial materials used for light shaping are realized using the periodic arrangement of materials, including negative-index materials, gradient-index materials, and angle or momentum dependent-index materials [14, 15, 16].

Research on these structural properties is a main concern of modern photonics, which is divided into sub-branches of photonic crystals, metamaterials, and topological photonics. Although these approaches enable drastic and sophisticated light shaping that is not possible with pure material properties, there is a fundamental limitation to the degree of freedom available from structural parameters of these systems due to the inherent nature of the periodicity. Thus, it is difficult to apply this approach to (as an extreme case) living biological systems that exhibit complex spatio-temporal behaviors. In order to overcome these limitations, high-order symmetries have been researched such as cavity, complex unit-cell [24], super-lattice [25], and super-symmetry [26].

1.1.4. Shaping light using scattering media

In this field, scattering due to inhomogeneous nature of media has been regarded as an unavoidable and inevitable loss of signal. However, there have been a lot of effort to utilize the enormous degrees of freedom that random media could provide. Theoretical and experimental studies have advanced our understanding on optical eigenstates [27] and light transport [28] in disordered structures, and recent researches exploit these properties to demonstrate disorder-enhanced transmission [29] and image transport [30] using transverse localization principle. Our modern technologies based on random scattering have now come to the stage of *in-situ* spatio-temporal focusing beyond diffraction limit by wisely exploiting scattering media with the aid of spatial light modulator [31] and even without it [12].

There have also been attempts to shape confined light within a membrane using turbulent media. In this case, optical properties of random scattering systems can be studied at a more fundamental level using top-down processes that precisely control the size and position of scattering elements. With these advantages, it is experimentally demonstrated that the eigenstate of the two-dimensional random scattering system exhibits various degrees of spatial field confinement and distribution, which can be quantitatively controlled (partially, at least) by arranging scattering elements in a quasi-random scheme rather than a complete random structure. Furthermore, functional devices such as spectrometers [32], logic gates [33] and solar-cells [34] are realized within disordered membranes and thus operating on chip-scale. These studies and developments have made remarkable and valuable advances in light shaping even though they used only a fraction of the potential degrees of freedom that random systems provide. Obviously, it is necessary to elucidate the ultimate boundary of possibilities and limitations of light shaping using random systems. This is the main subject of this thesis.

1.1.5. Summary

i. The shape of light is defined by the distribution of electromagnetic vector fields and the process of shaping light is then to redistribute the intensity and phase of an optical field to obtain the desired light shape.

ii. Shaping light within a membrane has been studied by realizing optical functions on chip-scale with the aid of a top-down process. The intrinsic spin-orbit interaction of confined light is expected to expand to the next-generation devices for light shaping.

iii. Structural properties beyond material properties are realized by periodic modulation of the permittivity on the wavelength scale, which is so-called photonic crystals, metamaterials, and topological photonics. However, these approaches are hard to manage complex systems due to the fundamental limitations of periodicity.

iv. Shaping light using random scattering systems has been developed to exploit the enormous degrees of freedom that a random system provides, bringing valuable practical techniques as well as theoretical understanding. However, more in-depth studies are needed to define the boundary of possibilities and limitations of light shaping using random systems.

1.2. Photonic crystals

1.2.1. Theoretical proposal of E. Yablonovitch: Photonic analogy of semiconductor

The concept of photonic crystals was initially proposed by E. Yablonovitch in 1987 [35]. In this monumental study, Yablonovitch considered a system made of dielectric materials arranged in a periodic structure and showed that this system had an electromagnetic band-gap due to the periodicity of the system, which can be used to control the rate of spontaneous emission and the properties of the radiation field by overlapping the electromagnetic band-gap with the electronic band-edge of an atom used as an emitter. Since it is known that photonic properties can be controlled using photonic crystals in an analogical reasoning to control electronic properties using semiconductors, photonic crystals have become the dominant concept for realizing light shaping using periodic structures.

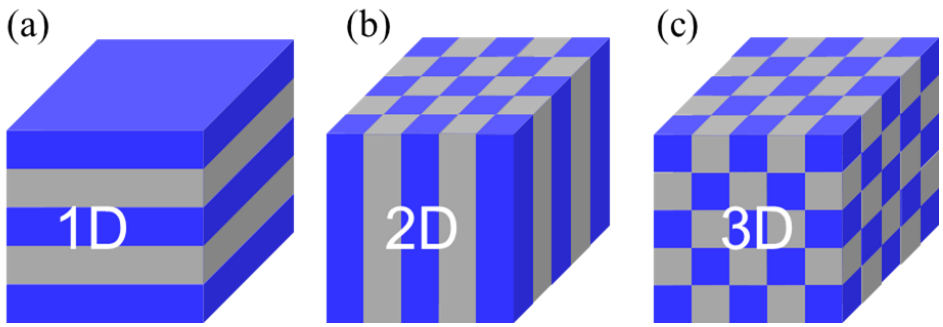

Figure 1-1. Conceptual diagrams of photonic crystals. Periodic structures on the wavelength-scale of light controls the properties of light propagating in a (a) 1D, (b) 2D, or (c) 3D spatial dimensions.

1.2.2. Photonic band structure: Bloch's theorem

Photonic crystals, like traditional solid crystals made of atoms, have discrete translational symmetry from the nature of periodic structures. If we call the unit length as the lattice constant a, then photonic crystals are defined by a distribution of dielectric materials in space in the form of $\varepsilon(\mathbf{r}) = \varepsilon(\mathbf{r} \pm \boldsymbol{a})$. In principle, photonic properties of this system can be understood from the following Maxwell equation,

$$\boldsymbol{\nabla} \times \left(\frac{1}{\varepsilon(\mathbf{r})} \boldsymbol{\nabla} \times \mathbf{H}(\mathbf{r}) \right) = \left(\frac{\omega}{c} \right)^2 \mathbf{H}(\mathbf{r}),$$

$$\mathbf{E}(\mathbf{r}) = \frac{i}{\omega \varepsilon_0 \varepsilon(\mathbf{r})} \boldsymbol{\nabla} \times \mathbf{H}(\mathbf{r}),$$

where $\mathbf{E}(\mathbf{r})$ and $\mathbf{H}(\mathbf{r})$ are the electric and magnetic fields, $\varepsilon_0 \approx 8.854 \times 10^{-12}$ Farad/m and $c \approx 2.997 \times 10^{-8}$ m/s are the vacuum permittivity and the vacuum speed of light, and $\varepsilon(\mathbf{r})$ is a scalar dielectric function, also called the relative permittivity.

However, because of the translational symmetry, the modes in photonic crystals should also have translational symmetry, or should commute with the translation operator $\hat{T}$ for any lattice vectors $\mathbf{R} = m_x a_x + m_y a_y + m_z a_z$ where m_x, m_y, m_z are arbitrary integers:

$$\hat{T}_{\mathbf{R}} e^{i\mathbf{k}\cdot\mathbf{r}} = e^{-i(\mathrm{k}_x m_x + \mathrm{k}_y m_y + \mathrm{k}_z m_z)} e^{i\mathbf{k}\cdot\mathbf{r}} = e^{-i\mathbf{k}\cdot\mathbf{R}} e^{i\mathbf{k}\cdot\mathbf{r}}.$$

From this relation, plane waves for any wavevector $\mathbf{k}$ are the eigenfunctions of translation operators with eigenvalues of $e^{-i\mathbf{k}\cdot\mathbf{R}}$, which means the states with modulations of $\mathbf{k}$ by an integer multiple $2\pi/\boldsymbol{a}$, or the reciprocal lattice vector $\mathbf{G}$, are degenerate. With this fact, and considering the mode of photonic crystals as a linear combination of plane waves, we can conclude that:

$$\mathbf{H}_{\mathbf{k}}(\mathbf{r}) = \sum_{\mathbf{m}} c_{\mathbf{k},\mathbf{m}} e^{i\mathbf{k}\cdot\mathbf{r}} = e^{i\mathbf{k}\cdot\mathbf{r}} \sum_{\mathbf{m}} c_{\mathbf{k},\mathbf{m}} e^{i\mathbf{G}\cdot\mathbf{r}} \equiv e^{i\mathbf{k}\cdot\mathbf{r}} \mathbf{u}_{\mathbf{k}}(\mathbf{r}),$$

where $c_{\boldsymbol{k}}$'s are expansion coefficients and $\mathbf{u}_{\mathbf{k}}(\mathbf{r})$ is a periodic function on the lattice

with the property of $\mathbf{u_k}(\mathbf{r} + \mathbf{R}) = \mathbf{u_k}(\mathbf{r})$ for all lattice vectors $\mathbf{R}$.

This result is commonly referred as Bloch's theorem and a state of the form $\mathbf{H_k}(\mathbf{r}) = e^{i\mathbf{k}\cdot\mathbf{r}}\mathbf{u_k}(\mathbf{r})$ is a Bloch states. Since electromagnetic modes of photonic crystals are Bloch states from the symmetry reason, all the information of such a mode is completely determined by wavevector $\mathbf{k}$ and the periodic function $\mathbf{u_k}(\mathbf{r})$. By solving the Maxwell equation stated in the first paragraph for the Bloch states with the periodic boundary condition, we can get the discrete eigenvalues ω_n for the specific value of $\mathbf{k}$, where n is a band index commonly attached by increasing order of ω. Since $\mathbf{k}$ is a continuous parameter for the Bloch state, $\omega_n(\mathbf{k})$ is expected to vary continuously in energy-momentum space as illustrated in Figure 1-2. This information is called the dispersion relation, or the band structure that contains optical properties of photonic crystals.

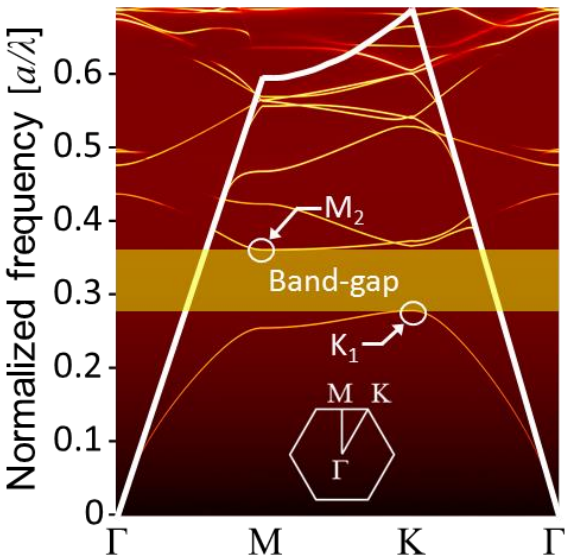

Figure 1-2. Band structure of a photonic crystal with hexagonal crystalline structure. Band-gap and band-edges are indicated by a yellow-shaded region and white circles, respectively.

1.2.3. Photonic band-gap: Inhibition of spontaneous emission

Since proposed in 1987, the most widely used property of photonic crystals is arguably a photonic band-gap, which is a frequency region where no electromagnetic modes are allowed. If the structure has strong enough lattice potentials, the band-gap can cover all possible propagating directions, resulting in a complete band-gap as depicted in Figure 1-2. A complete photonic band-gap could totally inhibit the spontaneous emission of emitter located inside the crystals if the energy of emission corresponds to the frequency range of the band-gap, as initially suggested by E. Yablonivitch. The size and localization of band-gap are engineered using structural parameters of photonic crystals, such as the crystalline structure, lattice constant, and filling factor.

Conversely, as E. M. Purcell showed in 1946 that the rate of spontaneous emission is enhanced in a cavity structure having a resonant mode with the same frequency of an emitter [36], photonic crystals with a complete band-gap can be used to enhance spontaneous emission rate by intentionally create a defect structure inside the photonic crystals. By adding this small internal structure inside a periodic background, we could easily manage the light-matter interaction between the photonic crystals and the emitter, which leads to developments of many modern photonic technologies such as photonic crystal cavity lasers [37], photonic crystal fibers [38], and photonic crystal sensors [39].

1.2.4. Photonic band-edges: Slow light effects

Apart from the material dispersion of bulk materials, photonic crystals exhibit a strong dispersion relation as a result of engineered structures. As indicated by white circles in band structure of Figure 1-2, the point at the boundary of the photonic band-gap, where the variation of the slope approaches to the zero-slope, is called photonic band-edge. In general, band-edges are located at the high symmetry point (for example, Γ, M, K, X, L, etc.) and do not necessarily be located at the boundaries of band-gap.

At the band edge, the group velocity of light v_g, defined by the inverse of the first-order dispersion $(dk/d\omega)^{-1}$, converges to zero, resulting in a slow light effect. The degree of slowness is then quantified by the slow-down factor, or the group index n_g, given by $n_g = c/v_g = c\,(dk/d\omega)$. Since the group velocity of light is slowed down, the eigenfunction at the band-edge forms a standing wave, which can be considered as a nearly stopped light. In this case, the light-matter interaction increases linearly with n_g, leading to enhanced gain and absorption coefficients. The slow light effect could also offer dispersion-free propagation with wide bandwidth [40]. These properties are the most promising property of band-edge, leading to many applications that handle dispersions of light and time-domain processing of optical signals including photonic crystal band-edge lasers [41], zero-dispersion waveguides [42], and delay tuning of slow-light pulses [43].

1.2.5. Shaping light using photonic crystals

As described in previous sections, the major physical property that consists photonic crystals is the dispersion relation, including the band-gap and band-edges, which is engineered using structured properties such as a crystalline structure, a periodicity,

and a filling factor. The idea of shaping light using photonic crystals has also been proposed and demonstrated, especially for very extreme aspects of light shaping such as a tight confinement in small area or a periodic modulation over large spatial domain.

Figure 1-3 shows typical examples of light shaping using photonic crystals and corresponding band-gaps. By combining a waveguide with a band-gap, it is possible to redirect a propagation direction of the light to a specific direction, or to prohibit a propagation into the structure by reflecting all energy of the mode [44]. In addition, a specific spatial electromagnetic field profile confined in wavelength-scale area would be realized using a defect structure embedded in photonic crystals with a complete band-gap, which blocks the propagation of light in all directions except inside the cavity. On the other hand, it is demonstrated that the band-edge can be used to control the spatial profile of light and the light-matter interaction over a large area [45] as shown in Figure 1-4, or to restrict the propagation direction of light toward specific symmetric points.

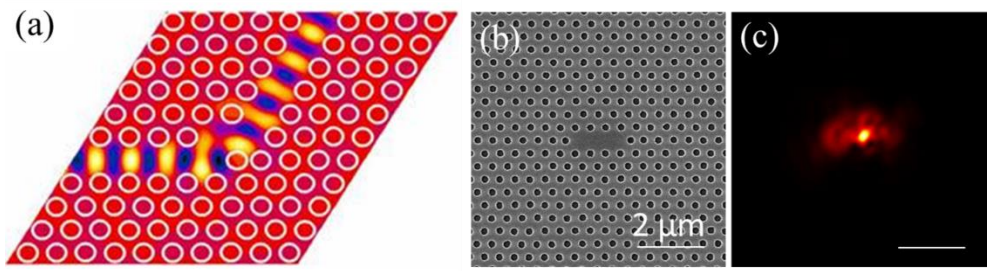

Figure 1-3. Typical examples of light shaping using a band-gap of photonic crystals. (a) Conceptual diagram of photonic crystal waveguide that redirects light propagation [44]. (b) Scanning electron microscope image for photonic crystal cavity structure. (c) Scanning near-field optical microscope image corresponding to the structure shown in (b).

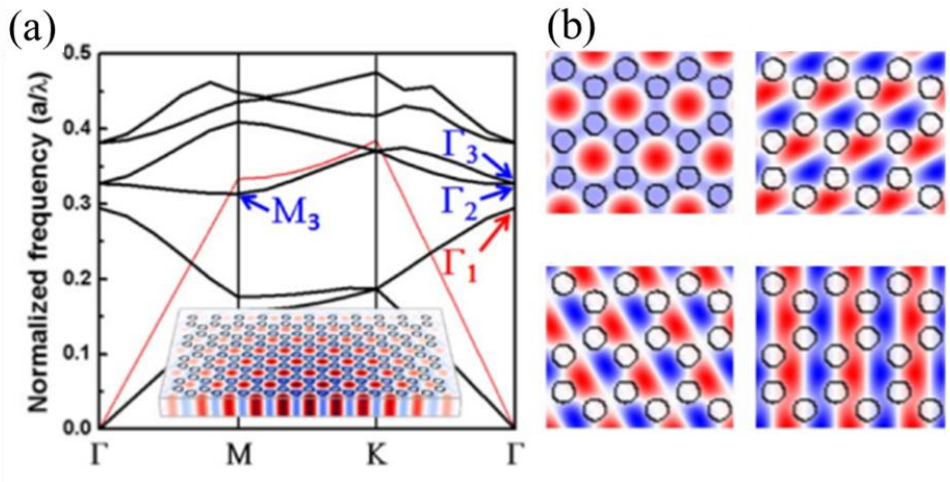

Figure 1-4. Typical examples of light shaping using a band-edge of photonic crystals [45]. (a) Band structure for a honeycomb lattice photonic crystal. The inset is a field profile of the Γ band-edge mode dispersed over a large area. (b) Transverse-electric field profiles for representative band-edge modes.

1.2.6. Issues of photonic crystals approach: Insufficient parameters

Light shaping using photonic crystals has a fundamental limitation that the number of available structural parameters is strictly limited, although this is a definite advantage that allows intuitive approaches to the design of devices. The degree of freedom inherent in structural parameters of the photonic crystal comes from the periodic backbone and the intra cavities. Here, the degree of freedom corresponding to the periodic backbone is typically exhausted for specifying a location of the band-gap or band-edges, which enforces to adjust the detailed shape of light required for a specific application using the remaining degree of freedom from the cavity. Therefore, in most cases, the key to the light shaping based on photonic crystals is the structure of a cavity, although the periodic backbone is solely used without a cavity for the purpose of managing macroscopic behaviors of light such as a transmission, a

polarization and a propagation direction. However, the information on the developed photonic crystal structures that we can use for analytical design is only a small library [46]. In order to overcome these limitations, high-order symmetries have been researched such as super-lattice [25], super-symmetry [26], complex unit-cell [24], coupled cavities [47]. However, even the complexity of these high-order symmetric structures is insufficient to apply photonic crystal approaches to (as an extreme case) living biological systems that exhibit complex spatio-temporal behaviors.

1.2.7. Summary

i. The concept of photonic crystal is proposed in 1987 by E. Yablonovich. A system made of dielectric materials arranged in a periodic structure exhibits a band-gap that corresponds to the periodicity of the system, which can be used to control the rate of spontaneous emission and the properties of the radiation field.

ii. An electromagnetic mode of a photonic crystal is a Bloch states inherent to the translational symmetry of the system. By solving the Maxwell equation using Bloch states and periodic boundary condition, we can find the dispersion relation, or the band structure that contains optical properties of photonic crystals.

iii. If the structure has strong enough lattice potentials, the band-gap can cover all possible propagating directions, resulting in a complete band-gap that could totally inhibit the spontaneous emission of emitter located inside the crystals. Conversely, the rate of spontaneous emission is enhanced in a photonic crystal if a cavity structure has a resonant mode with the same frequency of an emitter.

iv. At the band edge, the group velocity of light converges to zero, resulting in a slow light effect. The eigenfunction at the band-edge forms a standing wave, which can be considered as a nearly stopped light. In this case, the light-matter interaction increases, and dispersion becomes negligible in wide bandwidth.

v. The idea of shaping light using photonic crystals has also been proposed and demonstrated, using the engineered dispersion relation of photonic crystals, especially for very extreme aspects of light shaping such as a tight confinement in small area or a periodic modulation over large spatial domain.

vi. Light shaping using photonic crystals has a fundamental limitation that the number of available structural parameters is strictly limited. Although there are further developments that use high-order symmetries, the complexity of photonic crystal approaches is still insufficient for a system with complex spatio-temporal behaviors.

1.3. Anderson localization

1.3.1. Theoretical proposals of P. W. Anderson: Localized eigenstates in a disordered lattice

The theoretical possibility of Anderson localization was first proposed by P. W. Anderson in 1958 [48]. Anderson proved that the hopping transport could be completely halted in a certain system where inhomogeneous broadening [49] causes the wave function to be localized in a small region of space. The hopping transport that Anderson considered is a quantum mechanical transport scenario, where a mobile entity localized in a site is transferred by quantum-mechanical jumps from site to site, and thus motion of free carriers and scattering by medium are not considered. Representative physical quantities are spin diffusion in a solid [50], impurity band conduction at low concentrations of impurities [51], and charge transport in an organic polymer [52].

Anderson described such a system with a simple model where each site has a random energy E_j that reflects energy fluctuations across sites and a mobile entity is transferred from site j to the site k by an interaction matrix element $V_{jk}(\mathbf{r}_{jk})$. The time-dependent probability amplitude a_j of a particle on the site j is then given by the following equation:

$$i\dot{a}_j = E_j a_j + \sum_{k \neq j} V_{jk} a_k.$$

In this model, Anderson showed that if $V(\mathbf{r}_{jk})$ decreases faster than $1/r^3$ and if the average value of V is below a certain critical value V_c, then the wave function of a mobile entity initially placed at site n at time $t = 0$ decreases rapidly with distance around site n and the amplitude of site n remains finite even at $t \rightarrow \infty$, which proves a complete halt of hopping transport.

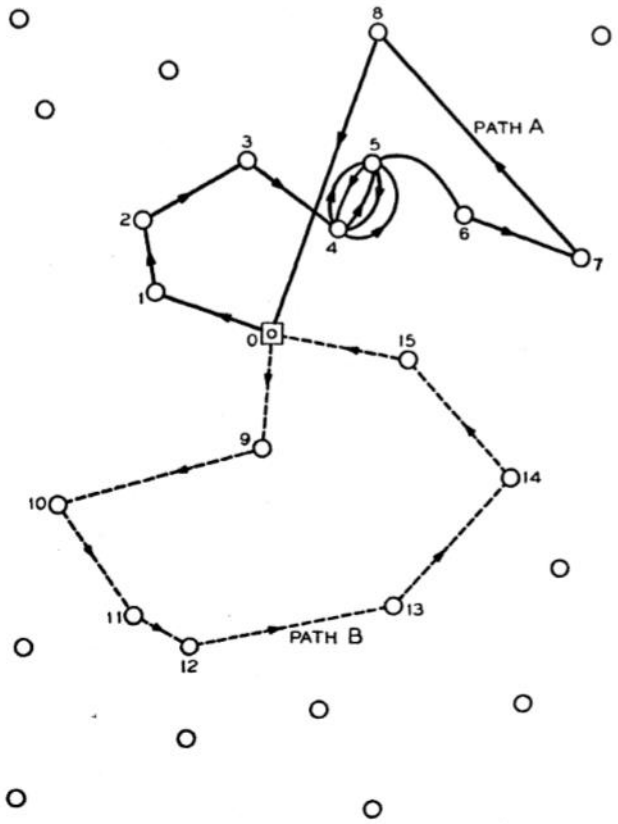

Figure 1-5. Schematic diagram of hopping transport in random lattices [48]. With this model, P. W. Anderson theoretically proved that the transport is halted as the wave functions are being localized in a small region of space. The original model that P. W. Anderson considered is a pure quantum mechanical system where mobile entities (such as spins or electrons) localized on sites are transported by quantum-mechanical jumps from site to site, not by motion of free carriers, which means scattering is not occurs as they move through a medium as well.

1.3.2. Localization of a light: White paint theory

Anderson's early model was a pure quantum mechanical system with no classical analogy. However, in 1985, approximately 30 years later, Anderson claimed that classical waves such as microwave, acoustic, and light propagation could be also localized in random media and these localization phenomena can be observed using macroscopic measures such as transmission and reflection [53]. Especially for light, a specific prediction was stated that the localization of classical electromagnetic wave would be easily observed in carefully prepared systems that resembles white paint, where high-dielectric-constant particles are embedded in low-dielectric-constant material such as vacuum, air, oil, or other transparent polymerizing liquid.

In a white paint system, the size a of the dielectric particles is very important, and should be carefully matched with the wavelength of light. If the scattering element is too small compared to the wavelength, scattering becomes weak according to the Rayleigh scattering law of $\sim k^4$ dependence, so the Ioffe-Regel factor [54] (see also Section 3.4.6) obtained by multiplying the wavenumber k and the mean-free-path l, decreases to $kl \sim (ka)^{-3}$, which is far less than the localization criterion value of ~1. Conversely, if the scatterer is too large, scattering process is ruled by the geometric-optics, and the scattering cross-section is proportional to a^2. In this case, the Ioffe-Regel factor becomes $kl \sim ka \geq 1$. Therefore, the optimum scattering for observing localization phenomena is the Mie resonance regime where the scale of scattering elements is comparable to the wavelength of light.

1.3.3. Pioneering experiments on photon localization

Pioneering experimental results on classical wave localization have been reported since the theoretical possibility was proposed by Anderson. Especially for a photon localization, the results from two groups are introduced here.

At first in 1997, about 20 years ago, Wiersma *et al.* [55] claimed the first experimental observation of Anderson localization of light using Gallium Arsenide (GaAs) semiconductor powder. These samples were prepared by grinding pure (99.999%) GaAs crystals to have an average particle sizes of 300 nm, 1 μm and 10 μm. The absorption coefficient κ of GaAs crystals was $\kappa \leq 1$ cm^{-1} at wavelength of 1,064 nm used in the experiment, and the refractive index is 3.48. With these systems, they investigated the transmission coefficient T according to sample thickness L and observed a quadratic dependence ($T \sim L^{-2}$) and a exponentially decaying form ($T \sim \exp(-L/l_{loc})$) in fine-grained powder as shown in Figure 1-6, which are the exact behaviors of localization transition predicted by Anderson [48] and the scaling theory of localization [56]. Whereas, the transmission coefficient of the classical diffusion process measured in coarse-grained powder changes linearly with the system size ($T \sim L^{-1}$).

Surprisingly, however, it was argued that the system-size dependence on transmission coefficients measured in these systems is not due to a strong localization of light. Scheffold *et al.* [57] claimed that data given in ref. [55] can be equally well explained by a classical diffusion process with reasonable amounts of absorption. And their samples have much lower turbidities than those given in ref. [55], so are comparable to samples with classical transport properties. After this criticism was raised, several groups [58, 59] got to investigate the system more closely to separate the effects of absorption and localization, including time-of-fight experiments, but no additional evidence of Anderson localization was found [60].

In 2013, which is relatively recent, the German group headed by G. Maret who raised the objection to the above work by Wiersma *et al.* reported direct measurement of the transition to localization of light, independent of absorption [61]. The system they studied is the Titanium Dioxide (TiO_2) powder, which is similar to the white paint model Anderson initially proposed in ref [53]. In this system, they injected a pulsed laser beam of visible wavelength with a repetition rate of 75 MHz and presented time-dependent measurements on the transmitted-light intensity distributions to provide direct evidence for a localization transition which cannot be explained by classical diffusion and absorption.

However, on the contrary at this time, Wiersma group [62] expressed doubts about the interpretation of the data provided in ref. [61], claiming that the effect of inelastic scattering was not sufficiently considered. In addition, the fact that the refractive index of TiO_2 sample ($n \sim 2.8$) is rather low compared to semiconductor samples ($n \sim 3.2$-3.6) makes it difficult to understand that the Anderson localization, which is not observed in semiconductors, occurs in the TiO2 system [60]. In the end, last year in 2016, Maret group's own research [63] has confirmed that it was not the Anderson localization, but the effects of organic impurities unintentionally mixed in the system, questioning whether the strong localization of light can be achieved in such a ‘white paint’ material where the disorder parameters are hardly to be increased any further.

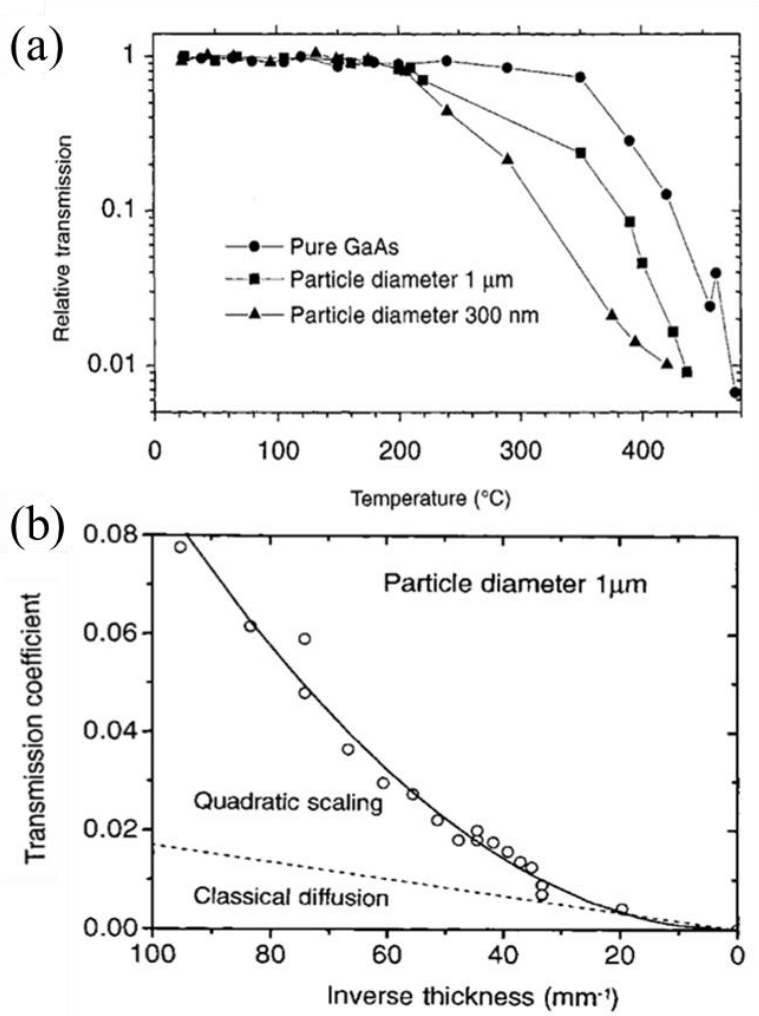

Figure 1-6. Pioneering experimental result on photon localization [55]. Wiersma *et al.* claimed the first observation of Anderson localization of light in GaAs powder system with the signatures of transmission. (a) The temperature dependence of transmissions measured in pure GaAs crystals and powder with average particle sizes of 1 μm and 300 nm. (b) The transmission coefficients measured as a function of the inverse thickness, which is extracted from the backscattering data.

1.3.4. Shaping light using Anderson localization principle

As described in the previous section, it is difficult to directly observe three-dimensional Anderson localization of light using semiconductor powder or white paint materials, which suggests that it would be impossible to use these phenomena for shaping light. However, apart from a fundamental understanding, it is feasible to realize light shaping using multiple scattering, the basic mechanism of Anderson localization, from an engineering point of view. Indeed, considerable levels of light shaping technologies have already been developed that take advantage of the enormous degrees of freedom random media provide, and improving these methods to handle a complex system is a cutting-edge area of light shaping.

Figure 1-7 shows a representative result that use a random medium and multiple scattering mechanism to achieve a perfect focusing beyond diffraction limit. The surface area of the incident light is pixelized by using a spatial light modulator [64] and each segment is phase-modulated by a leaning algorithm, which lead to a tightly focused beam profile that ten times smaller than that of the diffraction limit size from a lens [65]. In most cases, these shaping methods use a spatial light modulator to exploit the degree of freedom provided by random media, which limit its use to slowly varying applications because of the slow electronic feedbacks from a detector or a camera. Recently, a real-time wavefront shaping method with a sub-microsecond time-scale is developed based on all-optical feedback mechanism of a field self-organization inside a multimode laser cavity [12], which is expected to be applicable to systems with complex spatio-temporal dynamics.

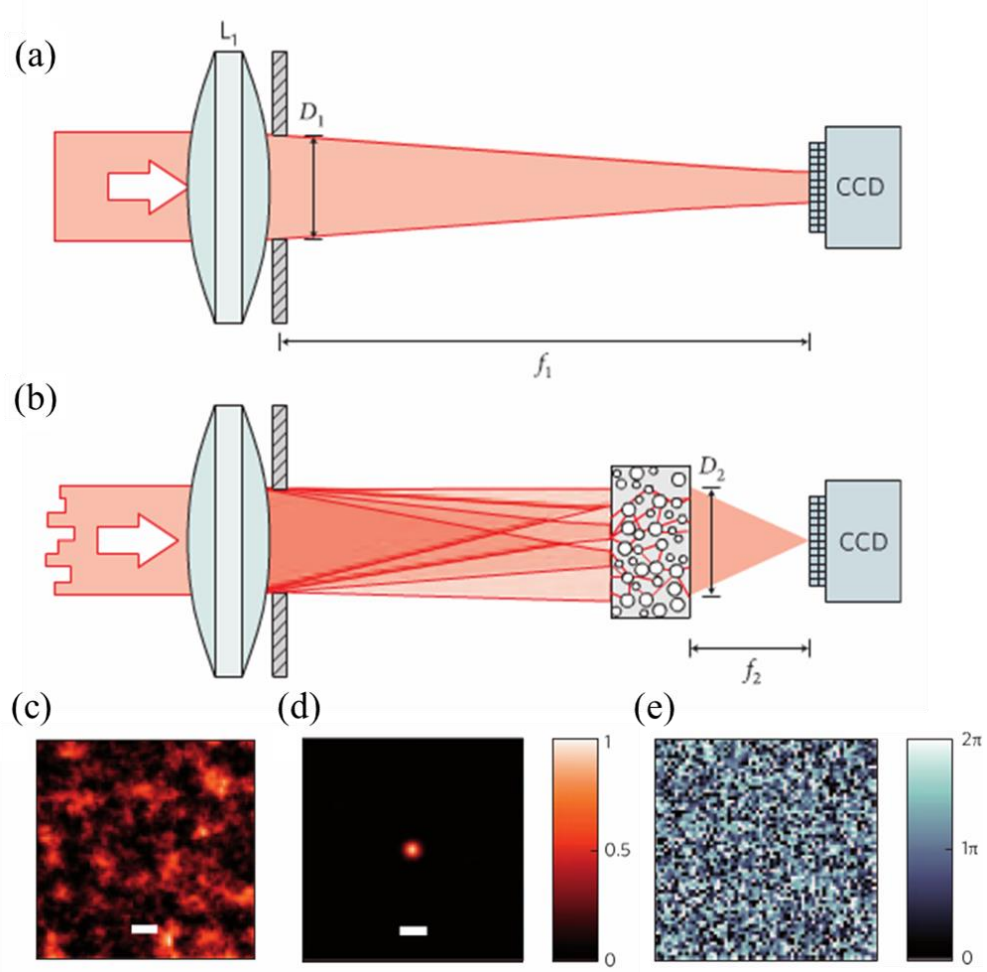

Figure 1-7. Light shaping using Anderson localization principle with spatial light modulator [65]. (a-b) Schematic diagram of experimental setup for (a) a system without disorder and (b) a system with disorder where light shaped by a spatial light modulator are incident and focused through a disordered medium. (c-e) Intensity distribution at the focal plane measured in (c) a system without disorder, (d) a system with a 6-μm layer of airbrush paint, and (e) the same system with (d) but after shaping with spatial light modulator. (f) Spatial pattern used in the spatial phase modulator to generate the intensity distribution shown (e).

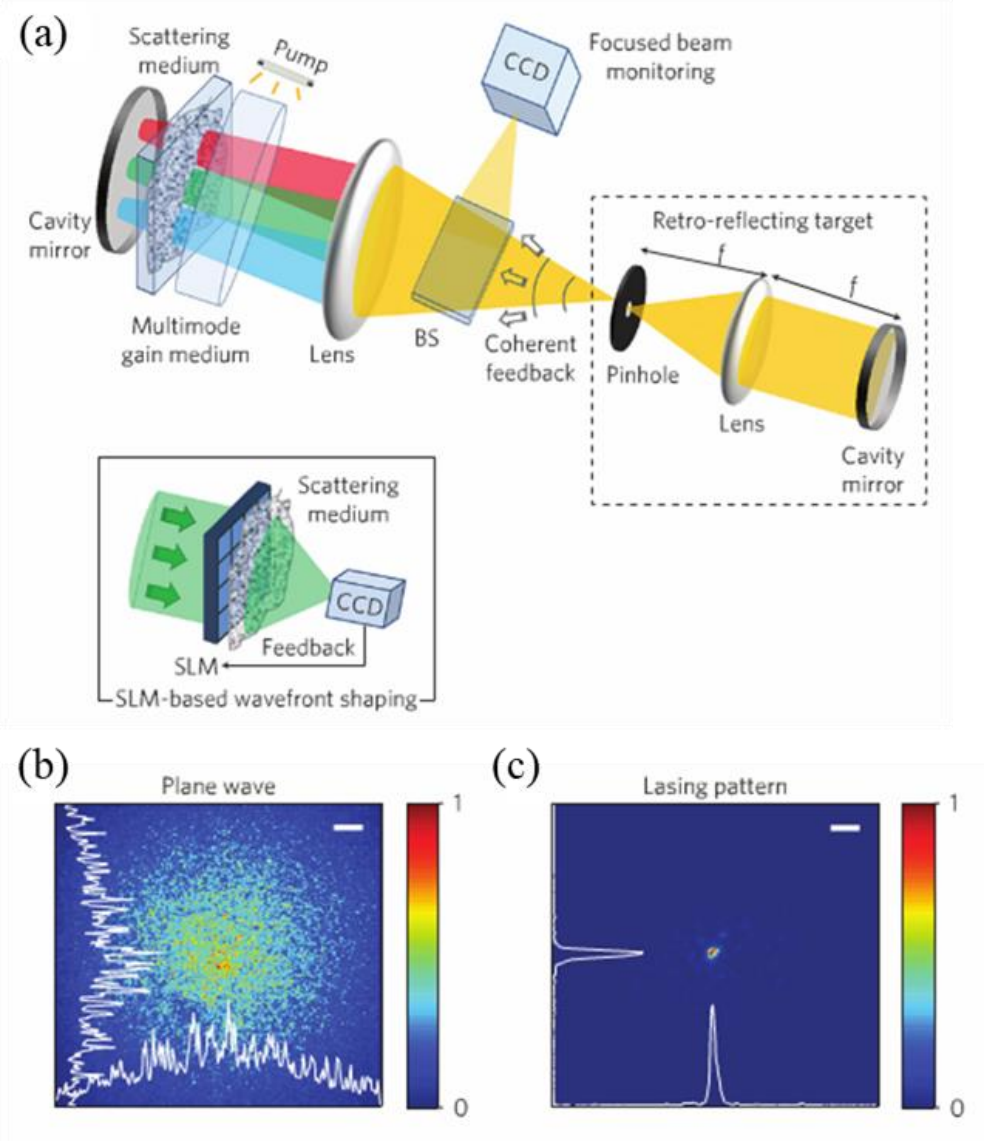

Figure 1-8. Light shaping using Anderson localization principle by all optical feedback [12]. (a) Schematic diagram of experimental setup. A scattering medium that supports thousands of independent spatial modes is located inside a cavity. (b-c) Intensity distributions at the target plane obtained by (b) conventional focusing of a plane wave through the diffuser and by (c) the all-optical feedback.

1.3.5. Issues of Anderson localization approach: Controlling vast degrees of freedom

Many techniques have been developed for propagating beam shaping using a scattering medium, based on a spatial light modulator with few exceptions such as all-optical feedback. However, these methods require huge and complicated external components in order to take advantage of the degree of freedom provided by a random medium, making its application on chip-scale very difficult. In addition, the solution from an engineering point of view (for example, learning algorithm-based feedback) is a phenomenological approach rather than a direct control over the internal degree of freedom inherent in a random scattering system. To realize a light shaping platform consisting of minimal physical and structural elements that can be applied to on-chip applications, a fundamental understanding of the underlying mechanism of Anderson localization principle and the study of the effects of structural degree of freedom should be preceded.

For this purpose, the direct control of a random scattering system is essential, which should be much more direct than those of the current approaches. More specifically, we need a system where its structural degrees of freedom such as a size, distance, and density of scattering elements can be precisely and directly controlled as we intended. By understanding the underlying scattering mechanism and the effect of structural degree of freedom, with the aid of this controllable disordered system, we can develop a light shaping platform composed of minimal components for on-chip applications. Many approaches have been attempted to realize such a system, including direct laser writing [66], optical induction [67], 3D printing [68] and so on. However, the most promising one is a top-down approach to a membrane based on modern semiconductor processing, as explained in Section 1.1.2.

1.3.6. Summary

i. The theoretical possibility of Anderson localization was first proposed by P. W. Anderson in 1958. Anderson proved that the hopping transport could be completely halted in a certain system where inhomogeneous broadening causes the wave function to be localized in a small region of space.

ii. In 1985, Anderson claimed that classical waves such as light propagation could be also localized in random media. In such a system, the size of the dielectric particles is very important, and should be carefully matched with the wavelength of light.

iii. Pioneering experimental results on photon localization have been reported using, for example, GaAs semiconductor and TiO_2 powder. However, none of these experimental results seem to demonstrate three-dimensional Anderson localization of light without controversy.

iv. Apart from a fundamental understanding of underlying physics, it is feasible to realize light shaping using random scattering media from an engineering point of view. For example, a real-time wavefront shaping with a sub-microsecond time-scale is demonstrated.

v. Developed methods for shaping light using scattering media require huge and complicated external components that make its application on chip-scale very difficult. A light shaping platform composed of minimal components for on-chip applications can be developed by understanding the underlying scattering mechanism and the effect of structural degree of freedom, with the aid of a controllably disordered system. The most promising one is a top-down approach to a membrane, based on modern semiconductor processing.

1.4. Objectives of this thesis

1.4.1. Development of an ideal platform for shaping a confined light

In this thesis, one of the main objective is to develop an ideal platform for light shaping in a membrane. As described in Section 1.1.2, confining and shaping light within a membrane have definite advantages over the current paradigm of propagating beam shaping, with a high potential for research and application in the most advanced fields of photonics. For this objective, a novel disordered system based on strongly scattering elements having similar scale with the wavelength of light will be proposed, and enormous degrees of freedom that such a disordered system could provide will be investigated to develop effective and direct ways of controlling structural parameters of the proposed system.

1.4.2. Characterization of eigenstates in the proposed platform

The second objective is to characterize how the shape of light evolves in the proposed strongly scattering system. Once this information is revealed, it can be used to predict spectro-spatial properties of the system for given structural parameters, which should be further investigated to understand underlying mechanism of scattering in a disordered system and to realize light shaping within a membrane. The most fundamental approach for this objective is to directly measure and analyze eigenvalues and eigenstates of a system. Therefore, in this thesis, spectral responses and electromagnetic field distributions of the proposed system will be investigated by selectively exciting individual eigenmodes and tracking its changes as a function of structural parameters.

1.4.3. Demonstration of light shaping on chip-scale devices

The third objective is to demonstrate light shaping on chip-scale devices with minimal physical and structural elements, and without any additional external components, which can be realized by directly controlling only the internal degree of freedom with an understanding of the spectro-spatial eigenmode information of the proposed platform. Therefore, in this thesis, shaping of confined light will be demonstrated by manipulating only structural parameters of the proposed strongly scattering system fabricated in a two-dimensional semiconductor material.

1.4.4. Summary

i. The first objective of this thesis is to propose a strongly scattering system with enough degree of freedom to shape light within a membrane and to develop a systematic method that can directly and effectively control the structural parameters of the proposed platform.

ii. The second objective of this thesis is to characterize spectral responses and electromagnetic field distributions of the proposed system by selectively exciting individual eigenmodes and tracking its changes as a function of structural parameters.

iii. The third objective of this thesis is to demonstrate shaping of confined light on chip-scale devices with minimal physical and structural elements by manipulating only structural parameters of the proposed strongly scattering system fabricated in a two-dimensional semiconductor material.

1.5. Conclusion

Shaping light has attracted great interest in the history of optical science. Especially for shaping light within a membrane, realization of optical functions on chip-scale, and the spin-orbit interaction of confined light are of interest. In this thesis, light shaping within a membrane will be studied using a strongly scattering system.

The shape of light is a distribution of electromagnetic vector fields and the process of shaping light is to redistribute the intensity and phase of an optical field to obtain the desired light shape. Shaping light confined in a membrane is of interest for the potential of realizing optical functions on chip-scale with the aid of a top-down process and the intrinsic spin-orbit interaction of confined light, which is expected to expand to the next-generation devices for light shaping. Structural properties beyond material properties are realized by periodic modulation of the permittivity on the wavelength scale, which is so-called photonic crystals, metamaterials, and topological photonics. However, these approaches are hard to manage complex systems due to the fundamental limitations of periodicity. In the other extreme, shaping light using random scattering systems has been developed to exploit the enormous degrees of freedom that a random system provides, bringing valuable practical techniques as well as theoretical understanding although more in-depth studies are needed to define the boundary of possibilities and limitations of light shaping using random systems.

A system made of dielectric materials arranged in a periodic structure is called a photonic crystal, which exhibits unique optical properties such as a photonic band-gap and band-edges. An electromagnetic mode of a photonic crystal is a Bloch states inherent to the translational symmetry of the system. By solving the Maxwell equation using Bloch states and periodic boundary condition, we can find the

dispersion relation, or the band structure that contains optical properties of photonic crystals. If the structure has strong enough lattice potentials, the band-gap can cover all possible propagating directions, resulting in a complete band-gap that could totally inhibit the spontaneous emission of emitter located inside the crystals. At the band edge, the group velocity of light converges to zero and the eigenfunction forms a standing wave, which can be considered as a nearly stopped light. The idea of shaping light using photonic crystals has also been proposed and demonstrated, especially for very extreme aspects of light shaping such as a tight confinement in small area or a periodic modulation over large spatial domain. Photonic crystal approaches, however, have limited number of available structural parameters to apply it for a system with complex spatio-temporal behaviors although there are further developments that use high-order symmetries.

The hopping transport could be completely halted in a certain system where inhomogeneous broadening causes the wave function to be localized in a small region of space. Classical waves such as light propagation could be also localized in random media. In such a system, the size of the dielectric particles is very important, and should be carefully matched with the wavelength of light. Pioneering experimental results on photon localization have been reported using, for example, GaAs semiconductor and TiO_2 powder. However, none of these experimental results seem to demonstrate three-dimensional Anderson localization of light without controversy. Apart from a fundamental understanding of underlying physics, it is feasible to realize light shaping using random scattering media from an engineering point of view. For example, a real-time wavefront shaping with a sub-microsecond time-scale has is demonstrated using scattering media although developed methods require huge and complicated external components that make its application on chip-scale very difficult. A light shaping platform composed of minimal components for on-chip

applications can be developed by understanding the underlying scattering mechanism and the effect of structural degree of freedom, with the aid of a controllably disordered system. The most promising one is a top-down approach to a membrane, based on modern semiconductor processing

The objective of this thesis is to propose a strongly scattering system with enough degree of freedom to shape light within a membrane and to develop a systematic method that can directly and effectively control the structural parameters of the proposed platform. Characterizations of the proposed system will then be followed by selectively exciting individual eigenmodes and tracking changes of spectral responses and electromagnetic field distributions as a function of structural parameters. And then, shaping of confined light on chip-scale devices with minimal physical and structural elements will be demonstrated by manipulating only structural parameters of the proposed strongly scattering system fabricated in a two-dimensional semiconductor material.

Chapter 2 – Photonic crystal alloys

2.1. Introduction

2.1.1. Disordered photonic structures for light shaping

As described in Chapter 1, the purpose of this thesis is to confine and shape light within a membrane using strongly scattering structures and it will be realized by applying top-down approaches based on modern semiconductor process technologies.

Before discussing disordered structures, however, it should be noted that ordered structures that has a complete periodicity and the translational symmetry, such as photonic crystals, exhibit very limited structural parameters. As explained in Section 1.2, these structures are not applicable for realizing complex shape of light, despite of its intuitive understanding and design. Therefore, it is necessary to extend the structural degree of freedom in any form other than the periodic structure, leading to the natural introduction of the disordered photonic structure.

The structural parameters of such a disordered photonic structure realized within a membrane can be precisely controlled, and according to these parameters, disordered photonic structures can be categorized into two branches of the lattice disorder and the compositional disorder as illustrated in Figure 2-1. The effect of scattering and the change of optical properties are quite different depending on which structural parameter induces disordered components. The disorder scheme, currently being studied as mainstream, is the lattice disorder that manipulates the crystalline structure itself. It can be seen as a top-down approach-based white paint scheme, which quantifies the degree of disorder using a filling factor or a deviation from the regular lattice structure. On the other hand, in this thesis, the disordered components exist in a diversity of the scattering strength at each lattice site while maintaining the

crystalline structure. The degree of freedom of the disordered structure is then related to basis photonic atoms and a specific configuration of an arrangement over an entire structure. The main difference between these two approaches is whether the crystalline symmetry is maintained.

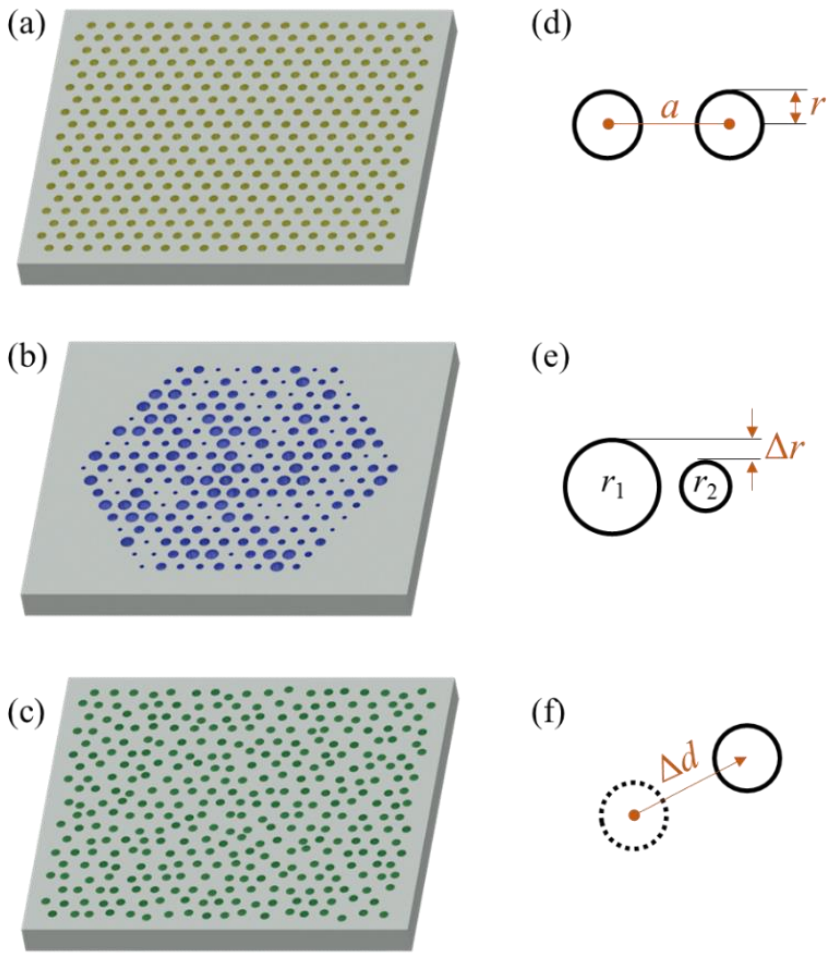

Figure 2-1. Representative disordered photonic systems confining light within a membrane and corresponding structural parameters. (a-c) Schematics of (a) the ordered structure (photonic crystals), (b) the compositional disorder (photonic crystal alloys), and (c) the lattice disorder (white paint scheme). (d-f) Structural parameters describing the disordered systems shown in (a-c) in the most simplified form.

2.1.2. Previous studies on lattice disorder

Lattice disorder has been actively studied by various groups around the world to investigate fundamental aspects as well as applications. Here are two examples of representative research cases.

Riboli *et al.* studied a disordered photonic structure based on a white paint scheme fabricated on a semiconductor membrane by measuring the spatial distribution of photoluminescence as displayed in Figure 2-2. They found that localized light can be exist in these systems and the resonance qualities of these localized modes depend on the filling factor of the structure. The interaction by the near-field probe tip that can affect the peak frequency of the localized mode was also demonstrated. In addition, Sarma *et al.* fabricated a disordered waveguide based on the lattice disorder and measured a spatial energy distribution over the waveguide according to the input beam with several spatial profiles. They found that the spatial distribution of intensity within the disordered waveguide changed significantly depending on the specific shape of the input fields due to the multiple scattering of the disordered medium as shown in Figure 2-3.

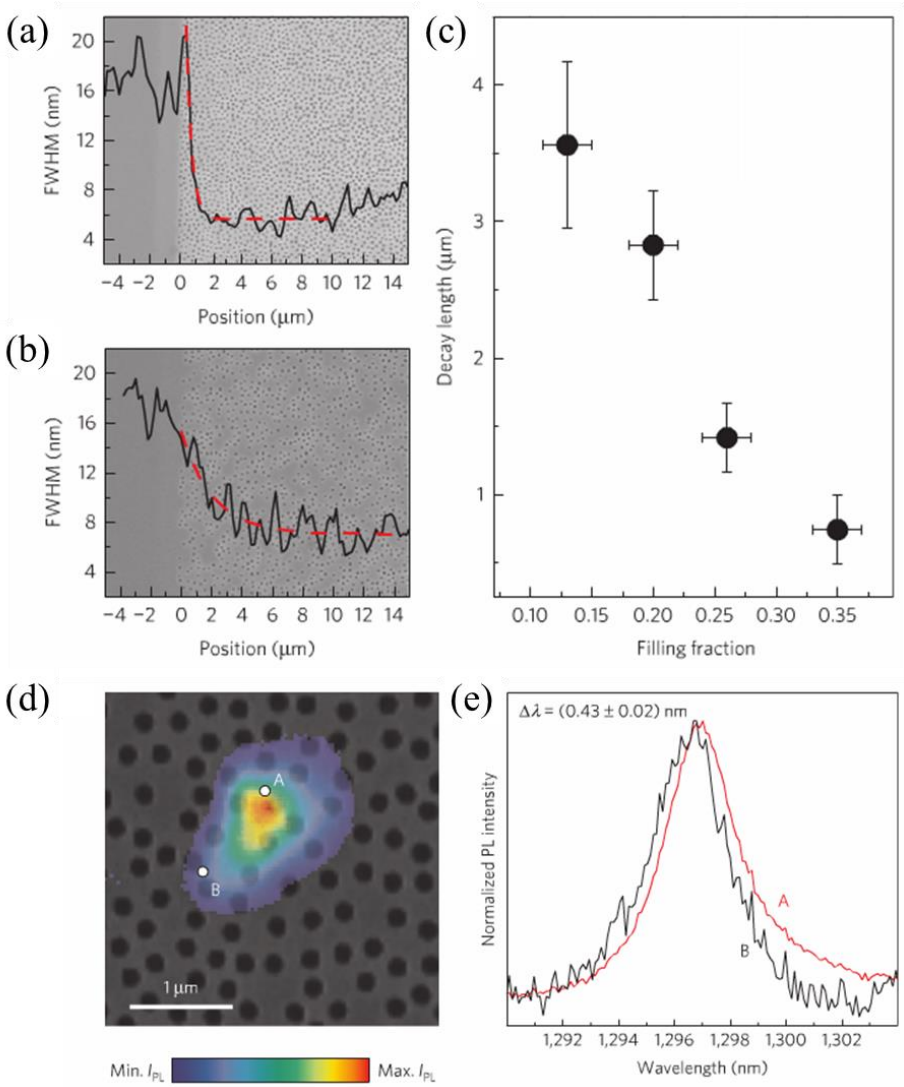

Figure 2-2. Investigation of decay length and spectral tuning of the localized modes using white paint scheme [69]. (a-b) Scanning electron microscope images of the disordered structures for filling factor (a) $f = 0.35$ and (b) $f = 0.13$, superimposed with spectral widths of frequency peaks as a function of penetration depth. (c) Decay length versus filling fraction. (d) Near-field mapping of the photoluminescence intensity. (e) Normalized near-field spectra measured at the maximum intensity (point A) and at a lower intensity (point B) shown in (d).

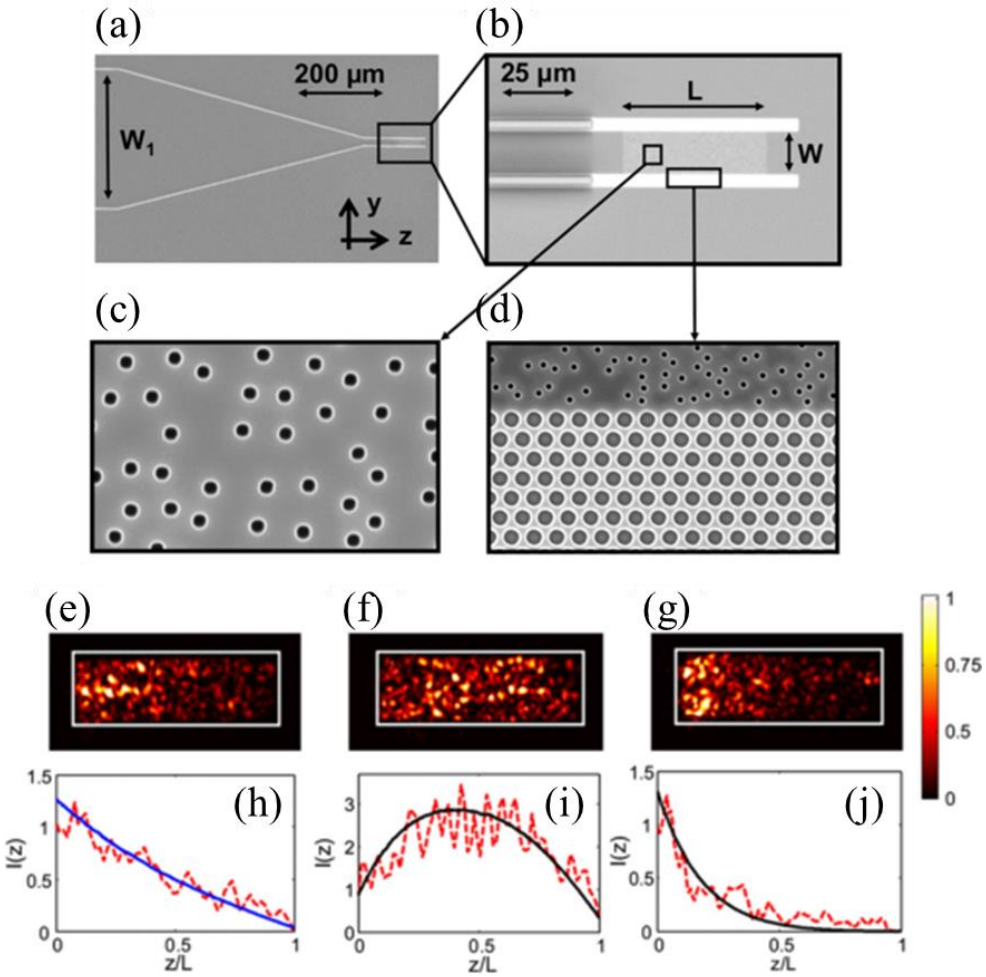

Figure 2-3. Control of intensity distribution inside the disordered waveguide using white paint scheme [70]. (a-d) Scanning electron microscope images of a fabricated disordered waveguide with a tapered lead: (a) Over-view of a ridge waveguide tapered to the disordered waveguide. Magnified images of (b) the disordered region of the waveguide, (c) randomly distributed air holes, and (d) the sidewalls made of regular triangular lattice of air holes. (e-g) Two-dimensional control of the intensity distribution for several input light fields. (h-j) The cross-section-averaged intensity distribution extracted from (e-g) as a function of input direction.

2.1.3. Previous studies on compositional disorder

The compositional disorder has received relatively less attention compared to the lattice disorder, and thus it is difficult to find related studies. The author's personal view of this is that the study of disordered systems has focused on lattice vibrations (phonon) populated in solid state systems as the primary scattering mechanism [71], and due to the experimental controllability using temperature, which is contrasted to the difficulty of realizing compositional disorder in solid state systems. Although it is now feasible to realize compositionally disordered system in photonic scale, the historical inertia seems to be continuing to this day.

There are two experimental references directly related to the compositional disorder, which were studied by H. Jeon group to which the author belongs. First, Kim *et al.* demonstrated a photonic analogy corresponding to the band-gap engineering in compound semiconductor systems using compositionally disordered system with a binary basis. Figure 2-4 displays their finding that the wavelength of the band-edge, which indicates an exact location of band-gap, gradually shifts when the composition ratio between the basis atoms changes 0 to 1 through the mixed crystal regime as well. In the subsequent study, they obtained experimental evidences that there is a spatially localized mode formed by Anderson's localization principle using a compositionally disordered system with a quaternary basis as shown in Figure 2-5.

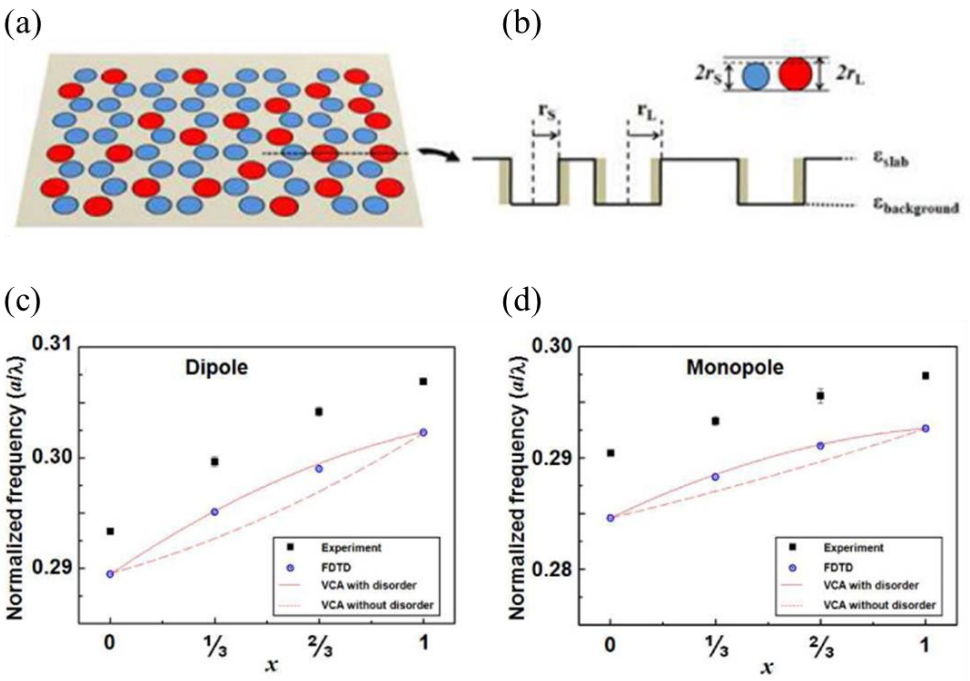

Figure 2-4. Demonstration of band-gap engineering using mixed photonic crystals with binary basis [72]. (a-b) Schematics of (a) the mixed photonic crystal with honeycomb lattice and (b) corresponding dielectric constant profile. (c-d) Experimental realization of band-gap engineering recorded by taking lasing frequency of (c) dipole mode and (d) monopole mode as a function of compositional ratio between binary basis atoms. Solid (dashed) curve is a numerically calculated band-edge frequency of the structure with (without) disorder.

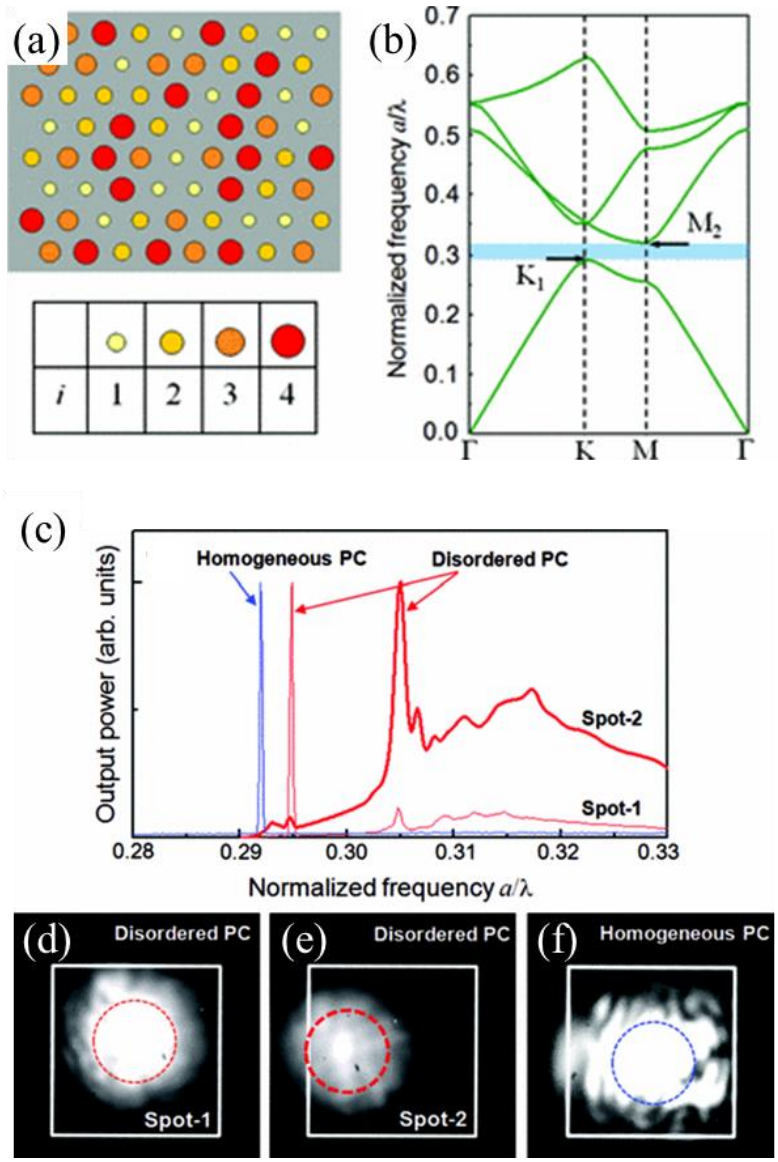

Figure 2-5. Simultaneous observation of extended and localized modes in compositionally disordered photonic crystals [73]. (a) Schematic of the compositional disorder with quaternary basis. (b) Photonic band structure of the homogeneous photonic crystals. (c) Spectra measured from the homogeneous and disordered samples at two different pumping spots. (d-f) Far-field images taken from (d) spot 1, (e) spot 2 of the disordered sample, and (f) the homogeneous sample.

2.1.4. Major differences between the two systems

On the experimental aspect, the most notable difference between the two disorder scheme is that the lattice-disordered system behaves more randomly than the compositionally disordered system does. That is, the disordered components embedded in deviations from a regular lattice bring more irregular and unpredictable optical properties rather than preserving the crystalline structure. Therefore, researchers tend to use lattice-disordered systems primarily for optical random systems and to realize functionalities based on these random properties [32, 34, 70]. However, this does not mean that the compositional disorder use disorder ineffectively and thus transition in this system is slower than the lattice-disordered system. As will be investigated in Chapter 3, compositionally disordered systems also modulate spectro-spatial properties of optical eigenstates very quickly and effectively. The important optical difference is that the responses to the compositional disorder appears in a wide spectro-spatial domain, which can be quantitatively predicted and thus be engineerable. This is mainly due to the crystalline symmetry that is conserved in the compositionally disordered system, regardless of the degree of disorder.

2.1.5. Summary

i. The structural parameters of disordered systems for shaping light confined within a membrane can be precisely controlled using top-down approaches, which can categorize disordered photonic structures into two branches of the lattice disorder and the compositional disorder.

ii. Lattice disorder has been actively studied by various groups around the world to investigate fundamental aspects as well as applications, mostly focused on optical random systems and functionalities related these random properties.

iii. The compositional disorder has received relatively less attention compared to the lattice disorder although it is now feasible to realize compositionally disordered system in photonic scale. The photonic version of band-gap engineering, and experimental evidences of localized modes have been studied so far.

iv. The important optical difference between these two disordered system is that the responses to the compositional disorder appears in a wide spectro-spatial domain, which can be quantitatively predicted and thus be engineerable. This is mainly due to the crystalline symmetry in the compositionally disordered system, conserved regardless of the degree of disorder.

2.2. Photonic crystal alloys

2.2.1. Motivation: Preserving the crystalline symmetry

The photonic crystal alloy proposed in this thesis is a photonic disordered system based on the compositional disorder, which has been rarely studied until now. In this system illustrated in Figure 2-6, the diversity of basis photonic atoms and the configuration of an arrangement of these atoms over the lattice site attribute to the disordered components, which are motivated to maintain the crystalline symmetry, regardless of the disorder strength. In the lattice-disordered system, which has been studied as a mainstream, the crystalline structure begins to collapse and even crystallinity itself is hard to define when the degree of disorder becomes strong. Thus, although some phenomenological engineering is possible with brutal approaches, it is nearly impossible to predict optical properties inferred from structural parameters, which limits researches and applications of photonic disordered systems realized within a membrane to completely random cases.

In the photonic crystal alloy platform proposed in this thesis, however, the effect of Bragg scattering [74] originated from periodic and coherent arrangement of scattering elements is still available regardless of the degree of disorder. Thus, the effects of quasi-random disordered components in this system can be quantified and predicted based on the crystalline structure and structural parameters, which brings an opportunity to understand effects of the tremendous degrees of freedom provided by strongly scattering structures. The realization of more advanced photonic functionalities will then be possible with these knowledge that enable to engineer optical properties into the desired direction.

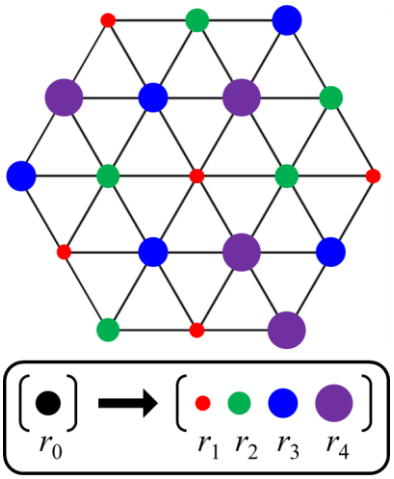

Figure 2-6. Schematic of a photonic crystal alloy implementing compositional disorder with quaternary basis. The crystalline symmetry of a crystal is strictly preserved regardless of the disorder strength defined by the relative size between the basis photonic atoms.

2.2.2. Quantification of the system

The structural degrees of freedom of photonic crystal alloys can be separated into those from basis photonic atoms and their spatial arrangement over lattice sites. In most cases, a photonic atom in a system is realized by the refractive index contrast with respect to the reference material constituting the membrane. Assuming that all basis atoms have the same refractive index as well as uniform circular shapes, the only remaining variable of each element is the radius r of photonic atom. This value can be specified as a function of the scattering strength γ that quantify the degree of disorder, and the average radius r_0, according to the definition of Conti *et al.* [75]:

$$r = r_0(1 + \gamma\xi),$$

where ξ is a deviation that uniformly varies within the range of $-1/2 \leq \xi \leq 1/2$. Then, parameters handling the degrees of freedom for the basis photonic atoms are

the following two parameters: the scattering strength γ that quantify the maximum radius difference as illustrated in Figure 2-7 and the filling factor r_0 that corresponds to the effective refractive index of the membrane. Visualizations of photonic crystal alloys are shown in Figure 2-8 for some representative values of the degree of disorder.

Once the basis atoms are determined, there remains degrees of freedom in their spatial arrangement over lattice sites. From a macroscopic point of view, the composition ratio between each basis atom can be controlled, or some constraints such as a mirror-symmetry, rotational symmetry, and any other conditional arrangement can be assigned to the configuration of arrangement. Especially for symmetries of the configuration, natural obvious effect is the resonance mode with the same symmetry applied to the corresponding configuration. From a microscopic point of view, the type of photonic atom placed at each lattice site controls the scattering strength at that sites. In principle, it is possible to independently control the scattering strength of every lattice site, in contrast to the lattice-disordered scheme where spatial shifting of a lattice site directly affects secondary scatterings from the neighboring sites. The conclusion of this idea will be a pixelated design of light shaping and a realization of corresponding arbitrary shape of light, which is the ultimate direction of light shaping using the proposed platform.

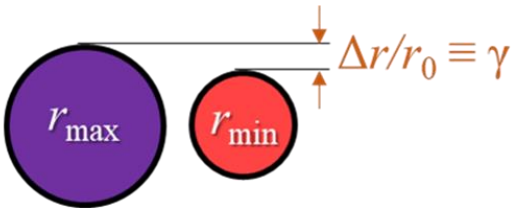

Figure 2-7. The definition of the degree of disorder [75]. The degree of disorder, that quantifies disorder strength of a system is defined by the maximal radius difference between basis photonic atoms normalized to the reference radius.

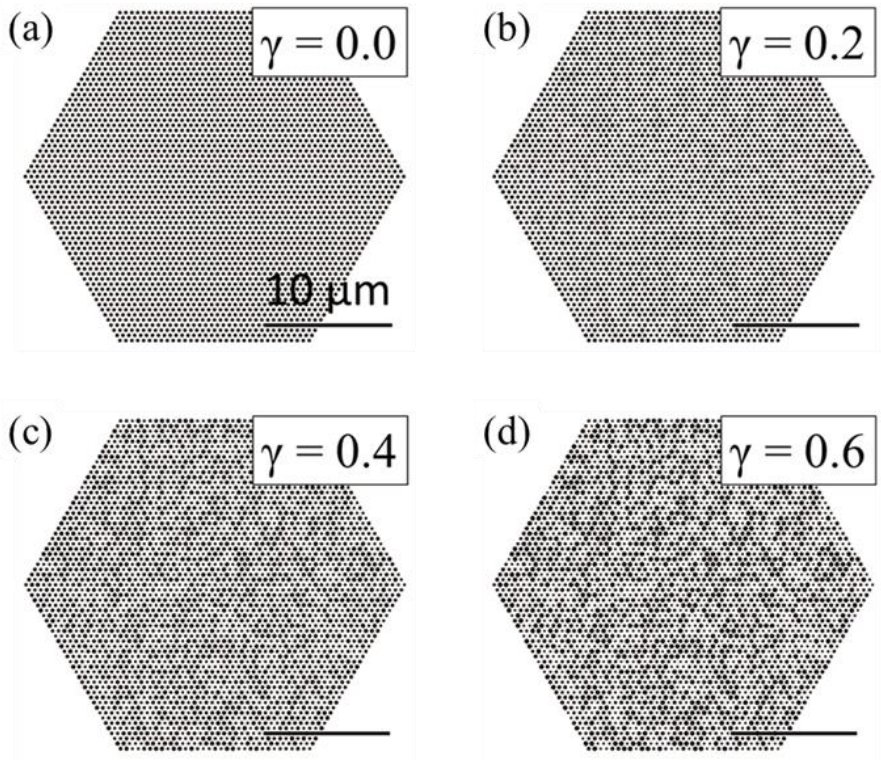

Figure 2-8. Visualizations of photonic crystal alloys with representative values of the degree of disorder. Each image is generated by arranging total of 3,169 photonic atoms with (a) γ = 0.0, (b) γ = 0.2, (c) γ = 0.4, and (d) γ = 0.6.

2.2.3. Fourier analysis: Ordered and disordered components

As mentioned several times in previous sections, photonic crystal alloy system retains crystallinity, regardless of the degree of disorder. In order to demonstrate and to quantify this idea, Fourier analysis on the proposed platform are performed. Results are shown in Figure 2-9, which are Fourier-transformed images of the original images shown in Figure 2-8 for visualization of the structures. The discrete bright spots that represent the ordered component corresponding to the reciprocal lattice of the hexagonal lattice structure, remain even at the strongest degree of disorder. Meanwhile, the disordered component appears in the form of thin mist dispersed over the entire momentum space, which gets thicker as the degree of disorder increases. These data vividly prove that the proposed platform preserves the crystalline symmetry, regardless of the degree of disorder

The relative ratio between the ordered and disordered components are quantified by the ordered overlap factor defined by $F_O \equiv \left[\int (I \cdot M) dk_x dk_y\right] / \left[\int I \, dk_x dk_y\right]$, where $I = I(k_x, k_y)$ is a Fourier-transformed intensity profile and $M(k_x, k_y) = \sum_{\boldsymbol{G}} exp\left(-\frac{(\boldsymbol{k}-\boldsymbol{G})^2}{2\sigma^2}\right)$ is a Gaussian integral mask having peak values of 1 at the reciprocal lattice points $\boldsymbol{G}$. Here, σ is the Gaussian RMS width set to $\sigma = 0.25G_0$ where G_0 is the magnitude of the primitive reciprocal lattice vector. The disordered overlap factor can then be obtained from the relationship, $F_{DO} = 1 - F_O$. It is obvious that the ordered component decreases while both the disordered component and the effective width increase as γ becomes larger as shown in Figure 2-10. Surprisingly however, these values fit excellently to exponential functions, resulting in their asymptotic values of 0.48, 0.52 in the ordered component, disordered component, respectively.

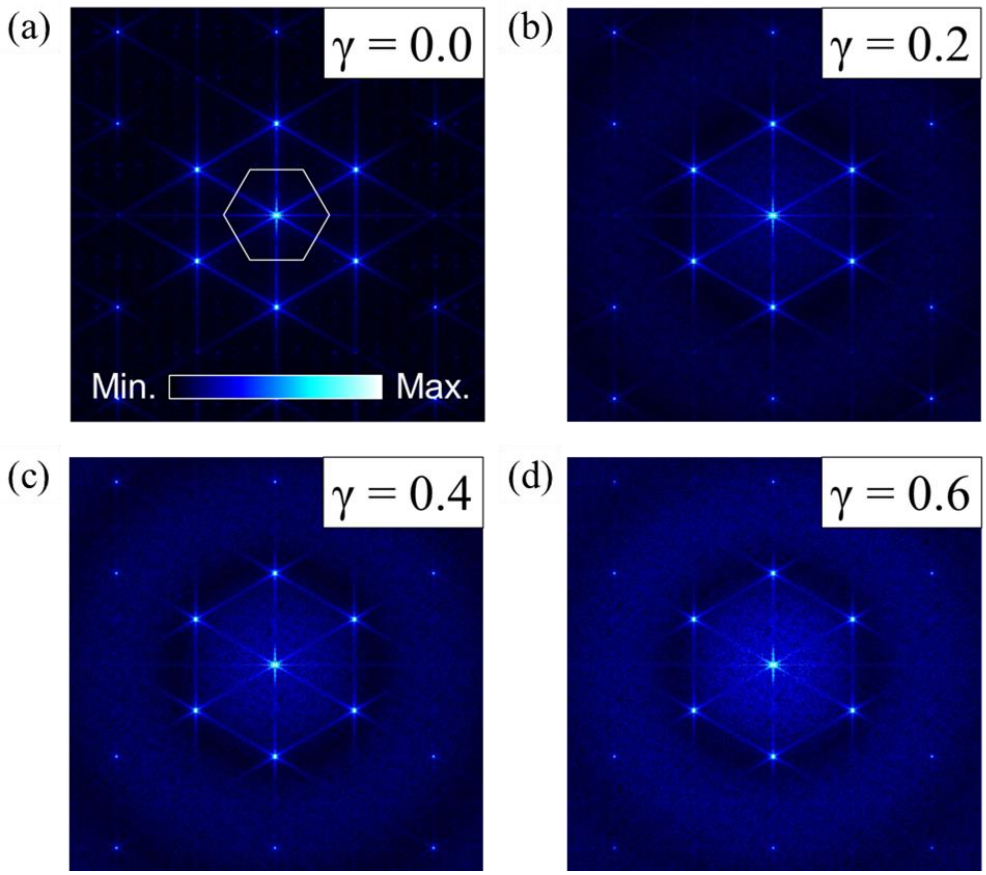

Figure 2-9. Fourier-transformed images of photonic crystal alloys with representative values of the degree of disorder. Each image is generated by taking a two-dimensional Fourier transform on the structures in real space corresponding to (a) γ = 0.0, (b) γ = 0.2, (c) γ = 0.4, and (d) γ = 0.6, shown in Figure 2-8.

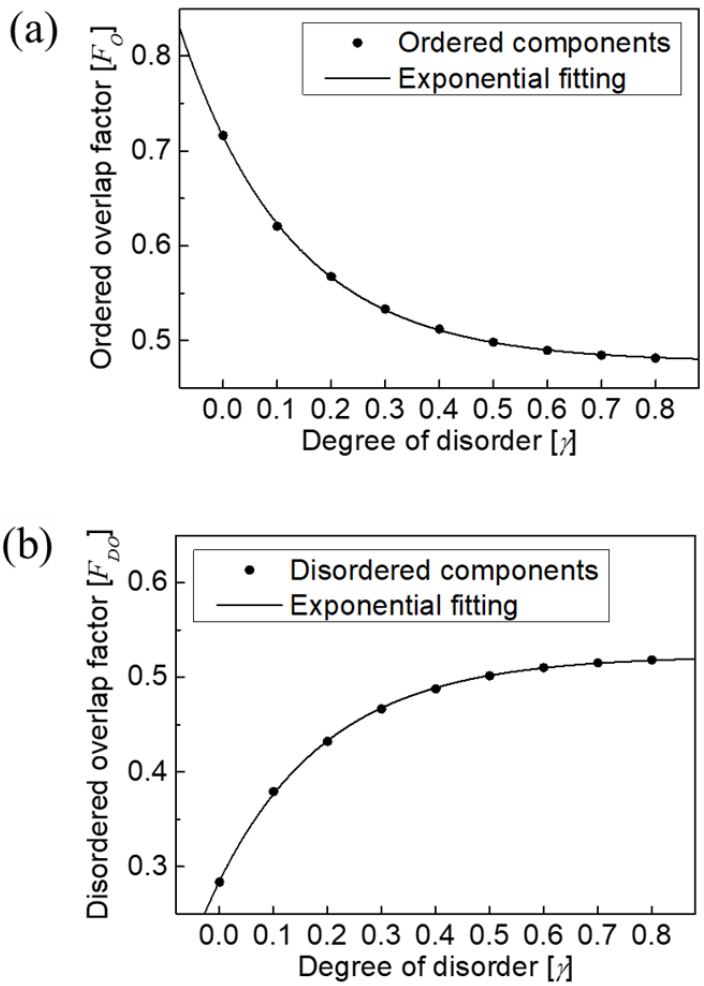

Figure 2-10. Relative ratio between the ordered and disordered components in Fourier space. (a) The ordered overlap factor F_O, defined by an integral of a Fourier-transformed intensity profile weighted at the reciprocal lattice points, quantifies the amount of ordered components characterized by the bright spots in Figure 2-9. (b) The disordered overlap factor F_{DO}, defined by $F_{DO} = 1 - F_O$, quantifies the disordered components in the form of thin mist dispersed over the entire momentum space.

2.2.4. Summary

i. Photonic crystal alloys attribute the disordered components to the diversity of basis photonic atoms and the configuration of an arrangement of these atoms over the lattice site, motivated to maintain the crystalline symmetry regardless of the disorder strength.

ii. The structural degrees of freedom of photonic crystal alloys can be separated into those from basis photonic atoms and their spatial arrangement over lattice sites, which can be further specified by the degree of disorder γ, the average radius r_0, and the configuration of an arrangement.

iii. The proposed platform preserves the crystalline symmetry, regardless of the degree of disorder. Both the ordered and disordered components change exponentially according to the degree of disorder as demonstrated and quantified by Fourier analysis.

2.3. Optical activation

2.3.1. Motivation: Examining all eigenmodes in the system

The system of interest in this thesis is a strongly scattering structure that confines and shapes light within the membrane. For the purpose of observing evolution of all modes within a specific energy range (here the band-gap) according to the change of the structural parameters, there are generally two types of optical methods that can be applied: active and passive approaches.

A passive measurement is an optical method that externally injects light source and examines how the injected photons are reflected, absorbed, and transmitted, which can be used to infer the information of light coupling to the structure. However, it is difficult to excite certain modes that depend on the details of light source such as polarization, propagation direction, and spatial profile. In addition, since the source and mode have the same energy, it is difficult to distinguish only significant signals from massive backgrounds. Above all, the effects of absorption from materials consisting the structure is an important but difficult matter.

On the other hand, in this thesis, photoluminescence responses are studied using gain materials embedded inside the structure that absorb a photon from external light source and re-emit a frequency-converted photon. Responses of the system can then be measured more clearly and precisely than those of passive approaches by physically separating the energy band of the excitation source and the mode emission, and by exciting nearly every existing mode with evanescent coupling from inside the structure. Also, it is possible to rule out the effect of absorption based on the population inversion mechanism.

2.3.2. Planar waveguide: Confining light within 2D slab structure

The membrane of the proposed platform is realized as a form of a planar waveguide whose thickness is set to $h_{slab} \sim 2n/\lambda \sim 230$ nm so that only the fundamental mode in the vertical direction could be formed in the energy band of interest ($\lambda \sim 1530$ nm), as shown schematically in Figure 2-11. Indium Phosphide (InP)-based semiconductor layer with a very high refractive index of $n_{slab} \sim 3.5$ is used as a slab waveguide that confines light inside the membrane by the mechanism of total internal refraction where the index contrast of the slab waveguide to the superstrate and substrate is important. The approach of this thesis is to secure the high-index-contrast by bonding the slab waveguide grown on a donor epi-wafer to a handling wafer of the low refractive index using a wafer-fusion technique [76] (see also Section 2.4.1). As the handling layer, fused silica is used which exhibits transparent optical properties at the energy band of interest. By exposing the other side to the air, the high-index-contrast is ensured while at the same time the probe tip approaches the sample surface and can detect the evanescent fields.

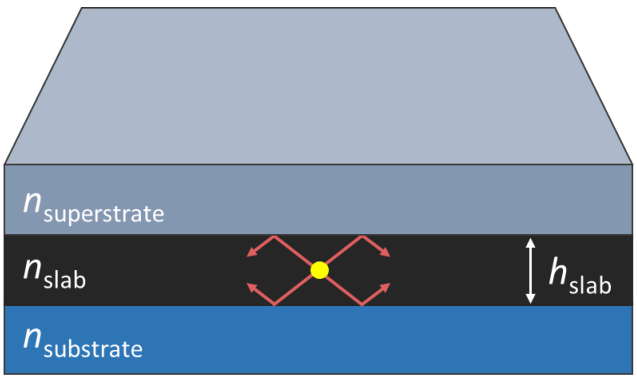

Figure 2-11. Schematic of a planar waveguide. The photons emitted from a light source inside the waveguide are confined within the membrane once the condition for total internal refraction is satisfied.

2.3.3. Multiple-quantum-well structure: Quantum confinement of charge carriers

An active layer used in this thesis is the multiple-quantum-well (MQW) structure made by alternately arranging materials with different values of energy band-gap in the normal direction to the wafer to spatially confine charge carriers in the material of smaller band-gap, which forces discrete energy values by the quantum confinement effect [77]. The thickness of each layer consisting MQW structures is adjusted for the condition that these discrete energy levels of an exciton generated by absorbing energy of excitation energy source can radiatively recombine at the desired energy (~1550 nm). For this sample, the author received an epi-wafer grown by molecular beam epitaxy method [76] from the France group led by C. Seassal.

Since the thickness of slab waveguide is adjusted to sustain only the fundamental mode as described in Section 2.3.2 anti-nodes of modes are formed at the center of the waveguide if we neglect a small asymmetry of index difference between superstrate and substrate. Thus, the overall MQW structure is located at the center of the slab waveguide to obtain the maximized spatial gain overlap (see also Section 3.3.5).

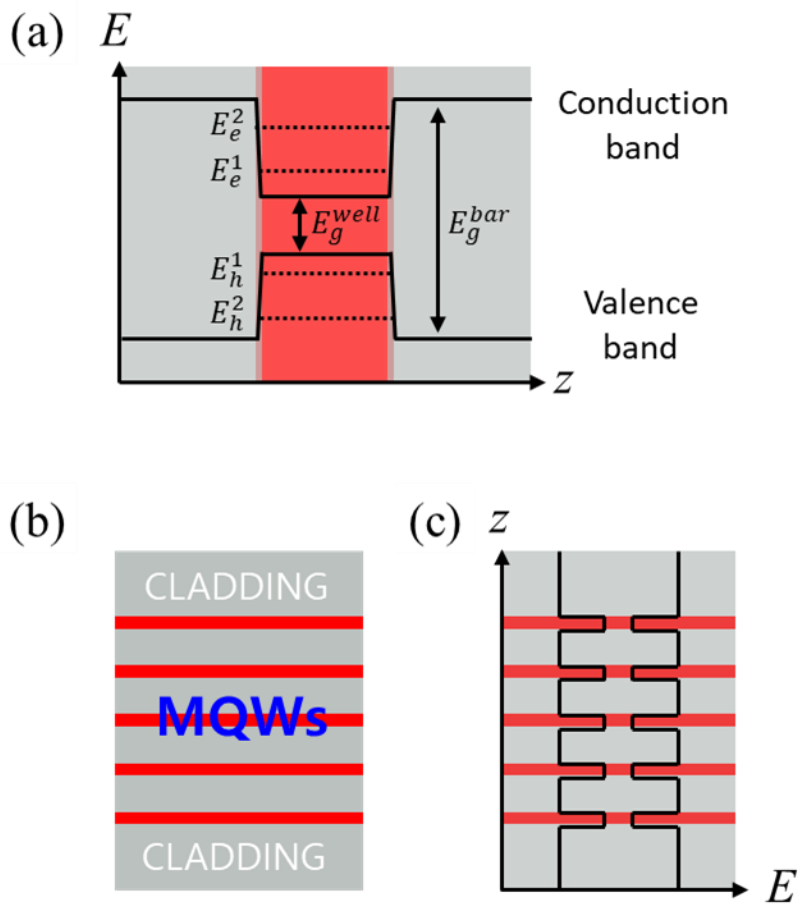

Figure 2-12. Schematics of multiple-quantum-well (MQW) structures designed to control discrete energy values of charge carriers. (a) A quantum well is formed by sandwiching a band-gap material such as a semiconductor between wider band-gap materials. (b) A MQW structure is grown by sequentially stacking each quantum well. (c) The energy band diagram corresponding to the MQWs shown in (b).

2.3.4. Laser operation: Exclusive study of eigenstates

In this thesis, an active approach using MQW structures are used for the expectation of lasing an eigenstate (or a mode) of the proposed platform. The modes in the system should be spatially well confined for this purpose. In the vertical direction, the mode is guided by the principle of total internal reflection with the aid of high-index-contrast slab waveguide, which is also laterally trapped inside the photonic crystal alloys by the multiple scattering mechanism. The mode localized in space has a small move volume V, a higher quality factor Q, and thus the larger Purcell enhancement factor [36], that is proportional to Q/V, than those of the extended Bloch state, where fields are distributed over the entire structure and interacts with the environment. Therefore, it is possible to exclusively distinguish only the modes formed by multiple scattering mechanism with enhanced photoluminescence.

The lasing state generally exhibits strong signal intensity and narrow linewidth as shown in Figure 2-13. Therefore, the mode can be clearly characterized with the very high signal-to-noise ratio with respect to background noises. Furthermore, the linewidth of the mode, which is usually quantified by the full width at half maximum (FWHM), is the minimum spectral resolution that can distinguish two adjacent states. For the lasing state, it usually has a very small value of less than 1 nm, which is definitely contrasted with the passive approach. So, it is possible to investigate many eigenstates existing in the structure without unwanted interferences.

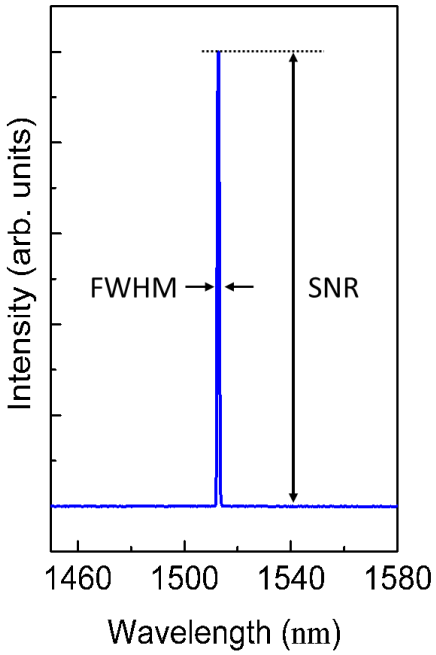

Figure 2-13. Representative spectrum of a laser. In most cases, eigenstates of a system can be studied with very clear signal once the states start to lase. A lasing state exhibits the high signal-to-noise ratio overwhelming other non-lased states and the narrow spectral width improving the spectral resolution of a measurement.

2.3.5. Summary

i. In this thesis, photoluminescence responses are studied using multiple-quantum-well structures embedded inside the system, which can physically separate the energy band of the mode emission from the excitation source, and can excite nearly every existing mode by evanescent coupling, and can rule out the effect of absorption by the population inversion mechanism.

ii. The membrane of the proposed platform is realized as a form of a planar waveguide whose thickness is adjusted to sustain only the fundamental mode in the vertical direction. The high-refractive-index of slab waveguide confines light inside the membrane by the total internal refraction.

iii. Multiple-quantum-well structures made by alternately arranging materials with different values of energy band-gap are used as active layers to derive discrete energy values by the quantum confinement effect, which is located at the center of slab waveguide to obtain the maximized spatial gain overlap.

iv. The mode localized by the multiple scattering mechanism has a larger Purcell enhancement factor than the extended Bloch state, thus allowing only the localized modes to be exclusively distinguished by the enhanced signal intensity.

2.4. Experimental tools

2.4.1. Sample preparation

The overall flow chart for sample preparation and the complete sample structure are schematically displayed in Figure 2-14 and Figure 2-15, respectively. At first, InP-based MQW epilayer structures was grown on an InP substrate using molecular beam epitaxy. The MQW section consists of four InAsP MQWs separated by InP barriers, totaling 230 nm in nominal thickness, which corresponds to ~$\lambda/2n$, where λ is the emission wavelength of the MQWs and n is the effective refractive index of the slab waveguide. Underneath the MQW section, an InGaAs etch-stop layer for selective chemical etching was grown ahead. The grown wafer was flip-bonded onto a fused silica substrate using a wafer fusion technique [76], resulting in an InAsP/InP MQW layer that is directly in contact with the silica substrate. The InP substrate and InGaAs etch-stop layer were then selectively removed in dilute HCl and $FeCl_3$ solutions, respectively. A 50-nm-thick silicon nitride hard mask layer was deposited on the exposed surface of the MQW epilayer using the plasma-enhanced chemical vapor deposition method (310PC, Surface Technology Systems) at a process temperature of 200°C. Electron-beam lithography (JBX-6300FS, JEOL) was then used to generate 2D photonic crystal alloy patterns, which was followed by reactive ion etching (RIE 80 Plus, Oxford Instrument) to sequentially transfer the patterns onto the silicon nitride hard mask layer and the MQW layer. Finally, the hard mask layer was removed using the same reactive ion etching process to complete device fabrication.

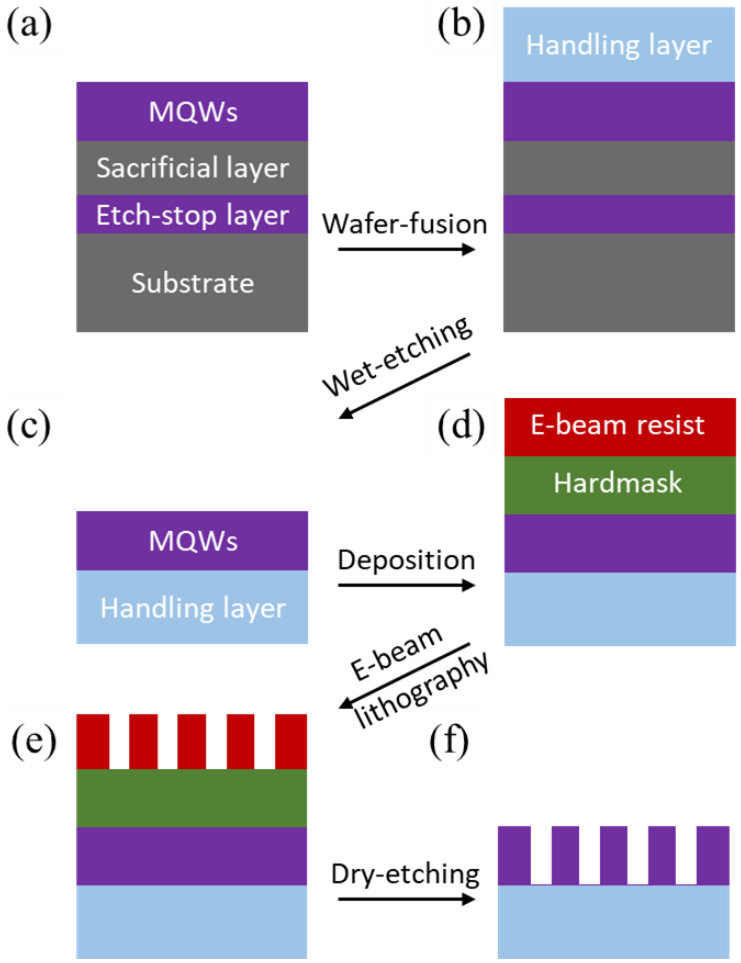

Figure 2-14. Process flow diagram used to fabricate photonic crystal alloys in a slab waveguide. (a) The epi-structure of a wafer embedding multiple-quantum-wells (MQWs). (b) A handling layer is bonded onto the MQWs by wafer-fusion method. (c) Unnecessary layers are removed by selective chemical etching. (d) A hard mask layer is deposited by the plasma-enhanced chemical vapor deposition method, and a resist layer is spin-coated. (e) Photonic crystal alloys are generated on the resist film by the e-beam lithography. (f) The patterns are transferred sequentially onto the MQWs using the reactive ion etching.

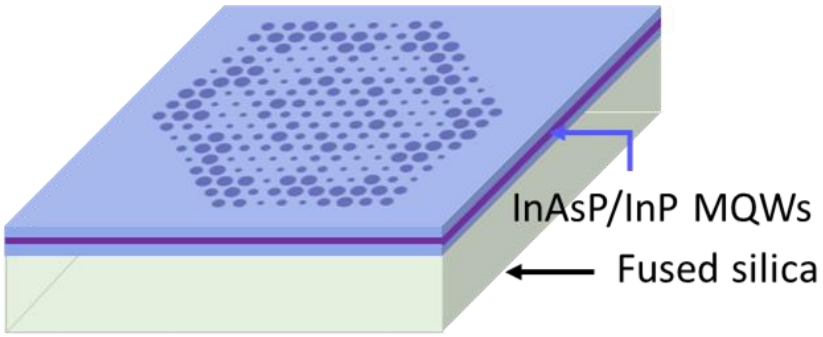

Figure 2-15. Schematic of the complete sample structure. The InAsP/InP multiple-quantum-well layer is a high-index guiding layer and the fused silica is a transparent low-index substrate at the emission band of multiple-quantum-wells (λ ~ 1550 nm).

2.4.2. Photoluminescence measurement

Photoluminescence measurements are performed using a home-made fiber-based setup [78], in which a cleaved butt-end fiber tip with a 62.5-μm core diameter is connected to a 1 × 2 multiplexing multimode fiber coupler, as schematically illustrated in Figure 2-16. The pump beam from a 1064-nm pulsed laser diode (PSL10, Multiwave Photonics), operating at a 500-kHz repetition rate with a 20-ns pulse duration, is coupled to the input port of the coupler. The cleaved fiber tip is brought in close proximity to the desired location on the sample surface as displayed in Figure 2-17. Scattered light output emitted from the sample is then detected via the same fiber tip and delivered to the output port of the coupler, which is, in turn, fed to an optical spectrum analyzer (Q8381A, Advantest) for spectral analysis.

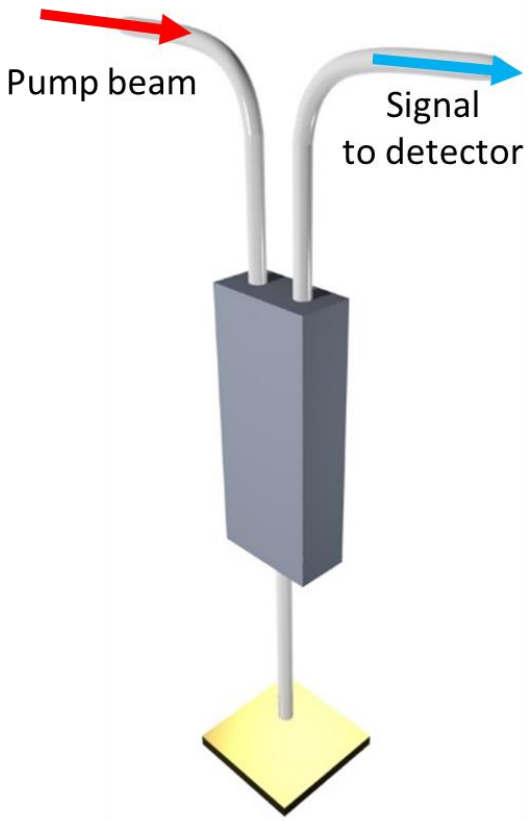

Figure 2-16. Schematic of a home-made fiber-based setup for photoluminescence measurement [78]. The cleaved butt-end fiber tip, used as a single channel for both optical excitation and collection, is connected to a 1 × 2 multiplexing fiber coupler. The input and output ports of the coupler are channels for a pump beam and a detector, respectively.

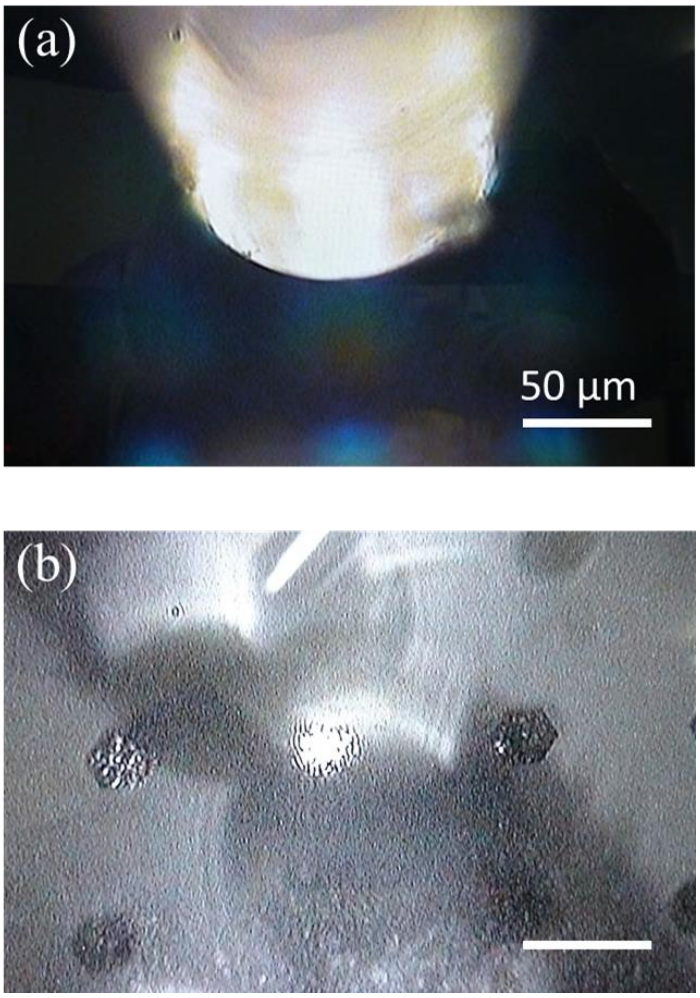

Figure 2-17. Microscope images demonstrating the operation of the photoluminescence measurement. (a) The cleaved fiber tip illustrated in Figure 2-16 under the condition of white light illumination. (b) An image showing the pump beam scattered from a photonic crystal alloy. The image is captured by focusing on the surface of the device without illumination.

2.4.3. Near-field measurement

A custom-designed scanning near-field optical microscopy (SNOM) setup [79], schematically shown in Figure 2-19, is used to obtain eigenmode profiles. The scanning part is made by integrating a scanning controller system (SMENA, NT-MDT) with an inverted optical microscope (Eclipse Ti-S, Nikon) and the detecting part is an assembly of a monochromator (microHR, Horiba), an InGaAs photodiode (DSS-IGA025T, Horiba), and a lock-in amplifier (SR830, Stanford Research Systems), operating in the near-infrared range.

The SNOM setup is operated in a collection where a pump beam is injected from the back side of the sample, through the transparent fused-silica substrate, by a laser diode modulated with an additional 1-kHz envelope as a reference signal to the lock-in amplifier. The near-field signal from samples is then recorded by a commercial dielectric SNOM probe (MF115_NTF/WA, NT-MDT) while the probe tip scans the front surface of the sample. In order to preserve relative positions of pump beam and sample during scanning process the scanning-by-probe scheme is used in which only the probe mounted in the scan head moves during the scanning process as schematically illustrated in Figure 2-18.

Representative pump beam profile of the near-field measurement setup is measured over a bare quartz surface at the pump beam frequency, which exhibits symmetric profiles as displayed in Figure 2-20. Line profiles across the maximum intensity point reveal near-gaussian beam shapes with a beam width of 9.2 μm in full-width at half-maximum. These excitation condition are controlled for the best measurement by adjusting the distance between the focal plane of the objective lens and the front side of the sample, and the corresponding changes of beam width and intensity are shown in Figure 2-20 and Figure 2-21.

For each scanning process the center wavelength of the monochromator is tuned to the wavelength of the corresponding mode. The amount of spectral shift caused by probe perturbation is measured to be less than 1 nm. The spectral resolution of the monochromator is managed using the slit width inside the monochromator, which is changed as measured in Figure 2-22. As an optimal compromise value between signal-to-noise ratio and mode distinguishability, ±1 nm for HWHM (half-width at half-maximum) is used in whole measurement. Spatial resolution of SNOM scanning are set to 17 pixels/μm in Chapter 3, and 20 pixels/μm in Chapter 4, respectively.

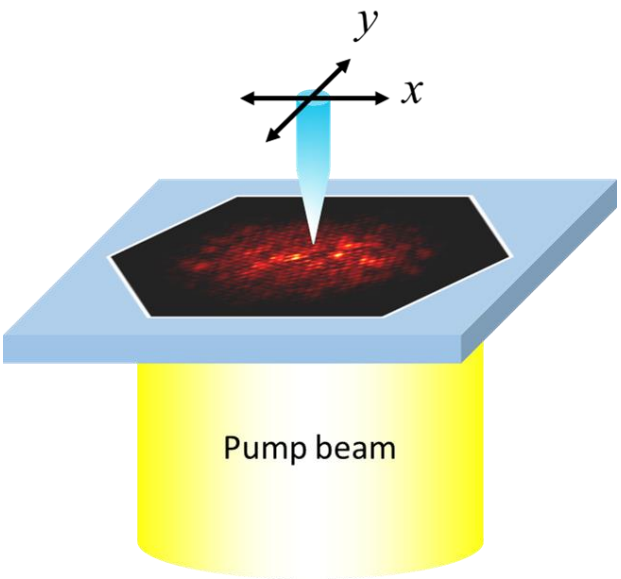

Figure 2-18. Schematic of a near-field measurement operating in the scanning-by-probe scheme. A sample is excited from the backside through the transparent substrate and the near-field signals are collected by scanning the probe over the front surface of the sample.

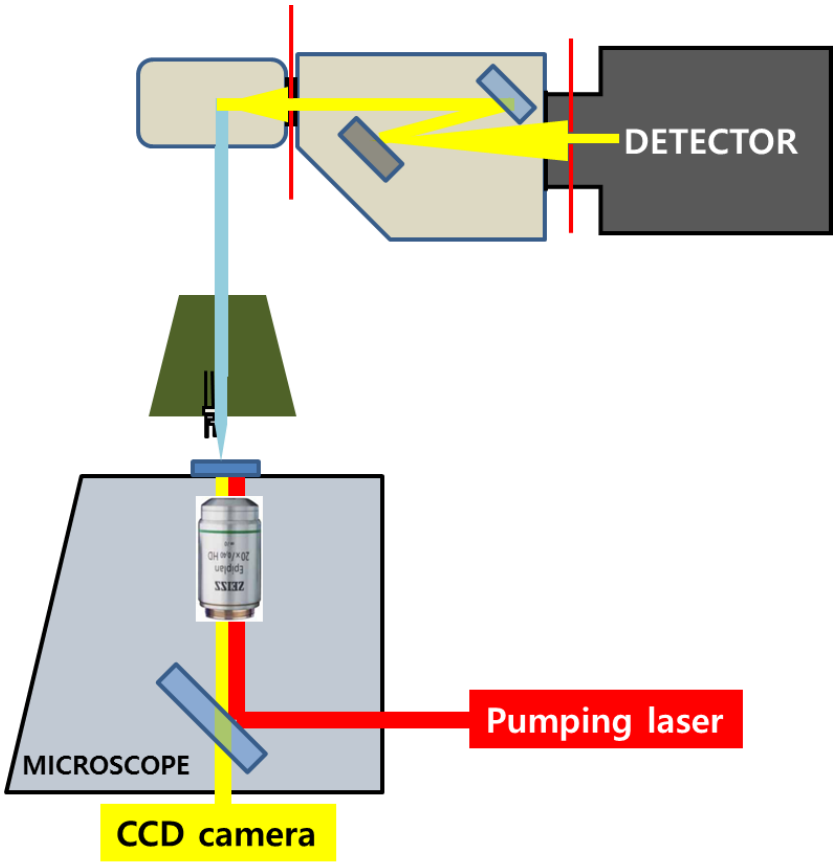

Figure 2-19. Schematic of the apparatus custom-designed for scanning near-field optical microscopy operating in a collection geometry [79]. The scanning part is constructed by integrating a scanning controller system with an inverted optical microscope. The detecting unit is composed of a monochromator, a photodiode, and a lock-in amplifier.

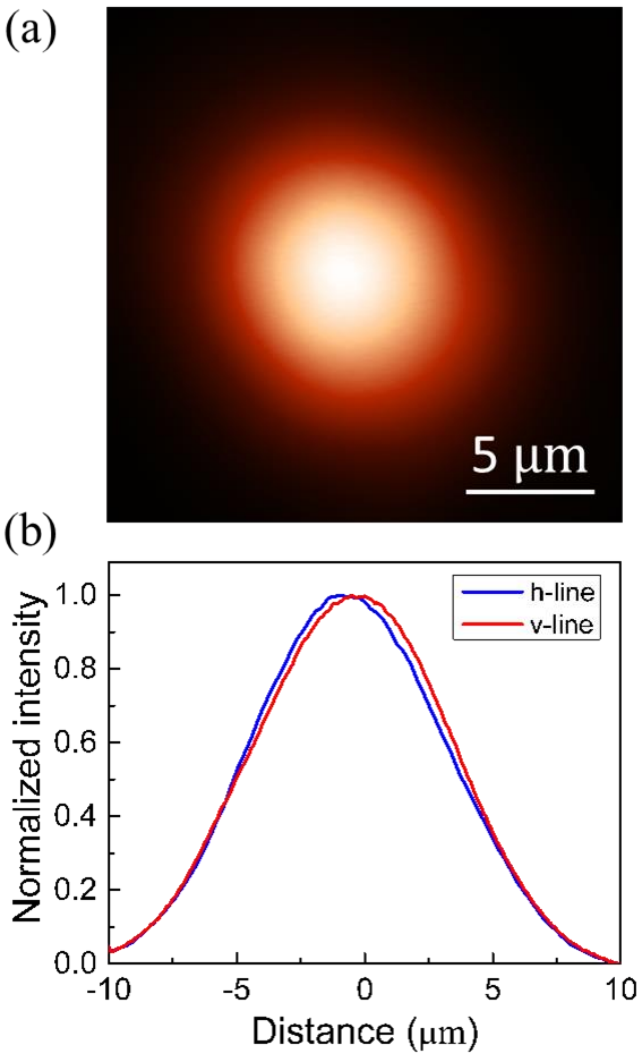

Figure 2-20. Representative pump beam profiles of the near-field measurement setup. (a) A Near-field profile of a representative pump beam measured over a bare quartz surface at the pump beam frequency. (b) Line profiles across the maximum intensity point of (a), which reveal near-gaussian beam shapes with a beam width of 9.2 μm in full-width at half-maximum.

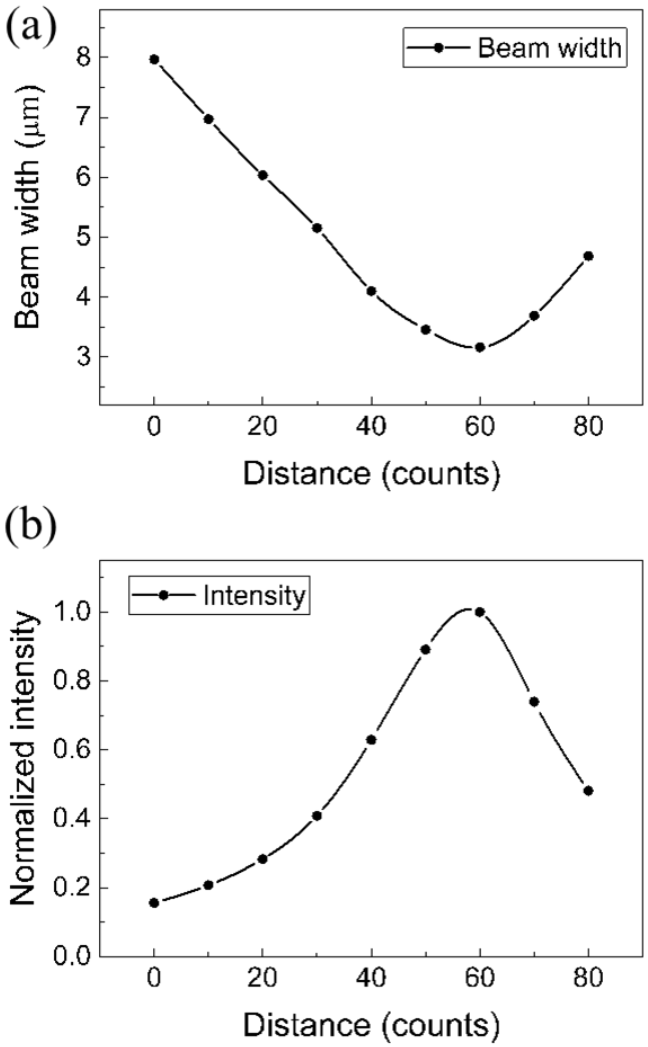

Figure 2-21. Excitation conditions of the near-field measurement setup. Pump beam conditions are measured as a function of the distance between the sample and the objective lens: (a) Beam width and (b) pump intensity can be intentionally adjusted for proper pumping conditions by modulating the distance between the focal plane of the objective lens and the front side of the sample.

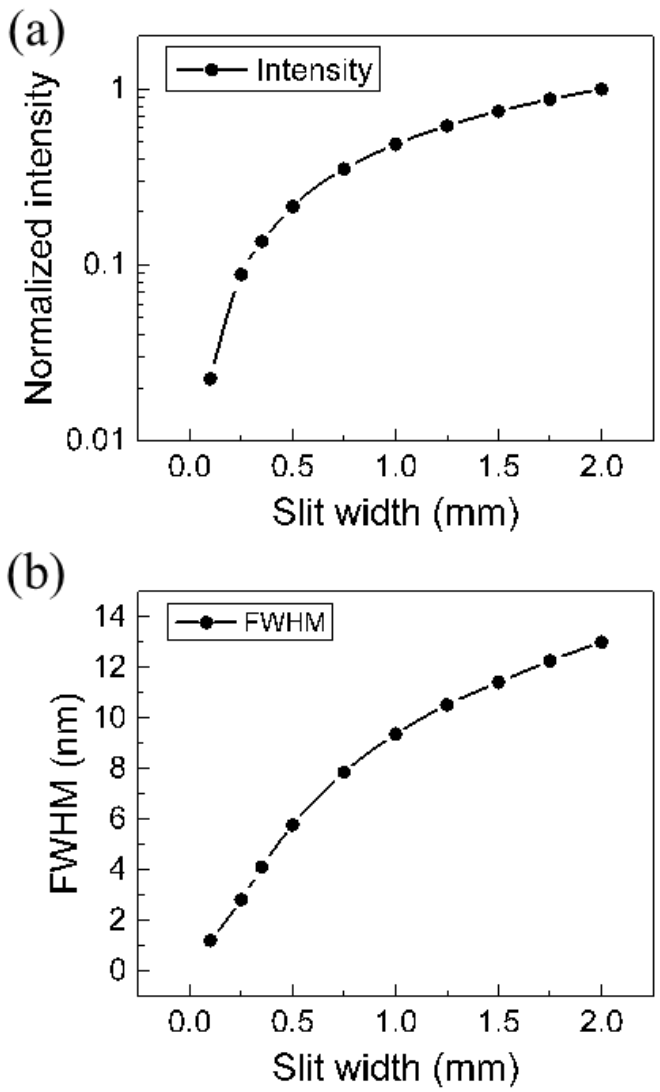

Figure 2-22. Detection conditions of the near-field measurement setup. The peak intensity and the linewidth (full-width at half-maximum) of the detection signal are measured as a function of the slit width inside the monochromator: In the range of accessible slit width (a) the intensity is changed about two orders of magnitude and (b) the linewidth is manageable from 1.2 nm to 13 nm.

2.4.4. Simulation method

Numerical simulations based on the finite-difference time-domain (FDTD) method are performed using a commercial package (FDTD solutions, Lumerical Solutions). For each model structure, the simulation domain size is set to cover a whole structure including proper paddings for the spatial resolution of 45 pixels/μm, which is sufficiently high to distinguish individual modes. A full 3D calculation as well as the so-called 2.5D FDTD method are used, where the last uses a set of effective 2D materials with effective refractive indices determined from the in-plane wavevector component, which offers 3D accuracy using only 2D computing resources although it is accurate for a specific simulation bandwidth [80]. In this thesis, $n_{\mathrm{eff}} = 2.7$ is used for the effective index of slab waveguide that embeds photonic crystal alloys.

To mimic real experimental conditions and to excite as many resonant modes existing in the model structure as possible, the dipole cloud approach is used where many dipoles with random positions, polarizations, and phases are incorporated within a virtual pump spot. Likewise, many randomly positioned time monitors are placed over the entire model structure to identify all the resonant modes from the resultant spectrum. In the analysis step, the apodization of time signals with a Gaussian profile is applied immediately before the Fourier-transformation to eliminate the start and end effects, and to extract the modal spectra without distortion. For the simulated $|E|^2$ distribution of resonant mode, the same approaches are generally taken, except that time monitors are replaced with 2D frequency-domain field monitors.

2.4.5. Summary

i. InP-based epi-wafer embedding multiple-quantum-well structures is bonded onto a fused silica substrate. After removing unnecessary layers, a hard mask layer is deposited, and a resist layer is spin-coated. Photonic crystal alloys are then generated on the resist film, which are transferred sequentially onto the multiple-quantum-well structures.

ii. Photoluminescence measurements are performed using a home-made fiber-based setup in which a cleaved butt-end fiber tip is connected to a 1 × 2 multiplexing fiber coupler. The cleaved fiber tip is brought in close proximity to the desired location on the sample surface to collect signal.

iii. A custom-designed scanning near-field optical microscopy (SNOM) setup, operating in a collection geometry and scanning-by-probe scheme, is used to obtain eigenmode profiles. A sample is excited from the backside through the transparent substrate and the near-field signals are collected by scanning the probe over the front surface of the sample.

iv. Numerical simulations based on the finite-difference time-domain method are performed using a commercial package. For the efficient and accurate calculations, so-called 2.5D FDTD method, the dipole cloud approach, randomly positioned time monitors, and the apodization of time signals are used.

2.5. Conclusion

The concept of a photonic crystal alloy was proposed for the motivation of preserving the crystalline symmetry with the expectation of predictable and engineerable optical properties over a wide spectro-spatial domain, and then optically activated to use the Purcell effect.

The structural parameters of disordered systems for shaping light within a membrane can be precisely controlled using top-down approaches, which can categorize disordered photonic structures into two branches of the lattice disorder and the compositional disorder. Lattice disorder has been actively studied by various groups around the world to investigate fundamental aspects as well as applications, mostly focused on optical random systems and functionalities related these random properties. The compositional disorder has received relatively less attention compared to the lattice disorder although it is now feasible to realize compositionally disordered system in photonic scale. The photonic version of band-gap engineering, and experimental evidences of localized modes have been studied so far. The important optical difference between two disordered system is that the responses to the compositional disorder appears in a wide spectro-spatial domain, which can be quantitatively predicted and thus be engineerable. This is mainly due to the crystalline symmetry in the compositionally disordered system, conserved regardless of the degree of disorder.

For the motivation of maintaining the crystalline symmetry regardless of the disorder strength, the disordered components in photonic crystal alloy systems are attributed to the diversity of basis photonic atoms and the configuration of an arrangement of these atoms over the lattice site. The structural degrees of freedom of photonic crystal alloys can then be separated into those from basis photonic atoms

and their spatial arrangement over lattice sites, which can be further specified by the degree of disorder, the average radius, and the configuration of an arrangement. Both the ordered and disordered components change exponentially according to the degree of disorder as demonstrated and quantified by Fourier analysis, which proves the preservation of crystalline symmetry in the proposed platform, regardless of the degree of disorder.

In this thesis, photoluminescence responses are studied using multiple-quantum-well structures embedded inside the system, which can physically separate the energy band of the mode emission from the excitation source, and can excite nearly every existing mode by evanescent coupling, and can rule out the effect of absorption by the population inversion mechanism. The membrane of the proposed platform is realized as a form of a planar waveguide whose thickness is adjusted to sustain only the fundamental mode in the vertical direction. The high-refractive-index of slab waveguide confines light inside the membrane by the total internal refraction. Multiple-quantum-well structures made by alternately arranging materials with different values of energy band-gap are used as active layers to derive discrete energy values by the quantum confinement effect, which is located at the center of slab waveguide to obtain the maximized spatial gain overlap. The mode localized by the multiple scattering mechanism has a larger Purcell enhancement factor than the extended Bloch state, thus allowing only the localized modes to be exclusively distinguished by the enhanced signal intensity.

InP-based epi-wafer embedding multiple-quantum-well structures is bonded onto a fused silica substrate. After removing unnecessary layers, a hard mask layer is deposited, and a resist layer is spin-coated. Photonic crystal alloys are then generated on the resist film, which are transferred sequentially onto the multiple-quantum-well structures. Photoluminescence measurements are performed using a home-made

fiber-based setup in which a cleaved butt-end fiber tip is connected to a 1 × 2 multiplexing fiber coupler. The cleaved fiber tip is brought in close proximity to the desired location on the sample surface to collect signal. A custom-designed scanning near-field optical microscopy (SNOM) setup, operating in a collection geometry and scanning-by-probe scheme, is used to obtain eigenmode profiles. A sample is excited from the backside through the transparent substrate and the near-field signals are collected by scanning the probe over the front surface of the sample. Numerical simulations based on the finite-difference time-domain method are performed using a commercial package. For the efficient and accurate calculations, so-called 2.5D FDTD method, the dipole cloud approach, randomly positioned time monitors, and the apodization of time signals are used.

Chapter 3 – Photonic band-tail states

3.1. Introduction

3.1.1. Theoretical predictions of S. John: Localized states inside the band-gap

Since the concept of photonic crystals was proposed by E. Yablonovitch in 1987, the same year, S. John [27] theoretically proved that a photon can be strongly localized if disorder is introduced to such a photonic lattice system. This discovery, which proved the emergence of strong localization of photons in a carefully prepared disordered system consisting of only real positive dielectric constants, is a historical milestone of photon localizations that recognized the important role of backbone crystallinity, a large-scale geometric resonance of scattering elements, and developed systematic theory of its effect, which leads to the conclusion beyond a single-scattering Mie resonance regime.

The most familiar example of such a resonance is the Bragg scattering observed in an electron of a perfect crystal. S. John noted that there is a pseudo-gap, or even a band-gap in an amorphous semiconductor, which is an electronic disordered system where a large-scale geometric resonance is persisted as a backbone mechanism [81, 82]. As a concept of photonics corresponding to this mechanism, S. John suggested photonic crystals with a moderate disorder of coherent arranged scattering elements, and revealed that a photonic pseudo-gap could exist in the Mie resonance regime of the system, as shown in Figure 3-1. In addition, the states in this pseudo-gap region are proved to be strongly localized by the Anderson localization mechanism, which thus verified that a disordered lattice structure made by coherently arranging scattering elements in a backbone crystallinity is a key system for predictable and

systematic observation of strongly localized photons in non-dissipative materials with real positive dielectric constant.

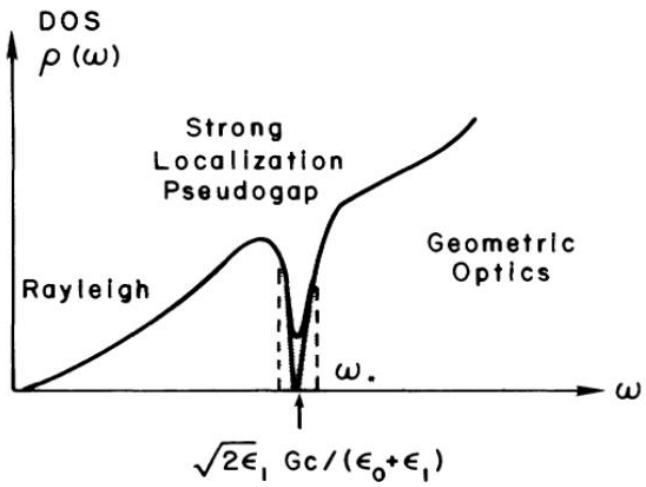

Figure 3-1. Photonic density of states in a disordered photonic crystal [27]. Strongly localized photonic states are expected in a pseudo-gap separating extended states in low-frequency Rayleigh scattering and high-frequency geometric-optics region.

3.1.2. Expected modal properties: Energy dependence of localization

While elucidating the importance of a delicate interplay between order and disorder for strong localization of photons, and corresponding presence of a pseudo-gap with strongly localized states, S. John also suggested that these localized states could be photonic band-tail states with modal properties very similar to the band-tail states of electronics [83, 84].

As described in Section 3.1.1, these strongly localized photonic states exist in the Mie resonance regime, a specific frequency window between the Rayleigh scattering and the geometric-optics region. S. John attributed the origin of the mobility-edge, a specific spectral position that separates extended states from localized states, to a photonic band-edge at which the restriction of coherent

backscattering to Bragg resonance is most drastic due to the macroscopic geometric resonance. Based on the perturbation theory, he showed that the effect of the disorder is then shifting the position of the photonic band-edge E_{BE} further into the gap E'_{BE}, and thus the mobility-edge E_{ME} of the photon is in the region between E_{BE} and E'_{BE} for weak disorder case. With respect to the frequency ω_{ME} of mobility-edge, he predicted that the coherence length ξ_{coh} of an extended state diverges as $\xi_{coh} \sim |\omega - \omega_{ME}|^{-1}$, a similar form given by the scaling theory of electron localization formulated by E. Abrahams *et al.* [56] and D. Thouless [82], while the localized state occur as a standing wave with an envelope function whose wavelength λ_{env} is modulated as a form of $\lambda_{env} \sim |\omega - \omega_{BE}|^{-1/2}$ [74].

3.1.3. Previous studies on photonic band-tail states

Since the importance of the coherent arrangement of scattering elements has been revealed, there have been many experimental studies designed to observe photonic band-tail states and their strong localization by using a system based on this mechanism. The most notable one is the study on transverse localization [85, 86] of the Israel group headed by M. Segev. With the aid of optical induction technique [67], Schwartz *et al.* [87] realized a 2D photonic lattice with random fluctuations where the index change Δn is generated by superimposing random fluctuations over a periodic background. Along the propagation axis of this 2D system, they injected a laser beam and directly imaged the intensity distribution at the lattice output, which vividly demonstrated the transverse localization of the laser beam with increasing disorder level as shown in Figure 3-2.

This study is not the localization of photonic band-tail states at all and they had to take an ensemble averaging to bring meaningful conclusions because the system

has no band-gap due to the small-index-contrast of $\Delta n/n_0 \sim 10^{-4}$ and the energy of laser beam ($\lambda = 512$ nm) is less likely to be an eigenstate of the system ($a = 11.2$ μm). Despite these limitations, their study has changed the paradigm of research on localization of light into a way of visualizing a localization of photon and directly measuring the extent of localization.

Subsequently, the mainstream of research on the disordered photonic lattice system proposed by S. John has established its experimental basis on direct measurements such as scanning near-field optical microscopy over samples fabricated by top-down approaches [88, 89, 90]. As a representative example, Obara group [88] observed spectral signature of photonic band-tail states in weak disorder regime as shown in Figure 3-3 and succeeded in directly measuring spatially localized mode profiles as displayed in Figure 3-4. Also, Spasenovi *et al*. [89] demonstrated the slow effect near band-edge and corresponding localized states by imaging near-field transmission signals in the photonic crystal waveguide as shown in Figure 3-5.

However, most of these studies have studied the lattice disordered system. As described in Section 2.1.4, these systems exhibit the fundamental limitation that predictable and systematic observations, one of the important optical properties of photonic band-tail states, are hard to be established with increasing disorder due to collapse of the crystallinity, which restricts available range of structural parameters systematically controlling optical properties of the band-tail states into a small region. Therefore, in order to realize the next generation light shaping platform handling photonic band-tail states over a wide spectro-spatial domain, a photonic crystal alloy is necessary that preserve the crystalline structure regardless of disorder strength.

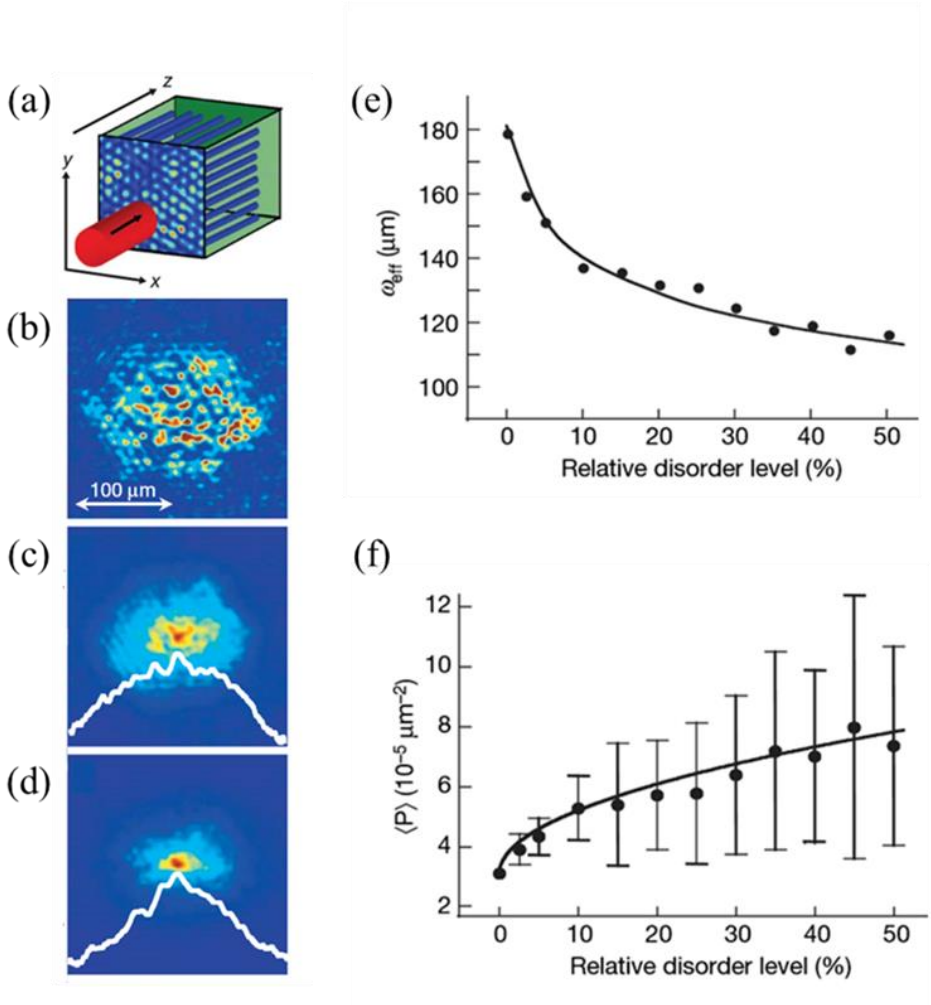

Figure 3-2. Transverse localization in disordered photonic lattices [87]. (a) Schematic of the transverse localization scheme where a probe beam is injected to a disordered lattice with transverse modulations and one invariant propagation direction. (b-d) Ensemble-averaged intensity distributions at the lattice output, (b) without disorder (c) with 15% and 45% disorder. (e) Ensemble-averaged effective width measured at the lattice output as a function of disorder level. (f) Average and standard deviations of inverse participation ratio as a function of disorder level.

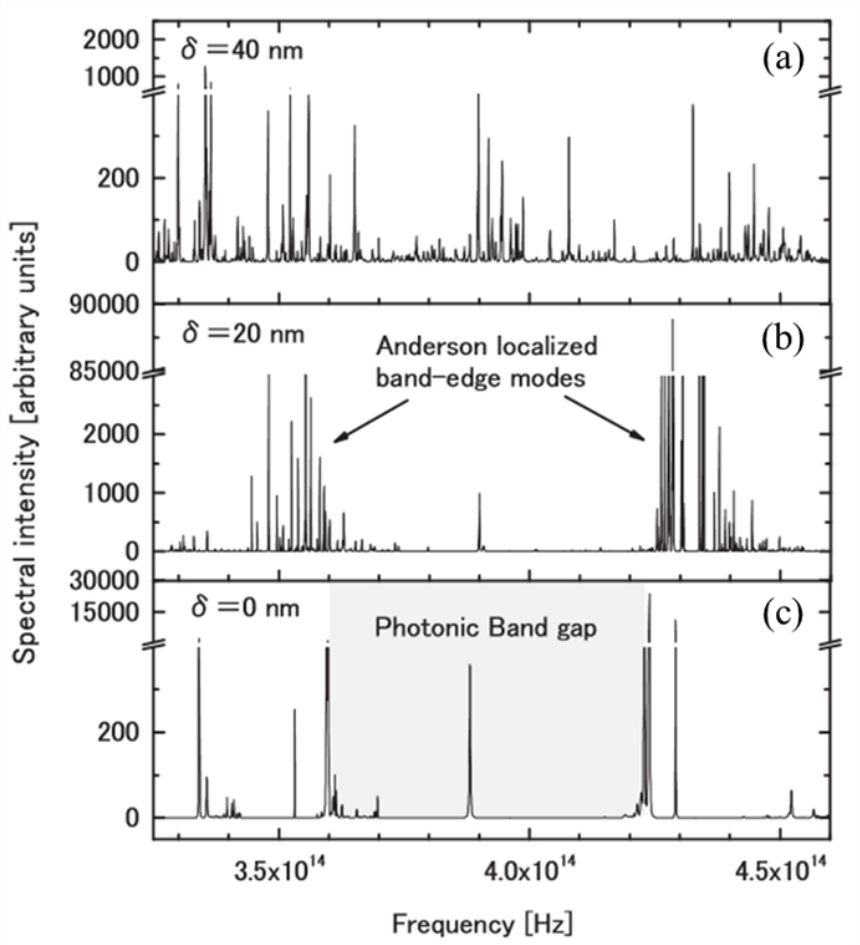

Figure 3-3. Optical modes around the band-gap in random photonic crystals [88]. Frequency spectra of random photonic crystals are computed with respect to the magnitude of randomness δ. (a) With the strong random deviation of δ = 40 nm, the system completely lose the dispersion characteristics of the normal photonic crystals. (b) The system with moderate randomness of δ = 20 nm exhibits sharp spikes around both sides of the band-gap. These peaks are attributed to the Anderson localized modes. (c) In an ordered case of δ = 0 nm, the spectrum reduces to that of the typical normal photonic crystal with a defect mode at the center of the band-gap.

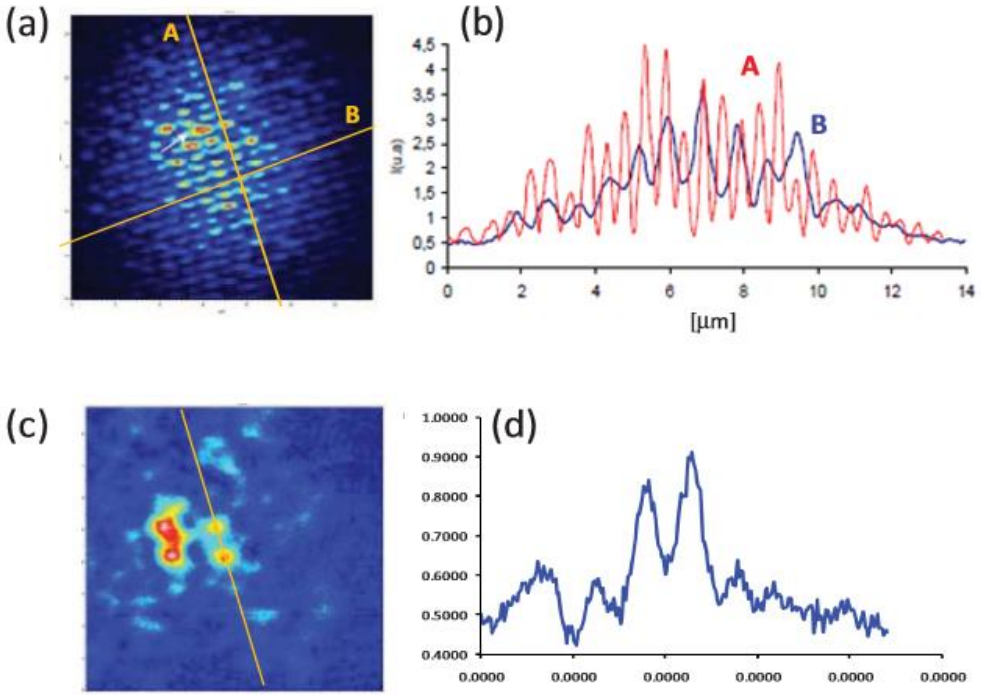

Figure 3-4. Spatial profiles obtained by near-field measurements in random photonic crystals [88]. (a-b) The obtained near-field profiles of the random photonic crystal with δ = 0 nm show (a) a spatially periodic mode profile and (b) line profiles. (c-d) The near-field profiles of the structure with δ = 10 nm show (c) a spatially localized mode profile and (d) a line profile with a localized exponential envelope.

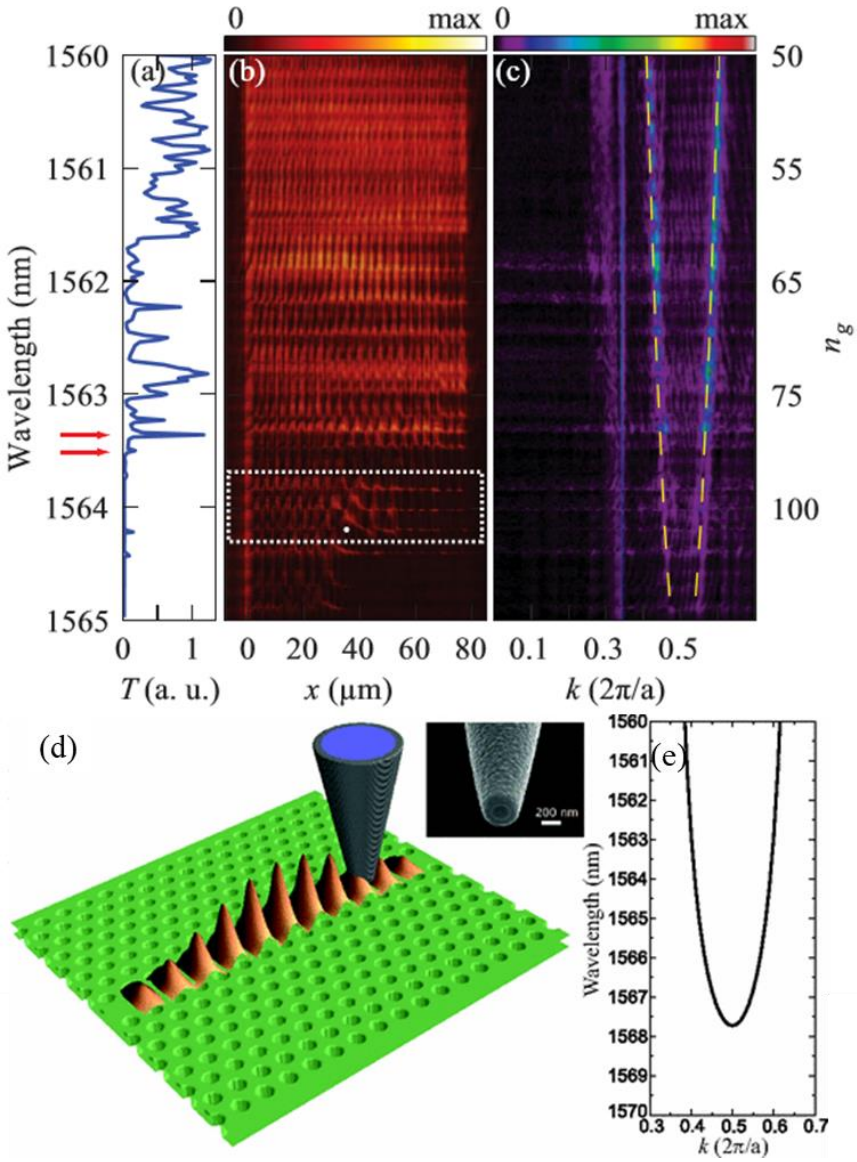

Figure 3-5. Localized states in a slow-light photonic crystal waveguide [89]. (a) A transmission spectrum of the waveguide measured with the probe far from the sample. (b) Near-field amplitudes as a function of wavelength and probe position. Light beam is launched from x = 0. (c) The dispersion of the waveguide obtained by a Fourier transform of real-space data. (d) A schematic of the photonic crystal waveguide and the probe. (e) Calculated dispersion relation of the photonic crystal waveguide.

3.1.4. Prerequisites for photonic band-tail states

Based on the discussion so far, it is possible to summarize one sufficient condition for observing and studying photonic band-tail states over a wide range of spectro-spatial domain, which offers sufficient degrees of freedom for realizing light shaping applicable to complex system.

First, a disordered system, with a capability of predictable and systematic observations regardless of disorder strength, is required. The photonic crystal alloy based on compositional disorder can be a good candidate because the crystallinity is actually preserved as described in Section 2.2.3. Second, a playground of the photonic band-tail states is near the band-edges inside the band-gap. Therefore, it is necessary to secure a wide band-gap to mitigate the spectral resolution required for identifying individual photonic band-tail state. Therefore, the high-index-contrast InP-based semiconductor membrane introduced in Section 2.3.2 is a good candidate. Third, photonic band-tail states are expected to be strongly localized in spatial domain. However, since there are also extended Bloch states in the same system, a proper experimental solution is needed to clearly distinguish localized band-tail states from extended Bloch states. For this, the difference in signal intensity due to the Purcell enhancement [36], in an optically activated system, can be a good measure as described in Section 2.3.4.

3.1.5. Summary

i. The concept of photonic lattices with a moderate disorder of coherently arranged scattering elements was proposed by S. John in 1987. In this system, a photon can be strongly localized in a pseudo-gap region by Anderson localization mechanism, resulting predictable and systematic optical properties.

ii. S. John also suggested that these localized states could be photonic band-tail states with predictable modal properties. These states are standing waves that occur near band-edges with a modulating envelope function whose wavelength is determined by the energy difference to the nearest band-edge.

iii. There have been many experimental studies designed to observe photonic band-tail states and their strong localization, however, these studies employed a lattice disordered system that is hard to establish predictable and systematic observations with increasing disorder due to the collapse of the crystallinity.

iv. One sufficient condition for observing and studying photonic band-tail states over a wide range of spectro-spatial domain is to preserve the crystalline structure regardless of disorder strength, to secure a wide band-gap for the spectral resolution, and to distinguish localized band-tail states from extended Bloch states.

3.2. System of interest

3.2.1. Photonic crystal alloy with random configuration: Maintaining band properties

In this thesis, the eigenstates and optical properties of photonic crystal alloy with random configuration will be investigated. For this purpose a slab waveguide embedding InAsP/InP MQWs is used to realize a photonic crystal alloy by the method described in Section 2.4.1. Representative scanning electron microscopy images are shown in Figure 3-6. The set of samples examined in this Chapter consists of a total of 9 disorder strengths, quantified by a degree of disorder γ ranging from 0 to 0.8 divided by the interval of 0.1, and for each degree of disorder, 10 kinds of configurations are realized to eliminate the influence of configuration-dependent effects. All individual systems consist of a total of 3,169 lattice sites, as shown in Figure 3-7. The air-holes placed at each location are randomly chosen from the quaternary basis photonic atoms whose radii are of equal intervals, with the same probability of 25%.

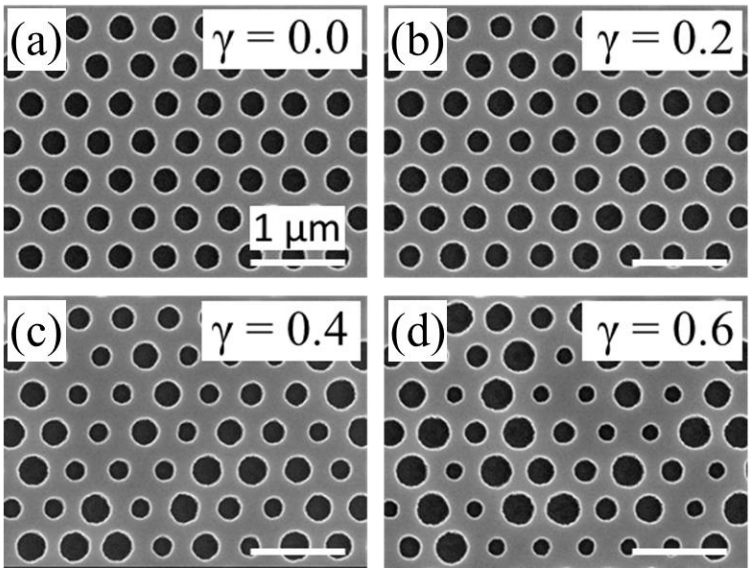

Figure 3-6. Representative scanning electron microscope images of the photonic crystal alloys. The samples are designed to have a lattice constant of a = 450 nm and an average radius of r_0 = 0.3a. The crystallinity is well preserved regardless of the disorder strength quantified by (a) γ = 0.0, (b) 0.2, (c) 0.4, and (d) 0.6.

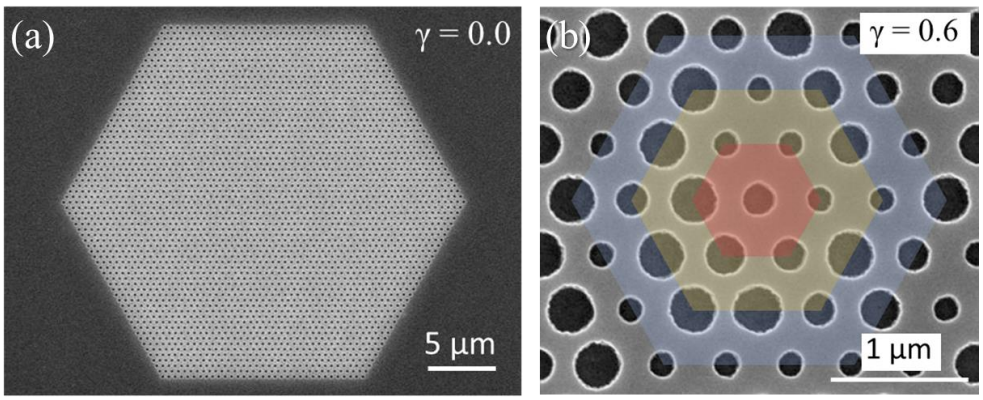

Figure 3-7. Overview and magnified images of the photonic crystal alloys. (a) Each sample is composed of 3,169 air-holes filling a hexagonal with side length of 14.4 μm. (b) Intentionally overlapped hexagons demonstrates the conservation of the crystalline symmetry.

3.2.2. Hexagonal crystal structure: Wide band-gap

As described in Section 3.1.4, it is important to ensure a wide photonic band-gap for successful observations of photonic band-tail states. In this thesis, a hexagonal lattice is employed for this purpose which could offer a very large complete band-gap [91, 92] in addition to using high-index-contrast materials. As displayed in Figure 3-8, a complete band-gap of this structure corresponds to ~300 nm and the dielectric and air band-edges [93] have different crystal momentums occurred at K- and M-symmetric points, respectively. Therefore, it is possible to secure a wide playground of photonic band-tail states to mitigate the spectral resolution required for identifying individual state, and the band-tail state originating from each band-edges can be classified by analyzing the distribution on the Fourier space

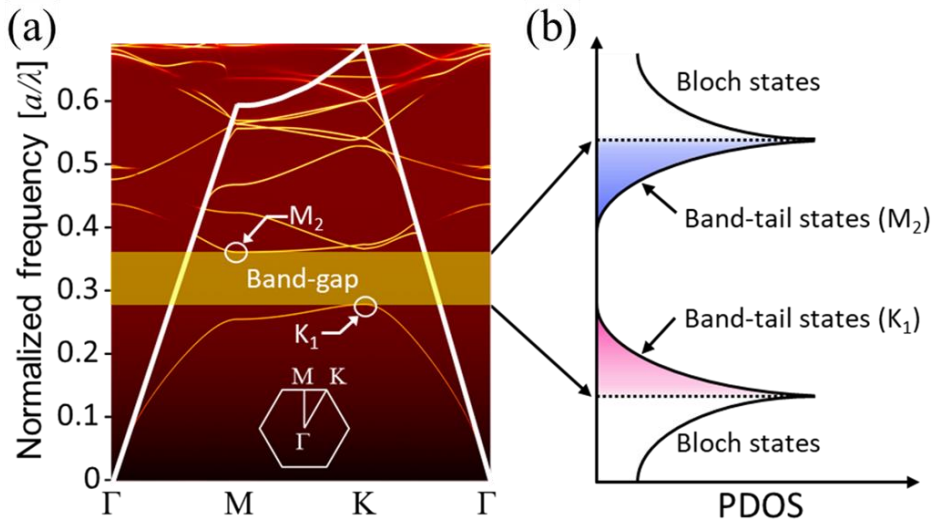

Figure 3-8. Band structures of photonic crystal alloys. (a) A band structure calculated for the photonic crystal in a slab waveguide composed of homogeneous air-holes consisting the hexagonal structure. (b) A conceptual diagram of photonic density of states illustrating the band-tail states in the band-gap region of disordered structure.

3.2.3. Slab waveguide embedding MQWs: Purcell enhancements of localized eigenstates

In this thesis, an optically activated disordered system is realized using MQWs as both a slab waveguide and a gain material. Thus, extended Bloch states and localized photonic band-tail states can be distinguished by signal strength, based on the principle described in Section 2.3.4. The MQW structure is in the form of sequentially integrating 4 pairs of InAsP/InP MQWs as illustrated in Figure 3-9. According to the sample preparation steps written in Section 2.4.1, the epi-wafer is bonded onto the handling layer and the unnecessary layers are removed. After the fabrication is completed the photoluminescence is measured by the setup described in Section 2.4.2. The peak wavelength and FWHM are measured to be $\lambda \sim 1533$ nm and $\Delta\lambda \sim 124$ nm, respectively.

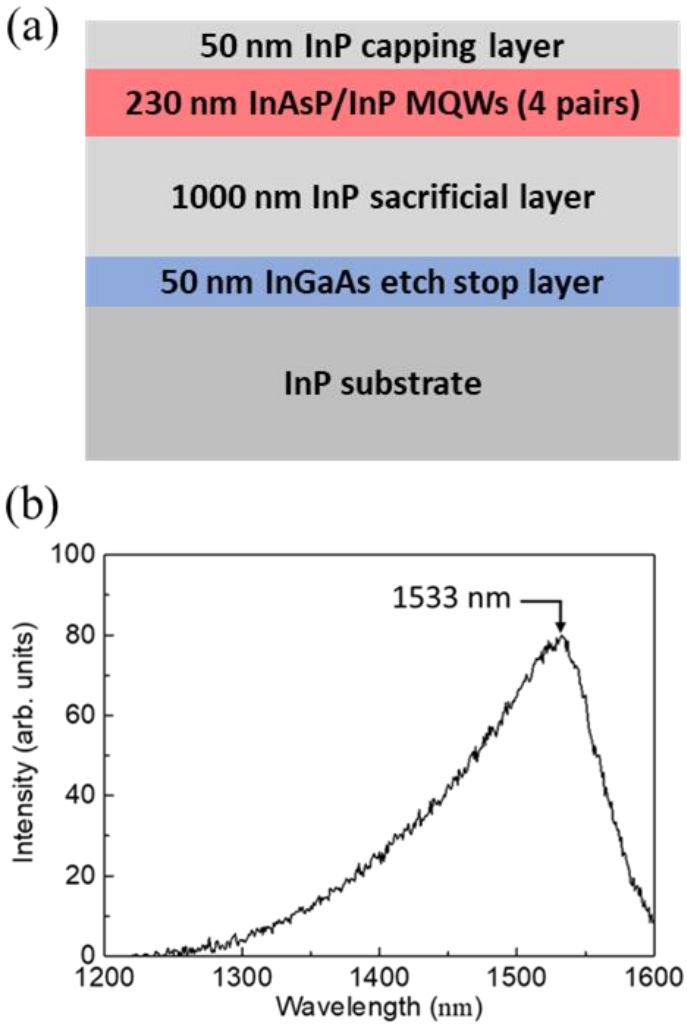

Figure 3-9. Characterizations of epi-wafer embedding multiple-quantum-wells (MQWs). (a) The epi-structure of a wafer with four pairs of InAsP/InP MQWs. All other unnecessary layers are removed by chemical etching, before and after attaching the fused silica as a handling layer. (b) Photoluminescence spectrum of the InAsP/InP MQWs having an emission peak at λ = 1533 nm.

3.2.4. Summary

i. The set of samples examined in Chapter 3 consists of a total of 9 disorder strengths, quantified by the degree of disorder γ ranging from 0 to 0.8 divided by the interval of 0.1, and for each γ, 10 kinds of configurations are realized to eliminate the influence of configuration-dependent effects.

ii. A hexagonal lattice is employed in addition to high-index-contrast materials to provide a very large complete band-gap of ~300 nm as a wide playground of band-tail states, which mitigates the spectral resolution of experimental setup required for identifying individual state.

iii. An optically activated disordered system is realized using MQWs as both a slab waveguide and a gain material. Thus, extended Bloch states and localized photonic band-tail states can be distinguished by signal strength, based on the Purcell effect.

3.3. Photoluminescence characterization

3.3.1. Spectral response: Lasing modes developed inside band-gap

Photonic crystal alloy systems described in Section 3.2 are investigated to identify optical modes by measuring photoluminescence (PL). Representative PL spectra are as shown in Figure 3-10 from which many modes, having very narrow linewidth and high signal-to-noise ratio, are confirmed. As verified in Section 3.3.7, these modes exhibit typical evidences of lasing modes and thus correspond to the eigenstates of the system.

For the periodic sample without disorder ($\gamma = 0.0$), only one lasing mode is observed. This is the K_1 band-edge mode that lase by the slow light mechanism [40] as described in 1.2.4, which is cross-validated by a band structure calculated for an 3D unit-cell approach and by a simulated spectrum calculated for the entire structure with an effective index approximation [80]. Therefore, the low-energy boundary of the complete band-gap can be identified using this K_1 band-edge position.

For the disordered samples, bundle of modes is generated around the K_1 band-edge and inside the band-gap. The number of lasing modes and spectral widths of lasing bundle increase as the degree of disorder of the system increases. These behaviors are also reproduced in the simulation spectra calculated for 2.5D full structures. For strong disorder regime of $\gamma \geq 0.6$, another bundle of lasing mode is found at shorter wavelength side. As γ increases further, the distribution of modes tends to be inconsistent in the measured data and the simulation data. This is because the modes at higher γ suffer more loss of gain with detailed explanation in Section 3.3.5.

The raw data for this spectral response can be re-plotted as a function of γ as displayed in Figure 3-11 to clearly identify the modal evolution with respect to the structural parameter in the system. Newly generated modes are inside the bandgap, and both the number and spectral distribution of these states are dependent on γ of the system. The modes observed in higher energy range from 1400 nm to 1500 nm are confirmed to be originated from the M_2 band-edge side by comparison with the simulation data including the entire band-gap, which is also cross-validated using eigenmode profiles in momentum space as described in Section 3.4.8.

In conclusion, there are two types of modes in this system that are developed from each side of the band-gap and grow to fill the entire band-gap region with increasing degree of disorder. These are referred to as K_1 and M_2 band-tail states, respectively, according to the spectral origin of the mode.

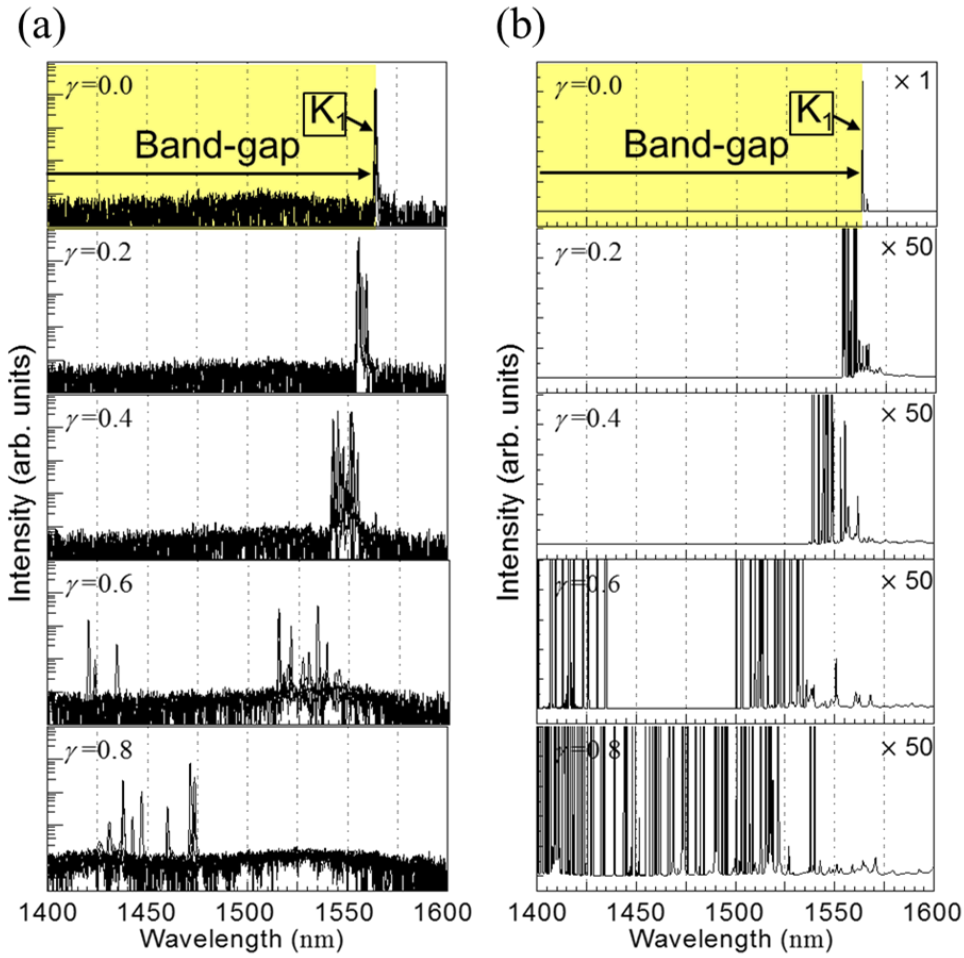

Figure 3-10. Representative photoluminescence spectra of the photonic crystal alloy devices. (a) Measured spectra of the devices with difference degrees of disorder (γ = 0.0, 0.2, 0.4, 0.6, and 0.8). Each spectrum is constructed by overlapping individual spectrum measured at different spatial locations on the same device. The excitation power density is maintained at 6.2 kW/cm^2. Each peak in the spectra corresponds to a laser line with a well-defined threshold. (b) Simulated $|E|^2$ spectra of the model structures designed to have same air-hole configurations and the physical dimensions of the devices as in (a).

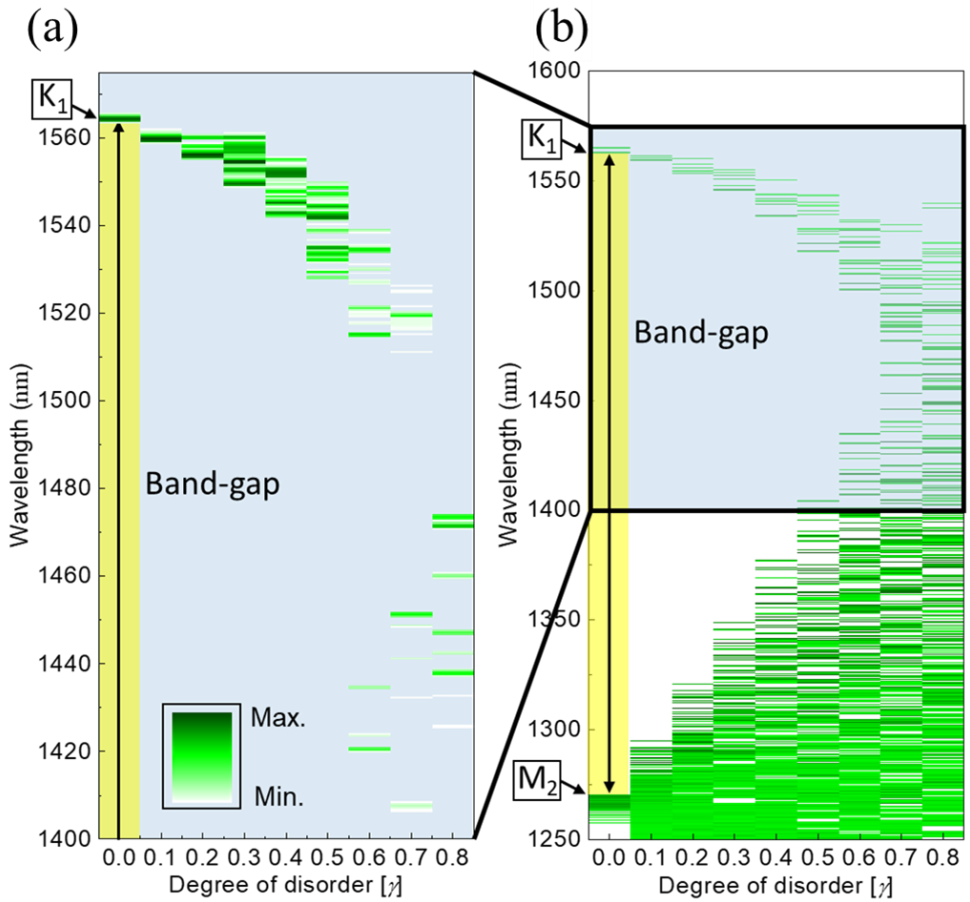

Figure 3-11. Representative spectral behaviors of the photonic crystal alloys as a function of the degree of disorder. (a) Measured photoluminescence spectra plotted as a function of the degree of disorder. The region shaded in yellow corresponds to the band-gap of homogeneous photonic crystal, which are depicted to emphasize that the lasing states are inside the band-gap. (b) Simulated $|E|^2$ spectra plotted as a function of the degree of disorder. The calculation is performed over an extended spectral range to include the entire band-gap, demonstrating that the lasing modes measured at the short wavelength side near λ ~ 1400 nm are originated from the other side of the band-gap and the M_2 band-edge.

3.3.2. Statistical identification of photonic band-tail states

To ensure generality and to exclude the effect of specificity in disorder configurations, statistical treatments are taken to the measured results by ensemble-averaging over samples with 10 kinds of different configurations. The result is shown in Figure 3-12, which presents both the averaged spectral positions of the upper and lower bounds of lasing modes in each bundle of band-tail state, by upward- and downward-pointing-triangles, along with standard deviations. The areas shaded in color are corresponding ranges of band-tail states estimated by simulations.

From this data, K_1 and M_2 photonic band-tail states are identified with statistical evidences. The long wavelength K_1 band-tail states are developed from the K_1 band-edge side and the spectral widths gradually increase according to the increase of γ. This statement is generally true for the M_2 band-tail states as well. Both band-tail states are then merged at higher degrees of disorder ($\gamma \geq 0.7$), making their spectral discrimination difficult although the near-field identification is still possible as confirmed in Section 3.4.8. It should be noted that the overall behavior is similar to that of an electronic disordered system [84].

The evolution of experimentally identified widths of the K_1 band-tail states has a maximum value at $\gamma = 0.5$, unlike our intuition, electronic cases [83, 94], and the simulation results that increase without bound. This discrepancy is because the system cannot sustain lasing of band-tail states at higher degrees of disorder due to the reduction of gain overlap between the modes and gain material as explained in Section 3.3.4.

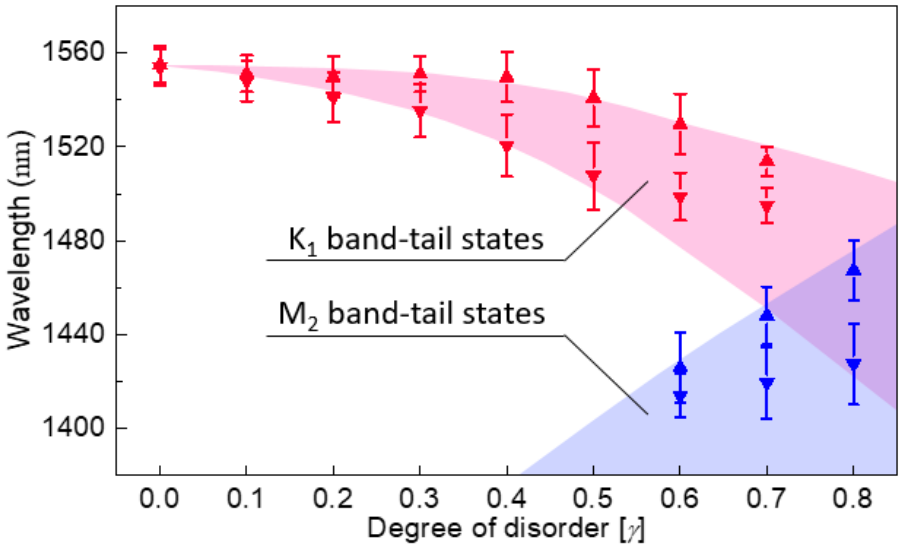

Figure 3-12. Statistical identification of photonic band-tail states. The average (▲, ▼) and standard deviation (I) of the spectral positions of the shallowest and the deepest lasing states are plotted, determined by an ensemble of 10 devices with different configurations. The regions shaded in red and blue are numerically calculated spectral area in which the K_1 and M_2 band-tail states are present, respectively.

3.3.3. Band-gap narrowing: Explanation based on virtual crystal approximation

It is natural that the positions of the band-edge and the corresponding band-gap change when disorder is introduced in the photonic crystal alloy system. According to the experimental data shown in Figure 3-11 and Figure 3-12, the direction of this change is toward in narrowing the band-gap. In this case, it is important to specify the exact position of the band-edge within the spectral width in which the band-tail states are distributed to determine whether the band-tail states are located inside the band-gap.

In a photonic crystal alloy system, the spectral location of band-edge and corresponding band-gap can be estimated by using a virtual crystal approximation [95, 96] originally developed for electronic semiconductor alloys. In this thesis, the radii of basis photonic atom are quantified so that the relative differences between nearest atoms are in the same intervals over each pair in basis set, as shown in Figure 3-13. Thus, the average radius remains at r_0 regardless of the degree of disorder, while the average area occupied by photonic atoms gradually increases with increasing γ. The effective refractive index of a slab waveguide that depends on a filling factor is also reduced accordingly, which affects the position of the band-gap and band-edges.

Applying the virtual crystal approximation where a photonic crystal alloy is approximated as a virtual perfect crystal of identical air-holes whose radius is given by $r_{VCA}^2 = \mathrm{Ave}(r^2)$, the spectral positions of the band-gap and band-edges are estimated as a function of the degree of disorder. As displayed in Figure 3-14, the upper bound of K_1 band-tail states corresponds to the K_1 band-edge of virtual crystals, which proves the experimentally identified band-tail states are indeed located inside the band-gap.

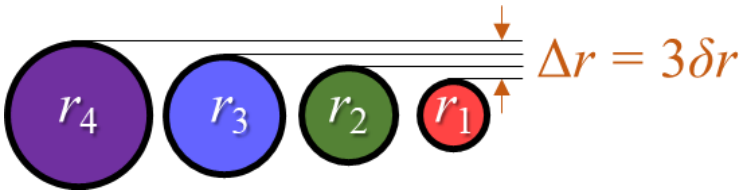

Figure 3-13. Origin of the band-gap narrowing. The basis photonic atoms in this system are quaternary air-holes with radii of equal differences δ*r* designed to maintain the average radius r_0 regardless of the disorder strength. According to this definition, the filling factor or the effective refractive index of the slab waveguide gradually decreases with increasing average volume of the basis air-holes.

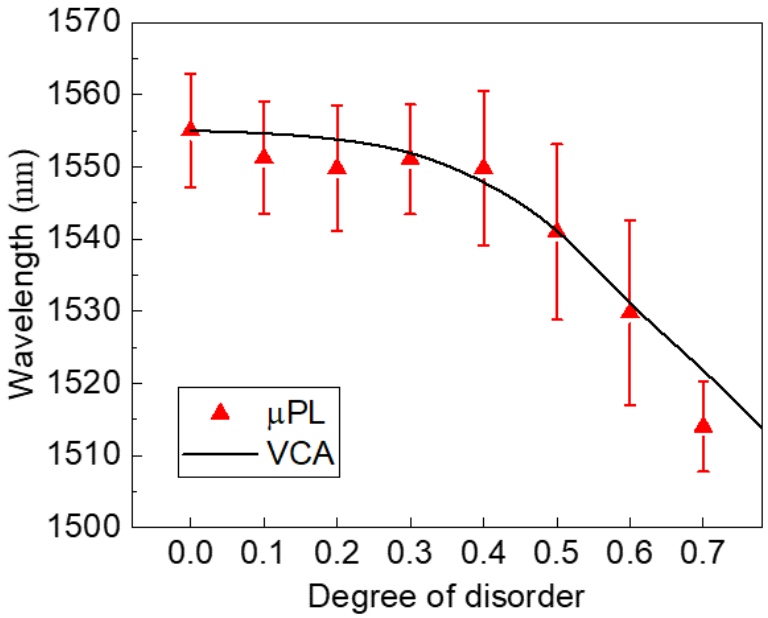

Figure 3-14. Estimation of the band-gap in photonic crystal alloy platform. The upper bound of the K_1 band-tail states (▲), determined by ensemble-averaging 10 realizations of the disordered configuration, indicates the positions of the experimentally measured band-gap. The solid line is a prediction based on a virtual crystal approximation that closely matches the experimental results.

3.3.4. Exponentially increasing penetration depth

Figure 3-15 shows the penetration depth, an energy range occupied by the band-tail states, as a function of γ. It is defined by the energy difference between the shallowest and deepest state, $|E_D - E_S|$, and measured to be super-linearly proportional to γ. In electronics, similar phenomena have been observed in semiconductor alloys as a form of exponentially increasing absorption edges, or the Urbach tails [94], which are mostly the disorder-induced localized states [83]. However, unlike our intuition, electronic cases, and the simulation results, the penetration depth does not increase without bound, having a peak at γ = 0.5. This is because the gain overlap between the modes and gain material is gradually reduced according to the γ.

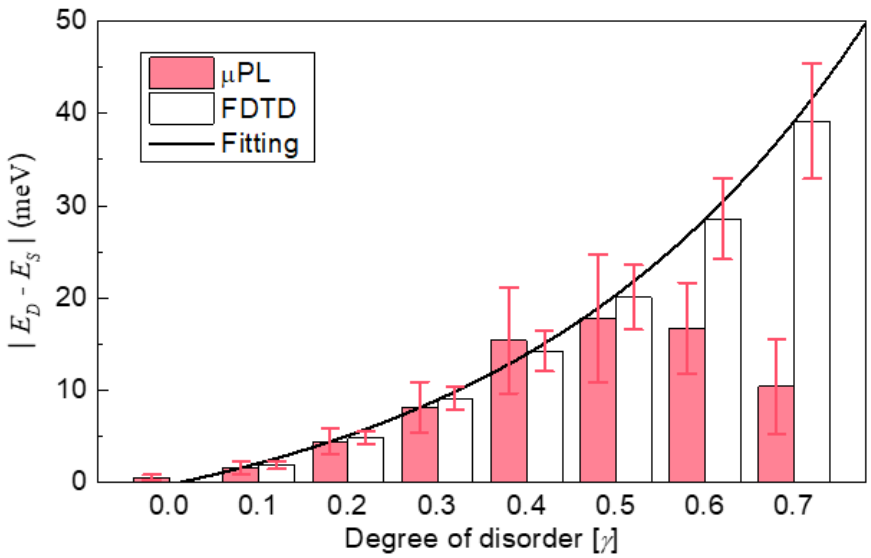

Figure 3-15. Energy range occupied by the K_1 band-tail states. The energy difference between the shallowest and deepest states are plotted as a function of degree of disorder. Red and white bars represent the statistical results from the measurement and the simulations, respectively. The discrepancy increases in the strong disorder regime because the mode is difficult to lase with a reduced gain overlap.

3.3.5. Gain overlap factor for lasing states

The gain overlap is an important factor to consider a lasing of an eigenmode, which attributes its origin to two different domains: spatial and spectral. The spatial overlap factor quantifies the relative portion of modal intensity that spatially coincides with gain material, which is formulated by $[\int(I \cdot M)dxdy]/[\int I\,dxdy]$, where $I = |E(x,y)|^2$ is the intensity profile of eigenmode and $M(x,y)$ is a 2D step function that have 1 in gain material and 0 otherwise. The spatial overlap factors are calculated for simulated mode profiles and the result is summarized in Figure 3-16. As expected, the spatial overlap factor of K_1 band-tail states decrease as γ increases, which increase lasing thresholds as well (see also Section 3.3.7).

On the other hand, the spectral overlap is estimated from the gain emission profile of MQW that has peak wavelength of λ ~ 1533 nm and FWHM of Δλ ~ 124 nm, as characterized in Section 3.2.3. Therefore, its value becomes rapidly worse for a band-tail state that is spectrally away from the MQW emission peak, which explains the experimental observation that the penetration depth for γ ≥ 0.6 is not consistent with theoretical expectations. For the M_2 band-tail states, however, the spatial gain overlap factor rather increases as a function of γ, because the M_2 band-edge is the air band, or a low index band. In addition, the spectral overlap of M_2 band-tail states also increases at higher γ. Therefore, the M_2 band-tail states lase only at high degrees of disorder (γ ≥ 0.6).

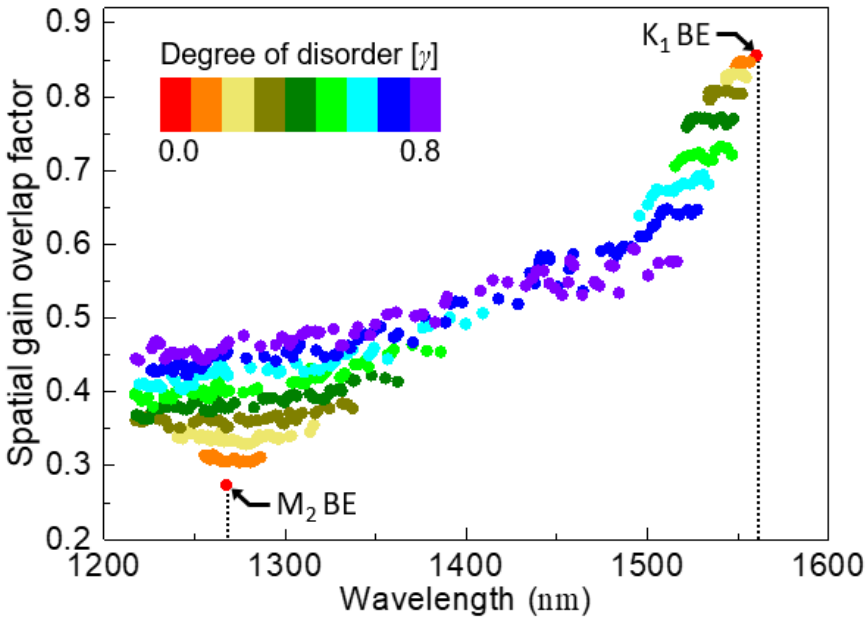

Figure 3-16. Spatial gain overlap factors of the band-tail states. The amount of modal intensity that spatially coincides with gain material is calculated for band-tail states with different degrees of disorders and state energies. In this calculation, photonic crystal alloys with the same disordered configuration are used to rule out the effect of configuration-specificity.

3.3.6. Bloch states vs. band-tail states

Eigenstates for a periodic structure with an infinitely large domain size are the Bloch states that constitute continuous photonic bands, as described in Section 1.2.2. For a real structure with a finite size, however, the Bloch states consist of quasi-continuous modes due to the domain boundary effect. This becomes apparent by comparing Figure 3-17(a), obtained by unit cell calculation with periodic boundary conditions, with the $\gamma = 0$ case in Figure 3-17(b) calculated for a full-size model structure. The latter consists of many discrete Bloch states outside the band-gap.

For finite structure calculations, it should be noted that the extended Bloch states indeed exhibit relatively weak intensities compared with localized band-tail states as described several times in this thesis. The Bloch states propagate through the structure and radiate to the infinity, or get absorbed by the perfect matching layer in FDTD simulations. On the contrary, the band-tail states are localized by the mechanism of multiple scattering and thus the corresponding photons stay long inside the structure, which appear strong intensity in both the measurement and the simulation. This intensity contrast is used to distinguish two kinds of states, the Bloch and the band-tail states, because the localized band-tail states only lase in the proposed system.

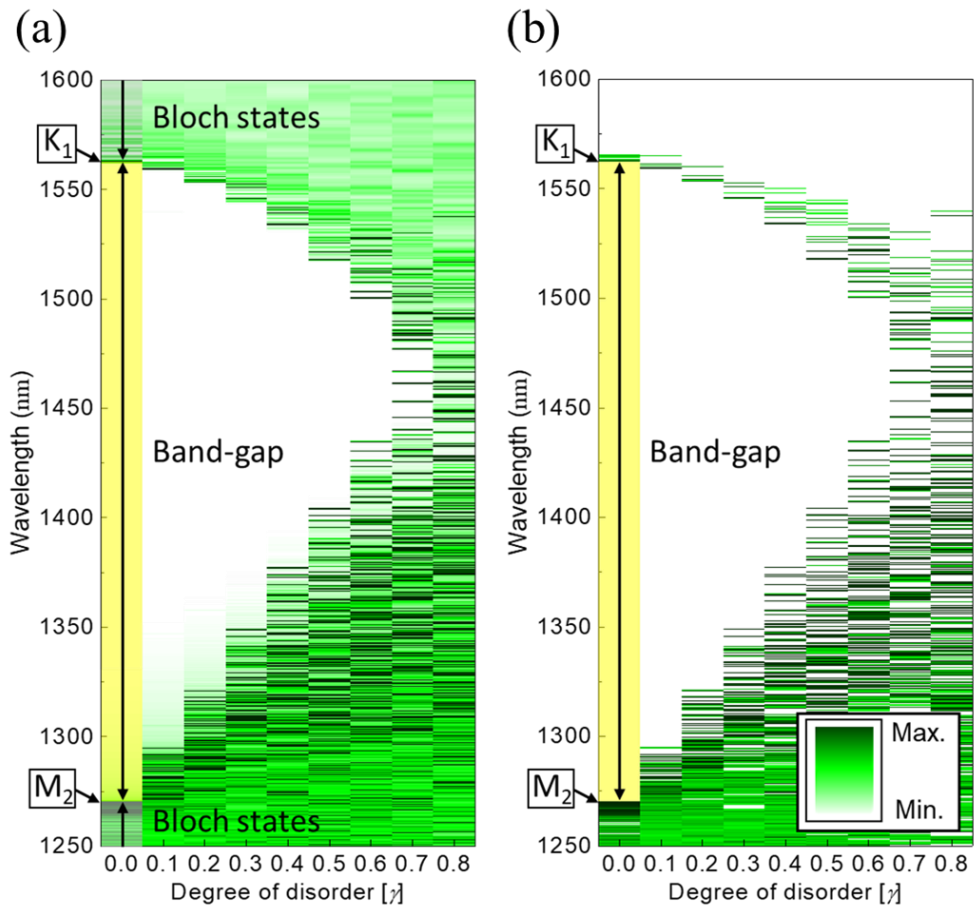

Figure 3-17. Bloch states in photonic crystal alloys. (a-b) Simulated $|E|^2$ spectra calculated for the photonic crystal alloys with a finite size presented in (a) a logarithmic scale and (b) a linear scale. The Bloch states consist of many discrete modes outside the band-gap and exhibit relatively weak intensities compared with the band-tail states because the Bloch states propagate through the structure and radiate to the infinity. On the contrary, the band-tail states have strong intensities because they are well localized and trapped inside the structures. This intensity contrast is used here to display each state with manipulations of the intensity scale.

3.3.7. Lasing performance of band-tail states

In Section 3.3.1, it is claimed that all the sharp peaks observed in the PL spectra are lasing modes. Indeed, the peaks exhibit narrow linewidths and high signal-to-noise ratios, which are strong indications for lasing action. Furthermore, light-in versus light-out relationships (*L*-*L* curves) manifest a strong nonlinear behavior with a well-defined threshold, a clear evidence for lasing [97, 98] as shown in Figure 3-18 where thresholds of modes with the most intense output are recorded for each device with given γ and disorder configuration, and *L*-*L* curves for a few selected devices are presented as well. It is noteworthy that the threshold generally increases as lasing wavelength is away from the peak emission wavelength of MQWs. As discussed in Section 3.3.5, this is due to the reduction of spectral and spatial gain overlap with gain material.

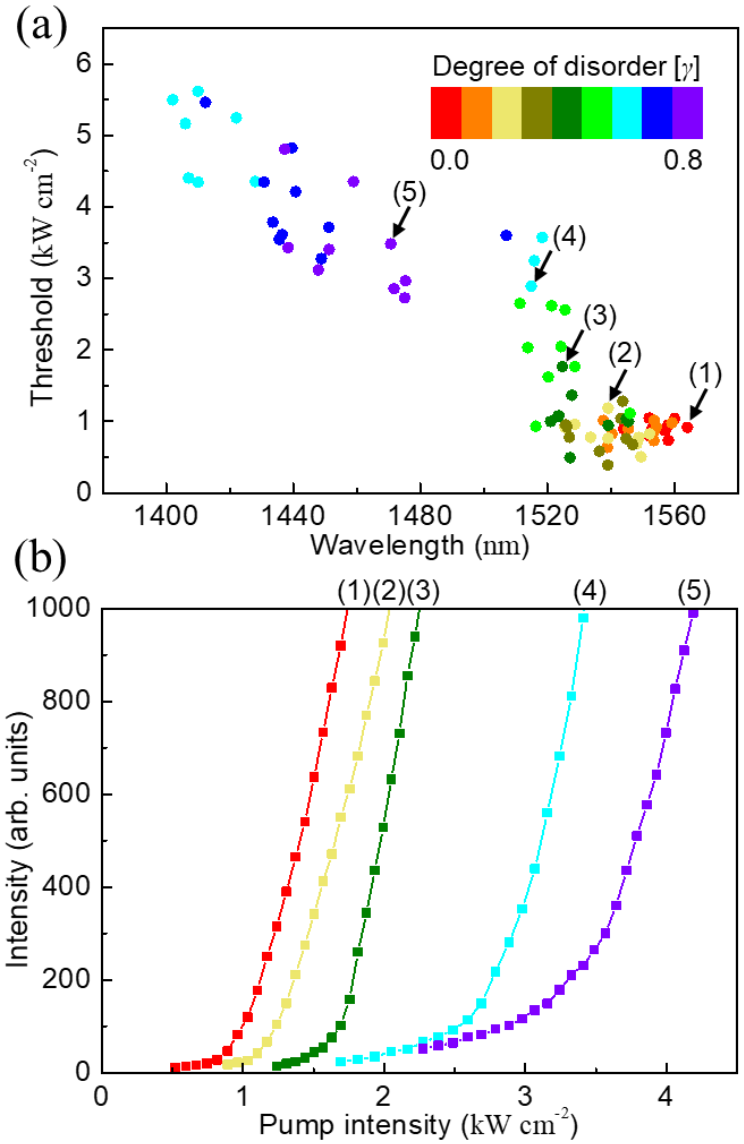

Figure 3-18. Lasing performance of the band-tail states. (a) Collection of laser thresholds and wavelengths. Each point corresponds to the most dominant band-tail state for a given device. (b) Light-in light-out characteristic curves for selected devices, each representing different degrees of disorder (γ = 0.0, 0.2, 0.4, 0.6 and 0.8). Strong nonlinear behaviors with well-defined thresholds indicate lasing actions.

3.3.8. Excitation dependence of modal energy

PL measurements in this thesis require excitation pumping energy for population inversion in gain materials and corresponding nonlinear properties of an optical gain medium undergo serious changes across the laser threshold from absorptive to transparent. Although it is very helpful to exclude the effects of material absorption when the measurement regime of interest is above the threshold just like in this thesis, one might concern about possible thermo-optic effects caused by hard optical excitation.

However, the change of refractive index due to optical pumping is negligible in magnitude compared to the high-index-contrast of the proposed platform, thus cannot produce any meaningful effect to measurements and subsequent conclusions. This fact is demonstrated in Figure 3-19 where the wavelength shift of a band-tail state is measured as a function of pump intensity. The spectral behavior of the band-tail state is stable in the range of interest and the thermo-optic change of modal energy is measured to be less than 10^{-4}.

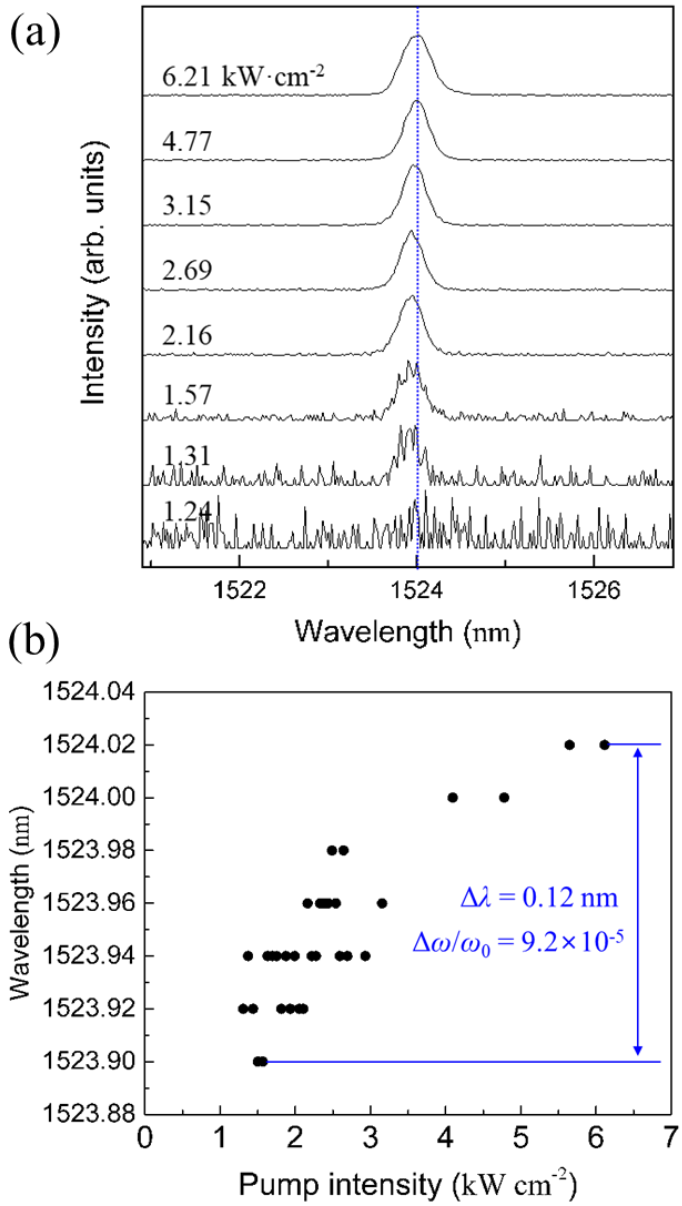

Figure 3-19. Excitation power density dependence of a modal energy. (a) The spectra and (b) the wavelength shifts of a band-tail state are measured as a function of pump intensity. The spectral behavior of the band-tail state is stable in the range of interest except the small amount of thermal effects.

3.3.9. Summary

i. PL measurements identified two types of modes in the proposed platform that were developed from each side of the band-gap and grew to fill the entire band-gap with increasing degree of disorder, which were referred to as K_1 and M_2 band-tail states according to the spectral origin of the mode.

ii. To ensure generality and to exclude the effect of specificity in disorder configurations, statistical treatments were taken by ensemble-averaging over samples with 10 kinds of different configurations. From this result, K_1 and M_2 band-tail states were verified with statistical evidences.

iii. The band-gap narrowing was observed in the proposed system, which was caused by gradually decreasing effective refractive index of a slab waveguide, as confirmed by applying the virtual crystal approximation to virtual perfect crystal of identical air-holes.

iv. The penetration depth of band-tail states was super-linearly proportional to the degree of disorder, which is similar to the Urbach tails observed in semiconductor alloys. However, unlike the electronic cases, the observed penetration depth did not increase without bound.

v. The discrepancy with the theoretical estimation was explained by the gain overlap between the modes and gain material, which is an important factor to consider a lasing of an eigenmode. Two different origins coming from spatial and spectral aspects attributed to the gain overlap factor.

vi. The Bloch states in a finite system consisted of quasi-continuous modes due to the domain boundary effect and had relatively weak intensities compared with localized band-tail states, which exhibited strong intensity in both the measurement and the simulation due to the mechanism of multiple scattering.

vii. Light-in versus light-out relationships of modes identified in the PL spectra manifested a strong nonlinear behavior with a well-defined threshold in addition to the narrow linewidth and high signal-to-noise ratio, which is a clear evidence for lasing.

viii. The population inversion in gain materials using excitation pumping energy was very helpful to exclude the effects of material absorption. Thermo-optic effects of hard optical excitation were negligible, and corresponding change of modal energy is measured to be less than 10^{-4}.

3.4. Near-field characterization

3.4.1. Eigenmode profiles: The most direct evidence of localization

Near-field distributions of individual eigenmode are investigated using SNOM apparatus described in Section 2.4.3 to directly characterize near-field optical properties of the photonic band-tail states. The representative near-field images are displayed in Figure 3-20 and Figure 3-22, which are measured at the deepest energy E_D and at the shallowest energy E_S ,respectively, of the K_1 band-tail states in a single set of devices for which PL spectra in Figure 3-10 are taken. Therefore, each SNOM image belongs to a single lasing mode in emission spectra, enabling direct comparisons not only among the SNOM images but also between PL spectra and field profiles. Figure 3-21 and Figure 3-23 are then numerically simulated $|E|^2$ profiles using the model structure with the same disordered configuration and physical dimensions that corresponds to the measured near-field images.

For the structure without disorder ($\gamma = 0.0$), eigenmode profile of the K_1 band-edge mode exhibits the extended Bloch mode profile occupying the entire excitation region although minor intensity fluctuations exist originated from structural inhomogeneity inevitably introduced during sample fabrication. With the disorder, however, a near-field distribution of K_1 band-tail state suffers very drastic change. As shown in Figure 3-20, the energy of deepest band-tail state is localized in a spatially isolated single-enveloped spot whose size shrinks as γ increases. At $\gamma = 0.6$, it is only a few lattices as small as approximately 1 μm. Whereas the shallowest band-tail state has a relatively large mode profile composed of loosely connected multiple segments where the size of each segment varies as well according to γ. These behaviors are well reproduced by FDTD simulations and result are shown in Figure 3-21 and Figure 3-23 calculated for the deepest and shallowest K_1 band-tail states, respectively.

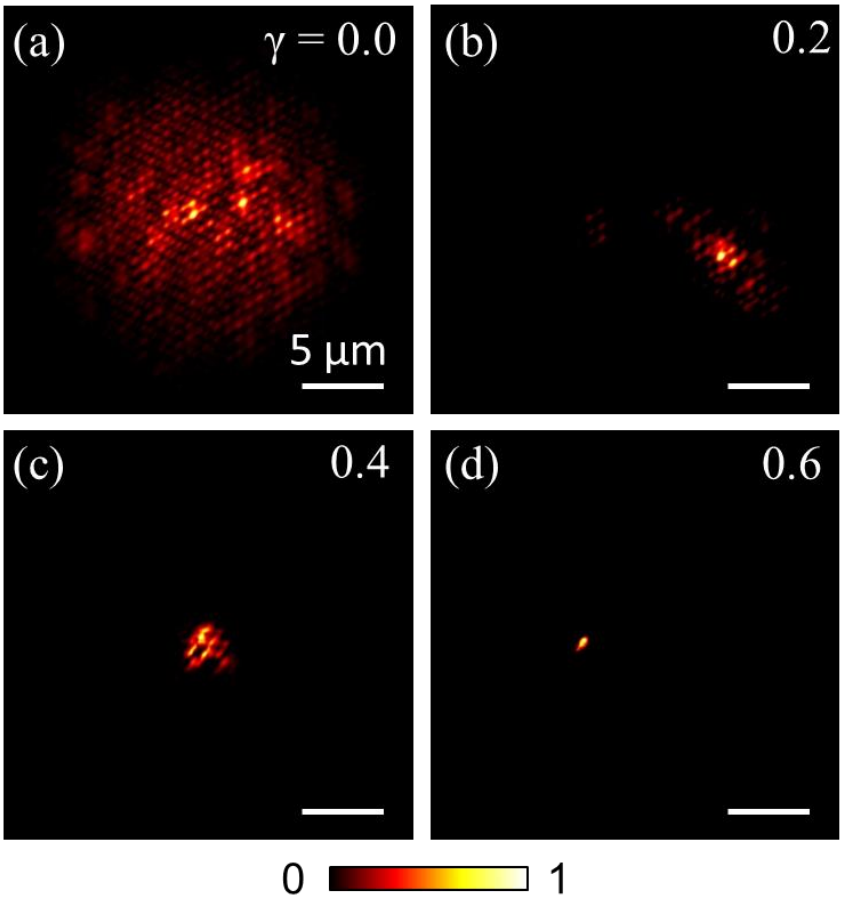

Figure 3-20. Representative near-field images of the deepest K_1 band-tail states. Each image corresponds to different degrees of disorder: (a) $\gamma = 0.0$, (b) 0.2, (c) 0.4, and (d) 0.6. All the images are eigenmode profiles measured using a scanning near-field optical microscopy setup customized to identify individual lasing modes, taken at a fixed excitation power density (~7 kW/cm^2) well above laser thresholds.

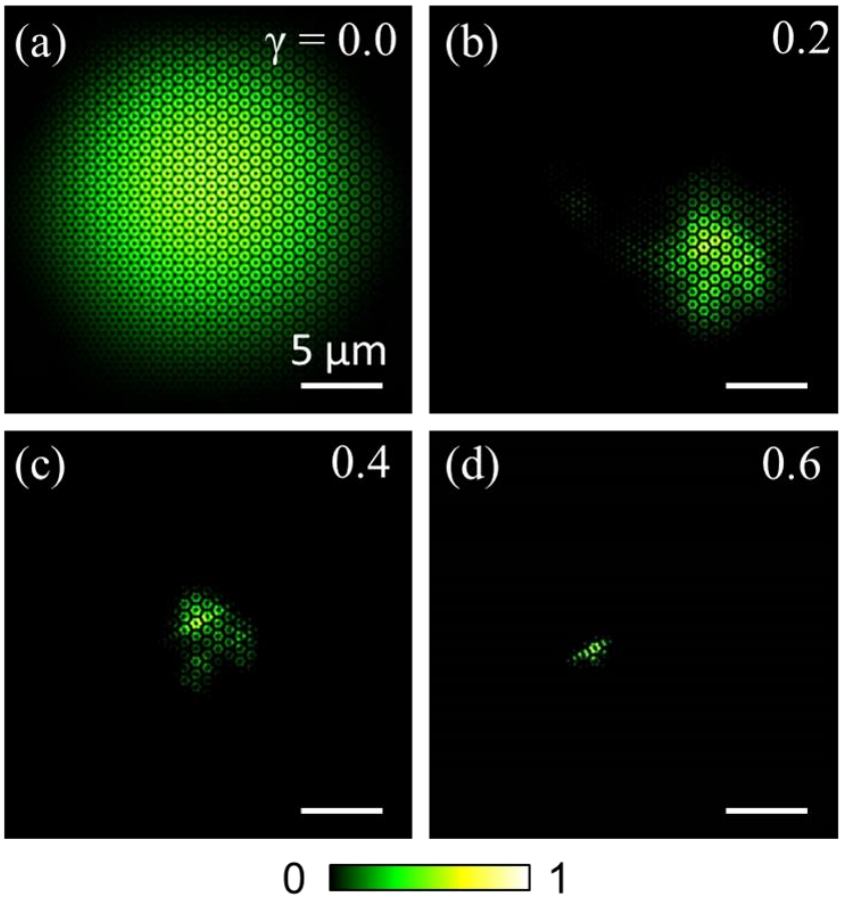

Figure 3-21. Simulated $|E|^2$ profiles for the deepest K_1 band-tail states. Each image corresponds to different degrees of disorder: (a) γ = 0.0, (b) 0.2, (c) 0.4, and (d) 0.6. The model structure for calculations employs the same disordered configuration and physical dimensions that corresponds to the measured images shown in Figure 3-20.

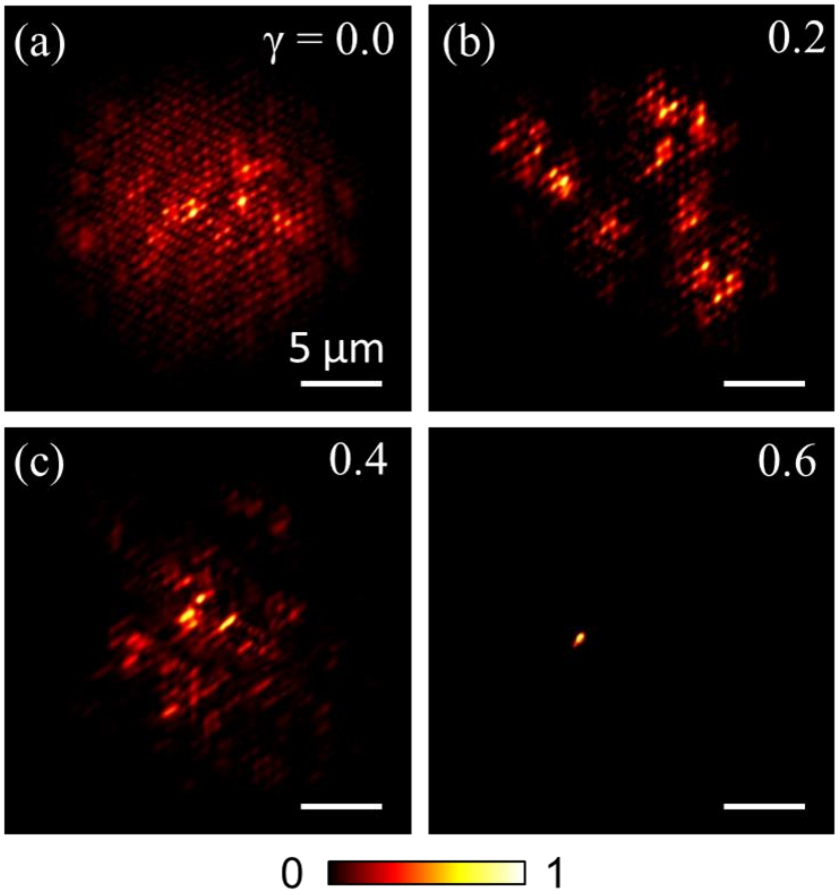

Figure 3-22. Representative near-field images of the shallowest K_1 band-tail states. Each image corresponds to different degrees of disorder: (a) γ = 0.0, (b) 0.2, (c) 0.4, and (d) 0.6. All the images are eigenmode profiles measured using a scanning near-field optical microscopy setup customized to identify individual lasing modes, taken at a fixed excitation power density (~7 kW/cm^2) well above laser thresholds.

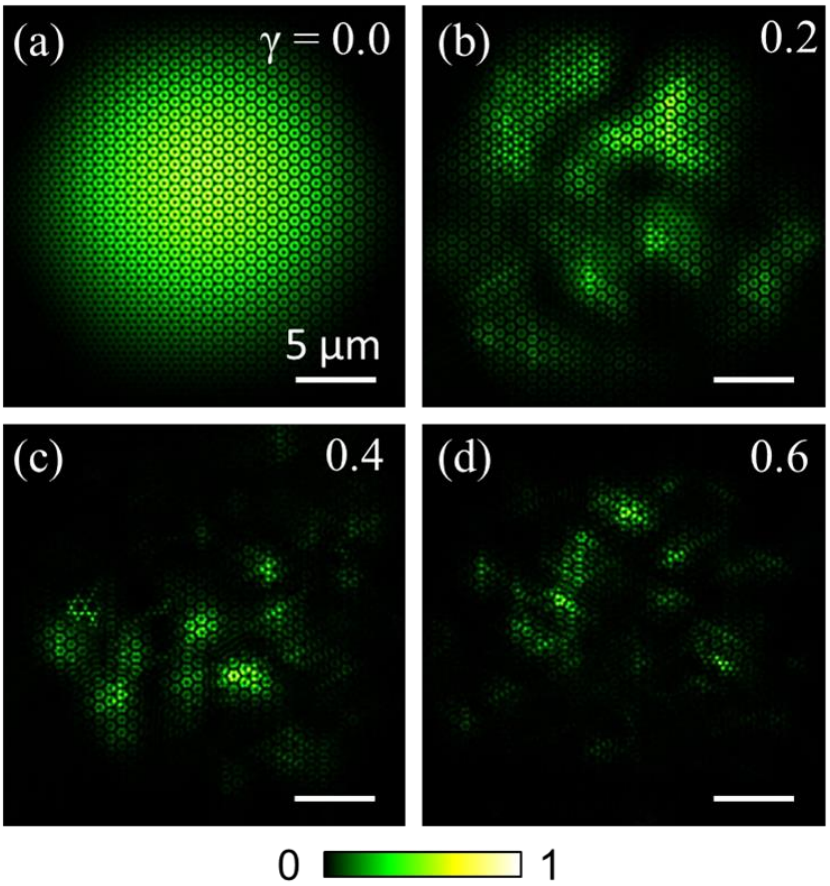

Figure 3-23. Simulated $|E|^2$ profiles for the shallowest K_1 band-tail states. Each image corresponds to different degrees of disorder: (a) γ = 0.0, (b) 0.2, (c) 0.4, and (d) 0.6. The model structure for calculations employs the same disordered configuration and physical dimensions that corresponds to the measured images shown in Figure 3-22.

3.4.2. Weak and strong localization

The evolution of eigenmode profiles observed in photonic crystal alloys are consistent with theoretical predictions made by P. W. Anderson [48, 99], which explain the localization by hopping probability. According to the description of Anderson's theory, the homogeneous and extended Bloch state in a perfect crystal loses its long-range phase coherence due to random potential fluctuations introduced in a disordered solid, resulting in multiple local domains linked together by hopping.

When a state has a small energy compared to potential fluctuations, envelopes of the wavefunction that represent physical sizes of each domain have long-tails, which is sufficient to maintain finite amplitudes across domains, and thus a mobile entity can transfer into other domains spread over the entire structure. This is the picture of weak localization [100, 101, 102, 103], which is consistent with the behavior observed in SNOM images of the shallowest band-tail states. For a deep state having higher energy than potential fluctuations, a mobile entity are localized in a single isolated domain because the envelope decays so fast that no hopping is possible between domains, leading the strong localization [104, 105, 106]. This conceptual picture is directly observed in the SNOM images of the deepest band-tail states.

The complete picture of modal evolution that includes intermediate energy states can be established with the observation in Figure 3-24, which contains near-field images of K_1 band-tail states measured at different state energies, but in the same device of a fixed degree of disorder. Here, it is demonstrated that both the strongly and weakly localized states can coexist in the same structure, as theoretically predicted in ref. [81] and previously observed in ref. [73, 104]. Furthermore, the results indicate that the near-field distribution of an eigenmode gradually changes its modal size and localization characteristic from a weak localization to a strong

localization as the band-tail state is located deeper inside the band-gap, which is qualitatively consistent with a theoretical study of Edward and Thouless [107]. In other word, an eigenstate with intermediate energy can have any modal size and localization property that system allows, which is a great advantage for light shaping.

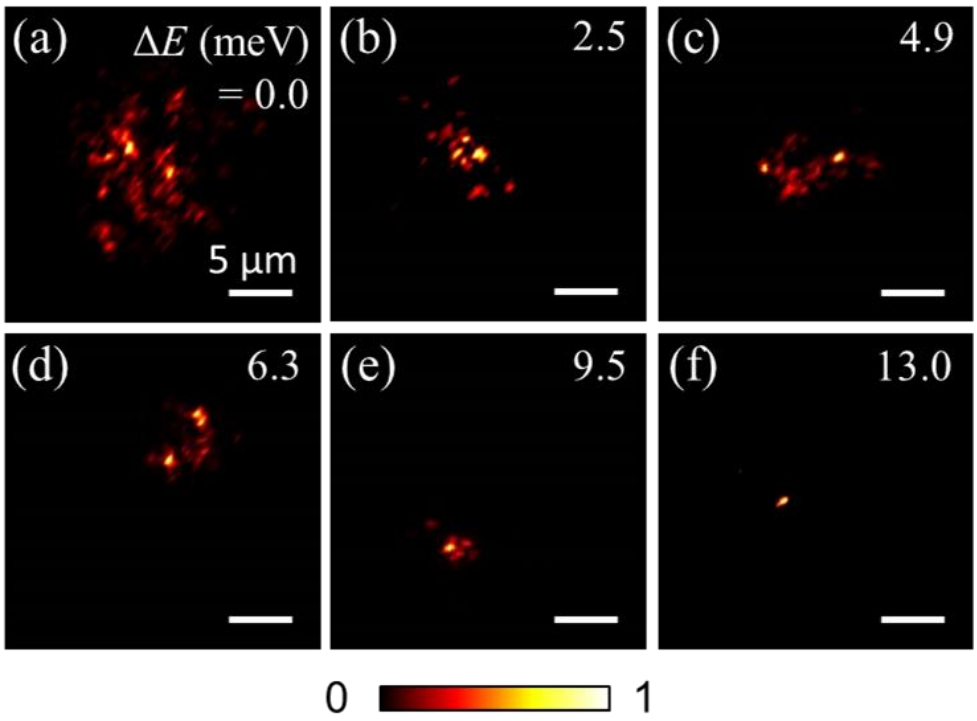

Figure 3-24. Near-field images of K_1 band-tail states with different state energies at a fixed degree of disorder γ = 0.6. The energy Δ*E* is presented by the difference from the K_1 band-edge: (a) Δ*E* = 0.0, (b) 2.5, (c) 4.9, (d) 6.3, (e) 9.5, and (f) 13.0 meV. All the images are eigenmode profiles measured using a scanning near-field optical microscopy setup customized to identify individual lasing modes, taken at a fixed excitation power density (~7 kW/cm^2) well above laser thresholds.

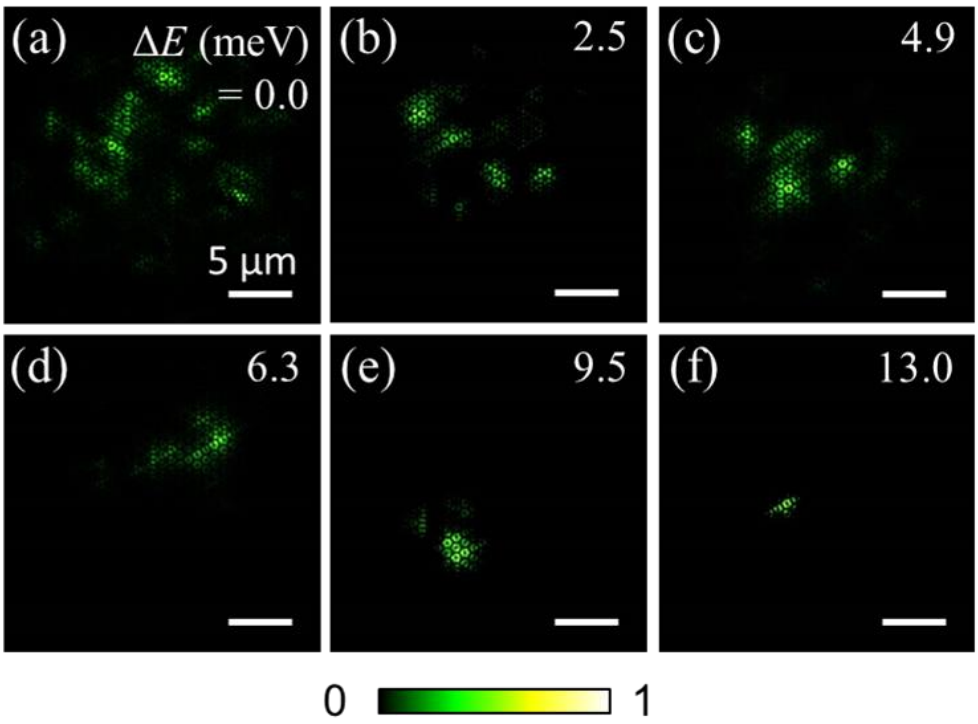

Figure 3-25. Simulated $|E|^2$ profiles of K_1 band-tail states with different state energies at a fixed degree of disorder γ = 0.6. The energy Δ*E* is presented by the difference from the K_1 band-edge: (a) Δ*E* = 0.0, (b) 2.5, (c) 4.9, (d) 6.3, (e) 9.5, and (f) 13.0 meV. The model structure for calculations employs the same disordered configuration and physical dimensions that corresponds to the measured images shown in Figure 3-24.

3.4.3. Quantification of modal extents

To quantify a modal extent of the band-tail state, a measure is required that could extract the strength of localization from measured near-field image. The inverse participation ratio, P^{-1}, that quantify the averaged moments of the eigenfunction [108], is a proper measure for this purpose as verified in several systems [87, 109, 110, 111]. Using the inverse participation ratio for a 2D system, the effective width of a band-

tail state is then defined by the following equation:

$$w_{eff} \equiv P^{-\frac{1}{2}} = \{[\int I(x,y)^2 dxdy]/[\int I(x,y)\, dxdy]^2\}^{-\frac{1}{2}}.$$

From the definition, it is clear that a contribution from a local domain $\Delta x \Delta y$ is weighted by the relative intensity difference to the domain with maximum intensity.

3.4.4. Localization of photonic band-tail states

The effective width, w_{eff}, defined in Section 3.4.3 is calculated for every near-field image taken from lasing modes of each device. The smallest value of w_{eff} is 1.13 μm at γ = 0.6, which corresponds to only $2.51a$. It is more than 10 times smaller than the maximum value of 12.0 μm at γ = 0.0.

The overall behavior is summarized in Figure 3-26, which directly confirms that the effective width of a band-tail state is a function of both the degree of disorder and the energy depth. The value of w_{eff} becomes smaller as γ increases and the state is deeper inside the band-gap. In order word, a band-tail state is the more localized in real space when not only it is in structure with stronger disorder, but also it has large energy difference to the band-edge. In terms of electronics, it means that a band-tail state has a physical extent governed by the size of the potential fluctuation localizing them, which is predicted by the Halperin-Lax theory [112]. The result in this thesis demonstrate the photonic version of it, which is supported by FDTD simulations that also reveal that the M_2 band-tail states exhibit a similar behavior. As claimed in Section 3.4.2, a band-tail state can have any modal extent that system allows.

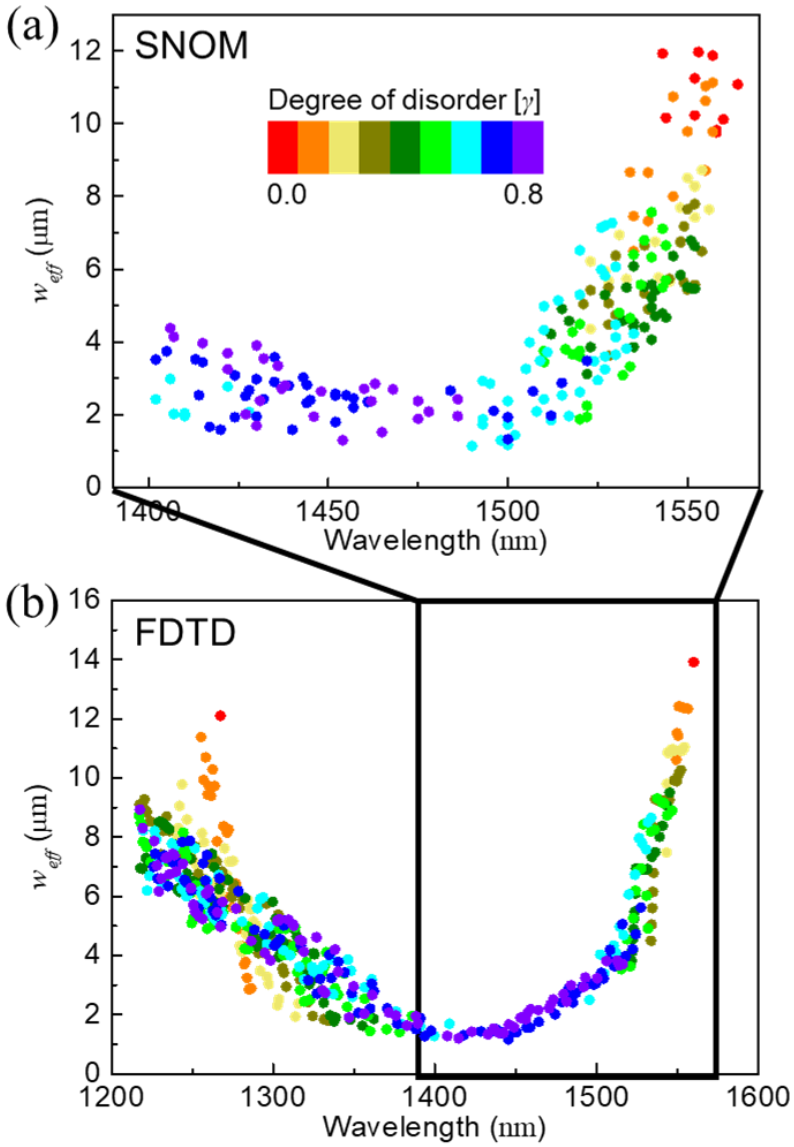

Figure 3-26. Spatial extents of the band-tail states. (a) Effective spatial widths of the band-tail states are extracted from the measured near-field images for every degree of disorder, band-tail state energies, and disordered configurations. (b) Simulated effective spatial widths of the band-tail states where calculations are performed over an extended spectral range to include the behavior of the M_2 band-tail states.

3.4.5. Energy dependence of localization: Explanation based on envelope function of band-tail states

The strong energy dependence of localization observed in Section 3.4.4 is exactly the optical properties of band-tail states predicted by S. John [74, 27]. Furthermore, it is a solid foundation of realizing predictable and systematic light shaping over wide spectro-spatial domain on chip-scale using photonic band-tail states.

The physical origin of these observation is explained by the envelope function that already mentioned a few times in previous sections. The Ioffe-Regel criterion [54], a localization criterion that requires the relative scale between the wavelength λ of light and the elastic mean-free-path l to be equal for a localization, is a historical criterion that has been in use for a long time in the field of Anderson localization. It determines if the scattering is in the Mie resonance regime so that interference between multiple paths drastically modifies the transport, because weak $\lambda^{-(d+1)}$ scattering dominates with extended profiles in Rayleigh regime or non-interfering transport dominates in geometric optics regime. In addition to this Mie resonance condition, S. John pointed that coherent arrangement of scattering elements could further mitigate localization criterion than in free-photon approximation case [74]. The photonic band-tail state appearing in the band-gap is approximately a standing wave having an envelope as illustrated in Figure 3-27, and according to the S. John's idea, localization of this envelope function is sufficient for the halt of transport, or for a localized state. Since a wavelength of the envelope function λ_{env} is determined by the deviation from the band-edge, $\lambda_{env} \sim |\omega - \omega_{BE}|^{-1/2}$, it is much easier to observe the energy dependence of localization for the band-tail states than those in other systems.

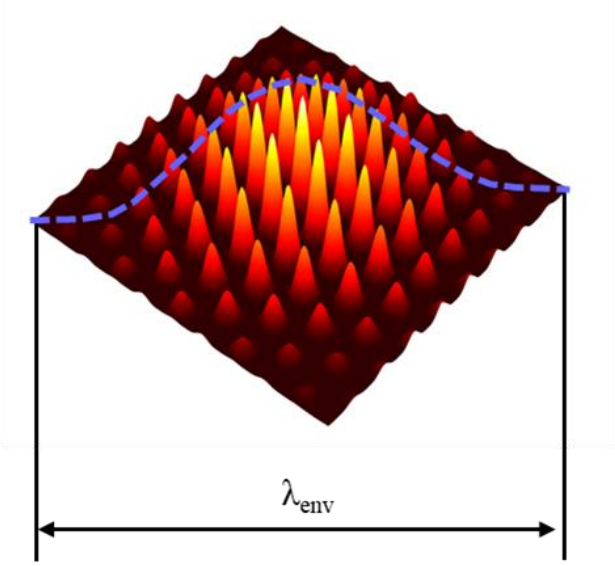

Figure 3-27. Schematic of representative field profile of a band-tail state. The band-tail state near the band-edge inside the band-gap is approximately a standing wave modulated by an envelope function whose wavelength is determined by the deviation from the band-edge [74].

3.4.6. Mean free path and Ioffe-Regel factor

The mean-free-path in a 2D disordered structure can be determined from the localization length ξ_{loc} using the relation $\xi_{loc} = l \cdot \exp(\pi kl/2)$, where k is the wavenumber and l is the mean-free-path [81]. The localization length, on the other hand, is extracted from a near-field intensity distribution by fitting this profile to the characteristic function of localized state, $I \sim \exp(-2r/\xi_{loc})$, which limits its approach only to the states with exponentially decaying near-field profiles. In this thesis, the deepest K_1 band-tail states of $\gamma \geq 0.3$ with strong localizations are analyzed as the most demonstrable cases. In addition, because a localized spot may not be isotropic in shape, the localization length of each mode is determined by taking an averaged-value over the six-fold symmetry directions of hexagonal lattice.

The result is shown in Figure 3-28(a). The localization lengths of the deepest K_1 band-tail states are in the range of 0.75 μm < ξ_{loc} < 4.5 μm for the degree of disorder $0.3 \leq \gamma \leq 0.7$. The mean-free-paths in the 2D plane are then estimated to be 100 nm < l < 200 nm using the obtained localization length and the effective in-plane wavenumber $k = n_{\text{eff}} k_0$, where n_{eff} is the effective refractive index of the fundamental waveguide mode. Apparently, both the mean-free-path and the localization length tend to become smaller as γ increases, implying localization gets stronger.

The localization criterion is developed using this information of the mean-free-path. According the reasoning on the envelope function described in the Section 3.4.5, the modified Ioffe-Regel criterion [74] can be defined as $k^* l \sim 1$ for the localization criterion of the band-tail states using the wavenumber of the envelope function $k^* = k_{env} = |k - k_{BE}|$. The values of modified Ioffe-Regel factors $k^* l$ are calculated for the same deepest states and are plotted in Figure 3-28(b), which distributed in 0.15 < $k^* l$ < 0.45. Therefore, the modified Ioffe-Regel condition is satisfied for the strongly localized band-tail states. This result theoretically supports the experimental observation in this thesis. The localization of the band-tail state originates from multiple scattering in disordered structures, leading to the Anderson localization.

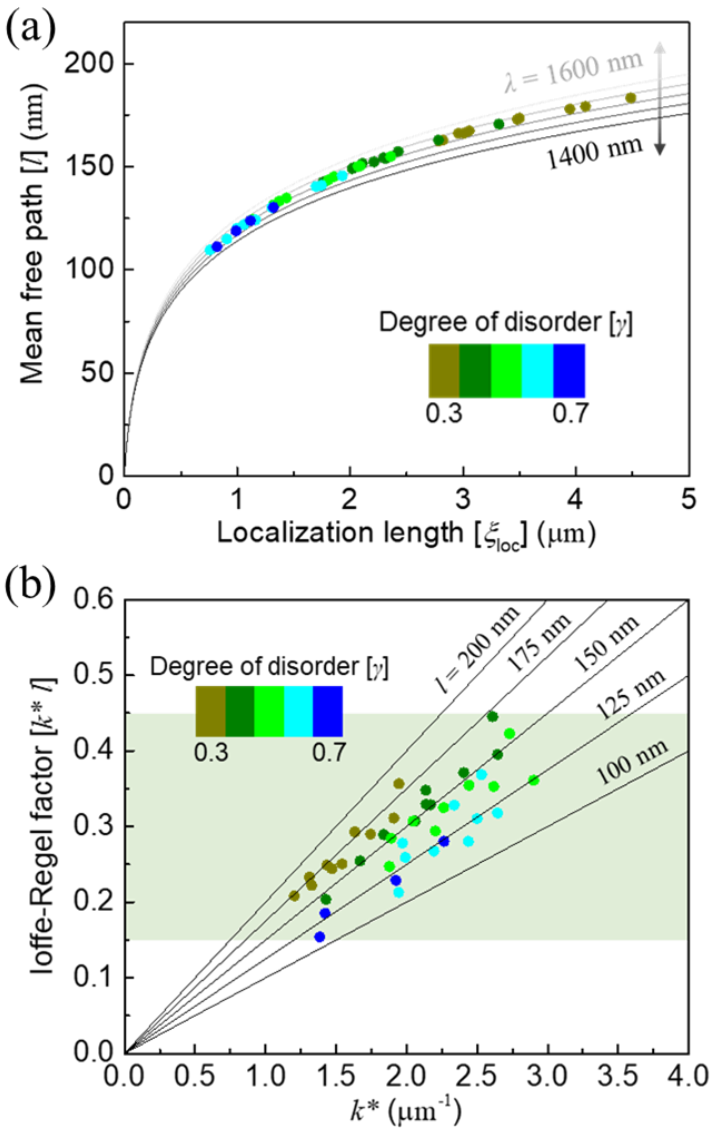

Figure 3-28. Localization criterion for the band-tail states. (a) The localization length and the mean-free-path for the deepest K_1 band-tail states of $\gamma \geq 0.3$, determined from exponentially decaying near-field profiles. The solid lines are theoretical guidelines calculated for specific wavelengths. (b) Modified Ioffe-Regel factors for the deepest band-tail states of $\gamma \geq 0.3$, plotted as a function of the wavenumber of envelop function k^*. The solid lines are guidelines for the mean-free-path l.

3.4.7. Eigenmode profiles of the other band-tail states

In addition to the K_1 band-tail states, near-field eigenmode profiles of the M_2 band-tail states are also measured. Figure 3-29 shows representative near-field distribution scanned at the lasing wavelength of the deepest M_2 band-tail states. For consistency, these images are taken from the same set of devices as the one used for the visualization of the K_1 band-tail states. From these images, it is clear that the deepest M_2 band-tail states are also strongly localized. The corresponding FDTD simulations reproduce the SNOM images quite well in terms of not only the location of local domain but also the degree of localization. However, it is not able to observe an entire transition from weak localization to strong localization for the M_2 band-tail states although it is done for the K_1 band-tail states, because only the deep states with $\gamma \geq 0.6$ lase in the M_2 band-tail states due to reason of the gain overlap described in Section 3.3.5.

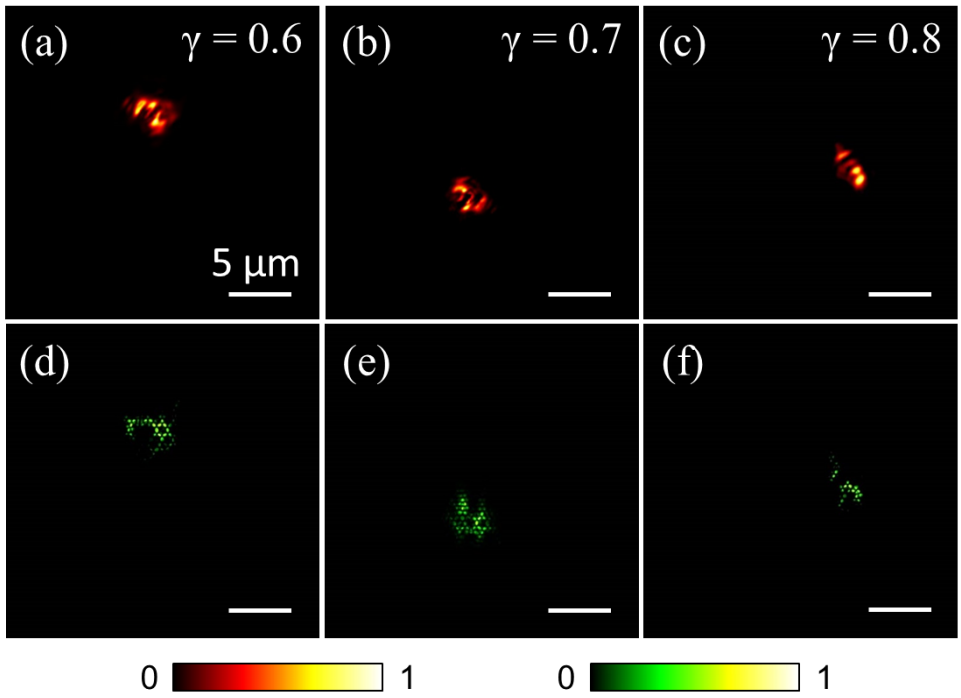

Figure 3-29. Representative mode profiles of the deepest M_2 band-tail states. (a-c) Near-field images measured for the deepest modes of different degrees of disorder: (a) γ = 0.6, (b) 0.7, and (c) 0.8. (d-f) Simulated $|E|^2$ profiles for the corresponding M_2 band-tail states: (d) γ = 0.6, (e) 0.7, and (f) 0.8.

3.4.8. Eigenmode profiles in momentum space

The evolutions of mode profiles are reconstructed in the reciprocal space. Representative simulated eigenmode profiles in momentum space are presented in Figure 3-30 and Figure 3-31 for the K_1 and M_2 deepest band-tail states, respectively. For the ordered case at γ = 0, each mode profile consists of bright discrete spots located at the K-points in the case of K_1 band-edge mode or the M-points in the M_2 band-edge mode. This fact is a definite evidence that these modes indeed band-edge modes having the K- or M-point symmetries. Similarly, for the disordered cases γ >

0, the band-tail states preserve the identities of the K- or M-point symmetries because the intense dots at the K- or M-points remain still brightly although blurred and non-periodic components are introduced. Therefore, two kinds of band-tail states, that is K_1 and M_2, can be identified by eigenmode profiles in momentum space, and this method is recommended since it is available even though their spectral discrimination is difficult due to the merging at higher degrees of disorder ($\gamma \geq 0.7$). Repeated investigations to many states over various energies and disorder configurations confirm that this argument is generally true for all band-tail states.

These observations and the corresponding modal evolution in real space lead to a complete picture on spectro-spatial behavior of band-tail states: two kinds of band-tail states, one starting from the K_1 band-edge and the other from the M_2 band-edge, gradually fill the band-gap from both ends as the degree of disorder increases and the localization extents of these states are determined from both the energy depth and the degree of disorder. On the spectral side alone, this scenario is conceptual extension of the photonic doping [113] to the extreme case of disordered system. The idea of linking the high- and low-index defect modes in a photonic crystal to donor and acceptor levels in an electronic system is parallelly extendable to the experimental observation in this thesis that demonstrates that the M_2 and K_1 continua of band-tail states in a photonic crystal alloy system correspond to the conduction and valence band-tail states in a disordered electronic system.

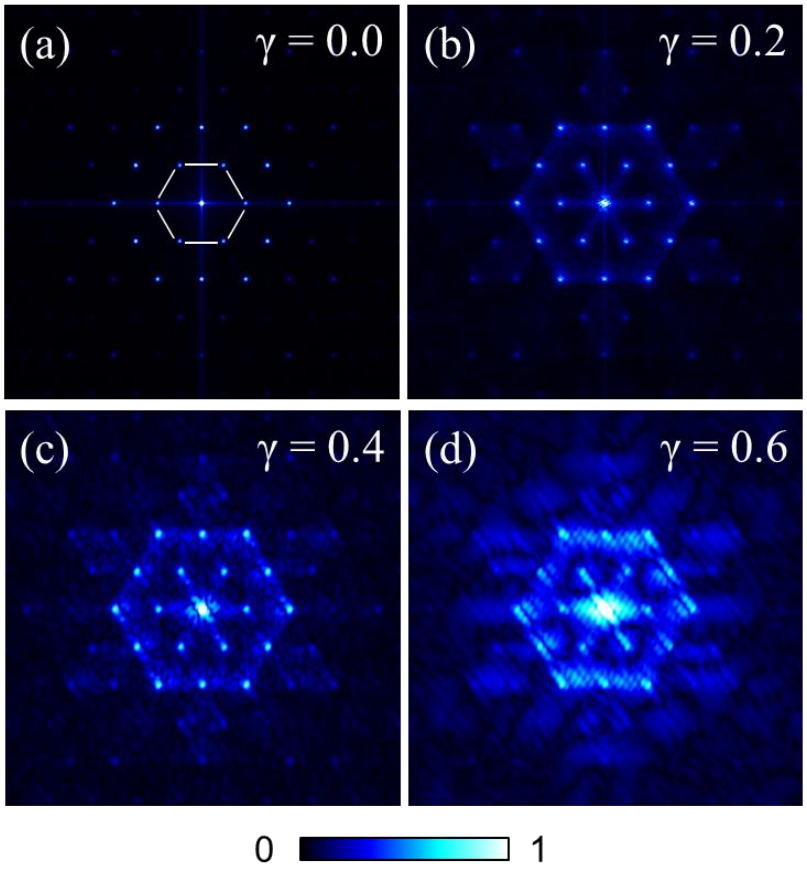

Figure 3-30. Representative simulated eigenmode profiles in momentum space of the K_1 band-tail states. Each image corresponds to different degrees of disorder: (a) γ = 0.0, (b) 0.2, (c) 0.4, and (d) 0.6. All the images are calculated using the model structure employing the same disordered configuration and physical dimensions with the real devices.

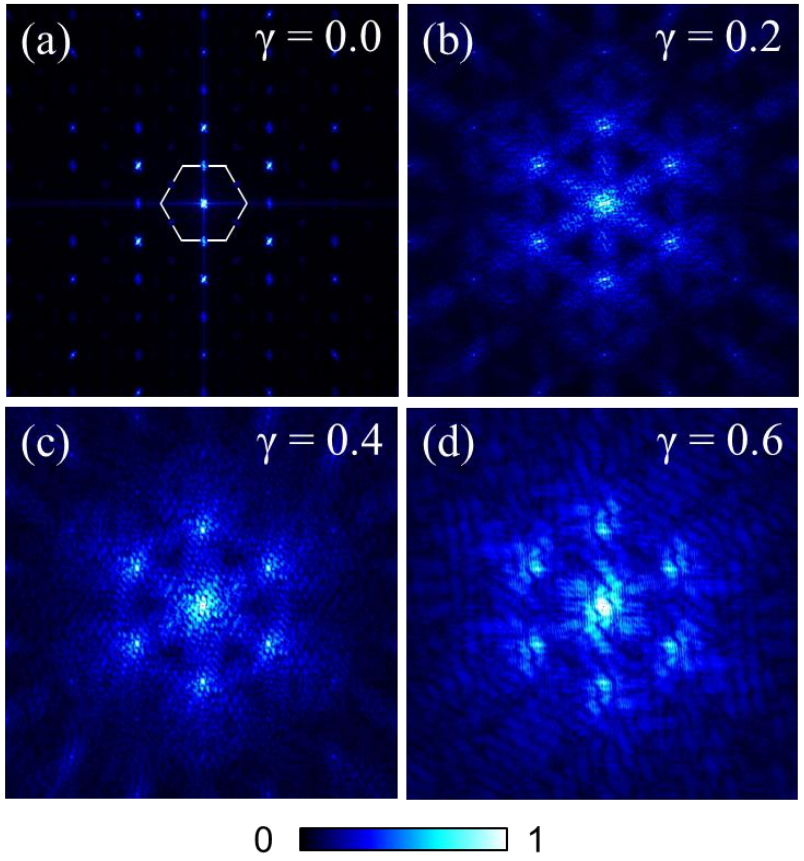

Figure 3-31. Representative simulated eigenmode profiles in momentum space of the M_2 band-tail states. Each image corresponds to different degrees of disorder: (a) γ = 0.0, (b) 0.2, (c) 0.4, and (d) 0.6. All the images are calculated using the model structure employing the same disordered configuration and physical dimensions with the real devices.

3.4.9. Effective width in momentum space

The effective width in the reciprocal space, k_{eff}, is also defined and calculated for which the integrand is substituted by a Fourier-transformed mode profile and the integration is performed over the 2D momentum space, according to the following definition:

$$k_{eff} \equiv \left\{\left[\int I(k_x,k_y)^2 dk_x dk_y\right]/\left[\int I(k_x,k_y)\, dk_x dk_y\right]^2\right\}^{-\frac{1}{2}},$$

where $I(k_x,k_y)$ is a Fourier-transformed intensity profile.

It is expected that k_{eff} exhibits opposite behavior to that of w_{eff} observed in real space. In other word, it should become larger as γ gets higher or the band-tail state goes deeper. Indeed, the results shown in Figure 3-32 confirm this expectation and it is well reproduced in simulations performed over enlarged spectral range that include behavior of the M_2 band-tail states as well.

Especially for the weakly disordered regime ($\gamma \leq 0.2$), the rate at which k_{eff} increases is much faster for the M_2 band-tail states than the K_1 band-tail states. The differential change is about 3.2 times, that is $\left(\Delta k_{eff}/\Delta\gamma\right)_M \sim 3.2\left(\Delta k_{eff}/\Delta\gamma\right)_K$. The meaning of this observation is that the M_2 band-edge is much more fragile than the K_1 band-edge. In other words, the K_1 band-edge has a higher inertia or resistance to the introduction of disorder, which may have a significant implication for the development of advanced photonic devices that use a band-edge mode and corresponding modal robustness is critically important to tightly control the degree of coherence [114].

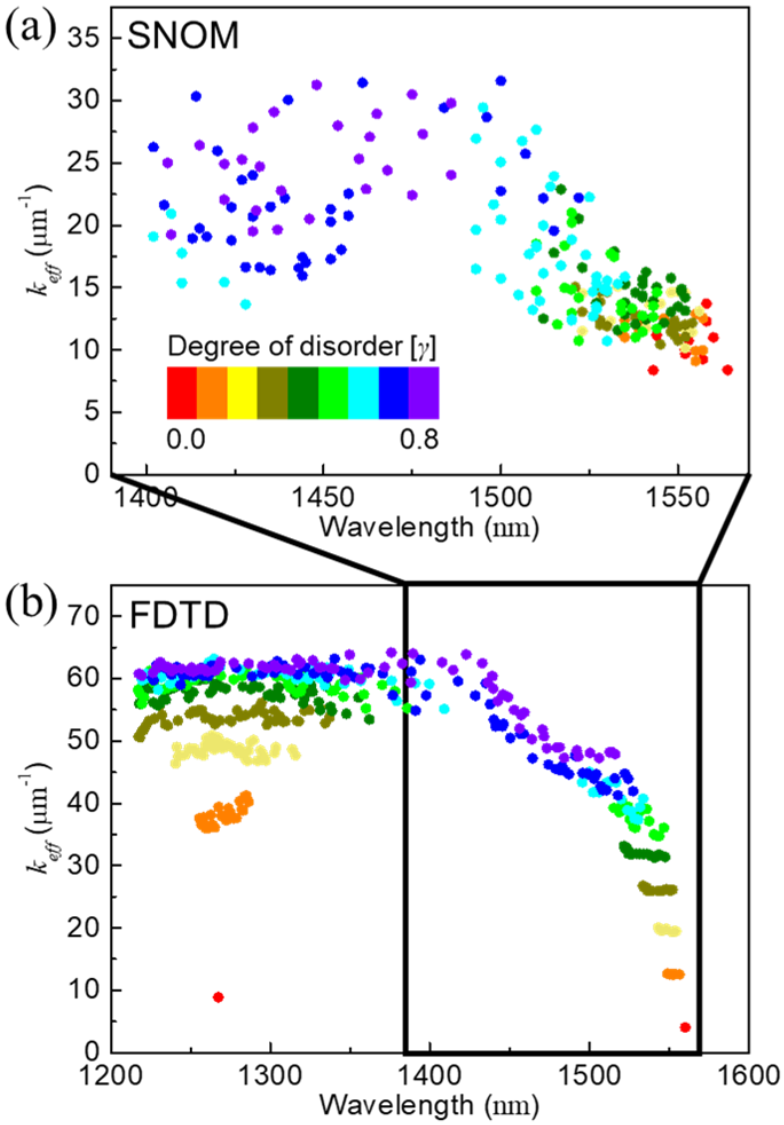

Figure 3-32. Effective widths in momentum space. (a) Effective widths of the band-tail states in momentum space are extracted from Fourier-transformed experimental near-field images. Each point corresponds to effective widths in real space shown in Figure 3-26. (b) Simulated effective widths of the band-tail states in momentum space where calculations are performed over an extended spectral range to include the behavior of the M_2 band-tail states.

3.4.10. Resolution dependence of Fourier space

In Section 3.4.9, it is noteworthy that the values of k_{eff} differ, roughly by a factor of two, between experiment and simulation data plotted in Figure 3-32. This is because the spatial resolutions used in SNOM measurements and FDTD simulations are different by the same factor. In order to demonstrate this dependence, effective width in both real and momentum space, that is w_{eff} and k_{eff}, are repeatedly calculated for a set of structural images with respect to several spatial resolutions. The effective width in real space, w_{eff}, is stable and practically unchanged against the variation of the resolution, however, the effective width in k-space, k_{eff}, heavily depends on the resolution although the overall dependence on γ persists.

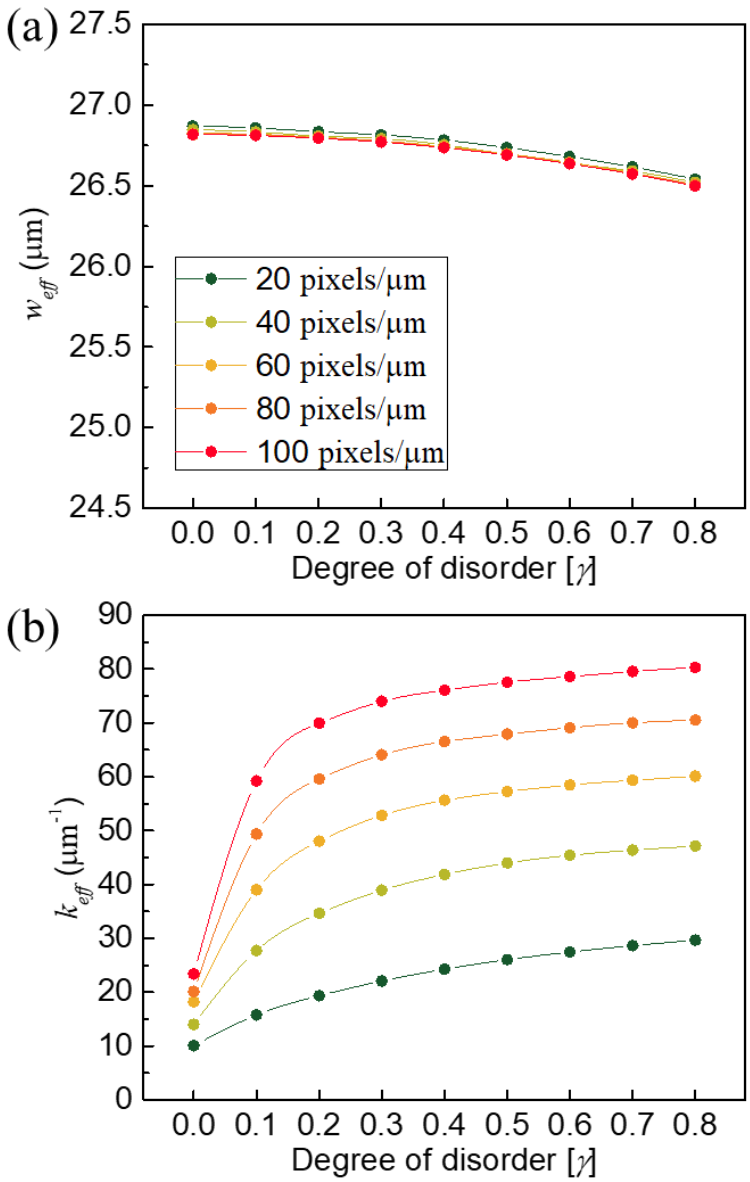

Figure 3-33. Resolution dependence of effective widths. (a) Effective widths for a set of structural images shown in Figure 2-8. Calculations are repeated for different resolutions (20, 40, 60, 80, and 100 pixels/μm). (b) Effective widths in momentum space for the same set of structural images.

3.4.11. Boundary dependence of modal extents

Intuitively, it is natural that an expansion of system size results in the increase of the extended Bloch state. However, such a simple scaling in modal area cannot true for a localized mode if the mode is already strongly confined within a local spot, and thus, is not interacting to the boundary of the system.

Figure 3-34, which is obtained by FDTD simulations, demonstrates this idea by quantifying the change of effective width for the deepest band-tail states as a function of the areal expansion of the system. As the system size expands by appending photonic atoms around the initial domain, the effective width of the band-tail states in weakly disordered system ($\gamma \leq 0.2$) monotonically increases, which is qualitatively consistent with the scaling properties of the Maxwell equations [93]. However, for the states in the more disordered systems ($\gamma \geq 0.3$), the effective width becomes completely insensitive to the system size.

This result indicates that the boundaries of a system could affect the formation of localized modes as previously studied in ref. [115], and verified it for the photonic band-tail states. Therefore, one should carefully examine the origin of localization to discriminate the disorder-induced localizations from the boundary-induced ones when claiming on Anderson localization. In this thesis, it is confirmed that the deepest band-tail states in the proposed platform with moderate disorder of $\gamma \geq 0.3$ are able to be strongly localized due to purely disorder-induced Anderson localization.

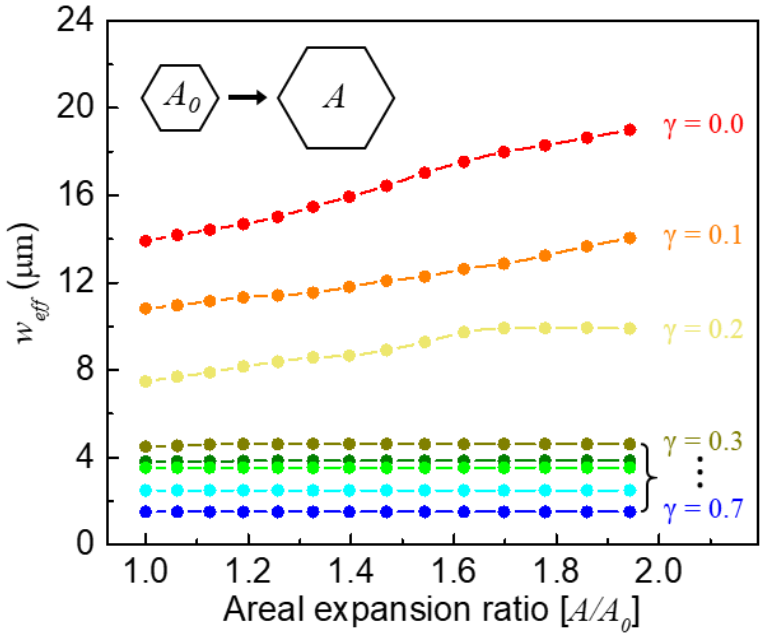

Figure 3-34. Boundary dependence of modal extents. Effective widths for the deepest band-tail states are calculated as a function of device size *A* normalized by initial area A_0. In this simulation, the disordered configuration is fixed to exclude the effect of configuration-specificity.

3.4.12. Excitation dependence of modal extents

One important premise of experimental methodology is that near-field modal properties should not be sensitive to the excitation strength with the similar reasons for PL measurements described in Section 3.3.8. To secure the experimental credibility, a light-in light-out characteristic in near-field regime, evolution of near-field spectrum and eigenmode profile, and SNR of near-field signals are investigated for the representative band-tail state of γ = 0.4 as a function of excitation strength, over the entire excitation power range available in SNOM setup, which are shown in Figure 3-35, Figure 3-36, and Figure 3-37, respectively. At low excitation below laser

threshold, no modal feature can be seen. But as the excitation strength approaches and goes beyond laser threshold (~1 kW/cm^2), a mode with sharp resonance, which corresponds to a tightly localized mode as confirmed by the eigenmode profiles, appears and maintain its modal properties both spectrally and spatially. Other band-tail states exhibit similar behaviors, regardless of their degrees of disorder and state energies.

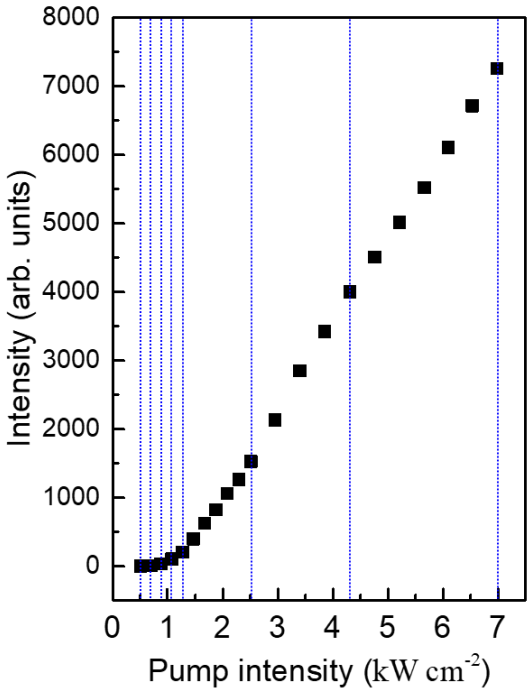

Figure 3-35. Representative light-in light-out characteristic curves in the near-field regime. The deepest K1 band-tail state of γ = 0.4 is measured using scanning near-field optical microscopy setup. Strong nonlinear behavior with well-defined threshold indicates lasing action. Blue dashed lines are guidelines of the representative pump intensity at which further investigation are followed in Figure 3-36 and Figure 3-37.

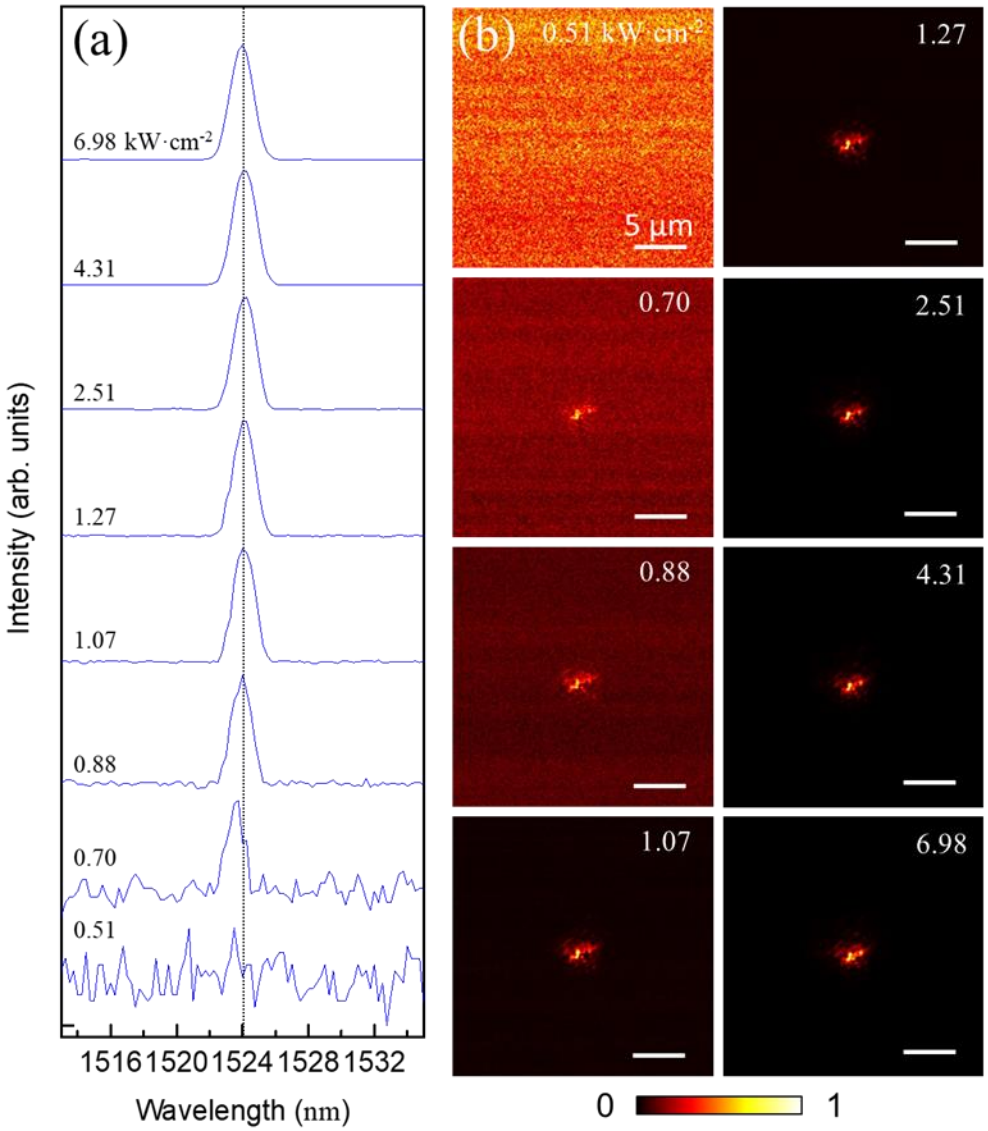

Figure 3-36. Excitation power density dependence of near-field modal properties. (a) Near-field photoluminescence spectra measured for representative pump intensities. The spectral behavior in the near-field regime is stable in the range of interest. (b) Near-field eigenmode profiles measured for the same set of pump intensities. The spatial behavior of the band-tail state is also stable in the range of interest.

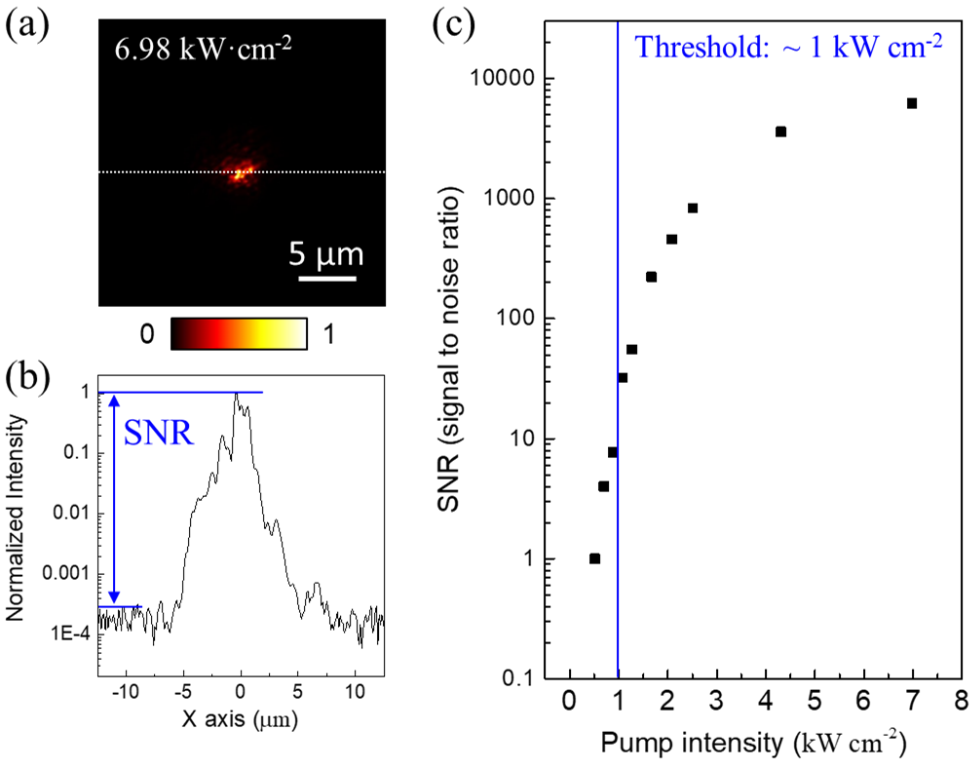

Figure 3-37. Excitation power density dependence of near-field signals. (a) A representative near-field eigenmode profile. (b) A line profile along the white dashed line shown in (a), which traverses the maximum intensity point. (c) Signal-to-noise ratio measured in the near-field regime as a function of pump intensity.

3.4.13. Summary

i. Near-field imaging of individual eigenmode revealed that the eigenmode profile of the band-edge exhibits the extended Bloch mode profile, and that of the deepest band-tail state is localized in a spatially isolated single-enveloped spot whereas that of the shallowest one has relatively large mode profiles composed of loosely connected multiple segments.

ii. The complete picture of modal evolution including the strong and weak localization indicated that an eigenstate with intermediate energy can have any modal size and localization property that system allows, which is a great advantage for light shaping.

iii. To quantify a modal extent of a band-tail state, the effective width was defined using the inverse participation ratio that measures the averaged moments of the eigenfunction.

iv. The effective width was calculated for every near-field image taken from lasing modes of each device and the result directly confirmed that a band-tail state is the more localized in real space when not only it is in structure with stronger disorder, but also it has large energy difference to the band-edge.

v. The strong energy dependence of localization was exactly the optical properties of band-tail states predicted by theoretical studies. Furthermore, it is a solid foundation of realizing predictable and systematic light shaping over wide spectro-spatial domain on chip-scale.

vi. The modified Ioffe-Regel condition, a localization criterion of the band-tail state, was satisfied for the strongly localized band-tail states. Therefore, the localization of the band-tail state originates from multiple scattering in disordered structures, leading to the Anderson localization.

vii. In addition to the K_1 band-tail states, near-field eigenmode profiles of the M_2 band-tail states were also measured and it was demonstrated that the deepest M_2 band-tail states are also strongly localized although an entire transition from weak localization to strong localization is not observable in the proposed system.

viii. Two kinds of band-tail states, that is K_1 and M_2, could be identified using eigenmode profiles in momentum space, and this method is recommended because it is available even though their spectral discrimination is difficult due to the merging at higher degrees of disorder.

ix. The effective width in the reciprocal space was also defined and calculated. The results exhibited opposite behavior to those observed in real space, which were well reproduced in simulations. Especially for the weakly disordered regime, the K_1 band-edge had a higher inertia to the introduction of disorder.

x. The effective width in real space was stable and practically unchanged against the variation of resolution, however, the effective width in k-space heavily depended on the resolution although the overall dependence on γ persists.

xi. The simple scaling in modal area, which is natural to the extended Bloch state, could not applicable for a localized mode because the mode is not interacting to the boundary of the system. The deepest band-tail states with moderate disorder of $\gamma \geq 0.3$ exhibited this property, leading to purely disorder-induced Anderson localization.

xii. One important premise of experimental methodology is that near-field modal properties should not be sensitive to the excitation strength. This credibility was verified to be secured by directly investigating near-field signals as a function of excitation strength, over the entire excitation power range available in SNOM setup.

3.5. Conclusion

The eigenmodes in a photonic crystal alloy were verified as the photonic band-tail states whose optical properties are highly reproducible, predictable, and tailor-designable over a wide spectro-spatial range across the complete band-gap and from only a few lattices to the entire structure, which is a great advantage for light shaping.

The concept of photonic lattices with a moderate disorder of coherently arranged scattering elements was proposed by S. John in 1987. In this system, a photon can be strongly localized in a pseudo-gap region by Anderson localization mechanism, resulting predictable and systematic optical properties. It was also suggested that these localized states could be a photonic band-tail state, which is a standing wave that occurs near band-edges with a modulating envelope function whose wavelength is determined by the energy difference to the nearest band-edge. There have been many experimental studies designed to observe photonic band-tail states and their strong localization, however, these studies employed a lattice disordered system that is hard to establish predictable and systematic observations with increasing disorder due to the collapse of the crystallinity. One sufficient condition for observing and studying photonic band-tail states over a wide range of spectro-spatial domain is then to preserve the crystalline structure regardless of disorder strength, to secure a wide band-gap for the spectral resolution, and to distinguish localized band-tail states from extended Bloch states.

The set of samples examined in this chapter consists of a total of 9 disorder strengths, quantified by the degree of disorder γ ranging from 0 to 0.8 divided by the interval of 0.1, and for each γ, 10 kinds of configurations were realized to eliminate the influence of configuration-dependent effects. And a hexagonal lattice was employed in addition to high-index-contrast materials to provide a very large

complete band-gap of ~300 nm as a wide playground of band-tail states, which mitigates the spectral resolution of experimental setup required for identifying individual state. Using multiple-quantum-well structures as both a slab waveguide and a gain material, optically activated disordered systems were realized. Thus, extended Bloch states and localized photonic band-tail states can be distinguished by signal strength, based on the Purcell effect

Photoluminescence measurements identified two types of modes that were developed from each side of the band-gap and grew to fill the entire band-gap with increasing degree of disorder, which were referred to as K_1 and M_2 band-tail states according to the spectral origin of the mode. To ensure generality and to exclude the effect of specificity in disorder configurations, statistical treatments were taken by ensemble-averaging over samples with 10 kinds of different configurations, which verifies K_1 and M_2 band-tail states with statistical evidences. The band-gap narrowing observed in the proposed system was caused by gradually decreasing effective refractive index of a slab waveguide, as confirmed by applying the virtual crystal approximation to virtual perfect crystal of identical air-holes. The penetration depth of band-tail states was super-linearly proportional to the degree of disorder, which is similar to the Urbach tails observed in semiconductor alloys. However, unlike the electronic cases, the observed penetration depth did not increase without bound. The discrepancy with the theoretical estimation was explained by the gain overlap between the modes and gain material, which is an important factor to consider a lasing of an eigenmode. The Bloch states in a finite system consisted of quasi-continuous modes due to the domain boundary effect and had relatively weak intensities compared with localized band-tail states, which exhibited strong intensity in both the measurement and the simulation due to the mechanism of multiple scattering. Light-in versus light-out relationships of modes identified in the PL spectra manifested a

strong nonlinear behavior with a well-defined threshold in addition to the narrow linewidth and high signal-to-noise ratio, which is a clear evidence for lasing. The population inversion in gain materials using excitation pumping energy was very helpful to exclude the effects of material absorption. The thermo-optic effect of hard optical excitation was negligible, and corresponding change of modal energy was measured to be less than 10^{-4}.

Near-field imaging of individual eigenmode revealed that the eigenmode profile of the band-edge exhibits the extended Bloch mode profile, and that of the deepest band-tail state is localized in a spatially isolated single-enveloped spot whereas that of the shallowest one has relatively large mode profiles composed of loosely connected multiple segments. The complete picture of modal evolution including the strong and weak localization indicated that an eigenstate with intermediate energy can have any modal size and localization property that system allows, which is a great advantage for light shaping. To quantify a modal extent of a band-tail state, the effective width was defined using the inverse participation ratio that measures the averaged moments of the eigenfunction. The effective width was then calculated for every near-field image taken from lasing modes of each device and the result directly confirmed that a band-tail state is the more localized in real space when not only it is in structure with stronger disorder, but also it has large energy difference to the band-edge. The strong energy dependence of localization was exactly the optical properties of band-tail states predicted by theoretical studies. Furthermore, it is a solid foundation of realizing predictable and systematic light shaping over wide spectro-spatial domain on chip-scale. The modified Ioffe-Regel condition, a localization criterion of the band-tail state, was satisfied for the strongly localized band-tail states. Therefore, the localization of the band-tail state originates from multiple scattering in disordered structures, leading to the Anderson localization. In addition to the K_1 band-

tail states, near-field eigenmode profiles of the M_2 band-tail states were also measured and it was demonstrated that the deepest M_2 band-tail states are also strongly localized although an entire transition from weak localization to strong localization was not observable in the proposed system. Two kinds of band-tail states, that is K_1 and M_2, were identified using eigenmode profiles in momentum space as well, and this method is recommended because it is available even though their spectral discrimination is difficult due to the merging at higher degrees of disorder. The effective width in the reciprocal space was also defined and calculated. The results exhibited opposite behavior to those observed in real space, which were well reproduced in simulations. Especially for the weakly disordered regime, the K_1 band-edge had a higher inertia to the introduction of disorder. The effective width in real space was stable and practically unchanged against the variation of resolution, however, the effective width in k-space heavily depended on the resolution although the overall dependence on γ persisted. The simple scaling in modal area, which is natural to the extended Bloch state, could not applicable for a localized mode because the mode is not interacting to the boundary of the system. The deepest band-tail states with moderate disorder of $\gamma \geq 0.3$ exhibited this property, leading to purely disorder-induced Anderson localization. One important premise of experimental methodology that near-field modal properties should not be sensitive to the excitation strength was verified to be secured by directly investigating near-field signals as a function of excitation strength, over the entire excitation power range available in SNOM setup.

Chapter 4 – Shaping band-tail lasers

4.1. Introduction

4.1.1. Random lasers: Laser in scattering media

Random lasers have been characterized by unpredictable complex behavior in broadband spectra. Figure 4-1 illustrates conceptual diagrams of lasing structures and corresponding spectral behaviors in a random laser, contrasted with those of a conventional laser. Unlike a regular laser, optical modes in a random laser are formed in a mirror-free way, such as realizing a gain membrane with complex morphology [116], immersing random scatterers in liquid gain [117], growing semiconductor nanorod in a random array [118], or just using a semiconductor powder [97].

Some of these approaches are classified into a random laser with incoherent feedback, or a diffusive feedback, which is characterized by a continuous spectrum without discrete components at resonant frequencies [119]. One can imagine the feedback process in a Fabry-Perot cavity where its one mirror at end-side is replaced by a scattering surface. In this structure, light scattering changes its direction every time scattered, thus resulting an open path of light, not a closed loop in one round trip like a regular laser. In this kind of laser, the only resonance is the emission line of active medium, which is much slowly narrowing than in regular lasers [120]. Representative experimental demonstrations are a photonic bomb [121], a powder laser [122], and a laser paint [123].

Conversely, some schemes [97, 124, 125] exploit multiple interferences among scattered light with recurrent resonances, matched to the wavelength of light. In contrast to the diffusive feedback, it is a random laser with coherent feedback. Due to the resonance, rich spectra behavior with discrete lasing modes can be observed in

this kind of laser. The two categories of random laser can be most clearly distinguished by photon statistics because the coherent emission follows the Poissonian photon distribution described by Poisson statistics, and the chaotic emission of diffusive mechanism leads to a bunched photon distribution corresponding to the Bose-Einstein statistics [119].

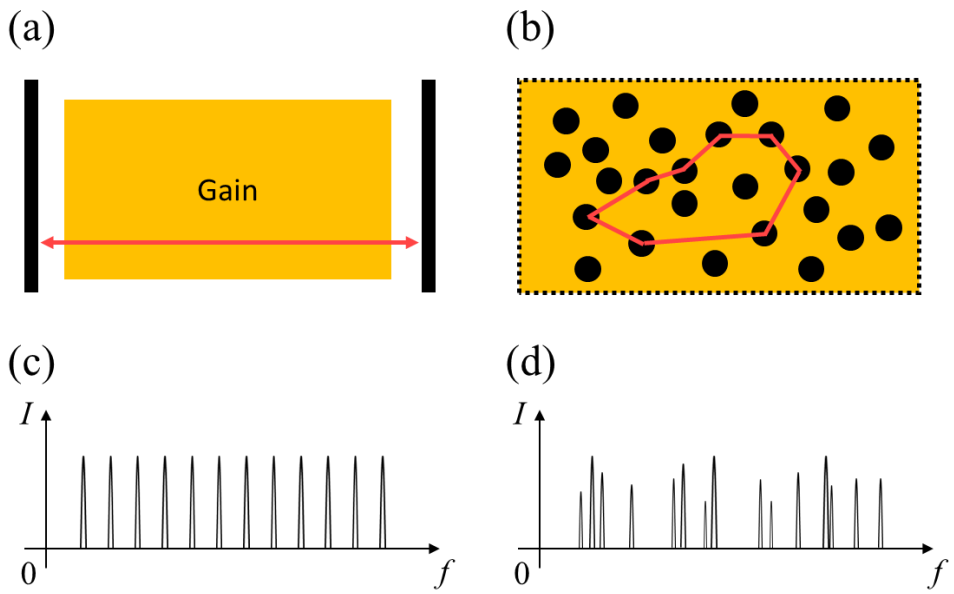

Figure 4-1. Conceptual diagrams of lasing structures and spectral behaviors. (a-b) Simplified lasing structures for (a) a cavity laser consisting of mirrors at both sides and gain materials inside the cavity and (b) a random laser based on optical modes formed by multiple scatterings between scattering elements imbedded in gain materials. (c-d) Representative spectral behaviors for (c) a cavity laser exhibiting equally-spaced free spectral ranges and (d) a random laser with the unpredictable rich spectral behavior.

4.1.2. Previous studies on shaping random laser

Due to its unique lasing mechanism, random lasers have distinct spectral footprints and near-field shapes contrasted with conventional lasers [126, 127, 128]. A major objective in this field is to control shapes of emitting light, and many innovative techniques have been developed to modulate spectral and spatial properties of random lasers using, for example, temperature [129, 130], external fields [131, 132], or pumping profiles [133, 134, 135] as a control parameter.

Some noteworthy studies are as follows. Wiersma *et al.* [129] demonstrated that the threshold and the bandwidth of random laser emission can be tuned by small changes in environment temperature, as displayed in Figure 4-2, using disordered dielectric material of which scattering strength is controlled externally via temperature. In addition, Gottardo *et al.* [131] reported switching of transport from a three-dimensional random walk to a quasi-two-dimensional type, controlled via an external electric field as shown in Figure 4-3, and observed anisotropic, extraordinary polarized emission in this system. The most studied approach to date is a pumping-based shaping of a random laser demonstrated in Figure 4-4. Leonetti *et al.* [133] showed that the random laser can be driven from a weakly interacting resonance to a regime of strongly interacting modes by engineering a mode-selective pumping of a random laser.

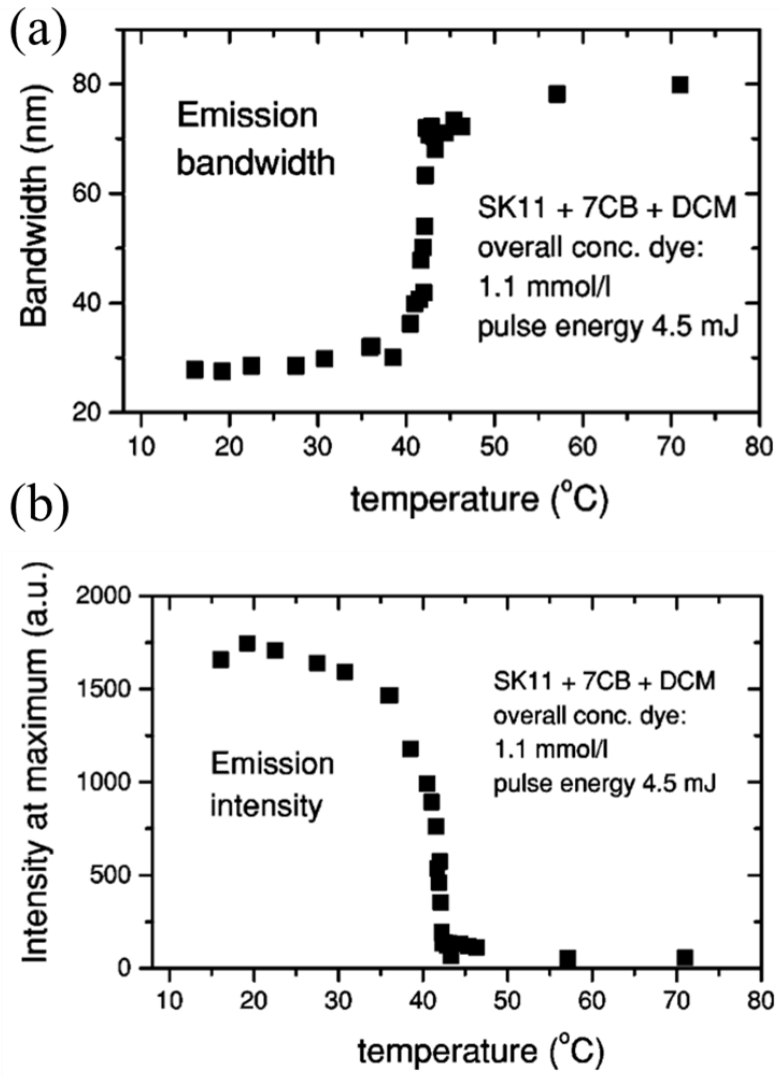

Figure 4-2. Emission properties of the random laser controlled by a temperature [129]. (a) Emission bandwidth as a function of temperature of the random lasing sample. A strong decrease below 42.5 ℃ is due to the enlargement of the scattering strength of the material, which brings the system in the condition that the total gain exceeds the losses. (b) Emission intensity versus temperature. The strong increase is observed as well with the same reason.

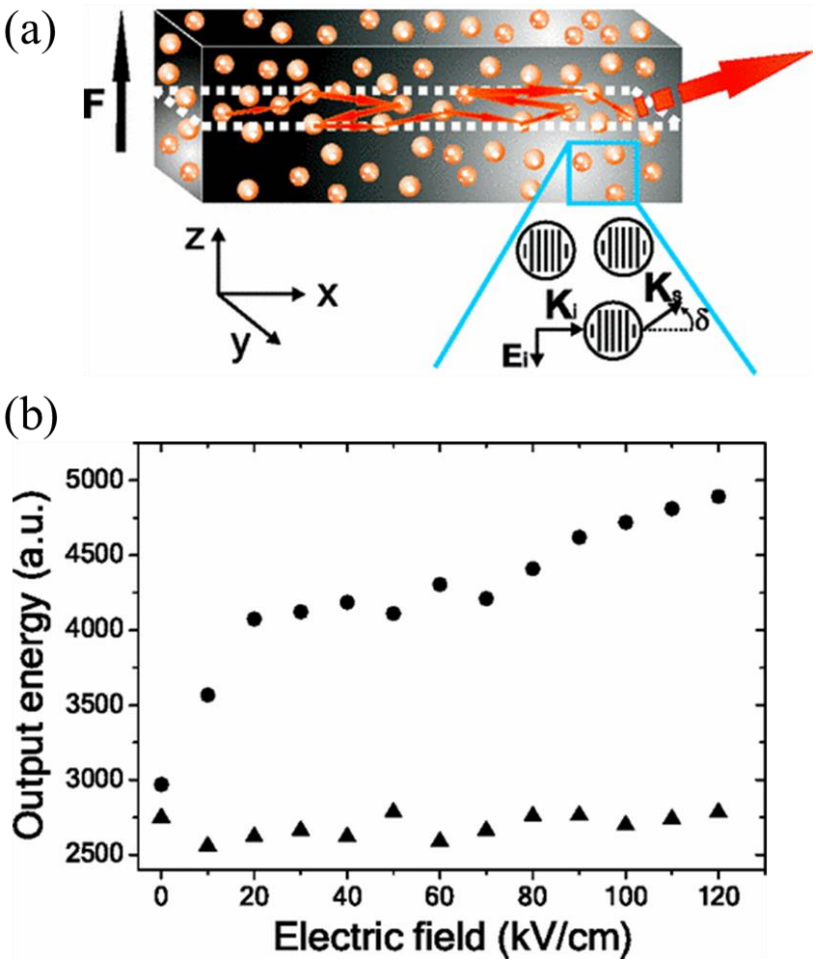

Figure 4-3. Schematic and emission property of the random laser controlled by an external electric field [131]. (a) Simplified representation of the system. The external electric field is applied in the *z* direction, which switches a 3D diffusion to a quasi-2D transport in the *x*-*y* plane, resulting an extraordinary polarized emission. (b) Output emission energy of the system in the *x* direction for the two polarization channels as a function of the applied field. The polarization ratio is controllable using the external electric field.

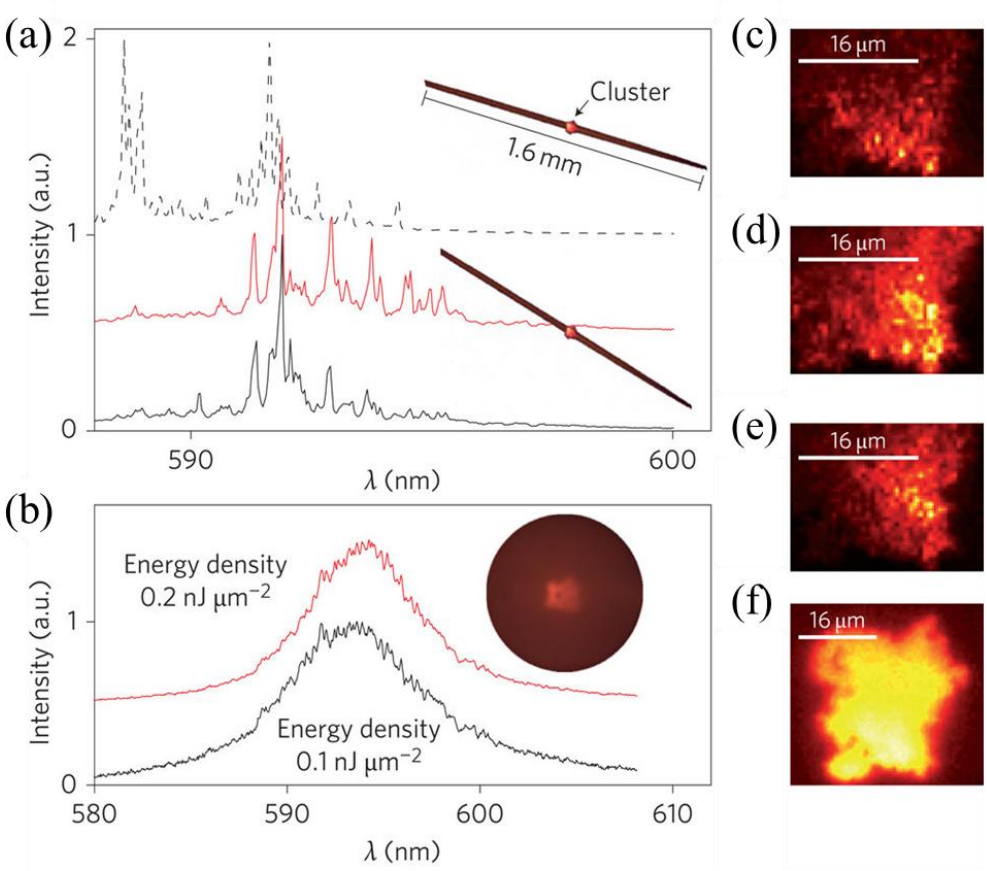

Figure 4-4. Emission properties of the random laser controlled by pumping profiles [133]. (a) Ensemble-averaged spectra from strip-shaped pumping profiles. Each spectrum is obtained by averaging 100 single shots. Top and bottom spectra are for a strip of the thickness of 16 μm, but with the difference of 15° tilting. The middle one is for the same condition with the bottom one, except the thickness of 32 μm. The insets sketch the pumping areas. (b) Spectra from disk-shaped pumping profiles of 1-mm diameter with different pump densities. (c-f) Intensity distributions of emitted lights in (a-b), obtained at a pumping fluence of 0.1 nJ/μm^2, with (c-e) the stripe pumping profile and (f) the circular pumping profile.

4.1.3. Recent approaches: Access to internal degree of freedom

Although successful and highly suggestive, most of shaping methods introduced in Section 4.1.2 have fundamental limitations that it requires additional external control factors, which might be desirable to be reserved for more advanced functionalities like an active modulation.

Recent approaches, however, have begun to directly manipulate a random configuration by carefully engineering the density and distribution of scattering elements [136]. The most notable achievement at this time is that of Schönhuber *et al.* [137]. They demonstrated a broadband laser emission with an almost diffraction-limited far-field profile, which is controlled by a scattering configuration as displayed in Figure 4-5. That is, using only an internal degree of freedom in random structure, without external control parameters, they succeed in controlling the beam divergence and emission directionality.

With these pioneering efforts including ones in Section 4.1.2 as well, the rich and complex behavior of random lasers have been significantly revealed, enabling better understanding of underlying mechanisms [138, 139, 140], and leading to practical applications [141, 142, 143]. However, due to the inherent complexity of the disordered system, it is still true that it is hard to predict or engineer modal properties of random lasers precisely, not to mention shaping near-field distribution.

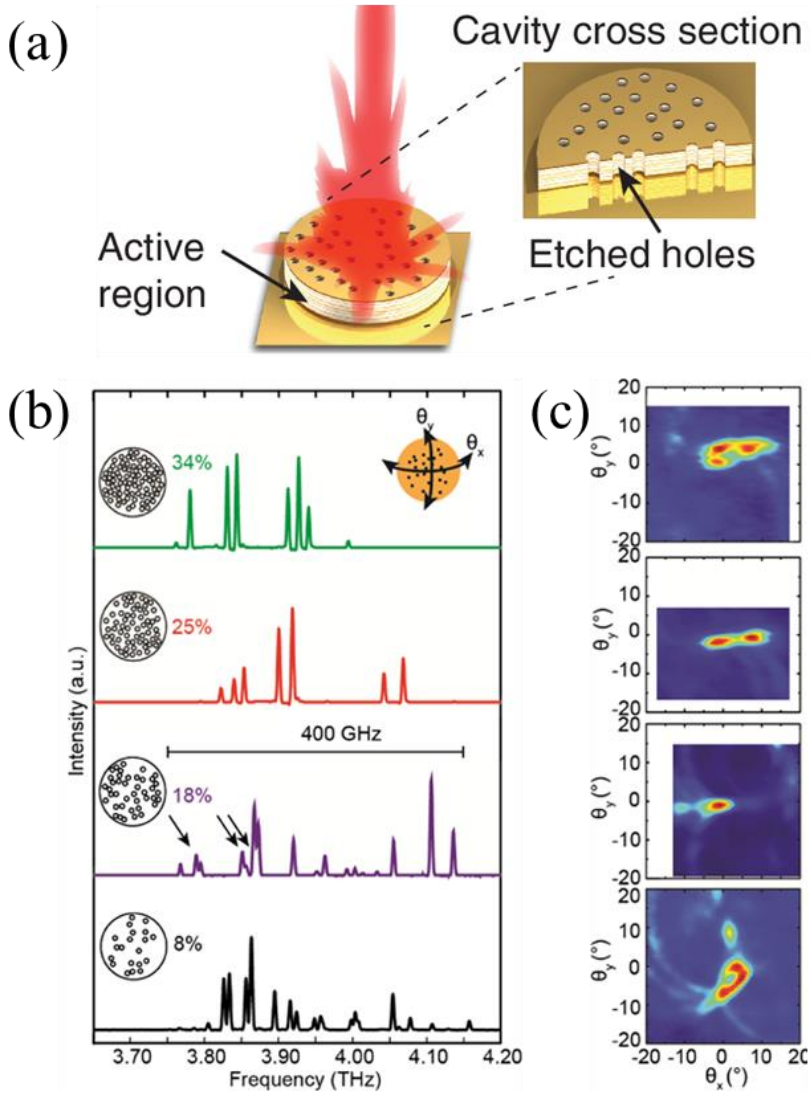

Figure 4-5. Schematic and emission properties of the random laser controlled by a scattering configuration [137]. (a) A schematic of the device with non-overlapping scattering elements consisting a scattering configuration. (b) Spectra measured for devices with different filling fractions (8, 18, 25, and 34%). Broadband emission of almost 400 GHz is achieved at 18% of filling fraction. (c) Far field emission of the random laser. Directional emission perpendicular to the device is observed.

4.1.4. Band-tail laser: Laser device based on band-tail states

The band-tail laser is a special class of random lasers, where a resonant mode of the lasing action is the band-tail state. Since the band-tail state is an eigenmode in the photonic crystal alloy, a special class of disordered photonic structures where the disorder is injected by a compositional ratio and a relative size of the constituent photonic atoms, the feedback mechanism in the band-tail laser is multiple scattering due to refractive index fluctuations, corresponding to coherent feedback in a mirror-free structure.

As shown in Section 4.2.2, a band-tail laser can exhibit typical spectral characteristics of random lasers when intentional engineering is not applied, which proves that it belongs to a category of a random laser. With clever idea and careful engineering, however, it could be so great candidate for light shaping within a membrane that realizes precise control on modal properties as well as near-field shapes, which will be demonstrated in this chapter. These predictability and manipulability over shapes of a random lasing mode in the proposed platform would extend its potential applications across many fields, including particle manipulation [144], cavity quantum electrodynamics [7], quantum many-body physics [145], optical data storage [8], optical communication [146], and quantum information technologies [147], which could use spatial degree of freedom and the spin-orbit coupling of confined light [20] to handle the light-matter interaction and information engineering.

4.1.5. Advantages for light shaping

In Chapter 3, it was revealed that spectral distribution of resonant modes and a physical modal extent of a band-tail state can be determined by a regular band structure, a disorder strength, and an energy depth of eigenstate. These predictable modal behaviors are great assets for light shaping, inherent to the photonic band-tail state, a lasing mode in a photonic crystal alloy and corresponding band-tail lasing platform.

In this chapter, several ideas for light shaping will be proposed, and be demonstrated using the proposed platform, which manipulate only internal structural degrees of freedom such as the number of photonic atoms, relative scattering strength among basis scatterers, and spatial configuration of all scattering elements over crystalline lattice sites. Shaping of modal density, modal property, and near-field profile will be demonstrated in Section 4.2, 4.3, and 4.4, respectively, by natural and reproducible ways that handle these structural parameters.

In addition, it will be clarified that the proposed approaches can shape a lasing mode with high precision over wide spectro-spatial range, and can be applied to any device with specific modal shapes. The band-tail laser and corresponding light shaping methods could expand its usability to the fields where conventional random lasers have been depreciated due to their random nature, especially where precise control on modal properties are required.

4.1.6. Summary

i. Random lasers have been characterized by unpredictable complex behavior in broadband spectra where, unlike a regular laser, optical modes are formed in a mirror-free way. Especially for a random laser with coherent feedback, discrete lasing modes can be observed due to the recurrent resonances.

ii. A major objective in this field is to control shapes of emitting light, and many innovative techniques have been developed to modulate spectral and spatial properties of random lasers using temperature, external fields, or pumping profiles as a control parameter.

iii. Most of developed shaping methods have fundamental limitations that it requires additional external control factors. Recent approaches, however, have begun to directly manipulate a random configuration by carefully engineering the density and distribution of scattering elements.

iv. The band-tail laser is a special class of random lasers, where a resonant mode of the lasing action is the band-tail state, an eigenmode in the photonic crystal alloy. The proposed lasing platform could be a great candidate for light shaping within a membrane with clever idea and careful engineering.

v. In this chapter, several ideas for shaping modal density, modal property, and near-field profile, which can be applied to any device with specific modal shapes, will be proposed and be demonstrated using only internal structural degrees of freedom of the proposed platform.

4.2. Shaping modal densities

4.2.1. Main idea for shaping modal density: Controlling photonic density of states

The first demonstration of light shaping, using the proposed platform, is to control photonic density of states and corresponding modal density. The main idea is to rearrange the configuration and place the strongly confined mode at the center of a device.

As verified in Chapter 3, modal properties of localized mode are not affected by a change of the device size, once the relative difference between the state energy and random fluctuations is so large that a state could become the Anderson-localized mode. One sufficient condition is a structure with enough scattering strength ($\gamma \geq 0.3$) and a state located deepest inside the band-gap. Therefore, if the Anderson-localized mode, satisfying the condition stated above, is located at the center of the device, it should be remained there when the device size is gradually reduced, whereas other modes on the periphery of the structure or those with relatively large field profiles are being removed in this process, as schematically illustrated in Figure 4-6.

This approach guarantees a single-mode operation, in principle, if the most strongly localized mode for the given disorder configuration is located at the center of the device. In addition, the modulation of modal density is expected to be gradual with respect to the device size, thus any modal density ranging from the single-mode and that of the original device can be achieved in between this process.

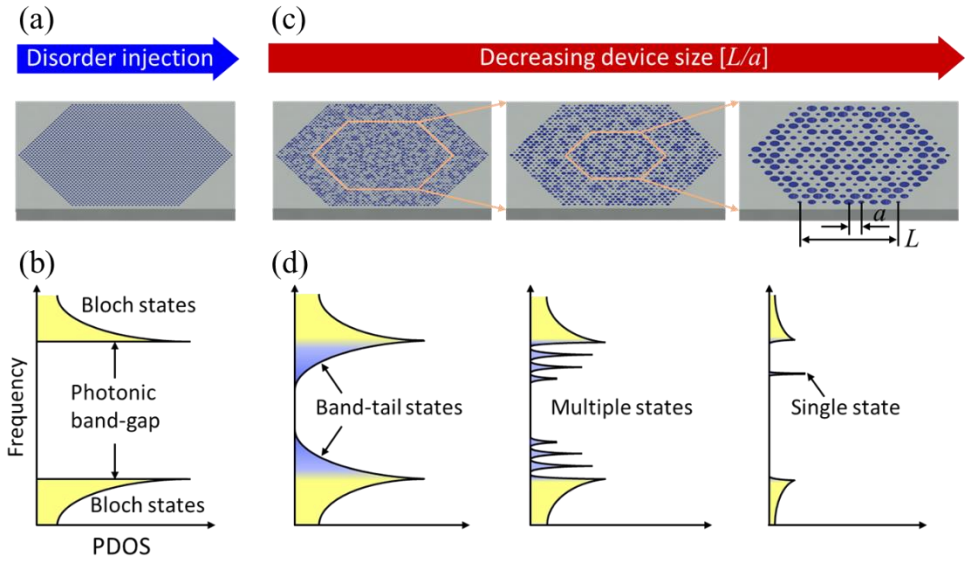

Figure 4-6. Schematics of the idea on shaping modal density. (a) An initial configuration and (b) corresponding photonic density of states (PDOS) before disorder injection. A periodic arrangement of photonic atoms suppresses the presence of states in the photonic band-gap. (c) Illustrations on the injection of disorder and successive reductions of device size, which generate the band-tail states inside the band-gap. (d) PDOS of the band-tail states is directly controlled by the device size, leaving only a single state located at the center of the device.

4.2.2. Spectral response: The single-mode random laser

To demonstrate the idea on modal density shaping and the single-mode operation a set of devices is fabricated for various sizes ranging from L/a = 5 to 32, where the size is quantified by the side length L normalized by the lattice constant a of the crystalline structure. The PL responses of this set are then investigated. The results are shown in Figure 4-7.

The PL spectra of larger devices (L/a = 30) is displayed in the upper row, which exhibit rich spectral behavior composed of many modes, similar to those of random lasers. Unlike the conventional random laser, however, these spectral responses are statistically predictable as a function of the band structure and the disorder strength quantified by the scattering strength γ: the band-edge is equal to one boundary of spectral packet that contains lasing modes, and γ determines the penetration depth that corresponds to the other boundary located inside the band-gap. In addition, the penetration depth exponentially increases with respect to γ as verified in Section 3.3.4.

These scenarios are consistent with the experimental observations displayed in Figure 4-7, Figure 4-8, Figure 4-9, and Figure 4-10, which corresponds to the evolution of lasing modes for γ = 0.3, 0.4, 0.5, and 0.6, respectively. The spectral width of lasing packet consistently increases according to γ, but is stable to small perturbations in device size. Furthermore, the number of lasing modes gradually decreases and eventually only one lasing mode survives when the device size becomes smaller. Although the specific device size that guarantees single-mode operation varies for the disorder strength, below a certain size (L/a = 9 for given configuration) all devices can operate in single-mode, regardless of γ. The lasing is stable and maintained up to $L/a \geq 8$. At smaller sizes, lasing stops because the quality factor of mode become worse rapidly, as described in Section 4.2.5. It is noteworthy that the wavelength of corresponding single-mode monotonically shifts with respect to γ as displayed in the bottom rows of displayed figures. This is originated from modal properties of the band-tail state, and will be one of mechanisms that shape a band-tail laser.

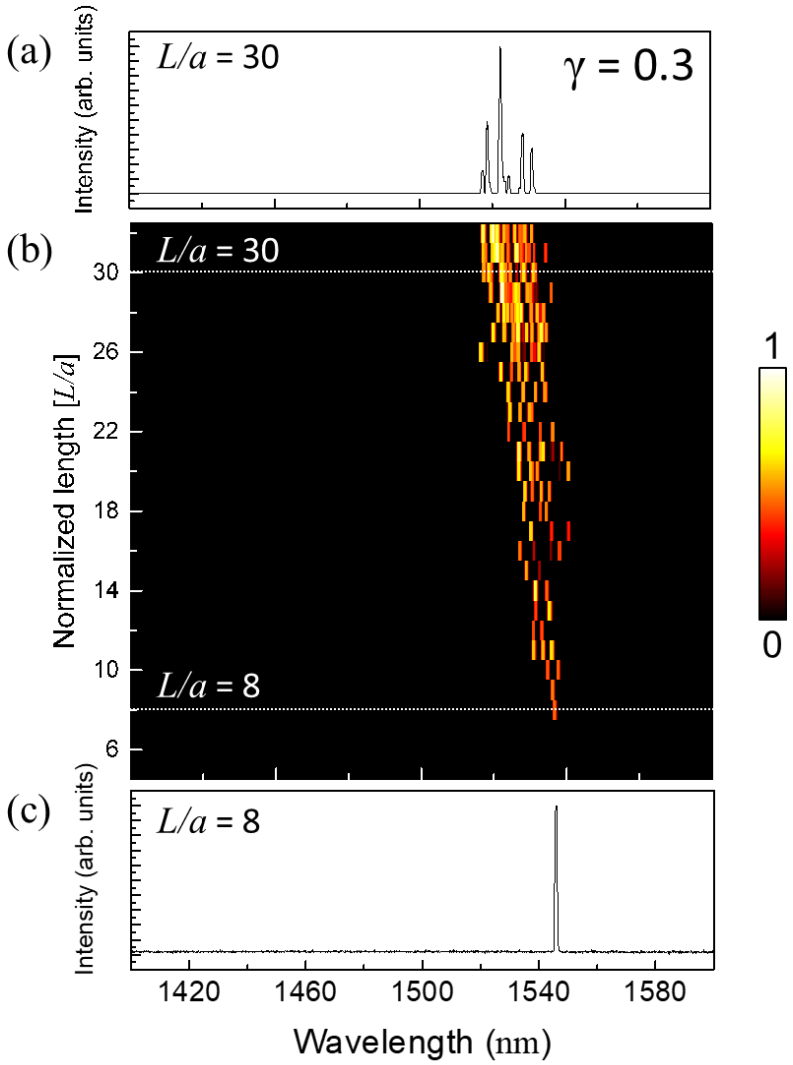

Figure 4-7. Evolution of lasing modes for band-tail lasers of γ = 0.3. (a) Photoluminescence spectrum measured for a device with size of L/a = 30. The typical spectral behavior of a random laser is observed, represented by multi-modes. (b) Spectral responses as a function of device size. The density of lasing modes is monotonically changed from multi-modes to a single-mode. (c) Spectrum measured for a device with size of L/a = 8, demonstrating a single-mode operation.

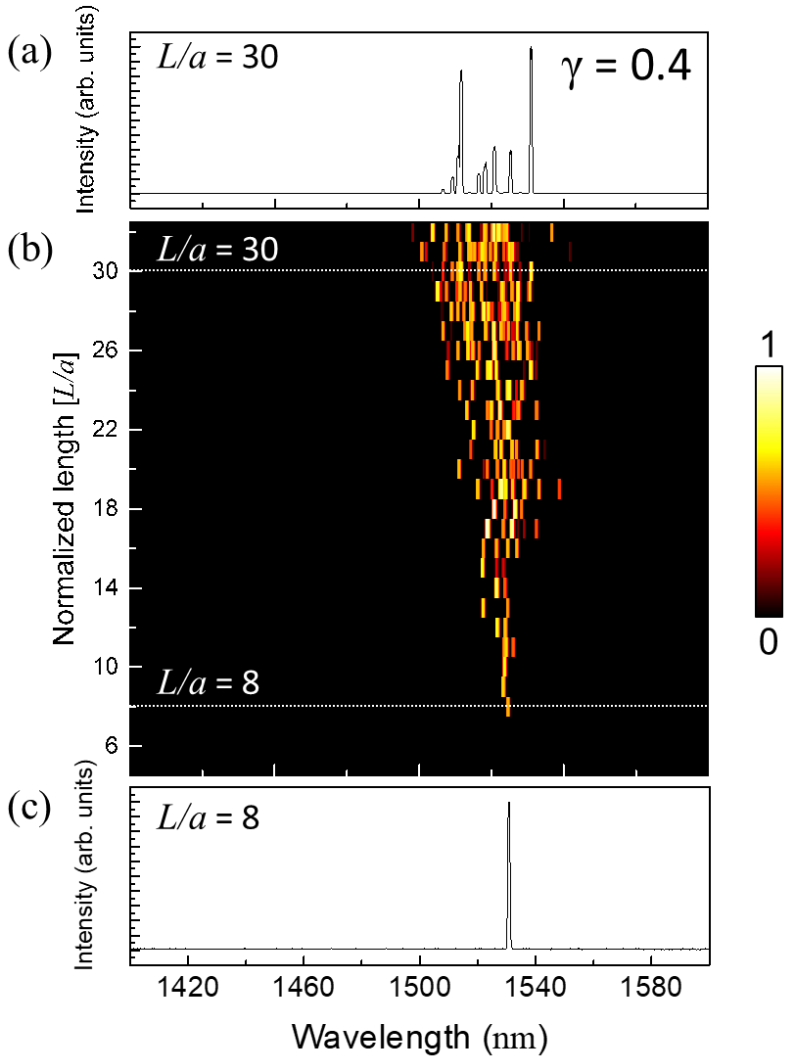

Figure 4-8. Evolution of lasing modes for band-tail lasers of γ = 0.4. (a) Photoluminescence spectrum measured for a device with size of *L*/*a* = 30. The typical spectral behavior of a random laser is observed, represented by multi-modes. (b) Spectral responses as a function of device size. The density of lasing modes is monotonically changed from multi-modes to a single-mode. (c) Spectrum measured for a device with size of *L*/*a* = 8, demonstrating a single-mode operation.

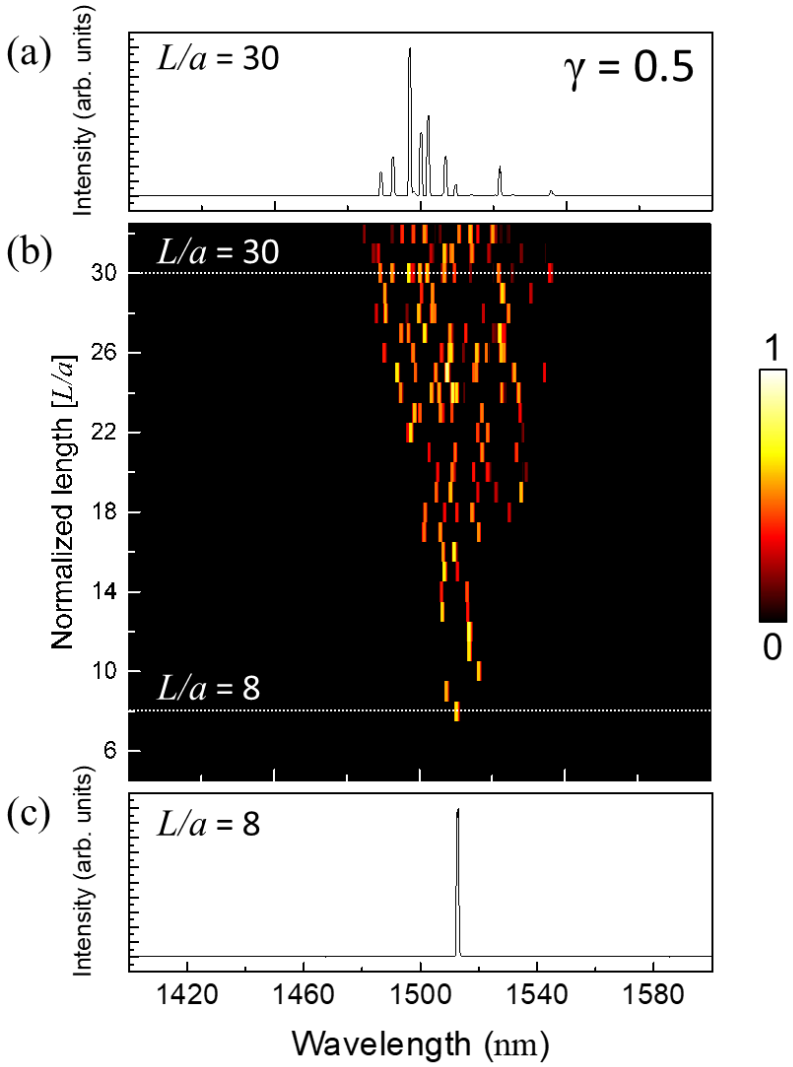

Figure 4-9. Evolution of lasing modes for band-tail lasers of γ = 0.5. (a) Photoluminescence spectrum measured for a device with size of *L*/*a* = 30. The typical spectral behavior of a random laser is observed, represented by multi-modes. (b) Spectral responses as a function of device size. The density of lasing modes is monotonically changed from multi-modes to a single-mode. (c) Spectrum measured for a device with size of *L*/*a* = 8, demonstrating a single-mode operation.

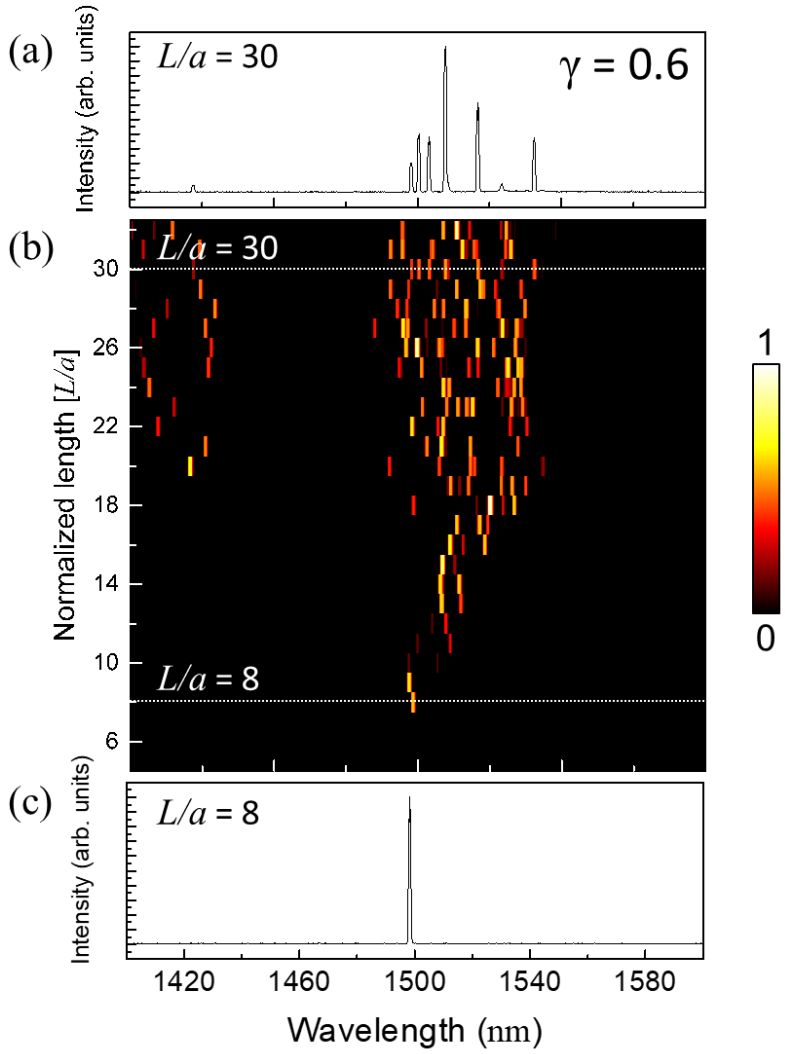

Figure 4-10. Evolution of lasing modes for band-tail lasers of γ = 0.6. (a) Photoluminescence spectrum measured for a device with size of *L*/*a* = 30. The typical spectral behavior of a random laser is observed, represented by multi-modes. (b) Spectral responses as a function of device size. The density of lasing modes is monotonically changed from multi-modes to a single-mode. (c) Spectrum measured for a device with size of *L*/*a* = 8, demonstrating a single-mode operation.

4.2.3. Near-field profiles: Elimination of peripheral modes

The transition from multi-modes to a single-mode is directly visualized by scanning near-field optical microscopy customized to identify individual modes, which is the same instrument used in Chapter 3 and described in Section 2.4.3. Figure 4-11 displays scanning electron microscope images and corresponding near-field distributions measured for a multi-mode device with sufficiently large size of L/a = 30 and a single-mode device with size of L/a = 8.

For the larger device, several states are spread at different localization over entire device, exhibiting various degrees of spatial extent. Among them, the state at the center of the structure is the Anderson-localized mode designed to be at that position with the smallest spatial extent. Thus, in the smaller device, this localized mode naturally survives while the other modes at the periphery are all eliminated, demonstrating that the photonic density of states in the proposed platform can be directly controlled with a natural and reproducible method that engineers the disorder configuration and the device size. It is confirmed that this idea holds for other scattering strengths as well.

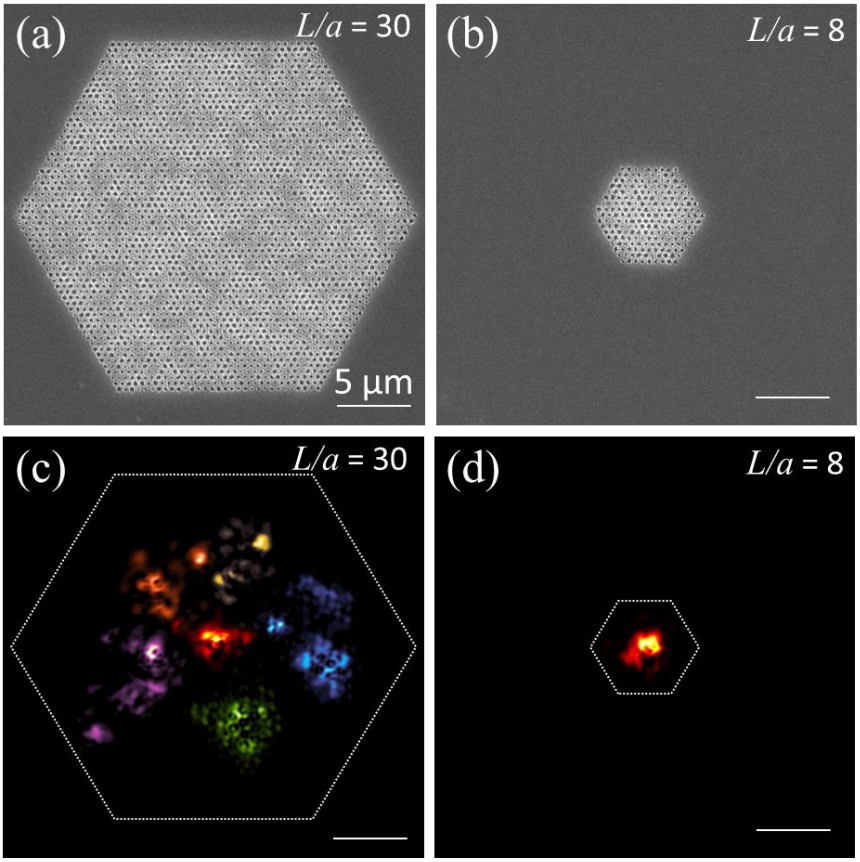

Figure 4-11. Structures and mode profiles of band-tail lasers. (a-b) Scanning electron microscope images of (a) a multi-mode device with size of L/a = 30 and (b) a single-mode device with size of L/a = 8. (c-d) Near-field eigenmode profiles corresponding to the device shown in (a-b), measured by scanning near-field optical microscopy setup. (c) For the multi-mode device (L/a = 30, γ = 0.5), several modes of different colors are visualized in a single image by overlapping all the eigenprofiles measured at each resonant wavelength. (d) For the single-mode device (L/a = 8, γ = 0.5), the only lasing mode with the Anderson-localized profile is observed at the center of the device.

4.2.4. Lasing performances: Compared to state-of-the-art cavity lasers

The lasing performance of band-tail lasers are characterized by comparing it with the well-known cavity structures. The near-field extent, lasing threshold, and slope efficiency are investigated for single-mode devices with the size of L/a = 8 as a function of the scattering strength.

The near-field distributions of band-tail lasers and cavity lasers are displayed in Figure 4-12. These images directly reveal that the band-tail lasing platform can embrace wide near-field extents observed in cavity systems. Furthermore, lasing performances of band-tail lasers is comparable to those of cavity lasers as summarized in Figure 4-13. The best threshold of the band-tail laser records 2.5 kW $\cdot cm^{-2}$ achieved at γ = 0.5, which is only 3.4 times worse than that of the L3 cavity laser. In addition, the slope efficiency is just 0.4 times lower than that of the best cavity system. These observations must be very encouraging for the potential of band-tail lasers because the compared lasers are already well studied and optimized systems. In fact, there are vast margins on degrees of freedom of structural parameters for further engineering, which can improve the performance of the band-tail laser.

Another interesting finding is the presence of optimal scattering strength (γ = 0.5 for the given configuration) for the lasing performance. This is because the vertical radiation takes over the dominant loss channel at this optimal value as described in Section 4.2.6, which can be deduced from the changes of modal quality factor with respect to γ. In-plane confinement, however, increases monotonically without limitation and is not a limiting factor to the lasing performance, which is consistent with the intuition figured out from the near-field images.

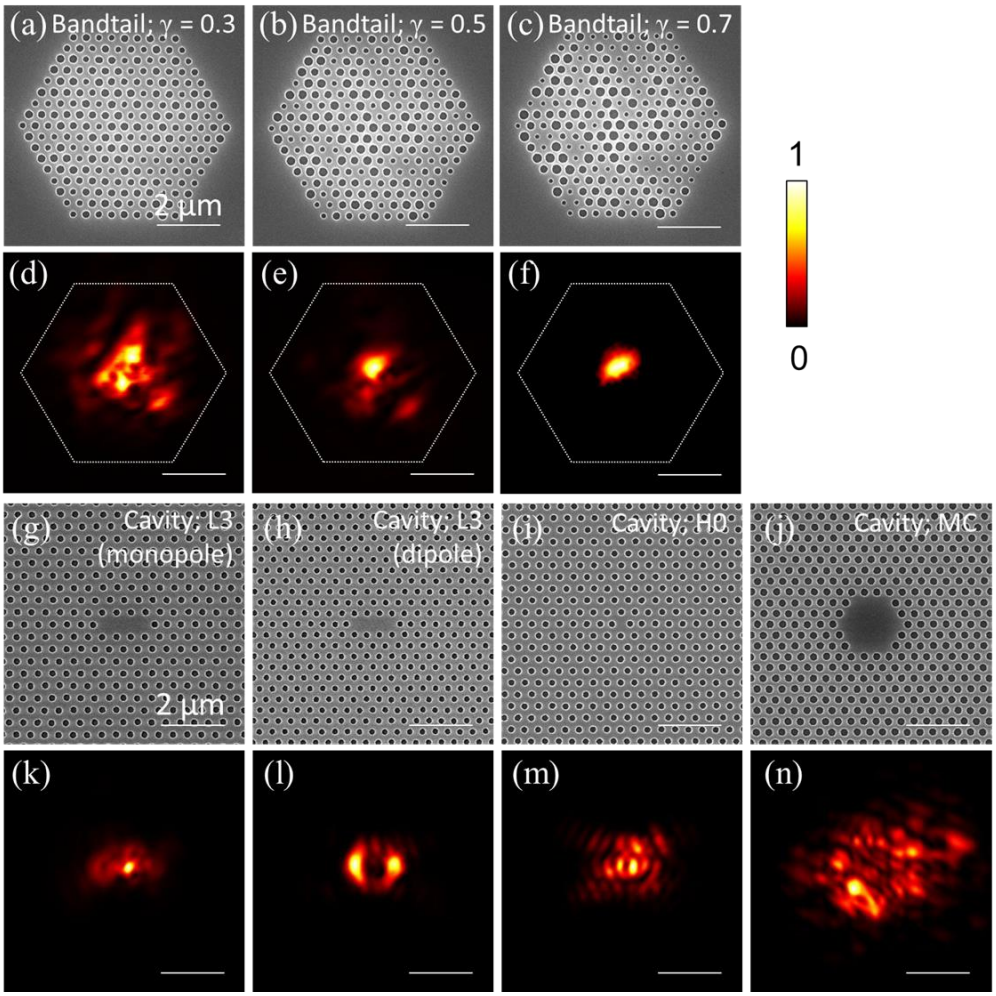

Figure 4-12. Structures and mode profiles of single-mode operating band-tail lasers and several cavity lasers. (a-c) SEM images for band-tail lasers with different degrees of disorder: (a) γ = 0.3, (b) 0.5, and (c) 0.7. (d-f) Corresponding single-mode profiles: (d) γ = 0.3, (e) 0.5, and (f) 0.7. (g-j) SEM images for each cavity structure: (g-h) L3 cavities with different structural parameters, (i) a H0 cavity, and (j) a microcavity. (k-n) Corresponding eigenmode profiles: (k) a monopole-like mode and (l) a dipole-like mode in the L3 cavity, (m) in the H0 cavity, and (n) in the microcavity.

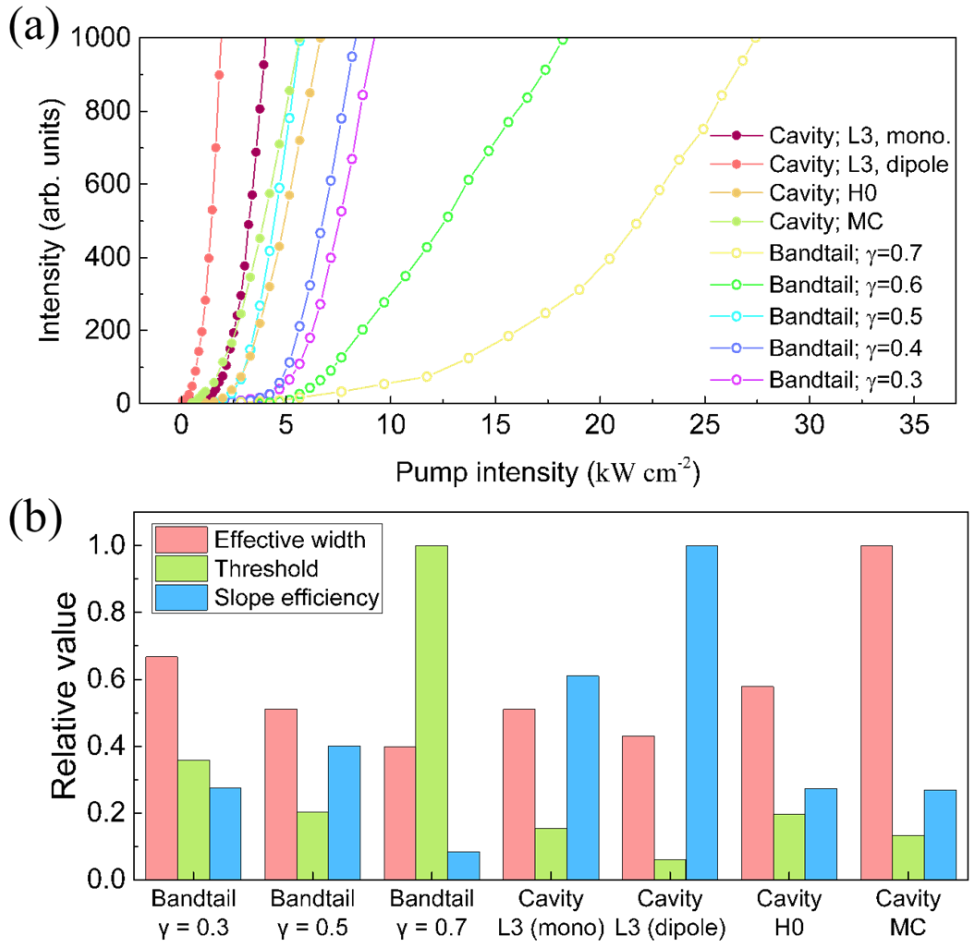

Figure 4-13. Laser performance characteristics of the band-tail laser. (a) Light-in light-out (L-L) characteristic curves of the devices shown in Figure 4-12. The band-tail laser records the best performance at γ = 0.5 with a threshold of 2.5 kW/cm^2. (b) Relative values of an effective width (red), threshold (green), and slope efficiency (blue) recorded for band-tail lasers and cavity lasers. Lasing performances of the band-tail lasers are measured to be comparable order with those of cavity lasers.

4.2.5. Boundary dependence of modal properties

In Section 4.2.2, it is experimentally observed that the lasing starts to cease when the size of the structure becomes smaller than a certain size. In other word, there is a critical device size at which the mode can interact with the boundary, resulting weakened confinement.

To cross-check this phenomenon and to quantify effect of device size, changes of mode properties such as the spectral shift and quality factor are recorded as a function of the normalized side length L/a using the finite-difference time-domain calculations for the same configuration used in experiment. The result shown in Figure 4-14 indicates that the critical size is approximately $L/a \sim 10$. The quality factor and the peak positions of the mode are steady without notable changes until the device size reaches $L/a \sim 10$. However, below this size, both values start to change significantly, which means increasing loss to the interaction with environment outside the device. For this configuration, lasing operation is experimentally confirmed up to the size of $L/a = 8$ where the Q-factor is estimated to be ~1500.

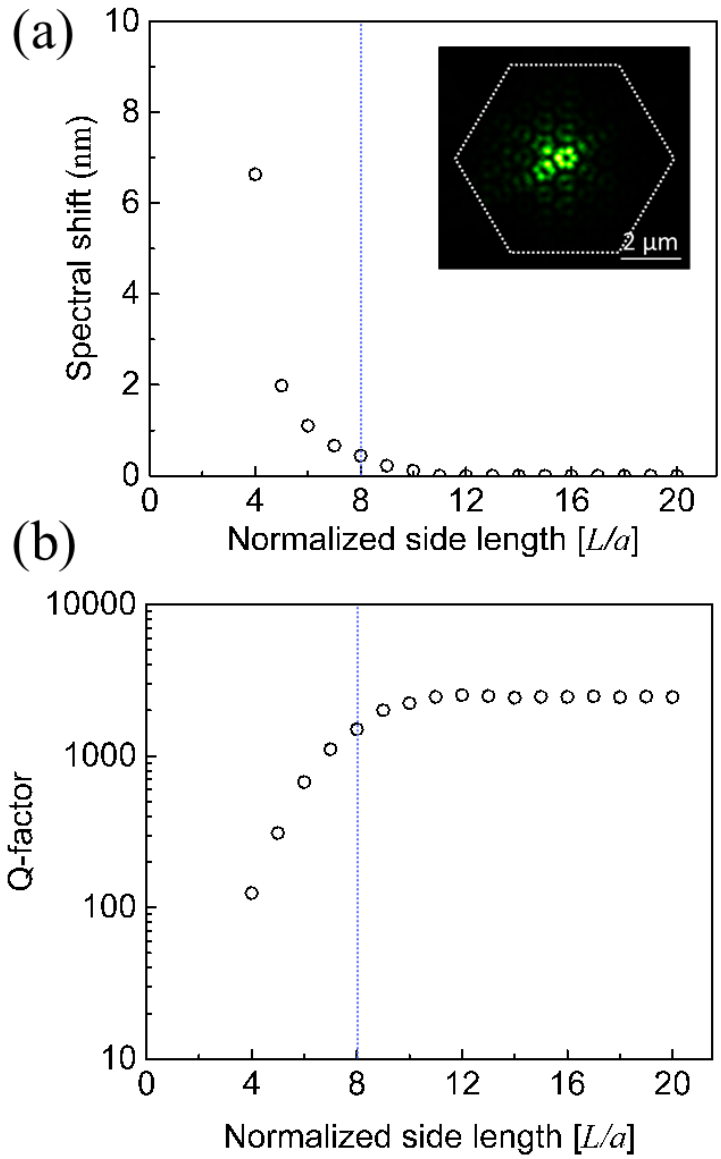

Figure 4-14. Boundary dependence of modal properties. (a) A Change of the peak mode wavelength as a function of a device side length *L* normalized by a lattice constant *a*. Blue dashed line indicates experimentally measured minimum device size that sustains a single-mode laser. (b) A dependence of a Q-factor of the mode as a function of the normalized side length *L*/*a*, displayed in a log-scale.

4.2.6. Dominant loss channel in a band-tail laser

For the given configuration, there is an optimal scattering strength on the lasing performance of a band-tail laser, for example at $\gamma = 0.5$, the experimentally observed value in Section 4.2.4. To understand how the scattering strength affects the threshold, the change of quality factor is recorded for both 3D and 2D structures using the finite-difference time-domain calculations for the same configuration used in experiment, with a hypothesis that two competing loss channels exist in a band-tail laser.

The result is displayed in Figure 4-15. the Q-factor calculated for 3D structure tends to have optimum value, which is a similar behavior with the measured results. However, for 2D calculation where only in-plane geometry is reflected in the model structure, the Q-factor continues to increase without bound. From these results, it is confirmed that the in-plane confinement increases monotonically and is not a limiting factor to the lasing performance. Then, the radiation in vertical direction considered only in 3D calculation becomes a dominant loss channel at higher scattering strength. This reasoning could also explain rapid degradation of lasing performances at $\gamma \geq 0.6$ observed in Section 4.2.4, which is hard to understand with near-field imaging alone because these data suggest better confinement in lateral direction at higher γ.

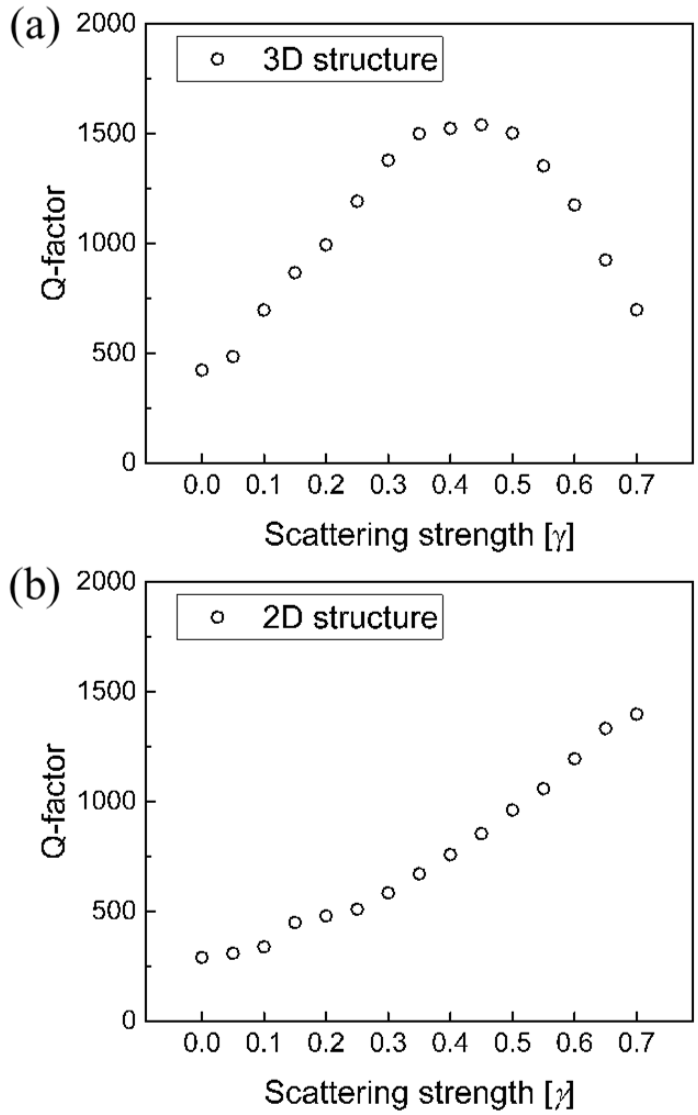

Figure 4-15. Computational evidences for vertical loss of band-tail laser. (a) Change of the Q-factors as a function of scattering strength. Here, the calculation model is a 3D structure that consider the vertical radiation as well as the lateral loss. (b) The same calculations are repeated for the 2D model structure in which effective index approximation are used to collapse 3D structure into effective 2D structure, which makes absolute Q-factor values different from the previous calculations.

4.2.7. Summary

i. The main idea for shaping modal density was to rearrange the configuration and to place the strongly confined mode at the center of a device. In principle, this approach guarantees a single-mode operation and any modal density ranging from the single-mode and that of the original device can be achieved.

ii. To demonstrate the idea, PL responses were measured as a function of the device size. Larger device exhibited statistically predictable rich spectral behavior, and the number of lasing modes gradually decreased according to the device size, leaving only one mode for single-mode operation.

iii. Near-field imaging directly visualized the transition from multi-modes to a single-mode. In the single-mode device, only the Anderson-localized mode was remained at the center of the device although several modes were spread over entire device in larger device.

iv. The lasing performance of band-tail lasers was characterized by comparing with well-known cavity structures. The proposed platform covered wide near-field extents and lasing performances, which were comparable to those of cavity lasers with vast margins for further improvements.

v. To cross-check the existence of a critical device size at which lasing starts to cease, FDTD simulation was employed. The mode properties were steady without notable changes until the device size reaches $L/a \sim 10$ where the loss due to the interaction with environment outside the device overwhelms.

vi. To understand how the scattering strength affects lasing performances, the change of quality factor was calculated for both 3D and 2D structures. From the result, it was confirmed that the dominant loss channel at higher scattering strength is radiation in vertical direction, not lateral confinement.

4.3. Shaping modal properties

4.3.1. Main idea for shaping modal properties: Adjusting basis scattering elements

In this section, the idea for shaping modal properties is developed and precise fine-tuning of modal properties will be demonstrated using the proposed platform. In Chapter 3, it is revealed that the spatial extent of an Anderson-localized mode is determined by the state energy and the scattering strength, and in Section 4.2.2 and Section 4.2.4, it is indeed observed that the wavelength and the spatial extent of lasing mode shift according to the scattering strength. Therefore, it is natural to assume that modal properties such as the state energy and the spatial extents can be shaped as intended using structural parameters.

What is important and necessary is to develop efficient working idea for modal shaping, and to investigate its effects in a systematic methodology. In order for clear studies, it is advantageous to use the device with size of single-mode operation (L/a = 8 for given configuration). Then, the resonant wavelength and the near-field extent of the only remaining mode can be investigated as a function of structural parameters. For this purpose, two structural parameters that control the degrees of freedom in basis scattering elements are managed: the filling factor r_0 and the scattering strength γ, which is systematically defined in Section 2.2.2. Once the effects of these parameters are revealed, modal properties can be shaped to the desired values through the control parameters r_0 and γ. More importantly, the proposed fine-tuning method can be applied to any device with any scatterer configuration because it handles only basis scattering elements.

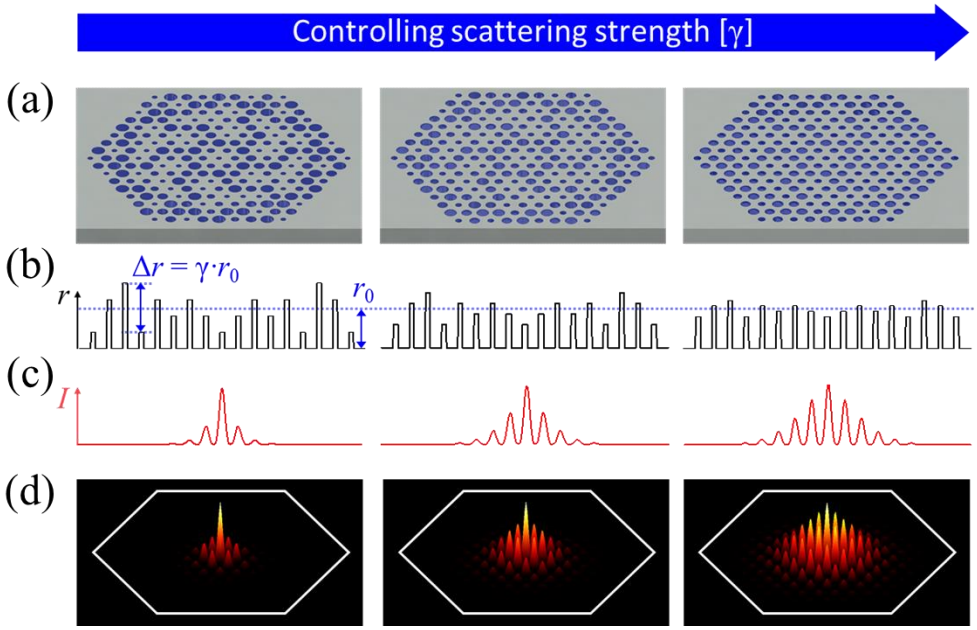

Figure 4-16. Schematics of the idea on shaping modal properties. (a) Illustrations on the successive control of scattering strength with fixed configuration. (b) Line profiles of relative radii of scattering elements (exaggerated in scale for clear visualization), corresponding to the device shown in (a). (c) Line profiles and (d) 2D modal profiles of near-field modal distributions, being adjusted by relative scattering strength among basis scattering elements.

4.3.2. Spectral response: Wide and precise control of lasing modes

To demonstrate the idea for shaping modal properties, the 2D parameter space (r_0, γ) is divided into 20 × 20 grid, ranging $\Delta r_0/a = 0.06$ and $\Delta\gamma = 0.40$, and the spectral responses of all device realized by using structural parameters at each grid site are recorded. The device-size is set to $L/a = 8$ and there are no constraints on the scatterer configuration in order to verify the generality of the proposed fine-tuning method.

The results are shown in Figure 4-17. Of the total of 400 devices, 251 (63% yield) devices lase and can operate in single-mode. For non-lasing devices, the Q-factors of mode are found to be relatively low at the corresponding parameters as described in Section 4.3.4. The spectral shift of the lasing mode is monotonic to both r_0 and γ, which can be directly confirmed from the representative spectra, presented by fixing each of parameters, displayed in Figure 4-18. For these two specific approaches, namely the r_0–varying and γ–varying schemes, experimentally recorded dynamic range is as $\Delta\lambda_{r\text{–varying}} = 64$ nm and $\Delta\lambda_{\gamma\text{–varying}} = 59.5$ nm while the entire 2D space gives $\Delta\lambda = 100.4$ nm for the given configuration.

Therefore, it is experimentally confirmed that the modal energy of a single-mode random laser can be precisely shaped in a range more than $\Delta\lambda \sim 100$ nm by controlling only the basis scattering elements, reserving other factors such as a scatterer configuration, a crystalline structure, and corresponding lattice constant. This is possible because the optical path in a random laser is longer than those of conventional lasers. For the same reason, very stable shaping is possible compared to fabrication tolerances. Furthermore, two kinds of structural parameters of the proposed approach offer extra degree of freedom that can be used for shaping other modal property in addition to the modal energy, which will be clarified in Section 4.3.3.

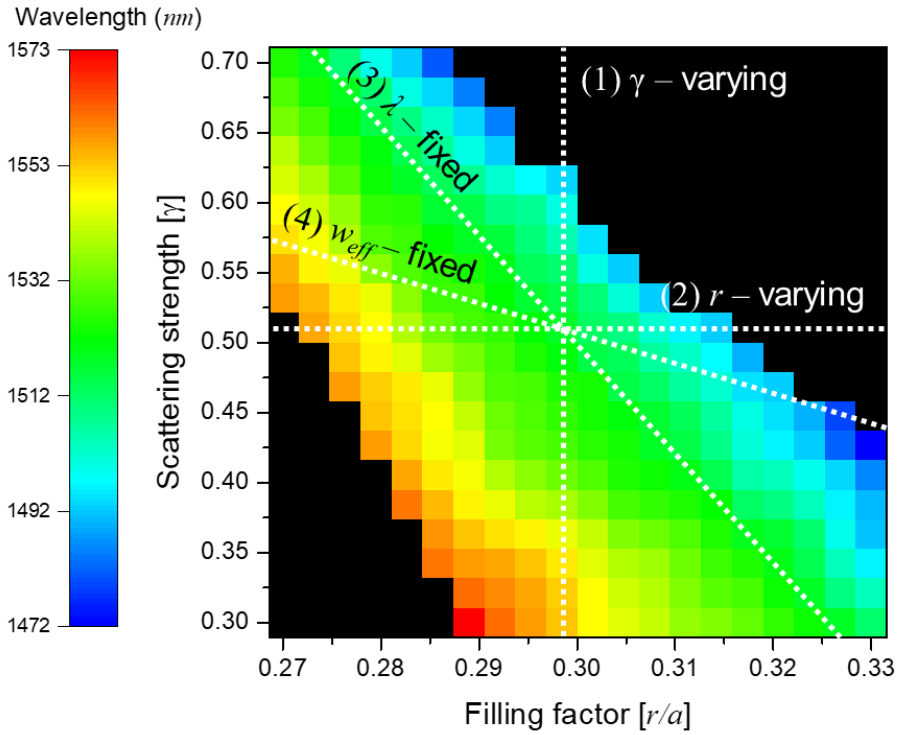

Figure 4-17. Mapping of single-mode lasing wavelength on 2D parameter space. The wavelength of the band-tail laser is measured from devices fabricated with structural parameters of varying filling factor *r*/*a* and scattering strength γ. The entire 2D space offers spectral range of Δλ = 101 nm. White dashed lines indicate representative fine-tuning schemes that so-called 'γ–varying', '*r*–varying', 'λ–fixed', and 'w_{eff}–fixed'.

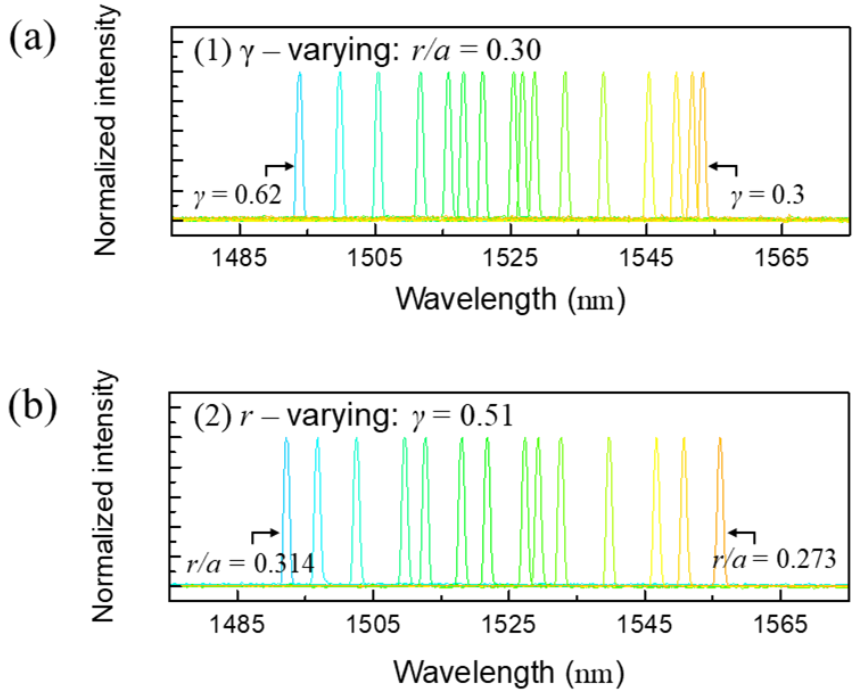

Figure 4-18. Spectral responses of a single-mode band-tail laser. Photoluminescence spectra are measured along (a) γ– and (b) *r*–varying schemes indicated in Figure 4-17. Peak lasing wavelengths are monotonically changed with similar spectral ranges of $\Delta\lambda_{r\text{–varying}}$ = 64 nm and $\Delta\lambda_{\gamma\text{–varying}}$ = 59.5 nm, demonstrating the effects of each parameter.

4.3.3. Degree of freedom in 2D parameter space: Exclusive modal control on both energy and confinement

Extra degree of freedom in 2D parameter space can be used for shaping other modal property in addition to the modal energy. Here, shaping of modal confinement is demonstrated, which is quantified by the effective width w_{eff} defined in Section 3.4.3.

As investigated in Section 4.3.2, the two control parameters r_0 and γ have similar dynamic ranges for the spectral response. However, this may not be the case for the spatial extent. Using this assumption as well as the extra degree of freedom provided by the 2D parameter space, it is possible to control λ and w_{eff} independently. This idea is verified in Figure 4-19, and quantified in Figure 4-20. When the modal properties of devices are measured following the λ–fixed line marked in Figure 4-17, the wavelength is fixed at $\lambda = 1519.0 \pm 1.8$ nm, but the modal extent is monotonically changed by 40% from $w_{\mathrm{eff}} = 2.57$ μm to 1.53 μm. That is, it is possible to control the near-field confinement over a wide range by manipulating only the basis scattering elements. Conversely, when the w_{eff}–fixed line is tracked, the modal extent is maintained at $w_{\mathrm{eff}} = 2.06 \pm 0.12$ μm while the wavelength is shifted by $\Delta\lambda = 70.3$ nm.

Thus, it is confirmed that both the wavelength and the spatial extent of a mode can be precisely shaped in a wide range. Moreover, it should be emphasized that this approach is not also limited to a specific configuration as with the method in Section 4.3.2, because it bases on control of the universal parameters r_0 and γ, which are orthogonal against the configuration. In fact, this generality is confirmed in Section 4.3.5 by simulations over several configurations, including C_6–symmetric one. Therefore, modal properties of a band-tail laser can be generally shaped with the proposed method.

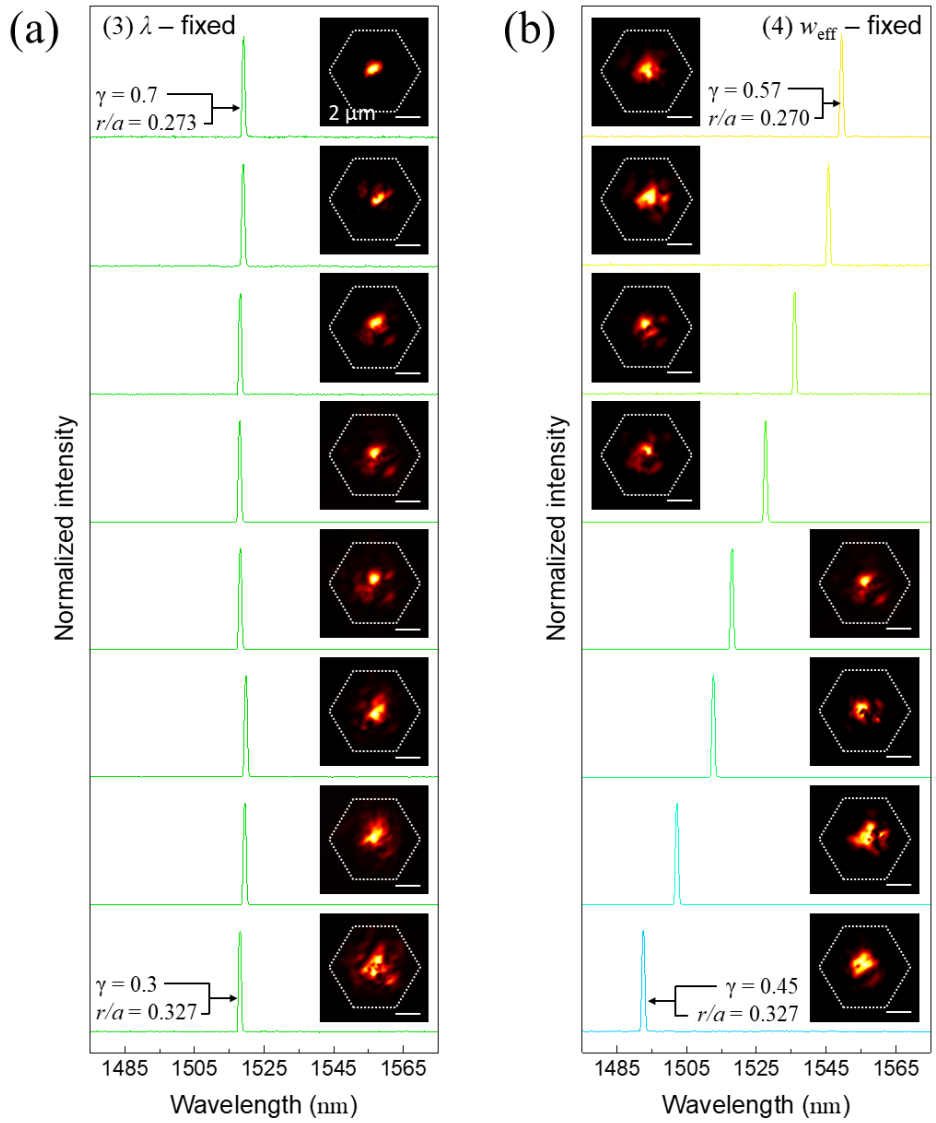

Figure 4-19. Modal properties of a single-mode band-tail laser. Photoluminescence spectra and near-field eigenmode profiles are measured along (a) λ– and (b) w_{eff}–fixed schemes indicated in Figure 4-17. Peak lasing wavelengths (modal area) are stable, but the modal area (peak lasing wavelength) is monotonically changed when λ–fixed scheme (w_{eff}–fixed scheme) is traced.

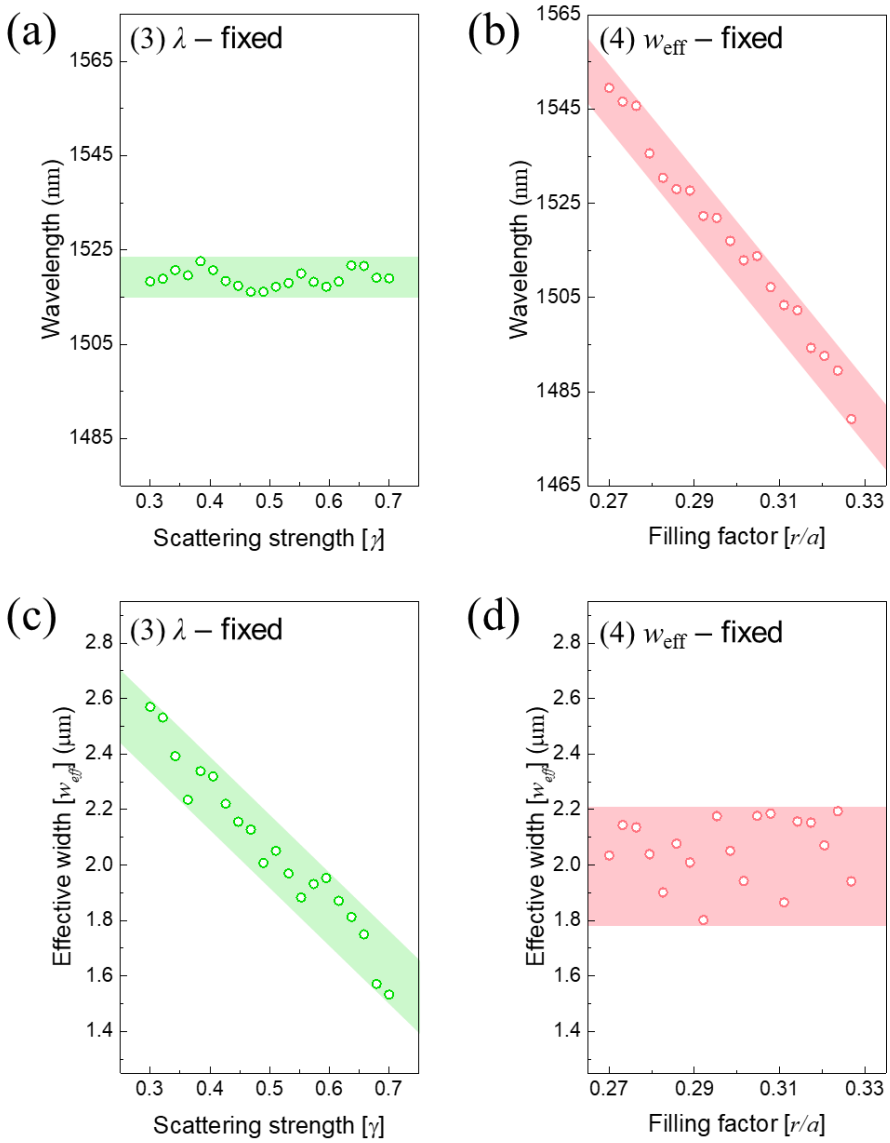

Figure 4-20. Quantification of modal properties of a single-mode band-tail laser. (a-b) Recorded lasing wavelength along (a) λ– and (b) w_{eff}–fixed schemes indicated in Figure 4-17. (c-d) Extracted effective width along (c) λ– and (d) w_{eff}–fixed schemes. The changes in wavelength and effective width are measured to $\Delta\lambda$ = 70.3 nm and $\Delta w/w_0$ = 0.4, respectively.

4.3.4. Computational evidences of measured results

In Section 4.3.2, it is claimed that the Q-factors of mode are relatively low for non-lasing devices. In order to confirm this, the wavelength and the Q-factor of the mode are calculated for 2D fine-tuning parameters of the scattering strength and the filling factor.

The calculation results are displayed in Figure 4-21. Comparing it with the measured result of Figure 4-17 in the Section 4.3.2, it can be recognized that there is a high correspondence between parameter subsets of the relatively low Q-factors in the computation result and the non-lased ones in the measured result. Therefore, the failure of a lasing action may be attributed to the loss of a mode, which increases when both parameters are out of moderate ranges at the same time.

In addition, comparing the simulated data to the measured one, one can see that the experimentally identified λ–fixed line have similar slope with the simulated one in Figure 4-21(a). Furthermore, it is more noteworthy that the w_{eff}–fixed line in the measured result exhibits higher correspondence to the Q-fixed line in Figure 4-21(b) rather than the λ–fixed line in Figure 4-21 (a), which implies that the modal confinement is dependent on the Q-factor.

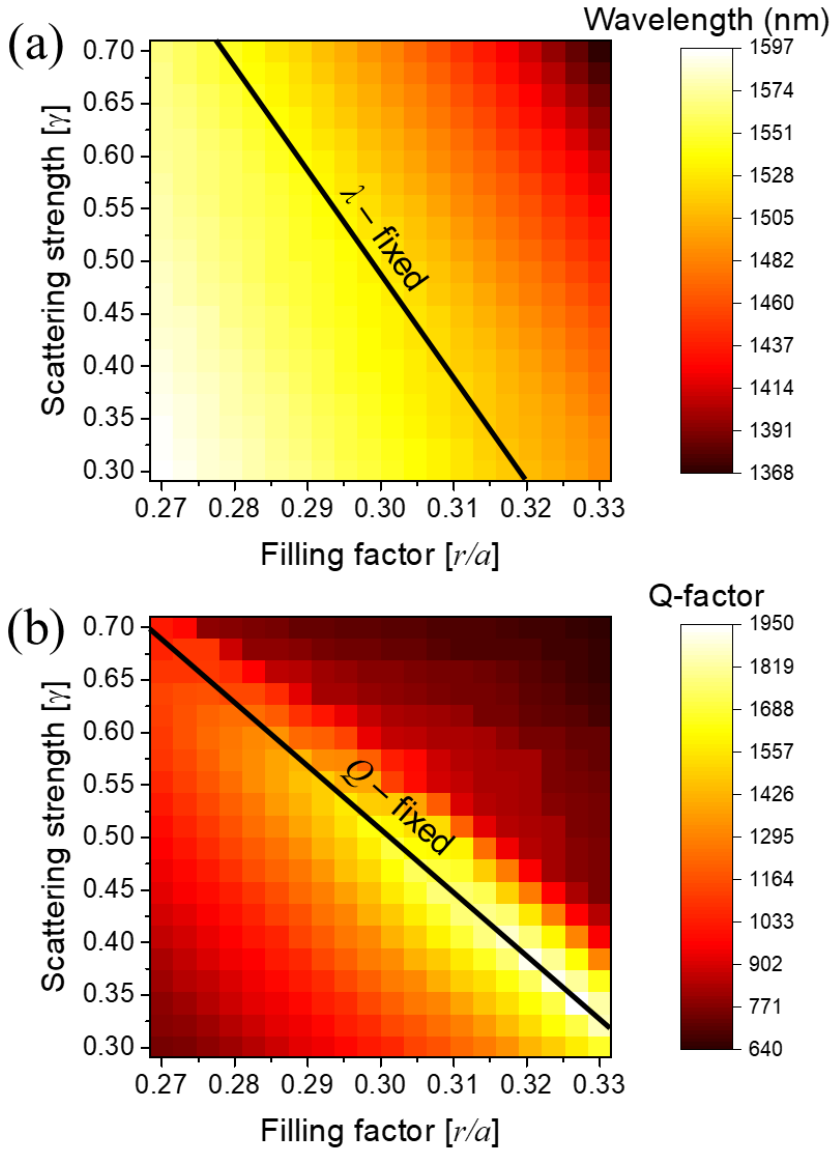

Figure 4-21. Computational mapping of modal properties on 2D fine-tuning parameter space. Mapping of (a) a resonant wavelength and (b) a Q-factor computed over 2D fine-tuning parameter space composed of the filling factor *r*/*a* and the scattering strength γ. The disordered configuration and parameter ranges used in this calculation are the same with those of Figure 4-17.

4.3.5. Computational evidences for the generality

In order to verify the generality of the proposed method for shaping modal properties, the wavelength changes of modes are calculated for several configurations. Figure 4-22 shows the representative results for two configurations, one without constraint and the other with C_6–symmetric constrain. The detailed explanation on the C_6–symmetric constrain can be found in Section 4.4.2.

From the data, computed over 2D fine-tuning parameter space composed of the filling factor r_0 and the scattering strength γ that vary within the same range used in experimental characterizations in Figure 4-17, it is confirmed that spectral responses to these structural parameters are not affected by the specific configuration. Therefore, the proposed method for shaping modal properties is not limited to a specific configuration used in the experiment, and can be generally used for any configuration including the C_6–symmetric case to shape modal properties of a band-tail laser.

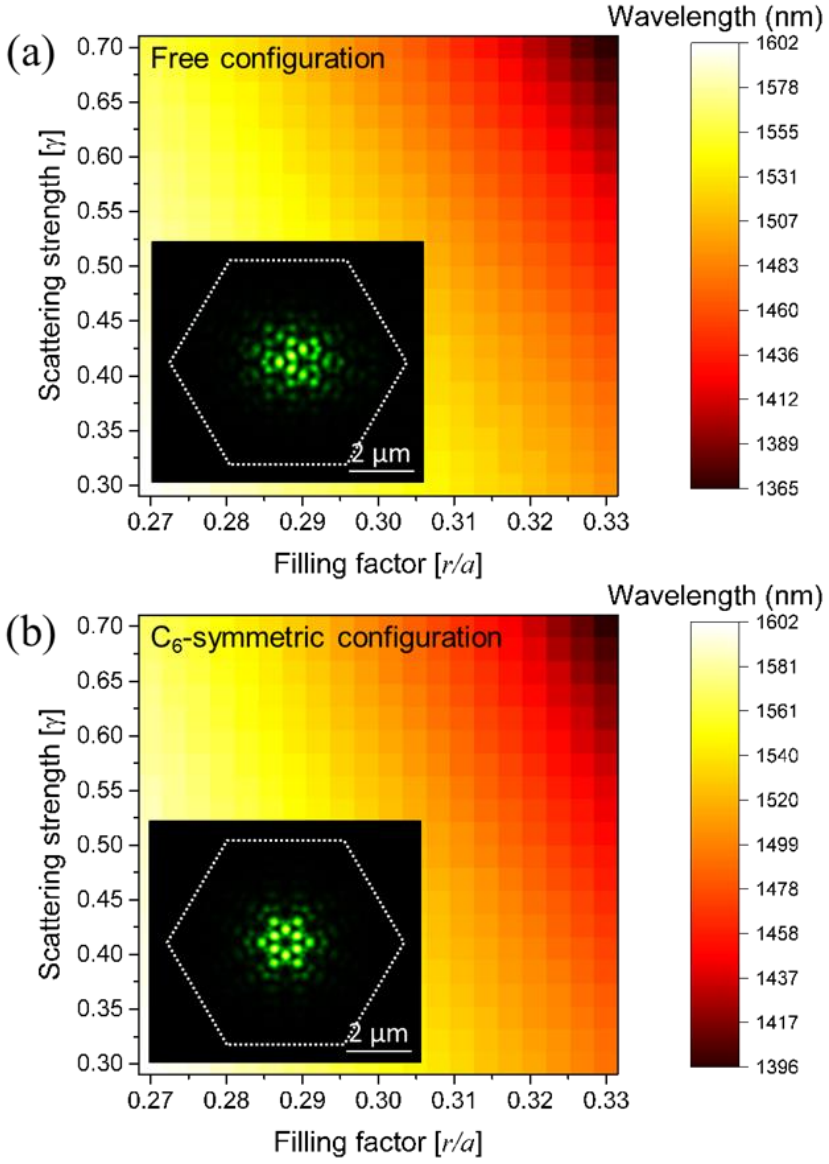

Figure 4-22. Computational mapping of modal properties for several scatterer configurations. Mapping of modal wavelength for configuration (a) without constraint and (b) with C_6–symmetric constraint, computed over 2D fine-tuning parameter space composed of the filling factor *r*/*a* and the scattering strength γ. Insets show simulated $|E|^2$ distribution of corresponding modes.

4.3.6. Summary

i. The idea for shaping modal properties was to use the experimentally observed fact that the spatial extent of an Anderson-localized mode is determined by the state energy and the scattering strength. For this purpose, the degrees of freedom in basis scattering elements were systematically identified.

ii. The spectral responses to the 2D parameter space (r_0, γ) were investigated. The spectral shift of the lasing mode was monotonic to both r_0 and γ, and the overall dynamic range of the platform recorded more than $\Delta\lambda \sim 100$ nm with very stable modulation compared to fabrication tolerances.

iii. Extra degree of freedom in 2D parameter space was used for shaping modal confinement in addition to modal energy. Both w_{eff} and λ were precisely and independently shaped in wide range of $\Delta w_{eff}/w = 0.4$ and $\Delta\lambda = 70.3$ nm along the λ– and w_{eff}–fixed schemes, respectively.

iv. The wavelength and the Q-factor of a mode were calculated for 2D fine-tuning parameter space (r_0, γ) in order to support experimental observations. From the result, the high correspondence between the experiment and the simulation was confirmed.

v. In order to verify the generality of the proposed method for shaping modal properties, the wavelength changes of modes were calculated for several configurations including C_6–symmetric one, and it was confirmed that spectral behavior are not affected by the specific configuration.

4.4. Shaping near-field profiles

4.4.1. Main idea for shaping near-field profiles: Engineering a configuration to place scatterers

The most enormous degree of freedom in the proposed platform is the spatial configuration of all scattering elements over crystalline lattice sites. Using the disordered configuration, the idea for shaping near-field profiles will be proposed and demonstrated in the following sections.

Figure 4-23 illustrates schematic representation of the configuration in a band-tail laser. Each lattice site over a crystalline structure can be any kind of scattering element, which is chosen from a basis set. If the basis set is a quaternary, the total number of realizations is given by $N = 4^n /S$ where n is the total number of independent lattice sites and S is the normalization factor that counts the symmetry. This huge number of possibility can be used for shaping a band-tail laser, especially to engineer near-field profiles. The size of a device is restricted to $L/a = 8$, which seems to be enough for a single-mode operation in most cases, from the experience in Section 4.2. Then, the total number of independent lattice sites and corresponding possible number of realizations become $n = 217$ and $N = 4^{217} \sim 10^{130}$, respectively. Here, the normalization factor S can generally be set to unity because symmetric realizations are not reducible in most applications where multiplexing in the spatial degree of freedom is important.

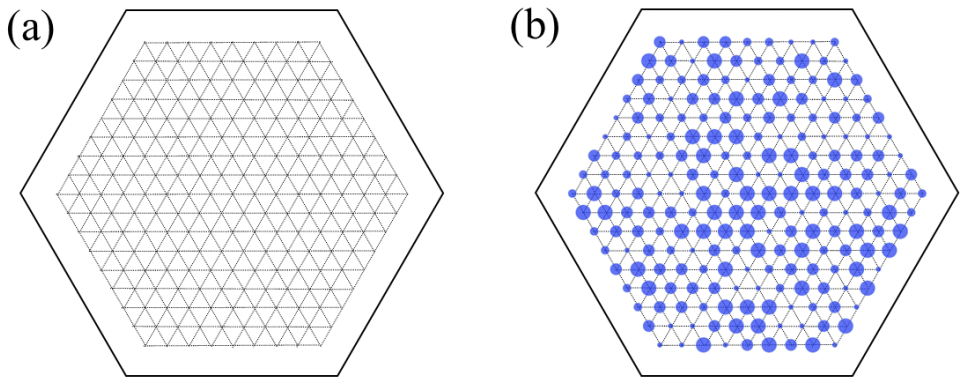

Figure 4-23. Schematics of the degree of freedom of a disordered configuration. (a) A representation of the lattice sites consisting a band-tail laser with a size of L/a = 8. The total number of independent lattice sites is n = 217. (b) An illustration of one possible realization of disordered configurations with quaternary basis. The total number of realizations is given by 4^n.

4.4.2. C_6–symmetric configuration for symmetric profiles

In this thesis, only a fraction of the enormous degrees of freedom associated with the configuration is studied as a proof-of-concept demonstration. The scope is restricted to the C_6–symmetric configuration (*i.e.* with a 6-fold rotational symmetry), which is schematically illustrated in Figure 4-24. Then, the number of independent lattice sites is reduced to n = 37, and corresponding number of possible realization is given by N = $4^{37} \sim 10^{22}$ where the normalization factor S is again set to unity due to the C_6–symmetric constraint. Although the number of possible realization is significantly lessened compared to the case without constraint, N ~ 10^{22} is still a plenty number for shaping band-tail lasers. In addition, a near-field shape for the configuration with C_6–symmetric constraint should also have the C_6–symmetry, which consequently makes it easy to understand the relationship between the configuration and corresponding modal profiles.

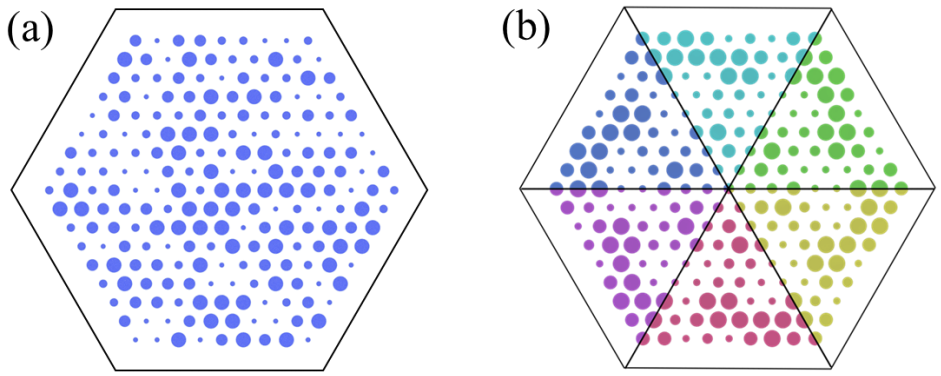

Figure 4-24. Schematics of the degree of freedom of a C_6–symmetric disordered configuration. (a) An illustration of one possible realization of completely random configurations. The number of independent lattice sites is n = 217. (b) One realization of C_6–symmetric disordered configuration designed to have 6-fold rotational symmetry. The number of independent lattice sites is reduced to n = 37 in this case.

4.4.3. Spectro-spatial response: Rough tuning with configuration

In the pool of configurations made by random number generations, configurations in which mode exhibits high Q-factors are carefully chosen for realizations. A total of 150 devices are fabricated and 126 samples (84% yield) become a single-mode laser. For each realization, the emission wavelength and the spatial extent of the near-field are measured to characterize the effect of configuration on modal properties where the latter is quantified by the effective width w_{eff}.

The results are shown in Figure 4-25. The modal properties are distributed in a range of $\Delta\lambda$ = 66 nm (1483 nm to 1549 nm) and Δw_{eff} = 2.01 μm (3.33 μm to 1.32 μm) with respect to the C_6-symmetric configurations. In particular, it is possible to monotonically shape the modal extent while fixing the wavelength (or vice-versa) as presented in Figure 4-26. For these configurations, modes have the same resonant

wavelength of $\lambda = 1515 \pm 1.1$ nm, but the near-field extent is changed 2.39 times from w_{eff} = 1.32 μm to 3.16 μm where only 3 lattices (w_{eff}/a = 2.93) is occupied with strongly localized profile at the maximum confinement. At the other extreme case, however, it is in the weak localization regime. Thus, it is possible to control modal properties in a wide range including both weak and strong regime by manipulating only the configuration while fixing other factors, which might be useful to sketch modal properties before applying fine-tuning method proposed in Section 4.3.

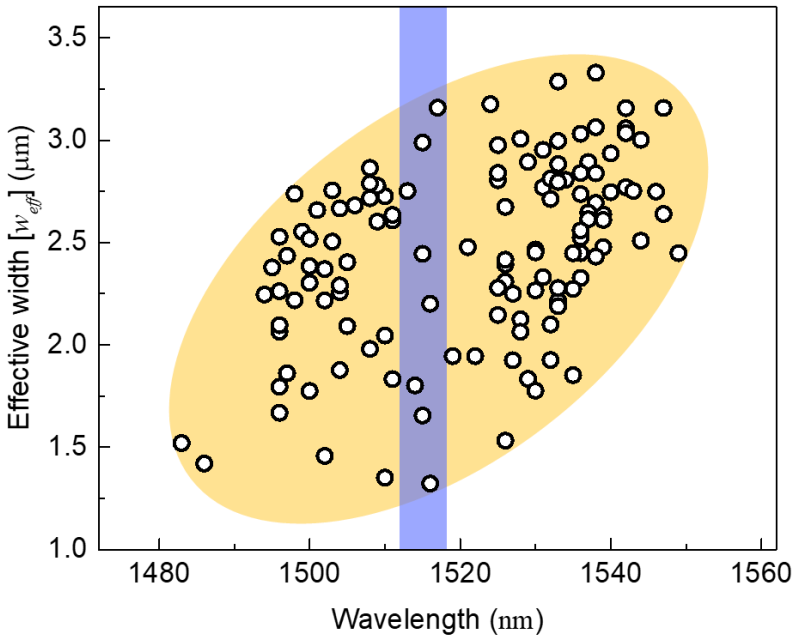

Figure 4-25. Mapping of modal properties with respect to the degree of freedom of C_6–symmetric configuration. Lasing wavelengths and effective widths are measured for devices with varying configurations, but without adjusting any other parameters. The overall dynamic range is measured to $\Delta\lambda$ = 66 nm and Δw_{eff} = 2.01 μm.

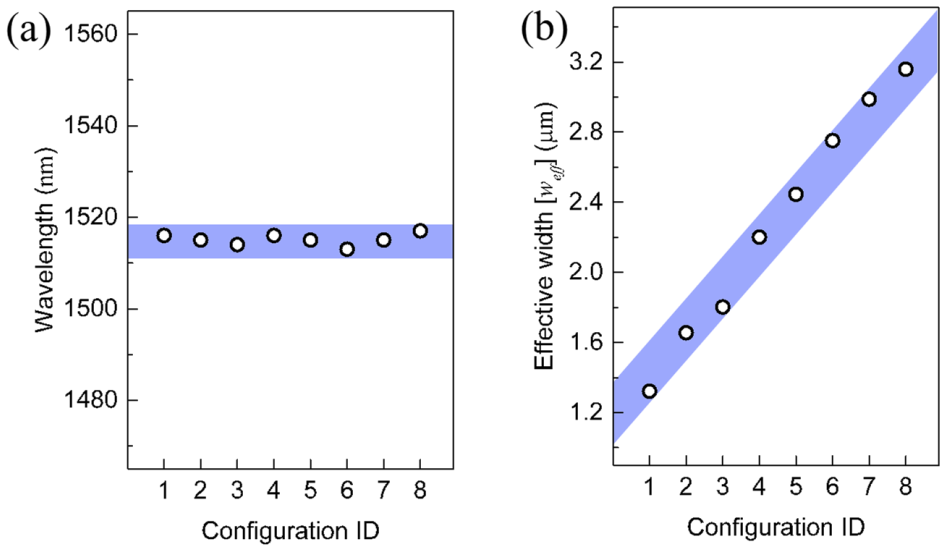

Figure 4-26. Modal properties with respect to the degree of freedom C_6–symmetric configuration. (a) Lasing wavelengths and (b) effective widths are measured for devices of configurations in blue-shaded region in Figure 4-25. The lasing wavelength is fixed but the effective width is modulated 2.39 times, demonstrating 'λ–fixed and w_{eff}–varying scheme' by the configuration.

4.4.4. Near-field shaping: From fundamental to high-order shapes

In addition to the control of modal properties, shaping of near-field patterns are also demonstrated using configurations as displayed in Figure 4-27. Here, unique near-field distributions similar to a ring shape are found in some configuration 4 and 5. The presence of 'zeros' in the light field implies that the lasing mode has an orbital angular momentum [2]. Actually, eigenstates with orbital angular momentum are found in Section 4.4.5 using numerical simulations, whose radius is varying from 0.80 μm to 1.73 μm. Furthermore, interesting high-order patterns such as roses and starfish shapes are realized in configuration 6-8, and spiral patterns of confined light are numerically identified in Section 4.4.5.

These observations suggest that the degree of freedom of random configuration can be wisely used to spatially shape the near-field distribution with sub-wavelength resolution although demonstrations in this section is at the level of proof-of-concept that randomly searches and finds desired modes by a chance. For practical applications, it is necessary to study the causality between the configuration and the near-field distribution in more depth, and also to develop efficient methods for generating arbitrary near-field shapes. Recent advances in computational optics, such as size-dependent phase delay [148], pixelated searching [149], or inverse design [150], originally developed for passive photonic devices, can elucidate feasible algorithms for active devices as well which are functionalized by multiple scattering mechanism. Once these premises are built, the proposed platform could incorporate and expand the currently known lasing platforms for more unlimited range of near-field patterns and confinements. Furthermore, the proposed approach has vast margins to realize more sophisticated near-field shaping and the more advanced devices having non-trivial near-field profiles such as angular momentum [151, 152], topological solitons [153, 154], optical Lissajous [155], or even any arbitrary shapes could be realized by improving current idea toward a pixelated scheme that freely adjusts scattering strength at each lattice site of crystalline structure to achieve desirable near-field shapes.

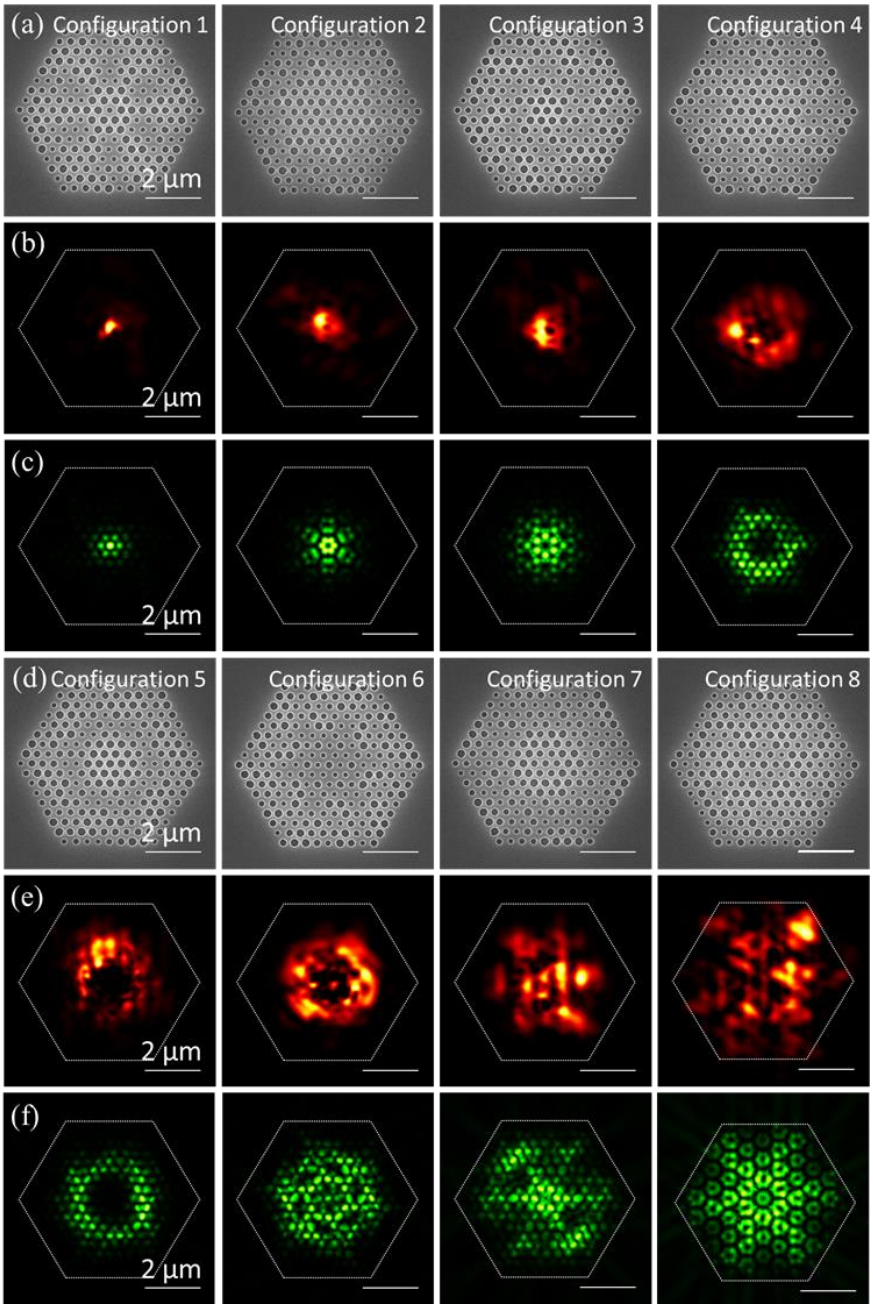

Figure 4-27. Near-field shaping of band-tail lasers for several configurations. (a,d) Scanning electron microscopy images of fabricated samples with configurations shown in Figure 4-26. (b,e) Measured near-field eigenmode profiles and (c,f) simulated near-field distributions corresponding to the device in (a, d).

4.4.5. Orbital angular momentum and spiral pattern of confined light

As stated in Section 4.4.4, it is possible to computationally generate modes having orbital angular momentum with the aid of C_6-symmetric configurations. Figure 4-28 visualizes the intensity distributions and the vector fields of the modes calculated by the FDTD-based method. From these data, it is confirmed that the modes have standing wave profiles produced by a superposition of propagating waves revolving around the center of structures in the clockwise and counter-clockwise directions. The modes have various radii ranging from a minimum of 0.80 μm to a maximum of 1.73 μm depending on the details of the configurations.

In addition, it is possible to produce modes with spiral patterns using the C_6-symmetric configurations. Figure 4-29 presents the intensity distributions and the vector fields of these modes calculated by FDTD simulations. From these data, it is confirmed that the wavevector of modes are spiral along the radial direction forming standing wave profiles produced by a superposition of propagating and counter-propagating waves. The modes exhibit clear spiral patterns whose degrees and direction of twisting depend on the details of the configurations.

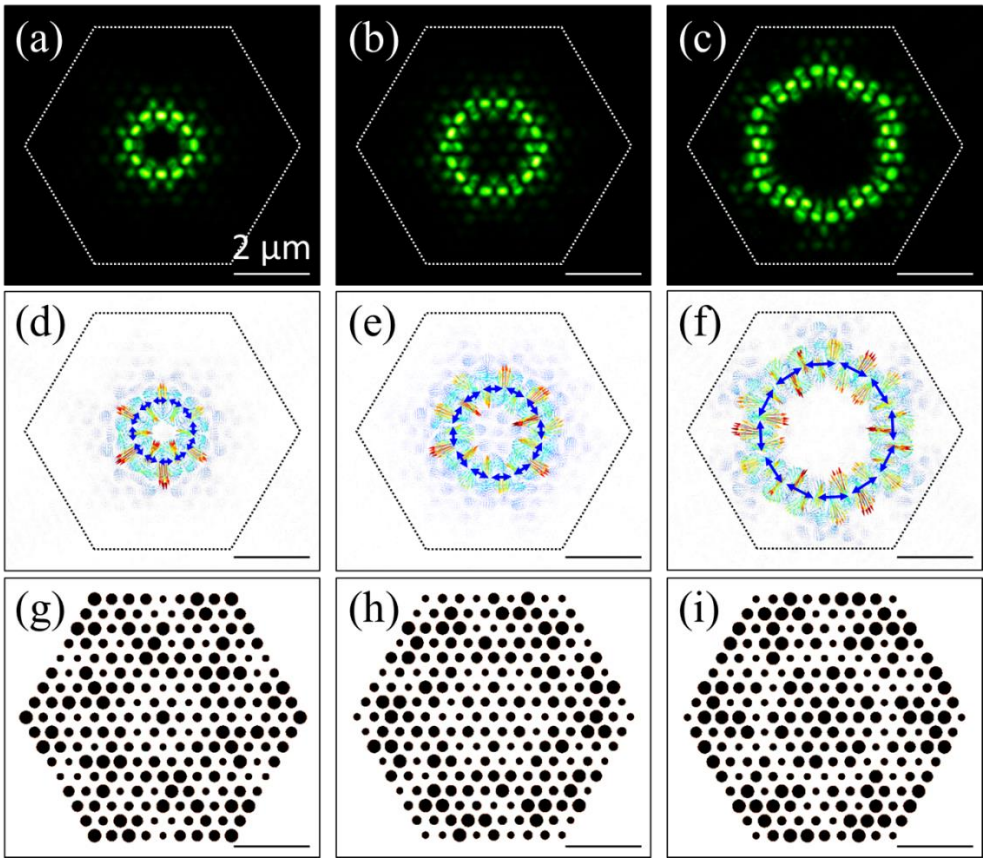

Figure 4-28. Computational evidences of orbital angular momentum. (a-c) Representative $|E|^2$ profiles calculated for band-tail states, exhibiting orbital angular momentum with several radii: (a) 0.80, (b) 1.26, and (c) 1.73 μm. (d-f) Vector mappings of the *E*-field. Blue arrows indicate wavevectors deduced from the phase information of the *E*-field. (g-i) Visualizations of corresponding configurations.

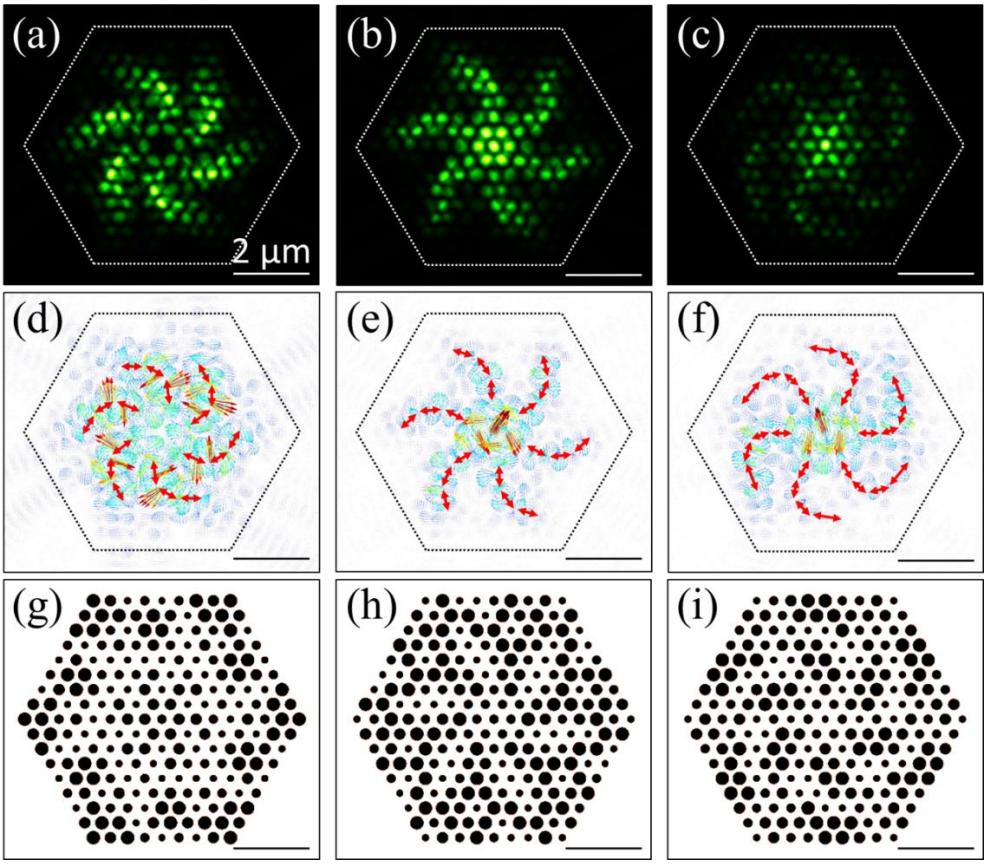

Figure 4-29. Computational evidences of spiral patterns. (a-c) Representative $|E|^2$ profiles calculated for band-tail states, exhibiting spiral patterns with several degrees of twisting. (d-f) Vector mappings of the *E*-field. Red arrows indicate wavevectors deduced from phase information. (g-i) Visualizations of corresponding configurations.

4.4.6. Summary

i. The most enormous degree of freedom in the proposed platform is the spatial configuration of all scattering elements over crystalline lattice sites, which is amount to $N \sim 10^{130}$ for a single-mode band-tail laser. Using the disordered configuration, shaping of near-field profiles was demonstrated.

ii. In this thesis, only a fraction of the configuration was studied as a proof-of-concept demonstration by restricting the scope to the C_6–symmetric configuration. Then, the number of possible realization was reduced to N ~ 10^{22}, and corresponding near-field shapes should have the C_6–symmetry.

iii. With respect to the C_6-symmetric configurations, the modal properties were distributed in a range of $\Delta\lambda$ = 66 nm (1483 nm to 1549 nm) and Δw_{eff} = 2.01 μm (3.33 μm to 1.32 μm). In particular, it was possible to monotonically shape the modal extent while fixing the wavelength (or vice-versa).

iv. In addition to the control of modal properties, shaping of near-field patterns were also demonstrated including interesting high-order patterns. These observations suggested that the degree of freedom of random configuration can be wisely used to spatially shape near-field distribution with sub-wavelength resolution.

v. It was possible to computationally generate modes having orbital angular momentum with the aid of C_6-symmetric configurations, which have standing wave profiles produced by a superposition of propagating waves revolving around in the clockwise and counter-clockwise directions.

vi. Spiral patterns using the C_6-symmetric configurations were also produced in FDTD simulations. The wavevector of modes were spiral along the radial direction and the mode exhibited clear spiral patterns whose degrees and direction of twisting depend on the details of the configurations.

4.5. Conclusion

The ideas for shaping a band-tail laser using structural degrees of freedom were proposed and control over modal densities, modal properties, and near-field profiles were demonstrated, which could incorporate and expand the currently known lasing platforms for more sophisticated modal shaping and advanced devices.

Random lasers have been characterized by unpredictable complex behavior in broadband spectra where, unlike a regular laser, optical modes are formed in a mirror-free way. Especially for a random laser with coherent feedback, discrete lasing modes can be observed due to the recurrent resonances. A major objective in this field is to control shapes of emitting light, and many innovative techniques have been developed to modulate spectral and spatial properties of random lasers using temperature, external fields, or pumping profiles as a control parameter. Most of developed shaping methods have fundamental limitations that it requires additional external control factors. Recent approaches, however, have begun to directly manipulate a random configuration by carefully engineering the density and distribution of scattering elements. The band-tail laser is a special class of random lasers, where a resonant mode of the lasing action is the band-tail state, an eigenmode in the photonic crystal alloy. The proposed lasing platform could be a great candidate for light shaping within a membrane with clever idea and careful engineering. In this chapter, several ideas for shaping modal density, modal property, and near-field profile, which can be applied to any device with specific modal shapes, was proposed and demonstrated using only internal structural degrees of freedom of the proposed platform.

The main idea for shaping modal density was to rearrange the configuration and to place the strongly confined mode at the center of a device. In principle, this

approach guarantees a single-mode operation and any modal density ranging from the single-mode and that of the original device can be achieved. To demonstrate the idea, photoluminescence responses were measured as a function of the device size. Larger device exhibited statistically predictable rich spectral behavior, and the number of lasing modes gradually decreased according to the device size, leaving only one mode for single-mode operation. Near-field imaging directly visualized the transition from multi-modes to a single-mode. In the single-mode device, only the Anderson-localized mode was remained at the center of the device although several modes were spread over entire device in larger device. The lasing performance of band-tail lasers was then characterized by comparing with well-known cavity structures. The proposed platform covered wide near-field extents and lasing performances, which were comparable to those of cavity lasers, with vast margins for further improvements. To cross-check the existence of a critical device size at which lasing starts to cease, FDTD simulation was employed. The mode properties were steady without notable changes until the device size reaches $L/a \sim 10$ where the loss due to the interaction with environment outside the device overwhelms. To understand how the scattering strength affects lasing performances, the change of quality factor was calculated for both 3D and 2D structures. From the result, it was confirmed that the dominant loss channel at higher scattering strength is radiation in vertical direction, not a lateral confinement.

The idea for shaping modal properties was to use the experimentally observed fact that the spatial extent of an Anderson-localized mode is determined by the state energy and the scattering strength. For this purpose, the degrees of freedom in basis scattering elements were systematically identified and corresponding spectral responses to the 2D parameter space (r_0, γ) were investigated. The spectral shift of the lasing mode was monotonic to both r_0 and γ, and the overall dynamic range of the

platform recorded more than $\Delta\lambda \sim 100$ nm with very stable modulation compared to fabrication tolerances. Extra degree of freedom in 2D parameter space was used for shaping modal confinement in addition to modal energy. Both w_{eff} and λ were precisely and independently shaped in wide range of $\Delta w_{\mathrm{eff}}/w = 0.4$ and $\Delta\lambda = 70.3$ nm along the λ– and w_{eff}–fixed schemes, respectively. The wavelength and the Q-factor of a mode were calculated for 2D fine-tuning parameter space (r_0, γ) in order to support experimental observations. From the result, the high correspondence between the experiment and the simulation was confirmed. In order to verify the generality of the proposed method for shaping modal properties, the wavelength changes of modes were calculated for several configurations including C_6–symmetric one, and it was confirmed that spectral behavior are not affected by the specific configuration.

The most enormous degree of freedom in the proposed platform is the spatial configuration of all scattering elements over crystalline lattice sites, which is amount to $N \sim 10^{130}$ for a single-mode band-tail laser. Using the disordered configuration, shaping of near-field profiles was demonstrated. In this thesis, only a fraction of the configuration was studied as a proof-of-concept demonstration by restricting the scope to the C_6–symmetric configuration. Then, the number of possible realization was reduced to $N \sim 10^{22}$, and corresponding near-field shapes should have the C_6–symmetry. With respect to the C_6-symmetric configurations, the modal properties were distributed in a range of $\Delta\lambda = 66$ nm (1483 nm to 1549 nm) and $\Delta w_{\mathrm{eff}} = 2.01$ μm (3.33 μm to 1.32 μm). In particular, it was possible to monotonically shape the modal extent while fixing the wavelength (or vice-versa). In addition to the control of modal properties, shaping of near-field patterns were also demonstrated including interesting high-order patterns. These observations suggested that the degree of freedom of random configuration can be wisely used to spatially shape near-field distribution with sub-wavelength resolution. Furthermore, it was possible to

computationally generate modes having orbital angular momentum with the aid of C_6-symmetric configurations, which have standing wave profiles produced by a superposition of propagating waves revolving around in the clockwise and counter-clockwise directions. Likewise, spiral patterns using the C_6-symmetric configurations were also produced in FDTD simulations. The wavevector of modes were spiral along the radial direction and the mode exhibited clear spiral patterns whose degrees and direction of twisting depend on the details of the configurations.

Chapter 5 – Conclusion and outlook

In this thesis, the concept of a photonic crystal alloy was proposed as an ideal platform for shaping light within a membrane. Strongly scattering elements arranged in a manner that preserves the crystalline symmetry could provide enormous degrees of freedom, which is sufficient to overcome fundamental limitations of existing light shaping platforms as well as to realize advanced optical functions on chip-scale including the spin-orbit interaction of confined light.

The eigenmodes of the proposed platform has been identified as the photonic band-tail states, and their optical properties are highly reproducible, predictable, and tailor-designable over a wide spectro-spatial range that includes the complete band-gap and the entire structure, which is a great advantage for light shaping. The penetration depth from the band-edge increases exponentially with respect to the disorder strength and the modal extent varies monotonically as a function of both the state energy and the disorder strength, occupying only a few lattices for the strongly localized state or the entire structure for the weakly localized state.

Furthermore, these comprehensive pictures of the localization transition in the band-tail states has been established by the exclusive studies on lasing modes by suppressing any undesired mode, but observing only the localized eigenstate of the proposed platform, which is distinguished by the high quality factor inherent to the localized nature. Such a clean environment provides a strong experimental foundation that accelerates our understandings on disordered systems for not only the underlying mechanism of multiple scattering in Anderson localization, but also a progressive development of light shaping devices.

Based on these powerful knowledges, light shaping within a membrane has been demonstrated by developing a band-tail laser, which exploits the photonic band-tail state of the proposed platform as a resonant mode for lasing. Several ideas for shaping modal density, modal property, and near-field profile of band-tail lasers have been proposed and successfully demonstrated by directly accessing and engineering only the internal structural degrees of freedoms, and thus, reserving other external knobs such as strain, temperature, pumping profile, and field gating for more sophisticated functionalities and device applications.

The band-tail laser, a conceptually novel random lasing platform, can operate in single-mode and their modal properties such as resonant wavelength, modal extent, and near-field distribution are highly engineerable in natural and reproducible ways that can be applied to any device with arbitrary modal shapes. The performance of a band-tail laser is comparable to those of cavity lasers in terms of threshold, slope efficiency, and near-field confinement. Several near-field shapes including interesting high-order shapes are realized as concept-of-proof demonstrations and computational evidences for angular momentum and spiral patterns are presented as well.

The engineering of the structural degrees of freedom in a band-tail laser is much more intuitive and effective than any disordered platform, and the controllability of corresponding optical properties far exceeds any existing laser. Therefore, it could incorporate the currently known small library of lasing platform and even expand its boundary by using random systems. More importantly, the proposed method has vast margins to realize more elaborate light shaping and non-trivial near-field shapes, and thus, to handle complex spatio-temporal dynamics required for next-generation photonic functionalities.

For practical applications, however, the proposed platform should be further investigated to understand the causality between the configuration and the near-field distribution in more depth. More specifically, it is necessary to develop efficient methods for generating on-demand near-field shapes, which is the long-sought primary objective of light shaping.

Recent advances in computational optics, such as size-dependent phase delay [148], pixelated searching [149], or inverse design [150] could be modified to provide feasible algorithms for photonic crystal alloy platforms as well. However, bearing in mind that the underlying shaping mechanism is the multiple scattering whose strength is manipulated in a pixelated scheme at each lattice site over the crystalline structure, it is better to pursue a more intuitive and physical approach that inevitably requires understanding of the shaping mechanism. The development process is probably slower and even more demanding than current brutal mapping and solving methods, but the methodology of modern computer science, represented by machine learning [156], will boost this process beyond what can be imagined. If the process is sufficiently progressed to predict resulting shapes with practical accuracy, its individual application to the real world will be far more fast, efficient and even robust, bringing the singularity of photonic technologies.

Once such an advanced shaping method is ready, it is time to begin serious study on the light-matter interaction mediated by confined light. Figure 5-1 illustrates only notable ones such as observing chiral propagation using the spin-momentum locking, generating orbital angular momentum in one direction, and manipulating particles by near-field of the band-tail state. These subjects are not only interesting in fundamental aspect, but also valuable assets to realize elaborate optical functions on chip-scale.

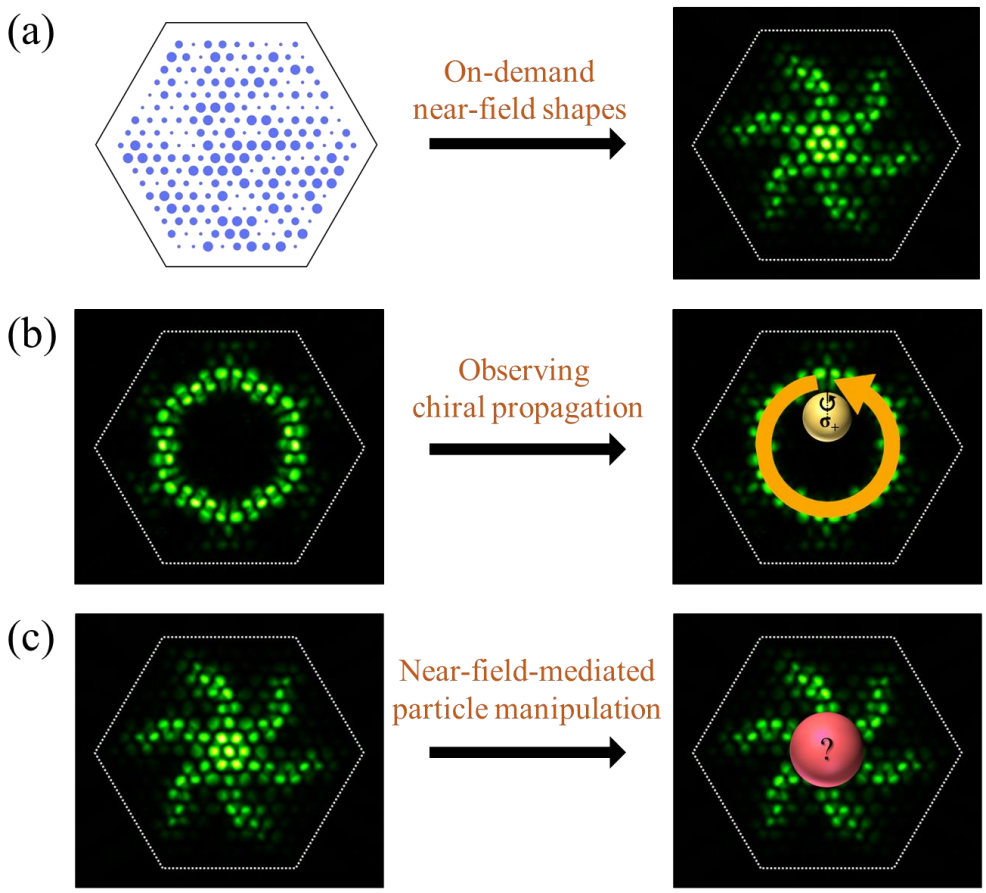

Figure 5-1. Conceptual illustration of topics for further study. (a) Generation of on-demand near-field profiles. The vast degrees of freedom of disordered configuration can be wisely used to produce arbitrary on-demand eigenmode profiles. (b) Observation of the chiral propagation. The orbital angular momentum propagating in one direction can be excited and observed by using the spin-momentum locking of confined fields. (c) Particle manipulation mediated by a near-fields of the band-tail state. The light-matter interaction between a particle and band-tail state, mediated by near-fields with non-trivial shapes, can be used for efficient on-chip manipulation of matters.

References

[1] J. I. Cirac and H. J. Kimble, "Quantum optics, what next?," *Nature Photon.,* vol. 11, 18-20, 2017.

[2] K. Dholakia and T. Čižmár, "Shaping the future of manipulation," *Nature Photon.,* vol. 5, 335-342, 2011.

[3] K. Uhrig, R. Kurre, C. Schmitz, J. E. Curtis, T. Haraszti, A. E. M. Clemen and J. P. Spatz, "Optical force sensor array in a microfluidic device based on holographic optical tweezers," *Lab Chip,* vol. 9, 661-668, 2009.

[4] N. Ji, D. E. Milkie and E. Betzig, "Adaptive optics via pupil segmentation for high-resolution imaging in biological tissues," *Nature Meth.,* vol. 7, 141-147, 2010.

[5] M. Gu, X. Li and Y. Cao, "Optical storage arrays: a perspective for future big data storage," *Light Sci. Appl.,* vol. 3, e177, 2014.

[6] J. P. Torres, "Optical communications: Multiplexing twisted light," *Nature Photon.,* vol. 6, 420-422, 2012.

[7] L. Sapienza, H. Thyrrestrup, S. Stobbe, P. D. Garcia, S. Smolka and P. Lodahl, "Cavity quantum electrodynamics with Anderson-localized modes," *Science,* vol. 327, 1352-1355, 2010.

[8] V. Parigi, V. D'Ambrosio, C. Arnold, L. Marrucci, F. Sciarrino and J. Laurat, "Storage and retrieval of vector beams of light in a multiple-degree-of-freedom quantum memory," *Nature Commun.,* vol. 6, 7706, 2015.

[9] F. M. Dickey, "Laser beam shaping: theory and techniques," *CRC press,* 2014.

[10] D. J. McCabe, A. Tajalli, D. R. Austin, P. Bondareff, I. A. Walmsley, S. Gigan and B. Chatel, "Spatio-temporal focusing of an ultrafast pulse through a multiply scattering medium," *Nature Commun.,* vol. 2, 447, 2011.

[11] L. H. Nicholls, F. J. Rodríguez-Fortuño, M. E. Nasir, R. M. Córdova-Castro, N. Olivier, G. A. Wurtz and A. V. Zayats, "Ultrafast synthesis and switching of light polarization in nonlinear anisotropic metamaterials," *Nature Photon.,* vol. 11, 628-633, 2017.

[12] M. Nixon, O. Katz, E. Small, Y. Bromberg, A. A. Friesem, Y. Silberberg and N. Davidson, "Real-time wavefront shaping through scattering media by all-optical feedback," *Nature Photon.,* vol. 7, 919-924, 2013.

[13] D. Naidoo, F. S. Roux, A. Douley, I. Litvin, B. Piccirillo, L. Marrucci and A. Forbes, "Controlled generation of higher-order Poincaré sphere beams from a laser," *Nature Photon.,* vol. 10, 327-332, 2016.

[14] S. Noda, M. Fujita and T. Asano, "Spontaneous-emission control by photonic crystals and nanocavities," *Nature Photon.,* vol. 1, 449-458, 2007.

[15] I. Staude and J. Schilling, "Metamaterial-inspired silicon nanophotonics," *Nature Photon.,* vol. 11, 274-284, 2017.

[16] L. Lu, J. D. Joannopoulos and M. Soljačić, "Topological photonics," *Nature Photon.,* vol. 8, 821-829, 2014.

[17] A. Aiello, P. Banzer, M. Neugebauer and G. Leuchs, "From transverse angular momentum to photonic wheels," *Nature Photon.,* vol. 9, 789-795, 2015.

[18] P. Lodahl, S. Mahmoodian, S. Stobbe, A. Rauschenbeutel, P. Schneeweiss, J. Volz, H. Pichler and P. Zoller, "Chiral quantum optics," *Nature,* vol. 541, 473-480, 2017.

[19] I. Söllner, S. Mahmoodian, S. L. Hansen, L. Midolo, A. Javadi, G. Kiršanskė, T. Pregnolato, H. El-Ella, E. H. Lee, J. D. Song, S. Stobbe and P. Lodahl, "Deterministic photon–emitter coupling in chiral photonic circuits," *Nature Nanotech.,* vol. 10, 775-778, 2015.

[20] K. Y. Bliokh, F. J. Rodríguez-Fortuño, F. Nori and A. V. Zayats, "Spin–orbit interactions of light," *Nature Photon.,* vol. 9, 796-808, 2015.

[21] A. Soumyanarayanan, N. Reyren, A. Fert and C. Panagopoulos, "Emergent phenomena induced by spin–orbit coupling at surfaces and interfaces," *Nature,* vol. 539, 509-517, 2016.

[22] V. R. Almeida, C. A. Barrios, R. R. Panepucci and M. Lipson, "All-optical control of light on a silicon chip," *Nature,* vol. 431, 1081-1084, 2004.

[23] G. T. Reed, G. Mashanovich, F. Y. Gardes and D. J. Thomson, "Silicon optical modulators," *Nature Photon.,* vol. 4, 518-526, 2010.

[24] S. Noda, M. Yokoyama, M. Imada, A. Chutinan and M. Mochizuki, "Polarization mode control of two-dimensional photonic crystal laser by unit cell structure design," *Science,* vol. 293, 1123-1125, 2001.

[25] S. Kocaman, M. S. Aras, P. Hsieh, J. F. McMillan, C. G. Biris, N. C. Panoiu, M. B. Yu, D. L. Kwong, A. Stein and C. W. Wong, "Zero phase delay in negative-refractive-index photonic crystal superlattices," *Nature Photon.,* vol. 5, 499-505, 2011.

[26] M. H. Teimourpour, D. N. Christodoulides and R. El-Ganainy, "Optical

revivals in nonuniform supersymmetric photonic arrays," *Opt. Lett.,* vol. 41, 372-375, 2016.

[27] S. John, "Strong localization of photons in certain disordered dielectric superlattices," *Phys. Rev. Lett.,* vol. 58, 2486, 1987.

[28] J. Wang and A. Z. Genack, "Transport through modes in random media," *Nature,* vol. 471, 345-348, 2011.

[29] P. Hsieh, C. Chung, J. F. McMillan, M. Tsai, M. Lu, N. C. Panoiu and C. W. Wong, "Photon transport enhanced by transverse Anderson localization in disordered superlattices," *Nature Phys.,* vol. 11, 268-274, 2015.

[30] S. Karbasi, R. J. Frazier, K. W. Koch, T. Hawkins, J. Ballato and A. Mafi, "Image transport through a disordered optical fibre mediated by transverse Anderson localization," *Nature Commun.,* vol. 5, 3362, 2014.

[31] T. Čižmár, M. Mazilu and K. Dholakia, " In situ wavefront correction and its application to micromanipulation," *Nature Photon.,* vol. 4, 388-394, 2010.

[32] B. Redding, S. F. Liew, R. Sarma and H. Cao, "Compact spectrometer based on a disordered photonic chip," *Nature Photon.,* vol. 7, 746-751, 2013.

[33] S. K. Bose, C. P. Lawrence, Z. Liu, K. S. Makarenko, R. M. van Damme, H. J. Broersma and W. G. van der Wiel, "Evolution of a designless nanoparticle network into reconfigurable boolean logic," *Nature Nanotech.,* vol. 10, 1048-1052, 2015.

[34] M. D. Kelzenberg, S. W. Boettcher, J. A. Petykiewicz, D. B. Turner-Evans, M. C. Putnam, E. L. Warren, J. M. Spurgeon, R. M. Briggs, N. S. Lewis and H. A. Atwater, "Enhanced absorption and carrier collection in Si wire arrays for photovoltaic applications," *Nature Mater.,* vol. 9, 239-244, 2010.

[35] E. Yablonivitch, "Inhibited Spontaneous Emission in Solid-State Physics and Electronics," *Phys. Rev. Lett.,* vol. 58, 2059, 1987.

[36] E. M. Purcell, "Resonance Absorption by Nuclear Magnetic Moments in a Solid," *Phys. Rev.,* vol. 69, 674, 1946.

[37] H. Altug, D. Englund and J. Vučković, "Ultrafast photonic crystal nanocavity laser," *Nature Phys.,* vol. 2, 484-488, 2006.

[38] T. A. Birks, J. C. Knight and P. S. J. Russell, "Endlessly single-mode photonic crystal fiber," *Opt. Lett.,* vol. 22, 961-963, 1997.

[39] E. Chow, A. Grot, L. W. Mirkarimi, M. Sigalas and G. Girolami, "Ultracompact biochemical sensor built with two-dimensional photonic crystal microcavity," *Opt. Lett.,* vol. 29, 1093-1095, 2004.

[40] T. Baba, "Slow light in photonic crystals," *Nature Photon.,* vol. 2, 265-473, 2008.

[41] C. Cho, J. Jeong, J. Lee and H. Jeon, "Photonic crystal band edge laser array with a holographically generated square-lattice pattern," *Appl. Phys. Lett.,* vol. 87, 161102, 2005.

[42] S. Kubo, D. Mori and T. Baba, "Low-group-velocity and low-dispersion slow light in photonic crystal waveguides," *Opt. Lett.,* vol. 32, 2981-2983, 2007.

[43] T. Baba, T. Kawasaki, H. Sasaki, J. Adachi and D. Mori, "Large delay-bandwidth product and delay tuning of slow light pulse in photonic crystal coupled waveguide," *Opt. Express,* vol. 16, 9245-9253, 2008.

[44] K. Rauscher, D. Erni, J. Smajic and C. Hafner, "Improved transmission for 60 photonic crystal waveguide bends," *Proceedings of Progress In Electromagnetics Research Symposium,* 25-28, 2004.

[45] D. Kim, S. Kim, J. Lee, S. Jeon and H. Jeon, "Free-standing GaN-based photonic crystal band-edge laser," *IEEE Photon. Tech. Lett.,* vol. 23, 1454-1456, 2011.

[46] G. T. Reed, "Silicon Photonics: The State of the Art," *Wiley,* 2008.

[47] S. Olivier, C. Smith, M. Rattier, H. Benisty, C. Weisbuch, T. Krauss, R. Houdré and U. Oesterlé, "Miniband transmission in a photonic crystal coupled-resonator optical waveguide," *Opt. Lett.,* vol. 26, 1019-1021, 2001.

[48] P. W. Anderson, "Absence of diffusion in certain random lattices," *Phys. Rev.,* vol. 109, 1492-1505, 1958.

[49] A. M. Portis, "Electronic structure of F centers: Saturation of the electron spin resonance," *Phys. Rev.,* vol. 91, 1071, 1953.

[50] N. Bloembergen, "On the interaction of nuclear spins in a crystalline lattice," *Physica,* vol. 15, 386-426, 1949.

[51] A. Miller and E. Abrahams, "Impurity conduction at low concentrations," *Phys. Rev.,* vol. 120, 745, 1960.

[52] G. Pfister, "Hopping transport in a molecularly doped organic polymer," *Phys. Rev. B,* vol. 16, 3676, 1977.

[53] P. W. Anderson, "The question of classical localization A theory of white paint?," *Phil. Mag. B,* vol. 52, 505-509, 1985.

[54] A. F. Ioffe and A. R. Regel, "Non-crystalline, amorphous and liquid electronic semiconductors," *Prog. Semicond.,* vol. 4, 237-291, 1960.

[55] D. S. Wiersma, P. Bartolini, A. Legendijk and R. Righini, "Localization of light in a disordered medium," *Nature,* vol. 390, 671-673, 1997.

[56] E. Abrahams, P. W. Anderson, D. C. Licciardello and T. V. Ramakrishnann, "Scaling theory of localization: absence of quantum diffusion in two dimensions," *Phys. Rev. Lett.,* vol. 42, 673-676, 1979.

[57] F. Scheffold, R. Lenke, R. Tweer and G. Maret, "Localization or classical diffusion of light?," *Nature,* vol. 398, 206-207, 1999.

[58] P. M. Johnson, A. Imhof, B. P. J. Bret, J. G. Rivas and A. Lagendijk, "Time-resolved pulse propagation in a strongly scattering material," *Phys. Rev. E,* vol. 68, 016604, 2003.

[59] T. Beek, P. Barthelemy, P. M. Johnson, D. S. Wiersma and A. Lagendijk, "Light transport through disordered layers of dense gallium arsenide submicron particles," *Phys. Rev. B,* vol. 85, 115401, 2012.

[60] S. E. Skipetro and J. H. Page, "Red light for Anderson localization," *New J. Phys.,* vol. 18, 021001, 2016.

[61] T. Sperling, W. Bührer, C. M. Aegerter and G. Maret, "Direct determination of the transition to localization of light in three dimensions," *Nature Photon.,* vol. 7, 48-52, 2013.

[62] F. Scheffold and D. S. Wiersma, "Inelastic scattering puts in question recent claims of Anderson localization of light," *Nature Photon.,* vol. 7, 934, 2013.

[63] T. Sperling, L. Schertel, M. Ackermann, G. J. Aubry, C. M. Aegerter and G. Maret, "Can 3D light localization be reached in 'white paint'?," *New J. Phys.,* vol. 18, 013039, 2016.

[64] N. Savage, "Digital spatial light modulators," *Nature Photon.,* vol. 3, 170-172, 2009.

[65] I. M. Vellekoop, A. Lagendijk and A. P. Mosk, "Exploiting disorder for perfect focusing," *Nature Photon.,* vol. 4, 320-322, 2010.

[66] J. Haberko, N. Muller and F. Scheffold, "Direct laser writing of three-dimensional network structures as templates for disordered photonic materials," *Phys. Rev. A,* vol. 88, 043822, 2013.

[67] J. W. Fleischer, T. Carmon, M. Segev, N. K. Efremidis and D. N. Christodoulides, "Observation of Discrete Solitons in Optically Induced Real Time Waveguide Arrays," *Phys. Rev. Lett.,* vol. 90, 023902, 2003.

[68] R. C. Rumpf, J. Pazos, C. R. Garcia, L. Ochoa and R. Wicker, "3D printed lattices with spatially variant self-collimation," *Prog. Electromagn. Res.,* vol. 139, 1-14, 2013.

[69] F. Riboli, N. Caselli, S. Vignolini, F. Intonti, K. Vynck, P. Barthelemy, A. Garardino, L. Balet, L. H. Li, A. Fiore, M. Gurioli and D. S. Wiersma, "Engineering of light confinement in strongly scattering disordered media," *Nature Mater.,* vol. 13, 720-725, 2014.

[70] R. Sarma, A. G. Yamilov, S. Petrenko, Y. Bromberg and H. Cao, "Control of Energy Density inside a Disordered Medium by Coupling to Open or Closed Channels," *Phys. Rev. Lett.,* vol. 117, 086803, 2016.

[71] I. M. Lifshitz, "The energy spectrum of disordered systems," *Adv. Phys.,* vol. 13, 483-536, 1964.

[72] S. Kim, S. Yoon, H. Seok, J. Lee and H. Jeon, "Band-edge lasers based on randomly mixed photonic crystals," *Opt. Express,* vol. 18, 7685-7692, 2010.

[73] S. Kim, J. Lee, H. Jeon, S. Callard, C. Seassal, S.-D. Song and H.-G. Park, "Simultaneous observation of extended and localized modes in compositional disordered photonic crystals," *Phys. Rev. A,* vol. 88, 023804, 2013.

[74] S. John, "Localization of light," *Phys. Today,* vol. 44, 32-40, 1991.

[75] C. Conti and A. Fratalocchi, "Dynamic light diffusion, three-dimensional Anderson localization and lasing in inverted opals," *Nature Phys.,* vol. 4, 794-798, 2008.

[76] C. Seassal, C. Monat, J. Mouette, E. Touraille, B. B. Bakir, H. T. Hattori, J. -L. Leclercq, X. Letartre, P. Rojo-Romeo and P. Viktorovitch, "InP bonded membrane photonics components and circuits: Toward 2.5 dimensional micro-nano-photonics," *IEEE J. Sel. Top. Quantum Electron.,* vol. 11, 395-407, 2005.

[77] C. Weisbuch and B. Vinter, "Quantum semiconductor structures: fundamentals and applications," *Academic press,* 2014.

[78] Y. Park, S. Kim, C. Moon and H. Jeon, "Butt-end fiber coupling to a surface-emitting Γ-point photonic crystal band edge laser," *Appl. Phys. Lett.,* vol. 90, 171115, 2007.

[79] N. Louvioin, D. Gérard, J. Mouette, F. de Fornel, C. Seassal, X. Letartre, A. Rahmani and S. Callard, "Local observation and spectroscopy of optical modes in an active photonic-crystal microcavity," *Phys. Rev. Lett.,* vol. 94, 113907, 2005.

[80] M. Hammer and O. V. Ivanova, "Effective index approximations of photonic crystal slabs: a 2-to-1-D assessment," *Opt. Quant. Electron.,* vol. 41, 267-283, 2009.

[81] P. A. Lee and T. V. Ramakrishnan, "Disordered electronic systems," *Rev. Mod. Phys.,* vol. 57, 287-337, 1985.

[82] D. J. Thouless, "Electrons in disordered systems and the theory of localization," *Phys. Rep.,* vol. 13, 93-142, 1974.

[83] S. John, C. Soukoulis, M. Cohen and E. N. Economou, "Theory of Electron Band Tails and the Urbach Optical-Absorption Edge," *Phys. Rev. Lett.,* vol. 57, 1777, 1986.

[84] P. van Mieghem, "Theory of band tails in heavily doped semiconductors," *Rev. Mod. Phys.,* vol. 64, 755-793, 1992.

[85] T. Pertsch, U. Peschel, J. Kobelke, K. Schuster, H. Bartelt, S. Nolte, A. Tünnermann and F. Lederer, "Nonlinearity and disorder in fiber arrays," *Phys. Rev. Lett.,* vol. 93, 053901, 2004.

[86] H. de Raedt, A. Lagendijk and P. de Veries, "Transverse localization of light," *Phys. Rev. Lett.,* vol. 62, 47-50, 1989.

[87] T. Schwartz, G. Bartal, S. Fashman and M. Segev, "Transport and Anderson localization in disordered two-dimensional photonic lattices," *Nature,* vol. 446, 52-55, 2007.

[88] S. Takeda, P. Viktorovitch and M. Obara, "Anderson localization of light in two-dimensional random photonic crystals," *ISAS 1st International symposium on IEEE,* 153-158, 2011.

[89] M. Spasenović, D. M. Beggs, P. Lalanne, T. F. Krauss and L. Kuipers, "Measuring the spatial extent of individual localized photonic states," *Phys. Rev. B,* vol. 86, 155153, 2012.

[90] A. Yamilov, X. Wu, X. Liu, R. P. H. Chang and H. Cao, "Self-optimization of optical confinement in an ultraviolet photonic crystal slab laser," *Phys. Rev. Lett.,* vol. 96, 083905, 2006.

[91] P. R. Villeneuve and M. Piche, "Photonic band gaps in two-dimensional square and hexagonal lattices," *Phys. Rev. B,* vol. 46, 4969, 1992.

[92] C. M. Anderson and K. P. Giapis, "Larger two-dimensional photonic band gaps," *Phys. Rev. Lett.,* vol. 77, 2949, 1996.

[93] J. D. Joannopoulos, P. R. Villeneuve and S. Fan, "Photonic crystals: putting a new twist on light," *Nature,* vol. 386, 143-149, 1997.

[94] F. Urbach, "The long-wavelength edge of photographic sensitivity and of the electronic absorption of solids," *Phys. Rev.,* vol. 92, 1324, 1953.

[95] J. A. van Vechten and T. K. Bergstresser, "Electronic structures of

semiconductor alloys," *Phys. Rev. B,* vol. 1, 3351-3358, 1970.

[96] A. Baldereschi and K. Maschke, "Band structure of semiconductor alloys beyond the virtual crystal approximation. effect of compositional disorder on the energy gaps in GaPxAs1-x," *Sold State Commun.,* vol. 16, 99-102, 1975.

[97] H. Cao, Y. G. Zhao, S. T. Ho, E. W. Seelig, Q. H. Wang and R. P. H. Chang, "Random laser action in semiconductor powder," *Phys. Rev. Lett.,* vol. 82, 2278-2281, 1999.

[98] M. C. Teich and B. Saleh, "Fundamentals of photonics," *Canada, Wiley interscience,* 1991.

[99] R. Abou-Chacra, D. J. Thouless and P. W. Anderson, "A self-consistent theory of localization," *J. Phys. C: Solid St. Phys.,* vol. 6, 1734-1752, 1973.

[100] M. P. van Albada and A. Lagendijk, "Observation of weak localization of light in a random medium," *Phys. Rev. Lett.,* vol. 55, 2692-2695, 1985.

[101] P. E. Wolf and G. Maret, "Weak localization and coherent backscattering of photons in disordered media," *Phys. Rev. Lett.,* vol. 55, 2696-2699, 1985.

[102] S. Etemad, R. Thompson and M. J. Andrejco, "Weak localization of photons: Universal fluctuations and ensemble averaging," *Phys. Rev. Lett.,* vol. 57, 575-578, 1986.

[103] M. Burresi, V. Radhalakshmi, R. Savo, J. Bertolotti, K. Vynck and D. S. Widersma, "Weak localization of light in superdiffusive random systems," *Phys. Rev. Lett.,* vol. 108, 110604, 2012.

[104] J. Fallert, R. J. Dietz, J. Sartor, D. Schneider, C. Klingshirn and H. Kalt, "Co-existence of strongly and weakly localized random laser modes," *Nature Photon.,* vol. 3, 279-282, 2009.

[105] J. Topolancik, B. Ilic and F. Vollmer, "Experimental observation of strong photon localization in disordered photonic crystal waveguides," *Phys. Rev. Lett.,* vol. 99, 253901, 2007.

[106] D. Laurent, O. Legrand, P. Sebbah, C. Vanneste and F. Mortessagne, "Localized modes in a finite-size open disordered microwave cavity," *Phys. Rev. Lett.,* vol. 99, 253902, 2007.

[107] J. T. Edwards and D. J. Thouless, "Numerical studies of localization in disordered systems," *J. Phys. C: Solid St. Phys.,* vol. 5, 807-820, 1972.

[108] F. Wegner, "Inverse participation ratio in 2+ ε dimensions," *Z. Phys. B Con. Mat.,* vol. 36, 209-214, 1980.

[109] N. C. Murphy, R. Wortis and W. A. Atkinson, "Generalized inverse participation ratio as a possible measure of localization for interacting systems," *Phys. Rev. B,* vol. 83, 184206, 2011.

[110] F. Evers and A. D. Mirlin, "Fluctuations of the inverse participation ratio at the Anderson transition," *Phys. Rev. Lett.,* vol. 84, 3960, 2000.

[111] R. Zimmermann and E. Runge, "Excitons in narrow quantum wells: disorder localization and luminescence kinetics," *Phys. Stat. Sol. (a),* vol. 164, 511-516, 1997.

[112] C. M. Soukoulis, M. H. Cohen and E. N. Economou, "Exponential band tails in random systems," *Phys. Rev. Lett.,* vol. 53, 616, 1984.

[113] E. Yablonovitch, T. J. Gmitter, R. D. Meade, A. M. Rappe, K. D. Brommer and J. D. Joannopoulos, "Donor and acceptor modes in photonic band structure," *Phys. Rev. Lett.,* vol. 67, 3380-3383, 1991.

[114] T. Quang, M. Woldeyohannes, S. John and G. S. Agarwal, "Coherent control of spontaneous emission near a photonic band edge: a single-atom optical memory device," *Phys. Rev. Lett.,* vol. 79, 5238-5241, 1997.

[115] D. M. Jović, Y. S. Kivshar, C. Denz and M. R. Belić, "Anderson localization of light near boundaries of disordered photonic lattices," *Phys. Rev. A,* vol. 83, 033813, 2011.

[116] Z.-F. Shi, X.-G. Sun, D. Wu, T.-T. Xu, Y.-T. Tian, Y.-T. Zhang, X.-J. Li and G.-T. Du, "Near-infrared random lasing realized in a perovskite CH3NH3PbI3 thin film," *J. Mater. Chem. C,* vol. 4, 8373-8379, 2016.

[117] S. García-Revilla, J. Fernández, M. A. Illarramendi, B. García-Ramiro, R. Balda, H. Cui, M. Zayat and D. Levy, "Ultrafast random laser emission in a dye-doped silica gel powder," *Opt. Express,* vol. 16, 12251-12263, 2008.

[118] M. Sakai, Y. Inose, K. Ema, T. Ohtsuki, H. Sekiguchi, A. Kikuchi and K. Kishino, "Random laser action in GaN nanocolumns," *Appl. Phys. Lett.,* vol. 97, 151109, 2010.

[119] H. Cao, "Lasing in random media," *Waves in Random Media,* vol. 13, R1-R39, 2003.

[120] R. V. Ambartsumyan, P. G. Kryukov and V. C. Letokhov, "Dynamics of emission line narrowing for a laser with nonresonant feedback," *J. Exp. Theor. Phys.,* vol. 24, 1129, 1967.

[121] R. V. Ambartsumyan, N. G. Basov, P. G. Kryukov and V. S. Letokhov, "A laser with nonresonant feedback," *J. Exp. Theor. Phys.,* vol. 24, 481, 1967.

[122] V. M. Markushev, V. F. Zolin and C. M. Briskina, "Powder laser," *Zh. Prikl.*

Spektrosk., vol. 45, 847, 1986.

[123] N. M. Lawandy, R. M. Balachandran, A. S. L. Gomes and E. Sauvain, "Laser action in strongly scattering media," *Nature,* vol. 368, 436-438, 1994.

[124] S. V. Frolov, Z. V. Vardeny, K. Yoshino, A. Zakhidov and R. H. Baughman, "Stimulated emission in high-gain organic media," *Phys. Rev. B,* vol. 59, R5284, 1999.

[125] K. Yoshino, S. Tatsuhara, Y. Kawagishi, M. Ozaki, A. A. Zakhidov and Z. V. Vardeny, "Amplified spontaneous emission and lasing in conducting polymers and fluorescent dyes in opals as photonic crystals," *Appl. Phys. Lett.,* vol. 74, 2590-2592, 1999.

[126] D. S. Wiersma, "The physics and applications of random lasers," *Nature Phys.,* vol. 4, 359-367, 2008.

[127] H. E. Türeci, L. Ge, S. Rotter and A. D. Stone, "Strong interactions in multimode random lasers," *Science,* vol. 320, 643-646, 2008.

[128] K. L. van der Molen, R. W. Tjerkstra, A. P. Mosk and A. Lagendijk, "A spatial extent of random laser modes," *Phys. Rev. Lett.,* vol. 98, 143901, 2007.

[129] D. S. Wiersma and S. Cavalieri, "Temperature-controlled random laser action in liquid crystal infiltrated systems," *Phys. Rev. E,* vol. 66, 056612, 2002.

[130] A. G. Ardakani, M. Hosseini, A. R. Bahrampour and S. M. Mahdavi, "Temperature tunable random laser using superconducting materials," *Opt. Commun.,* vol. 285, 1900-1904, 2012.

[131] S. Gottardo, S. Cavalieri, O. Yaroshchuk and D. S. Wiersma, "Quasi-Two-Dimensional Diffusive Random Laser Action," *Phys. Rev. Lett.,* vol. 93, 263901, 2004.

[132] A. G. Ardakani, S. M. Mahdavi and A. R. Bahrampour, "Tuning of random lasers by means of external magnetic fields based on the Voigt effect," *Opt. Laser Technol.,* vol. 47, 121-126, 2013.

[133] M. Leonetti, C. Conti and C. Lopez, "The mode-locking transition of random lasers," *Nature Photon.,* vol. 5, 615-617, 2011.

[134] N. Bachelard, J. Andreasen, S. Gigan and P. Sebbah, "Taming random lasers through active spatial control of the pump," *Phys. Rev. Lett.,* vol. 109, 033903, 2012.

[135] T. Hisch, M. Liertzer, D. Pogany, F. Mintert and S. Rotter, "Temperature tunable random laser using superconducting materials," *Phys. Rev. Lett.,* vol.

111, 023902, 2013.

[136] D. S. Wiersma, "Clear directions for random lasers," *Nature,* vol. 539, 360-361, 2016.

[137] S. Schönhuber, M. Brandstetter, T. Hisch, C. Deutsch, M. Krall, H. Detz, A. M. Andrews, G. Strasser, S. Rotter and K. Unterrainer, "Random lasers for broadband directional emission," *Optica,* vol. 3, 1035-1038, 2016.

[138] X. Jiang and C. M. Soukoulis, "Time dependent theory for random lasers," *Phys. Rev. Lett.,* vol. 85, 70, 2000.

[139] A. L. Burin, M. A. Ratner, H. Cao and R. P. H. Chang, "Model for a random laser," *Phys. Rev. Lett.,* vol. 87, 215503, 2001.

[140] L. S. Froufe-Pérez, W. Guerin, R. Carminati and R. Kaiser, "Threshold of a random laser with cold atoms," *Phys. Rev. Lett.,* vol. 102, 173903, 2009.

[141] B. Redding, M. A. Choma and H. Cao, "Speckle-free laser imaging using random laser illumination," *Nature Photon.,* vol. 6, 355-359, 2012.

[142] R. C. Polson and Z. V. Varden, "Random lasing in human tissues," *Appl. Phys. Lett.,* vol. 85, 1289-1291, 2004.

[143] R. Choe, A. Corlu, K. Lee, T. Durduran, S. D. Konecky, M. Grosicka-Koptyra, S. R. Arridge, B. J. Czerniecki, D. L. Fraker, A. DeMichele, B. Chance, M. A. Rosen and A. G. Yodh, "Diffuse optical tomography of breast cancer during neoadjuvant chemotherapy: A case study with comparison to MRI," *Med. Phys.,* vol. 32, 1128-1139, 2005.

[144] M. Padgett and R. Bowman, "Tweezers with a twist," *Nature Photon.,* vol. 5, 343-348, 2011.

[145] A. González-Tudela, C. L. Hung, D. E. Chang, J. I. Cirac and H. J. Kimble, "Subwavelength vacuum lattices and atom–atom interactions in two-dimensional photonic crystals," *Nature Photon.,* vol. 9, 320-325, 2015.

[146] N. Bozinovic, Y. Yue, Y. Ren, M. Tur, P. Kristensen, H. Huang, A. E. Willner and S. Ramachandran, "Terabit-scale orbital angular momentum mode division multiplexing in fibers," *Science,* vol. 340, 1545-1548, 2013.

[147] A. Nicolas, L. Veissier, L. Giner, E. Giacobino, D. Maxwin and J. Laurat, "A quantum memory for orbital angular momentum photonic qubits," *Nature Photon.,* vol. 8, 234-238, 2014.

[148] L. Wang, S. Kruk, H. Tant, T. Li, I. Kravchenko, D. N. Neshev and Y. S. Kivshar, "Grayscale transparent metasurface holograms," *Optica,* vol. 3, 1504-1505, 2016.

[149] B. Shen, P. Wang, R. Polson and R. Menon, "An integrated-nanophotonics polarization beamsplitter with 2.4 × 2.4 μm2 footprint," *Nature Photon.,* vol. 9, 378-382, 2015.

[150] A. Y. Piggott, J. Lu, K. G. Lagoudakis, J. Patykiewicz, T. M. Babinec and J. Vučković, "Inverse design and demonstration of a compact and broadband on-chip wavelength demultiplexer," *Nature Photon.,* vol. 9, 374-377, 2015.

[151] G. Molina-Terriza, J. P. Torres and L. Torner, "Twisted photons," *Nature Phys.,* vol. 3, 305-310, 2007.

[152] G. K. L. Wong, M. S. Kang, H. W. Lee, F. Biancalana, C. Conti, T. Weiss and P. S. J. Russell, "Excitation of orbital angular momentum resonances in helically twisted photonic crystal fiber," *Science,* vol. 337, 446-449, 2012.

[153] Y. V. Kartashov, A. Ferrando, A. A. Egorov and L. Torner, "Soliton topology versus discrete symmetry in optical lattices," *Phys. Rev. Lett.,* vol. 95, 123902, 2005.

[154] J. W. Fleischer, G. Bartal, O. Cohen, O. Manela, M. Segev, J. Hudock and D. N. Christodoulides, "Observation of vortex-ring “discrete” solitons in 2D photonic lattices," *Phys. Rev. Lett.,* vol. 92, 123904, 2004.

[155] I. Freund, "Bichromatic optical Lissajous fields. Optics communications," *Opt. Commun.,* vol. 226, 351-376, 2003.

[156] L. Zdeborová, "Machine learning: New tool in the box," *Nature Phys.,* vol. 13, 420-421, 2017.

국문 초록

빛을 제어하여 원하는 광학적 특성을 형성하는 것은 오랜 기간 연구되어온 광학 및 광자학 분야의 중요한 주제 중 하나이다. 빛의 세기와 편광을 비롯하여 주파수와 위상, 나아가 전자기장의 시공간적 분포를 자유롭게 조절하는 것은 기초과학적인 관점에서 추구하는 중요한 목표임은 물론이고, 빛의 형상을 다루는 응용과학과 산업분야의 기반기술로서 더욱 진보된 광학적 기능성과 부가가치를 창출할 수 있기 때문이다.

빛의 제어는 빛이 진행하는 매질의 전자기학적 물성에 대한 이해를 바탕으로 매질의 광학적 특성을 시공간적으로 조절하여 빛의 형상을 제어하는 연구를 통칭한다고 볼 수 있다. 파장에 대한 분산관계, 편광에 대한 복굴절, 비선형성 등으로 대표되는 매질의 재료적 특성에 기반한 제어가 역사적으로 주요하게 연구되어온 방법론이지만, 물질의 공간적 배치에 따른 경계면에서의 반사, 회절, 산란 등의 구조적 특성에 대한 연구도 활발히 이루어지고 있으며 광자결정, 메타물질, 위상 광자학 등 이미 현대 광자학의 큰 줄기를 이루고 있다. 이러한 재료·구조적 방법론을 기반으로 빛을 제어하여 구조화된 빛(structured light)을 형성하는 것, 그리고 이를 응용하여 기존의 광학계를 개선하고 새로운 광소자를 구현하는 것이 빛의 제어에 대한 연구의 본질이라 할 수 있다.

따라서 한정된 재료 내에서 빛의 제어에 대한 방법론은 결국 물질의 시공간적 배치에 대한 문제로 귀결된다. 주기적인 배열을 기초로 하는 구조는 직관적인 설계를 바탕으로 많은 분야에 사용되고 있지만, 제한적인 구조 변수에 기인하는 근본적인 이유로 복잡도가 요구되는 광학계에는 적용하기 어렵다는 한계가 있다. 반면, 특별한 제한을 두지 않고 매질을 무질서하게 배치하는 광학적 무질서계는 구조적 자유도가 계의 크기에 따라 증가하지만 광학적

특성을 예측하고 원하는 형태로 발현시키기 위해 많은 자원이 소모된다. 즉, 구조적 자유도와 예측 가능성은 상보적인 관계에 있다.

본 학위 논문에서는 이를 효과적으로 절충하여 현실의 복잡계에 대응되는 빛의 형상을 구현할 수 있는 충분한 수준의 자유도를 확보하면서도 광학적 특성에 대한 예측 및 설계가 용이한 광자결정합금 플랫폼을 제안하였다. 구조 내의 광원자를 다양화하여 자유도를 확보하되 근본이 되는 결정구조를 유지함으로써 개별 격자점에서의 산란강도를 독립적으로 조절하여 전체적인 광학계를 픽셀단위로 설계할 수 있게 하였다.

이러한 광학계의 분광학적 특성을 조사하여 고유모드가 광 띠틈 내부에 발현되는 광자 띠꼬리임을 밝히고, 모드가 분포하는 에너지 범위는 결정구조와 산란강도에 의해 결정됨을 확인하였다. 그리고 모드의 에너지와 구조의 산란강도에 따라 공간적인 근접장 형태가 약한 국지화에서 강한 국지화를 아우르는 다양한 형태로 넓은 공간적 범위에 걸쳐 분포함을 발견하였다. 이로써 광자결정합금 플랫폼 내의 고유모드인 광자 띠꼬리의 국지화 현상을 실험적으로 입증하였다. 또한 그 모드 특성은 넓은 주파수 대역과 공간적 범위 내에 예측 가능한 형태로 분포하기 때문에 빛의 제어에 매우 유용할 수 있음을 보였다.

광자 띠꼬리를 공진모드로 하여 발진하는 새로운 광소자인 띠꼬리 레이저의 개념을 제안하고 InAsP/InP 다중양자우물을 내재하는 평판 도파로에 이를 구현해 2차원 박막 내에서의 빛의 제어를 직접적으로 시연하였다. 광자결정합금계 내부의 구조적 변수만을 이용하여 모드 개수를 멀티모드에서 단일모드까지 점진적으로 조절할 수 있으며, 단일모드로 작동하는 띠꼬리 레이저의 모드 에너지와 모드 크기를 정밀하게 제어할 수 있음을 확인하였다. 나아가 모드의 근접장 형태를 기본모드부터 고위모드까지 다양하게 변화시킬 수 있음을 시연하였다.

띠꼬리 레이저에서 구조적 자유도에 기반한 빛의 제어에 대한 설계는 기존의 플랫폼들보다 훨씬 직관적이고 효과적이며, 제어 가능한 광학적 특성의 범위와 실제 시연의 수준은 알려진 어떠한 레이저 플랫폼보다 우수했다. 띠꼬리 레이저의 성능 또한 현 세대의 공동 레이저와 견줄 수 있는 수준이었다. 따라서 본 논문에서 제안하는 빛의 제어 수단으로서의 광자 띠꼬리와 띠꼬리 레이저 플랫폼은 현재까지 알려진 레이저 플랫폼을 통합하는 한편, 막대한 구조적 자유도에 대한 직관적인 설계를 바탕으로 더욱 넓은 범위에서 정교하게 빛을 제어하고 다양한 근접장 형태를 구현하는데 널리 활용됨으로써 빛의 제어에 기초하는 다양한 분야의 발전에 기여할 수 있을 것으로 기대한다.

주요어: 빛의 제어, 구조화된 빛, 근접장 제어, 빛의 국지화, 광자 띠꼬리, 띠꼬리 레이저, 광자결정합금, 랜덤 레이저

학번: 2011-23275